UNIVERSITAT JAUME I

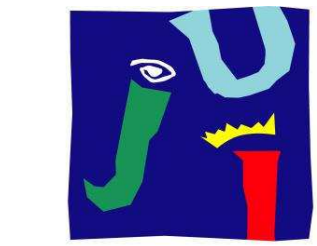

UNIVERSITAT JAUME·I

Macro- and nanoscale self-assembled amino acid derivatives as reduction-sensitive and photoactive materials

Ph.D. Thesis

Diego Navarro Barreda

Supervisors

Juan Felipe Miravet Celades

Francisco Galindo Honrubia

Castelló de la Plana, May 2022

Programa de Doctorat en Ciències

Escola de Doctorat de la Universitat Jaume I

Macro- and nanoscale self-assembled amino acid derivatives as reduction-sensitive and photoactive materials

Memòria presentada per Diego Navarro Barreda per a optar al grau de doctor per la Universitat Jaume I

Doctorand

Diego Navarro Barreda

DIEGO\| NAVARRO \|BARREDA Digitally signed by DIEGO\| NAVARRO\| BARREDA Date: 2022.05.05 20:01:25 +02'00'

Directors

Juan F. Miravet Celades

JUAN FELIPE\| MIRAVET\| CELADES Firmado digitalmente por JUAN FELIPE\| MIRAVET\|CELADES Fecha: 2022.05.05 20:30:47 +02'00'

Francisco Galindo Honrubia

GALINDO HONRUBIA FRANCISCO - 20154900T Firmado digitalmente por GALINDO HONRUBIA FRANCISCO - 20154900T Nombre de reconocimiento (DN): c=ES, serialNumber=IDCES-20154900T, givenName=FRANCISCO, sn=GALINDO HONRUBIA, cn=GALINDO HONRUBIA FRANCISCO - 20154900T Fecha: 2022.05.05 21:27:09 +02'00'

Castelló de la Plana, maig 2022

Grant Fundings

The research presented in this thesis has been funded by:

- Grant FPU16/02681, supported by Ministerio de España de Educación, Cultura y Deporte.
- Grant CTQ2015-71004-R, supported by Ministerio de España de Economía y Competitividad.
- Grant RTI2018-101675-B-I00, supported by Ministerio de España de Ciencia, Innovación y Universidades.
- Grant AICO/2020/322, supported by Generalitat Valenciana.
- Grant UJI-B2018-54, supported by Universitat Jaume I.
- Grant UJI-B2018-30, supported by Universitat Jaume I.

Creative Commons License

Publications

Thesis by a compendium of publications:

D. Navarro-Barreda, C.A. Angulo-Pachón, B. Bedrina, F. Galindo, J. F. Miravet, A Dual Stimuli Responsive Supramolecular Gel Provides Insulin Hydrolysis Protection and Redox-Controlled Release of Actives, Macromol. Chem. Phys. 221 (2020) 1900419. https://doi.org/10.1002/macp.201900419. (2020 JOURNAL IMPACT FACTOR 2.527)

D. Navarro-Barreda, C.A. Angulo-Pachón, F. Galindo, J. F. Miravet, Photoreversible formation of nanotubes in water from an amphiphilic azobenzene derivative, Chem. Commun. 57 (2021) 11545–11548. https://doi.org/10.1039/d1cc04319f. (2020 JOURNAL IMPACT FACTOR 6.222)

D. Navarro-Barreda, B. Bedrina, F. Galindo, J. F. Miravet, Glutathione-responsive molecular nanoparticles from a dianionic bolaamphiphile and their use as carriers for targeted delivery, J. Colloid Interface Sci. 608 (2022) 2009–2017. https://doi.org/10.1016/j.jcis.2021.10.142. (2020 JOURNAL IMPACT FACTOR 8.128)

D. Navarro-Barreda, B. Bedrina, C.A. Angulo-Pachón, J. F. Miravet, D. Pérez-Sala, F. Galindo, Structure-performance relationships of four lysosomal markers used for the imaging of HT-29 cancer cells and a cellular model of lysosomal storage disease (Niemann-Pick C), Dye. Pigment. 201 (2022) 110236. https://doi.org/10.1016/j.dyepig.2022.110236. (2020 JOURNAL IMPACT FACTOR 4.889)

"This thesis has been accepted by the co-authors of the publications listed above that have waived the right to present them as a part of another Ph.D. thesis."

Conferences

This work has been presented in the following conferences:

Molecular nanogels oriented to the solution of biomedical challenges. Diego Navarro Barreda; César Augusto Angulo Pachón; Francisco Galindo Honrubia; Juan Felipe Miravet Celades. IV Simposio de Investigadores Jóvenes de la Real Sociedad Española de Química. Badajoz (España). 2017 *(Poster Presentation)*

Self-assembled Molecular Nanoparticles Containing Disulfide Moieties as Stimuli Responsive Nanocarriers. Diego Navarro Barreda; César Augusto Angulo Pachón; Francisco Galindo Honrubia; Juan Felipe Miravet Celades. XXXVII Reunión Bienal de la Real Sociedad Española de Química. San Sebastián (España). 2019 *(Poster Presentation)*

Glutathione-responsive molecular nanoparticles from a dianionic bolaamphiphile and their use for targeted delivery. Diego Navarro Barreda; Begoña Bedrina Broch; Francisco Galindo Honrubia; Juan Felipe Miravet Celades. 35th Conference of the European Colloid & Interface Society. Athens, Grecia. 2021. *(Poster Presentation)*

Acknowledgements

M'agradaria començar aquesta secció mostrant el més sincer agraïment als meus supervisors Juan F. Miravet, coordinador del grup d'investigació *'ORGNANO - Nanomaterials Moleculars Orgànics amb Aplicacions Biomèdiques'*, i Francisco Galindo, coordinador del grup d'investigació *'FYS - Fotoquímica i Sensors'*, de la Universitat Jaume I. Dos excel·lents professionals als quals us agraïsc les vostres enormes capacitats per a guiar-me i ajudar-me sempre que ho he necessitat.

En segon lloc, m'agradaria agrair a aquelles persones, el treball i el suport de les quals han contribuït directament als resultats obtinguts en aquesta tesi doctoral. Especialment, al Dr. César A. Angulo-Pachón per la teua ajuda i savis consells en el pla sintètic, a Begoña Bedrina per la teua aportació en la part biològica i assajos cel·lulars, i a la Dr. Dolores Pérez-Sala per oferir-nos la possibilitat d'estudiar els nostres sistemes en altres models cel·lulars de rellevància.

També, vull agrair a tots els companys i companyes del grup d'investigació, alguns presents, uns altres ja doctorats, que m'han acompanyat en aquesta etapa i han compartit laboratori amb mi: en els inicis d'aquest camí, al Dr. Felip-León i al Dr. Ojeda-Flores, i recentment, al Dr. Muñoz-Resta, a la Dr. Torres-Martínez, a Ana Bernal, Víctor Pozo, Carla Arnau, Jean Colombari i Ana López. Gràcies, perquè heu sigut un pilar fonamental en tot moment. Aprofite per a estendre els meus agraïments als companys de treball d'altres grups d'investigació pels seus consells i ajuda rebuda, així com als estudiants que temporalment van formar part del grup. A tots, moltes gràcies.

Esment especial per als meus familiars i amics, per la vostra paciència i suport, i sobretot per ajudar-me a desconnectar, calmar la meua ment, i oblidar-me per

moments de la tesi doctoral. Com va dir Ciceró, "*La persecució, fins i tot de les millors coses, ha de ser calmada i tranquil·la*". De manera especial vull agrair a Lorena, estic summament agraït i orgullós de tindre't al meu costat tots els dies. No tinc cap dubte que el teu suport incondicional i la teua confiança en mi ha sigut essencial per a poder completar aquesta etapa. Química de formació, i actualment, professora d'educació secundària, sé que amb la teua especial vocació per la química un futur amb nous científics està assegurat.

Finalment, vull agrair al Ministeri d'Educació, Cultura i Esport d'Espanya per concedir-me una ajuda predoctoral (FPU) i a la Universitat Jaume I per brindar-me la possibilitat d'aconseguir el màxim grau acadèmic en la meua carrera.

Gràcies a tots els que m'heu ajudat en aquest viatge.

Abstract

This Ph.D. thesis, entitled "Macro- and nanoscale self-assembled amino acid derivatives as reduction-sensitive and photoactive materials", focuses on the design, development and characterization of chemical compounds based on amino acids that self-assemble into macro- and nanomaterials, which are studied and evaluated in biomedical applications such as controlled release or bioimaging.

Being a thesis made by a compendium of articles, it is structured into eight chapters, four of which correspond to the published articles, preceded by two initial chapters (general introduction and objectives of the thesis), and ending with two final chapters (general discussion and conclusions).

In Chapter 1, a general introduction is included concerning the current knowledge on the use of macro, micro and nanoscale materials used in biomedical applications, justifying the importance and relevance of the contents included in this thesis. A general description of the field of supra-molecular gels is presented, focusing on gels derived from amino acids and peptides. An overview of nanomedicine is also presented, highlighting the importance of nanoparticles in the development of this field. The advantages that they offer over classical medicine, prominent examples, studies and advances in the field are exposed. A brief introduction regarding bioimaging and small organic fluorophores is also included.

Chapter 2 presents the general and specific objectives addressed in each chapter of this Ph.D. thesis.

In Chapter 3, the study of two supramolecular gelators that contain a central disulfide bond and two carboxylic acid groups at the ends of the molecule is presented. It is shown that those hydrogels (gels in an aqueous medium) can respond to stimuli. On the one hand, they respond in a reducing environment by transforming the disulfide unit into the corresponding thiols after reduction. On the other hand, due to the presence of carboxyl groups, hydrogels show a response associated with the pH of the medium. Taking advantage of these properties, controlled release studies are carried out. For this purpose, a dye (bromophenol blue) is used to monitor its release in the presence of a reducing species (TCEP). The pH-responsive property is used for the controlled release of the hormone insulin. It is shown that insulin is loaded onto hydrogels, and these hydrogels prevent insulin degradation against acid and enzymatic (pepsin) hydrolysis. It is concluded that this behaviour would enable the use of these hydrogels for the oral administration of drugs, among other possible applications.

In Chapter 4, the formation in aqueous media of nanoparticles from an bolaamphiphilic molecule (a molecule with hydrophilic groups at both ends of a hydrophobic central chain) is described. This molecule incorporates a central disulfide bond to generate nanoparticles capable of responding to a reducing stimulus (glutathione). The nanoparticles are used as a nanocarrier for a lipophilic mitochondrial marker ($DiOC_6(3)$). It is shown that the nanoparticles, due to the presence of the disulfide groups, quench the fluorescence of the marker, which is recovered after its subsequent release. The internalization of this fluorescent probe in human colorectal adenocarcinoma cells (HT-29) is studied. It was determined that a greater internalization of the probe is achieved when it is encapsulated in the nanoparticles. On the other hand, a significant increase in intracellular fluorescence is observed when cancer cells are previously stimulated

to increase glutathione levels. It is concluded that these new molecular nanoparticles could be considered a theranostic tool by simultaneously achieving targeted delivery of lipophilic substances and signalling high levels of an analyte, in this case, glutathione.

In Chapter 5, a dipeptide derived from valine and glycine that self-assembles to form nanotubes in aqueous media is presented. This molecule has an azobenzene unit that enables responsiveness to light. Irradiation with ultraviolet light (wavelength of 365 nanometres) causes *trans-cis* isomerization of the azobenzene unit, resulting in subsequent disassembly of the nanotubes. Interestingly, nanotubes can be recovered in solution either by thermal recovery (*trans*-isomer thermodynamically more stable) or photoinduced by irradiation with visible light (wavelength of 457 nm) that causes *cis-trans* isomerization, restoring the nanotubes. It can be affirmed that this control of the formation/disassembly of molecular nanotubes using light could constitute a relevant tool to develop intelligent systems with biomedical applications, such as ultraviolet light-mediated drug delivery, or actuators as nanotubes can convert light into another type of energy, in this case, assembly/disassembly movement.

In Chapter 6, four new derivatives of BODIPY functionalized with pseudo-peptide chains that tend to aggregate are reported. This study aims to determine which structural factors most notably influence aggregation, internalization, intracellular localization and organelle visualization. In an aqueous medium, at concentrations in the micromolar range, three compounds tend to form weakly emissive nanoparticles while one remains soluble and highly fluorescent. On the other hand, in the nanomolar concentration range, all compounds are soluble in

water. The cellular internalization of the compounds in human colon adenocarcinoma cells (HT-29) is studied. All compounds are absorbed by HT-29 cells, but the molecule with the amino acid lysine present in its structure is the one that shows greater internalization and clearer lysosomal localization. Indeed, very promising results in this regard were obtained in a cellular model (human adrenal carcinoma SW13/cl.2 cells) of lysosomal storage disease (Niemann-Pick type C).

Finally, Chapter 7 includes a discussion section of the global results and their significance and Chapter 8 lists the general conclusions of the doctoral thesis.

Resum en valencià

La present tesi doctoral, amb títol *"Macro- and nanoscale self-assembled amino acid derivatives as reduction-sensitive and photoactive materials"*, se centra en el disseny, desenvolupament i caracterització de compostos químics basats en aminoàcids que, mitjançant autoassemblatge, donen lloc a materials macro i nanoscòpics, els quals s'estudien i avaluen en aplicacions del camp de la biomedicina, com l'alliberament controlat de fàrmacs o la visualització cel·lular.

En tractar-se d'una tesi realitzada per compendi d'articles, aquesta s'estructura en 8 capítols, quatre d'ells corresponen als articles publicats, més dos capítols inicials (introducció general i objectius de la tesi) i dos capítols finals (discussió general i conclusions).

En el Capítol 1, s'inclou una introducció general en relació amb els coneixements actuals sobre materials macro, micro i nanoscòpics utilitzats en aplicacions biomèdiques, justificant la importància i rellevància dels continguts que s'engloben en aquesta tesi. Es presenta una descripció general del camp dels gels supra-moleculars, centrant un apartat, especialment, als gels derivats d'aminoàcids i pèptids. També es presenta una visió general de la nanomedicina destacant la importància de les nanopartícules en el desenvolupament d'aquest camp. S'exposen els avantatges que aquestes ofereixen respecte a la medicina clàssica, principals exemples, estudis i avanços en el camp. També s'inclou una breu introducció sobre fluoròfors orgànics i visualització cel·lular amb fluorescencia.

En el Capítol 2, es presenten els objectius generals i específics que s'aborden en cada capítol de la tesi doctoral.

En el Capítol 3, es presenta l'estudi de dos gelants supramoleculars que contenen un enllaç disulfur central i dos grups d'àcid carboxílic en els extrems de la molècula. Es demostra que els hidrogels (gels formats en medi aquós) tenen capacitat de resposta a estímuls. D'una banda, responen en un entorn reductor en transformar la unitat de disulfur en els corresponents tiols després de la reducció. D'altra banda, els hidrogels a causa de la presència dels grups carboxil mostren resposta associada al pH del medi. Aprofitant ambdues propietats, es duen a terme estudis d'alliberament controlat. Per a això, s'utilitza un colorant (blau de bromofenol) per a monitorar el seu alliberament en presència d'una espècie reductora (TCEP). En canvi, la propietat de resposta al pH s'utilitza per a l'alliberament controlat de l'hormona insulina. Es va demostrar que la insulina es carrega en els hidrogels i aquests eviten la seua degradació enfront de la hidròlisi àcida i enzimàtica amb pepsina. Es conclou que aquest comportament podria permetre l'ús d'aquests hidrogels per a l'administració oral de fàrmacs, entre altres possibles aplicacions.

En el Capítol 4, es descriu la formació en medis aquosos de nanopartícules a partir d'una molècula bolaanfifílica (molècula amb dos grups hidrofílics en els extrems d'una cadena central hidrofòbica). Aquesta molècula incorpora de nou un enllaç disulfur central amb l'objectiu de generar nanopartícules amb capacitat de resposta a estímuls reductors (principalment, glutatió). Les nanopartícules s'utilitzen com nanoportadors d'un marcador mitocondrial lipofílic ($DiOC_6(3)$). Es demostra que les nanopartícules, a causa de la presència dels grups disulfur, desactiven la fluorescència del marcador, la qual es recupera després del seu posterior alliberament. A més a més, s'estudia la internalització d'aquesta sonda fluorescent en cèl·lules de adenocarcinoma colorectal humà (HT-29). Es determina que s'aconsegueix una major internalització de la sonda quan aquesta es troba encapsulada en les nanopartícules. D'altra banda, s'observa un augment

significatiu de la fluorescència intracel·lular quan les cèl·lules canceroses són prèviament estimulades per a augmentar els nivells de glutatió. Es conclou que aquestes noves nanopartícules moleculars podrien considerar-se una eina teranòstica en aconseguir simultàniament el lliurament dirigit de substàncies lipofíliques i l'assenyalament d'alts nivells d'un analític, en aquest cas el glutatió.

En el Capítol 5, es presenta un dipèptid derivat dels aminoàcids valina i glicina que s'autoassembla per a formar nanotubs en medis aquosos. Aquesta molècula presenta una unitat de azobenzè que li confereix capacitat de resposta a la llum. La irradiació amb llum ultraviolada (longitud d'ona de 365 nanòmetres) provoca la isomerització *trans-cis* de la unitat de azobenzè, el que produeix el posterior desencadellament dels nanotubs. Interessantment, es poden recuperar els nanotubs en dissolució ja siga per recuperació tèrmica (isòmer *trans* més estable termodinàmicamente) o fotoinduïda mitjançant la irradiació amb llum visible (de longitud d'ona de 457 nm) que provoca la isomerització *cis-trans*, restaurant els nanotubs. Es pot afirmar que aquest control de la formació/desencadellament dels nanotubs moleculars utilitzant llum podria constituir una eina rellevant per a desenvolupar sistemes intel·ligents amb aplicacions biomèdiques com l'administració de fàrmacs mediada per llum ultraviolada o com a un model de transductor biomèdic en ser aquest capaç de convertir la llum en una altra mena d'energia, en aquest cas, moviment d'assemble/desencadellament.

En el Capítol 6, es presenten quatre nous derivats de BODIPY funcionalitzats amb cadenes pseudopeptídiques que presenten tendència a l'agregació. S'estudia quins factors estructurals influeixen més notablement en l'agregació, en la internalització i localització intracel·lular, i la capacitat d'aquestes molècules per a visualitzar correctament determinats orgànuls cel·lulars. S'observa que en medi

aquós, a concentracions en el rang micromolar, tres dels compostos tendeixen a formar nanopartícules feblement emissives mentre que un d'ells roman soluble i altament fluorescent. A concentració nanomolar, sembla que tots els compostos són solubles en aigua. S'estudia la internalització cel·lular dels compostos en cèl·lules de adenocarcinoma de còlon humà (HT-29). Tots els compostos son internalitzats per les cèl·lules HT-29, però en particular el compost amb el aminoàcid lisina present en la seua estructura es el que va mostrar una major internalització i una localització lisosomal més clara. A més, el derivat de lisina presenta resultats molt prometedors en un model cel·lular (cèl·lules SW13/cl.2 de carcinoma suprarenal humà) de malaltia d'emmagatzematge lisosomal (Niemann-Pick tipus C).

En el Capítol 7, s'inclou una secció de discussió dels resultats globals i la seua significació. Finalment, en el capítol 8, es descriuen les conclusions generals de la tesi doctoral.

Resumen en castellano

La presente tesis doctoral, con título "*Macro- and nanoscale self-assembled amino acid derivatives as reduction-sensitive and photoactive materials*", se centra en el diseño, desarrollo y caracterización de compuestos químicos basados en aminoácidos con capacidad de autoensamblaje que dan lugar a materiales macro y nanoscópicos, los cuales se estudian y evalúan en aplicaciones del campo de la biomedicina, como la liberación controlada de fármacos o la visualización celular.

Al tractarse de una tesis realizada por compendio de artículos, ésta se estructura en 8 capítulos, cuatro de ellos corresponden a los artículos publicados, más dos capítulos iniciales (introducción general y objetivos de la tesis) y dos capítulos finales (discusión general y conclusiones).

En el Capítulo 1, se incluye una introducción general con relación a los conocimientos actuales sobre la utilización de materiales macro, micro y nanoscópicos en aplicaciones biomédicas justificando la importancia y relevancia de los contenidos que se engloban en esta tesis. Se presenta una descripción general del campo de los geles supra-moleculares, centrando un apartado, especialmente, a los geles derivados de aminoácidos y péptidos. También se presenta una visión general de la nanomedicina destacando la importancia de las nanopartículas en el desarrollo de este campo. Se exponen las ventajas que éstas ofrecen respecto a la medicina clásica, principales ejemplos, estudios y avances en el campo. También se incluye una breve introducción sobre fluoróforos orgánicos y visualización celular mediante fluorescència.

En el Capítulo 2, se presentan los objetivos generales y específicos que se abordan en cada capítulo de la tesis doctoral.

En el Capítulo 3, se presenta el estudio de dos gelantes supramoleculares que contienen un enlace disulfuro central y dos grupos de ácido carboxílico en los extremos de la molécula. Se demuestra que los hidrogeles (geles en medio acuoso) tiene capacidad de respuesta a estímulos. Por una parte, responden en un entorno reductor al transformar la unidad de disulfuro en los correspondientes tioles tras la reducción. Por otro lado, los hidrogeles debido a la presencia de los grupos carboxilo muestran respuesta asociada al pH del medio. Aprovechando ambas propiedades, se llevan a cabo estudios de liberación controlada. Para ello, se utiliza un colorante (azul de bromofenol) para monitorizar su liberación en presencia de una especie reductora (TCEP). En cambio, la propiedad de respuesta al pH se utiliza para la liberación controlada de la hormona insulina. Se demuestra que la insulina se carga en los hidrogeles y éstos evitan su degradación frente a la hidrólisis ácida y enzimática (pepsina). Se concluye que este comportamiento podría permitir el uso de estos hidrogeles para la administración oral de fármacos, entre otras posibles aplicaciones.

En el Capítulo 4, se describe la formación en medios acuosos de nanopartículas a partir de una molécula bolaanfifílica (molécula que tienen grupos hidrofílicos en ambos extremos de una cadena central hidrofóbica). Esta molécula incorpora de nuevo un enlace disulfuro central con el objetivo de generar nanopartículas con capacidad de respuesta a estímulos reductores (principalmente, glutationa). Las nanopartículas se utilizan como nanoportador de un marcador mitocondrial lipofílico ($DiOC_6(3)$). Se demuestra que las nanopartículas, debido a la presencia de los grupos disulfuro, desactivan la fluorescencia del marcador, la cual se

recupera tras su posterior liberación. Se estudia la internalización de la sonda fluorescente en células de adenocarcinoma colorrectal humano (HT-29). Se determina que se consigue una mayor internalización de la sonda cuando ésta se encuentra encapsulada en las nanopartículas. Por otro lado, se observa un aumento significativo de la fluorescencia intracelular cuando las células cancerosas son previamente estimuladas para aumentar los niveles de glutationa. Se concluye que estas nuevas nanopartículas moleculares podrían considerarse una herramienta teranóstica al lograr simultáneamente la entrega dirigida de sustancias lipofílicas y señalar altos niveles de un analítico, en este caso la glutationa.

En el Capítulo 5, se presenta un dipéptido derivado de valina y glicina que se autoensambla para formar nanotubos en medios acuosos. Esta molécula presenta una unidad de azobenceno que le confiere capacidad de respuesta a la luz. La irradiación con luz ultravioleta (longitud de onda de 365 nanómetros) provoca la isomerización *trans-cis* de la unidad de azobenceno, lo que produce el posterior desensamble de los nanotubos. Interesantemente, se pueden recuperar los nanotubos en disolución ya sea por recuperación térmica (isómero *trans* más estable termodinámicamente) o fotoinducida mediante la irradiación con luz visible (de longitud de onda de 457 nm) que provoca la isomerización *cis-trans*, restaurando los nanotubos. Se puede afirmar que este control de la formación/desensamble de nanotubos moleculares utilizando luz podría constituir una herramienta relevante para desarrollar sistemas inteligentes con aplicaciones biomédicas, como, por ejemplo, la administración de fármacos mediada por luz ultravioleta, o el uso de estos nanotubos como transductores biomédicos al ser éstos capaces de convertir la luz en otro tipo de energía, en este caso, movimiento de ensamble/desensamble.

En el Capítulo 6, se presentan cuatro nuevos derivados de BODIPY funcionalizados con cadenas pseudopeptídicas que presentan tendencia a la agregación. Se estudia qué factores estructurales influyen más notablemente en la agregación, en la internalización y localización intracelular, y la capacidad de estas moléculas para visualizar correctamente determinados orgánulos celulares. Se observa que en medio acuoso, a concentraciones en el rango micromolar, tres de los compuestos tienden a formar nanopartículas débilmente emisivas mientras que uno de ellos permanece soluble y altamente fluorescente. A concentración nanomolar, parece que todos los compuestos son solubles en agua. Se estudia la internalización celular de los compuestos en células de adenocarcinoma de colon humano (HT-29). Todos los compuestos son internalizados por las células HT-29, pero en particular la molécula con el aminácido lisina presente en su estructura es la que muestra una mayor internalización y una localización lisosomal más clara. Además, el derivado de lisina presenta resultados muy prometedores en un modelo celular (células SW13/cl.2 de carcinoma suprarrenal humano) de enfermedad de almacenamiento lisosomal (Niemann-Pick tipo C).

En el Capítulo 7, se incluye una sección de discusión de los resultados globales y su significación. Finalmente, en el Capítulo 8, se describen las conclusiones generales de la tesis doctoral.

Abbreviations and acronyms

^{13}C-NMR	Carbon-13 nuclear magnetic resonance
^{1}H-NMR	Hydrogen-1 nuclear magnetic resonance
1D, 2D, 3D	One, two, three-dimension
a.u.	Arbitrary units
Ala	L-Alanine
ANOVA	Analysis of variance
APCI	Atmospheric pressure chemical ionization
Arg	L-Arginine
ATP	Adenosine triphosphate
Azo	Azobenzene
BODIPY	Boron-dipyrromethene
Boc	Tert-Butyloxycarbonyl
ca.	Circa
calcd	Calculated
Cbz, Z	Benzyloxycarbonyl group
CCD	Charge-coupled device
CLSM	Confocal laser scanning microscopy
CTCF	Corrected total cell fluorescence
Csa	Cystamine
Da	Dalton
DCC	*N,N'*-Dicyclohexylcarbodiimide
DCR	Derived count rate
Di	Intensity averaged diameter
$DiOC_6(3)$	3,3'-Dihexyloxacarbocyanine Iodide
DIPEA	*N,N*-Diisopropylethylamine
DLC	Delocalized lipophilic cation
DLS	Dynamic light scattering
DMAP	4-Dimethylaminopyridine
DMEM	Dulbecco's Modified Eagle's Medium
DMF	*N,N*-Dimethylformamide
DMSO	Dimethyl sulfoxide
DNA	Deoxyribonucleic acid
DPH	1,6-Diphenylhexatriene
DPSS	Diode-pumped solid-state
DTT	Dithiothreitol
e.g.	Exempli gratia
EDCI	1-Ethyl-3-(3-dimethylaminopropyl)carbodiimide
EDTA	Ethylenediaminetetraacetic acid
ELISA	Enzyme-linked immunosorbent assay

EMA	European Medicines Agency
EPR	Enhanced permeability and retention
ERETIC	Electronic reference to access in vivo concentrations
ESI	Electrospray ionization
FCM	Flow cytometry
FDA	Food and Drug Administration
FF	Diphenylalanine
FLIM	Fluorescence-lifetime imaging microscopy
Fmoc	Fluorenylmethoxycarbonyl group
FRET	Förster resonance energy transfer
FSC	Forward scatter
G′	Loss modulus
G′′	Storage modulus
GI	Gastrointestinal
Glt	Glutaric acid
Glu	L-glutamic acid
Gly	Glicine
GSH	Glutathione
HRMS	High-resolution mass spectrometry
i.e.	Id est
Ile	L-isoleucine
IQR	Inter-quartile range
Kcps	Kilocounts per second
LED	Light-emitting diode
Leu	L-Leucine
LMWGs	Low molecular weight gelators
Lys	L-Lysine
Mgc	Minimum gelator concentration
MPS	Mononuclear phagocytic system
MS	Mass spectrometry
MTR	MitoTracker Red
MTT	(3-(4,5-dimethylthiazol-2-yl)-2,5-diphenyltetrazolium bromide
NACET	*N*-Acetylcysteine ethyl ester
Nap	2-Naphthylmethyl ether
NCL	Nanomedicine Characterization Laboratory
NIR	Near-infrared
NMR	Nuclear magnetic resonance
NPs	Nanoparticles
Nvoc	Nitroveratryloxycarbonyl group
Pa	Pascal
PB	Phosphate-buffered

PBS	Phosphate-buffered saline
PdI	Polydispersity index
PET	Photoinduced electron transfer
PEG	Polyethylene glycol
PEGDA	Polyethylene glycol diacrylate
Phe	L-phenylalanine
PLGA	Poly(lactic-co-glycolic acid)
Pr	n-Propylamine
PVA	Polyvinyl alcohol
RES	Reticuloendothelial system
RNA	Ribonucleic acid
ROI	Region of interest
SDS	Sodium dodecyl sulfate
SEM	Scanning electron microscopy
SGF	Simulated Gastric Fluid
SI	Supporting information
SSC	Side scatter
Std dev	Standard deviation
Suc	Succinic acid
TBTU	*O*-(Benzotriazol-1-yl)-*N*,*N*,*N*',*N*',-tetramethyluronium tetrafluoroborate
TCEP	Tris(2-carboxyethyl)phosphine
TCSPC	Time-correlated single-photon counting
TEM	Transmission electron microscopy
TFA	Trifluoroacetic acid
THF	Tetrahydrofuran
TOF	Time-of-flight
TPP	Tri-phenyl-phosphonium
Tris	Tris(hydroxymethyl)aminomethane
Tyr	L-Tyrosine
UV-Vis	Ultraviolet visible
Val	L-Valine
ϕ	Fluorescence quantum yield
ϕ_{Δ}	Singlet oxygen quantum yield
λ	Wavelength
λ_{abs}	Maximum absorption wavelength
$\lambda_{exc/em}$	Excitation/emission wavelength
λ_{max}	Maximum absorption/emission wavelength
τ	Fluorescence lifetime

Compound Chart

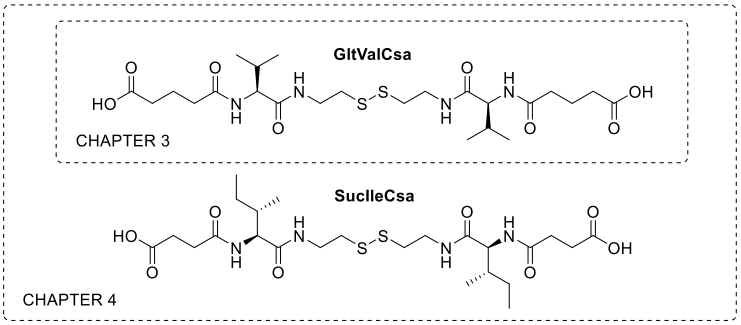

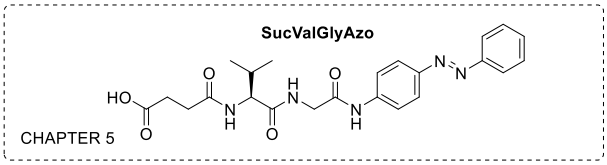

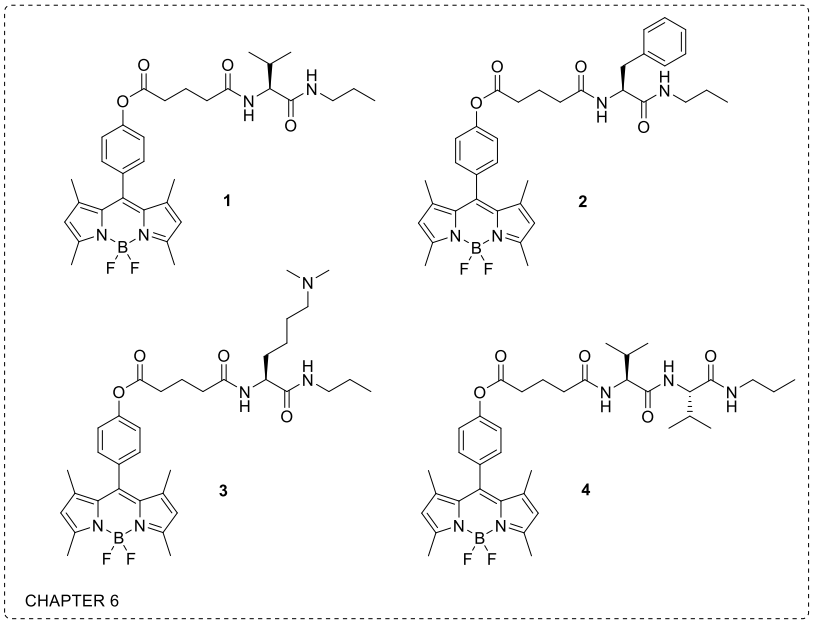

Table of Contents

Chapter 1

General Introduction

1.1 Supra-molecular Gels

Beyond a shadow of a doubt, molecular (or supra-molecular) gels have become a hugely relevant class of soft materials since the beginning of the nineties, attracting a growing and steady interest in researchers year after year. As a matter of fact, hundreds of publications regarding molecular gels can be easily encountered at the touch of a button (**Figure 1.1**). The field of supramolecular gels is a fascinating area whose interest lies in the challenges and difficulties that remain in understanding their structures, properties, and the participating processes in the formation of such gels.[1]

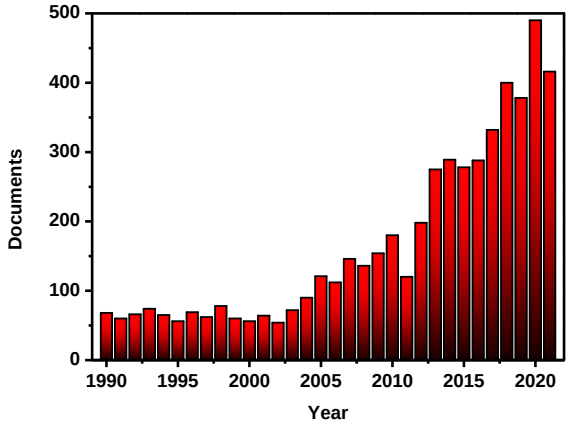

Figure 1.1. A rapid assessment of the field of supra-molecular gels representing the number of publications over the last three decades (results returned from "*molecular Pre/3 *gel" search in Scopus).

There is a potpourri of definitions for supra-molecular gels. However, there is a widely held view that these gels arise from the self-assembly of "small" molecules

(arbitrarily molecular weights <2000 Da, which is why they are often referred to as low-molecular-weight gelators, LMWGs) into a network that percolates and immobilizes the solvent, preventing its free flow.[2] Beginning with the molecules in the solvated and uncoiled state, the self-assembly process is triggered by stimuli, namely, temperature, ultrasounds, pH, salt concentration or chemical reactions.[3] Here, the molecules assemble *via* non-covalent interactions (such as hydrogen bonding, van der Waals and London dispersion forces, hydrophobic interactions, π-π stacking, and coordination bonding) into supramolecular nanoscale or microscale anisotropic structures (1D or 2D) that further entangle, branch, and/or cross-link to form a network (3D) (**Figure 1.2**).[4,5] This hierarchical self-assembly results in a viscoelastic material that, despite being predominantly liquid in composition, has the rheological properties of solid-like materials: *G'* (elastic modulus, *i.e.* solid-like, behaviour) > *G''* (viscous modulus, *i.e.* liquid-like, behaviour).[6]

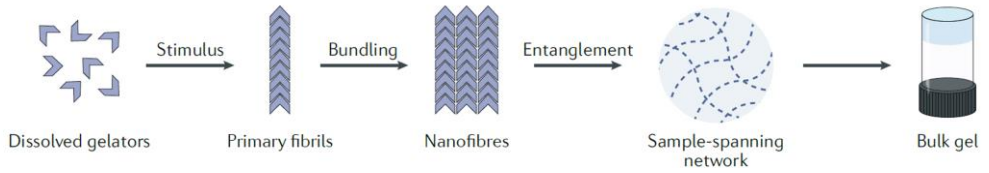

Figure 1.2. Hierarchical self-assembly of supra-molecular gels. Reprinted with permission from "Shaping and Structuring Supramolecular Gels" by P. R. A. Chivers, D. K. Smith, 2019, Nat. Rev. Mater., 4, 463-478.

A myriad of molecules has been reported to act as gelators since the initial reports of gelating systems, including peptides, ureas, sugars, steroids, bile acids, lipids, nucleobase derivates, and long-chain alkanes.[7] Although gelation is often happily proved by inverting a vial and observing the lack of flow under gravity, it is worth mentioning that the discovery *a priori* of new gelators is something

that persists impracticable.[1,8] Whereas it is useful the effort put forth to explain and predict gelation, including both theoretical and experimental approaches,[9–18] whether a molecule will form a gel or not is a question mark that remains unanswered. Parameters such as solvent polarity, viscosity, solvent-gelator interactions, gelator solubility, pH or added salts/additives, and, on a more general level, gelator concentration, final temperature, ageing time, or the preparation methods have a pivotal role in the gelation outcomes (**Figure 1.3**).[2,19] Therefore, a full description of such parameters/factors when a gel is been reported must be necessary to ensure reproducibility, to understand the processes involved in the gelation process, and to predict gel properties.[20]

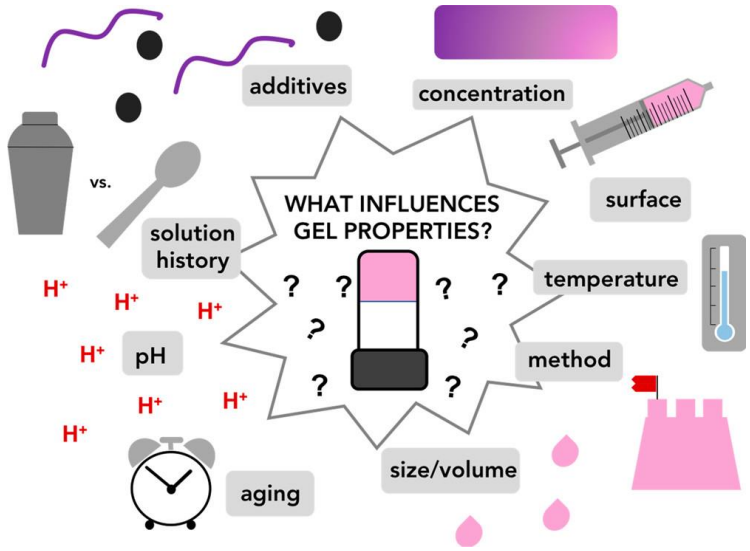

Figure 1.3. Displaying how many parameters affect the outcomes of the gelation processes. Reprinted with permission from "Controlling the Assembly and Properties of Low-Molecular-Weight Hydrogelators" by E. R. Draper, D. J. Adams, 2019, Langmuir, 35, 6506-6521.

Once gels are formed, to escalate the understanding of these complex systems, a proper characterization is required to inquire into the gel properties and determine the future potential applications.[21,22] At this point, it is stated that the

properties of the gels are the result of the primary one-dimensional assembly and how these fibres entangle, cross-link, and interact with each other. As such, it is necessary to characterize gels taking a "bottom-up" perspective, from molecular interactions to macroscopic behaviour.[23] There is an array of techniques that have been used to assess gels such as spectroscopy,[24–27] microscopy,[28,29] small-angle scattering[30,31] computational modelling[32,33] and rheology,[34–38] to name but a few. Importantly, transmission and scanning electron microscopes have been widely used to access information on the network, assuming that the data for dried gels represents those for the solvated gels. Some works have discussed the validity of this assumption, showing that drying artefacts can occur, leading to aggregation and structural changes.[39] That is why cryogenic techniques have increased in use as images can be collected in the solvated gel state. Not to mention, confocal microscopy allows imaging of the unaltered 3D gel network.[40]

As far as applications are concerned, most gels applied in everyday life and for biomedical applications are based on polymers (PEG, PEGDA, PLGA, PVA, Chitosan, etc.).[41,42] Several limitations and barriers prevent molecular gels from having the same impact as their polymeric counterparts. In general terms, many self-assembled supra-molecular gels are often difficult to manipulate because they are formed through weak interactions. The networks obtained are more vulnerable and fragile, hindering or preventing their mainstreaming as functional materials. However, this pattern is changing and several new approaches and strategies have recently emerged, providing the guidelines to generate molecular gels with spatial and temporal control.[6]

As previously mentioned, molecular gels are formed *via* weak, non-covalent interactions which yield systems that can be modified, rearranged, or even

unpicked in response to environmental stimuli such as temperature, light, pH, saline effects, and chemical species (**Figure 1.4**).[13,43] The supramolecular self-assembly process is reversible *per se*, enabling recyclability, responsiveness, self-healing and injectability.[44] This underlying reversibility has led to supra-molecular gels being used in biomedical (and other) applications.[3,5,45] On the contrary, reversibility is not present in polymer networks with covalent crosslinks, and physical polymer gels because, unfortunately, the cross-links are permanently present, making polymeric gels less interesting for such applications.

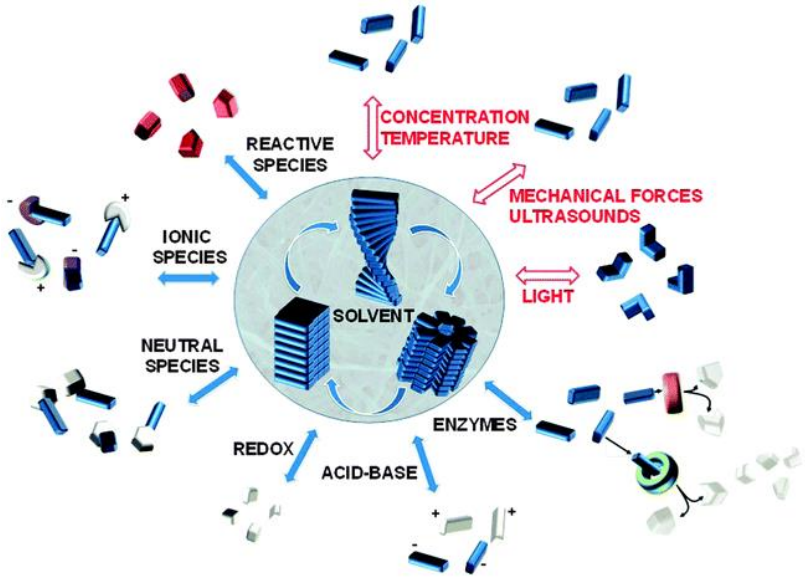

Figure 1.4. Classification of the different physical (red) and chemical (black) stimuli applied for assembly/disassembly of supra-molecular gel. Reprinted with permission from "Control of Molecular Gelation by Chemical Stimuli" by M. D. Segarra-Maset, V. J. Nebot, J. F. Miravet, B. Escuder, 2013, Chem. Soc. Rev., 42, 7086-7098.

1.1.1 Amino acid/peptide molecular gels

For biomedical applications, a special focus is given to low-molecular-weight gelators based on amino acids or short peptides. Peptide-based gels are desirable as their present high biocompatibility, good biodegradability, and non-immunogenicity.[46] A further advantage is the fact that peptide gelators can also be easily, molecularly functionalized with numerous moieties to enhance or modify their properties. Functionalizing the C- and N-terminal of amino acids with protecting groups (fluorenylmethoxycarbonyl, Fmoc; carboxybenzyl, Cbz; 2-naphthylmethyl ether, Nap; etc.), aromatic derivatives (pyrene, naphthalene, and so on), and attaching long-chain alkyl groups are among the most widely used approaches to perform peptide gelators.[47]

Nonetheless, supra-molecular peptide gels require a careful and precise design to achieve an appropriate balance between hydrophilic (aided by charged residues such as Arg, Lys, Glu) and hydrophobic (aided by residues such as Ala, Val, Leu, Tyr, Phe) forces so that the self-assembly process will prevail over solubilization or precipitation phenomena.[48] Peptide-based gelation depends on the exact structure and conformation of the molecules involved. Indeed, it is reported that peptides of identical composition (identical hydrophobicity/hydrophilicity balance) but with a different sequence can self-assemble into unlike structures and, therefore, yield gels with distinct properties.[49] But, this dependency on the exact structure, in practice, has its positive side as it means that any change in response to a stimulus can result in significant macroscopic changes, which are particularly advantageous to developing stimuli-responsive systems.[50] Especially, responsiveness to biomolecules and endogenous stimulus (*i.e.,* internal biochemical stimulus) is highly demanded in biomedical applications.[51]

Therefore, peptide supra-molecular gels encompass all the factors and features required by every system under development to be applied in advanced applications. As such, many studies on peptide supra-molecular gels can easily be found in the literature for biomedical applications, including drug delivery and cell proliferation, tissue engineering, antibacterial, antifungal, anti-inflammatory, anticancer, wound healing, bioimaging and 3D bioprinting (**Figure 1.5**).[52] This represents the outcomes of the research efforts aimed at developing and validating novel systems based on low-molecular-weight peptide gelators.

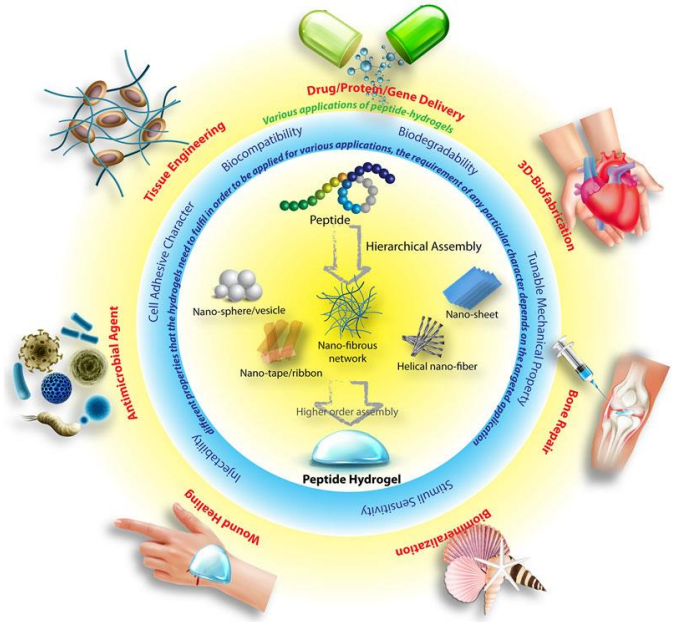

Figure 1.5. Schematic illustration of the hierarchical peptide self-assembly, required parameters for hydrogels to be used in the biomedical field, and some examples of therapeutic applications. Reprinted with permission from "Rational Design of Peptide-based Smart Hydrogels for Therapeutic Applications" by S. Das, D. Das, 2021, Frontiers in Chemistry, 9, 770102.

Some specific examples of peptide-based supra-molecular gels are outlined hereunder. Recently, a new family of short-five amino acid peptides has been

described for cell delivery and tissue engineering applications as syringe-injectable hydrogels that support encapsulation, proliferation, and viability of oligodendrocyte progenitor cells (OPCs).[53] For cancer research, a mitochondria-penetrating tripeptide containing diphenyl alanine (FF) as a building unit has been reported.[54] The short peptide amphiphile co-assembled with its enantiomeric analogue and induced severe mitochondrial disruption of cancer cells both *in vitro* and *in vivo*, showing a potent strategy to fight cancer. Also, concerning cancer therapy, a self-assembled peptide-based supramolecular hydrogel bearing chlorambucil, a chemotherapy agent, and tyroservatide, a peptide anticancer drug, has been developed.[55] This hydrogel showed improved stability against enzyme degradation, enhanced penetration to tumour cells and efficient inhibition of proliferation of various tumour cells, making these hydrogels a promising candidate for delivery drug systems. In another approach for drug release applications, a UV-responsive supramolecular gel based on phenylalanine and nitroveratryloxycarbonyl (Nvoc), as a photo-labile moiety, has been reported.[56] The Nvoc-FF peptide hydrogel disassembles in response to UV light irradiation, allowing the suitable release of the hormone insulin.

Furthermore, injectable biomaterials are particularly paving the way for a new generation of vehicles for targeted drug delivery applications. Low-molecular-weight cationic injectable hydrogels have been reported for *in vivo* delivery of an anti-inflammatory drug, diclofenac, in a mouse model.[57] These hydrogels exhibit ideal rheological properties applied as injectable hydrogels for *in vivo* applications. Finally, at the cutting edge of supra-molecular hydrogel technology, 3D bioprinting applications have emerged. To cite just one example, two bio-inks based on oppositely charged dipeptide were bio-printed using a layer-by-layer strategy for cell culture applications. During 3D printing, the Fmoc-dipeptide bio-inks self-assemble into β-sheet structures, which further

interact by oppositely electrostatic interactions yielding in situ gelation. The 3D hydrogel environment enabled a faster and steady proliferation of cells than that in 2D Petri dishes.[57]

In the light of the above considerations, we might conclude that supra-molecular gels, especially those derived from amino acids/peptides, are fascinating materials that will keep this area of research busy in the future as there is plenty of room for improvement. Although molecular gels fabrication is at an early stage, it can be envisaged the development of functional gels with the desired properties could open up an increasing range of advanced applications in the foreseeable future. Inspired by what other researchers have been doing with responsive gels in the biomedical field over the last years and motivated to contribute to the mainstreaming of low-molecular-weight gelators (LMWGs) in direct and tangible applications, this thesis undertakes the development and study of two new supra-molecular gelators to be applied as controlled drug delivery systems. Hydrogels with responsiveness to a reductive and pH-changing environment were prepared, which offered protection against enzymatic hydrolysis and controlled insulin release (**Chapter 3**).

1.2 Nanomedicine

Nanomedicine is the application of nanotechnology to medicine. Nanomedicine uses nanometre-scale materials (or nanostructures) and nano-enabled techniques to prevent, diagnose and treat diseases.[58] However, the definition of nanomaterial is not straightforward. Several regulatory bodies and other institutions have defined the term' nanomaterial' in many ways, but these

definitions are not yet unified.[59] Whatever the case, a nanomaterial is generally defined as any material with one, two or three dimensions on the nanoscale, which, in turn, ranges from approximately 1 to 100 nanometers.[60] However, this arbitrary value jumps up to around 500 nm in nanomedicine as this is the length scale on which biomolecules play their roles, *i.e.*, regulating the functions and processes that occur in the cellular environment (**Figure 1.6**).[61]

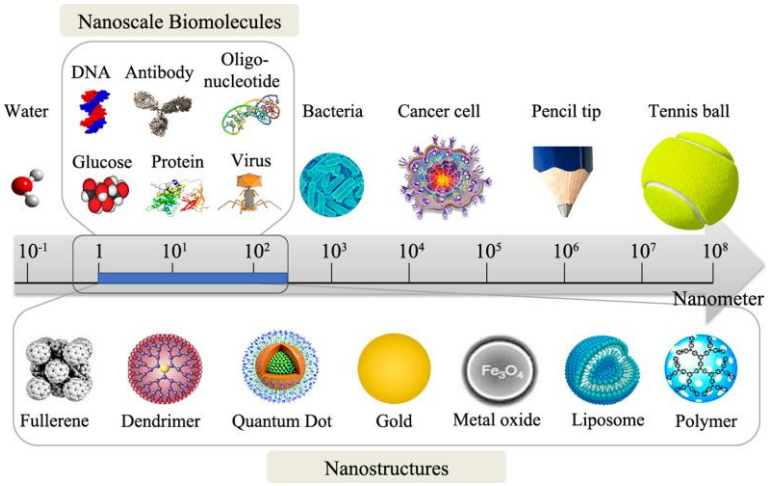

Figure 1.6. The length scale of nanomedicine (blue line). Some examples of nanoscale biomolecules and nanostructures are also displayed. Adapted with permission from "Nanoparticles Carrying Biological Molecules: Recent Advances and Applications" by S. Saallah, I. W. Lenggoro, 2018, KONA Powder Part. J., 35, 89-111.

Once again, an overwhelming number of types and classifications of nanomaterials have been proposed in the literature depending on size, composition, shape, or origin.[62] Overall, most current nanomaterials used for biomedical applications can be classified into four categories: carbon-based nanomaterials (fullerenes, carbon nanotubes, carbon nanofibers, etc.), organic-based nanomaterials (liposomes, polymer nanoparticles, micelles, dendrimers, etc.), inorganic-based nanomaterials (magnetic nanoparticles, quantum dots,

silica nanoparticles, metal nanoparticles, etc.), and hybrid nanosystems (multiphase nanomaterial, hybrid nanofibers, metal-organic frameworks, etc.).[63]

Nanomedicine is an emerging, rapidly evolving science that, despite being relatively new, has become a major focus for all researchers.[64] A cautionary example of this clear interest can be seen in the novel coronavirus (COVID-19) pandemic because merely one year since the first cases of infection were reported, two nanomedicine-based mRNA vaccines were ready for use.[65] The growing interest in nanomedicine relies on the fact that nanoscale materials, above mentioned, provide the opportunity of targeting tissues, organs, individual cells and even proteins and other biomolecules due to their sizes, shapes and surface chemistry. Owing to such factors, nanomedicine is present in many applications (**Figure 1.7**),[66] comprising drug/gene delivery,[67–69] therapies[70], sensing,[71,72] imaging,[73,74] tissue engineering[75,76] and biomedical devices.

The main goal of nanomedicines is to overcome the limitations and barriers that affect conventional pharmaceutical agents and classical formulations. Difficulty in disposing of such active agents after therapy, low selectivity to the targeted tissue, lack of stability and solubility, and decreasing bioavailability are among the most significant problems and obstacles that outdated therapies confront.[77] On the contrary, nanomedicines modify the pharmacokinetics and biodistribution of drugs (and other molecular agents), enhancing the therapeutic and diagnostic efficiency.[78]

It is worth taking a quick look back (**Figure 1.8**). The development of nanomedicine dates to the 1990s, when the first nanoscale materials to solve health problems arose. The emergence of the first-generation nanomedicines was, to a degree, the result of scientific tools that enabled in the early 1980s to

measure and assess materials at the nanoscale. All changed with the development of electron, scanning tunnelling and atomic force microscopes. Many of these first-generation nanomedicines have been clinically established as successful medicines and entered routine clinical uses.[79] One example is Abraxane®, a protein-drug conjugate approved in the United States in 2005 for breast cancer.[80] While the first nanomedicines are relevant in terms of reducing toxicity compared to the free drugs, their efficacy does not offer the expected improvement.[81]

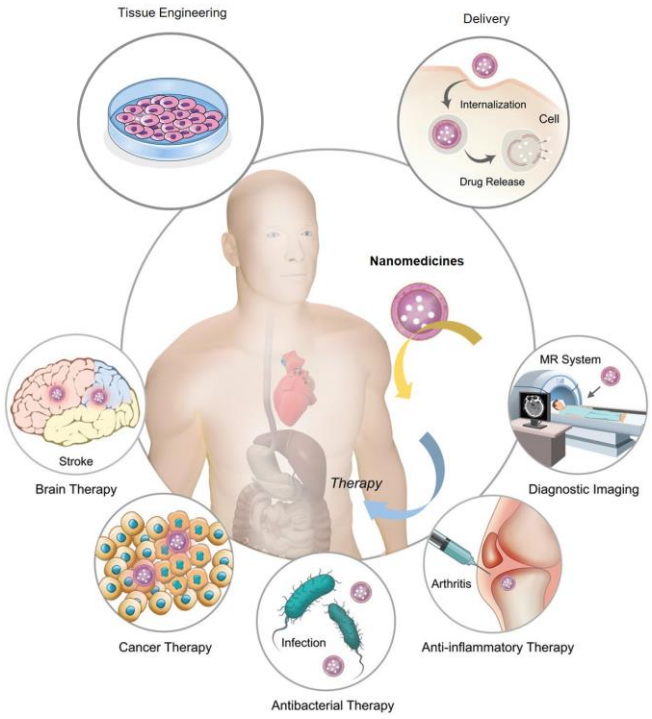

Figure 1.7. Schematic showing the main application areas of nanomedicine. Adapted with permission from "Nanocatalytic Medicine" by B. Yang, Y. Chen, J. Shi, 2019, Adv. Mater., 31, 1901778.

The major hurdles that nanomedicine still had at the beginning of the twenty-first century (and to this day), such as the ability to deliver cargo to specific body

sites, undesired side-effects, and enhanced efficacy, showed the crucial need for a next-/second-generation of nanomedicines.[82] Then, the focus was on overcoming the barriers and limitations of their predecessors by increasing system complexity, employing targeting mechanisms and using novel materials. These second-generation are currently entering clinical trials.[83] An example of this approach is MM-302, a PEGylated antibody–liposomal doxorubicin conjugate for targeted cancer therapy.[84] More recently, the state-of-the-art in nanomedicine (third-generation nanomedicines) relates to the integration of therapy and diagnosis (theranostic) to yield multifunctional nanosystems.[81] Theranostic nanomaterials, designed focusing on the imaging agent, therapeutic agent and targeting moieties, can deliver cargos at desired body sites as well as image/signal specific positions and sense pathological factors/molecules simultaneously or sequentially.[85] However, further progress needs to be achieved as, to date, there are no theranostic platforms available for clinical use.

A wide range of diseases has successfully been studied using nanomedicines.[86–89] Two-thirds of this research has focused on cancer therapy and cancer diagnosis.[90] Indeed, the earliest licensed and marketed nanomedicine approved by the U.S. Food and Drug Administration (FDA) in 1995 was a PEGylated liposomal formulation for a cancer treatment called Doxil® (liposomal doxorubicin).[91,92] Since then, the field of nanomedicines has witnessed significant progress,[93] being more than 50 marketed nanomedicines approved by the FDA and/or the European Medicines Agency (EMA).[94,95] Currently, marketed nanomedicines include liposomes formulations, nanocrystals, lipid nanoparticles, polymeric nanodrugs, micellar nanoparticles, protein-based nanoparticles and metal-based nanoparticles.[96]

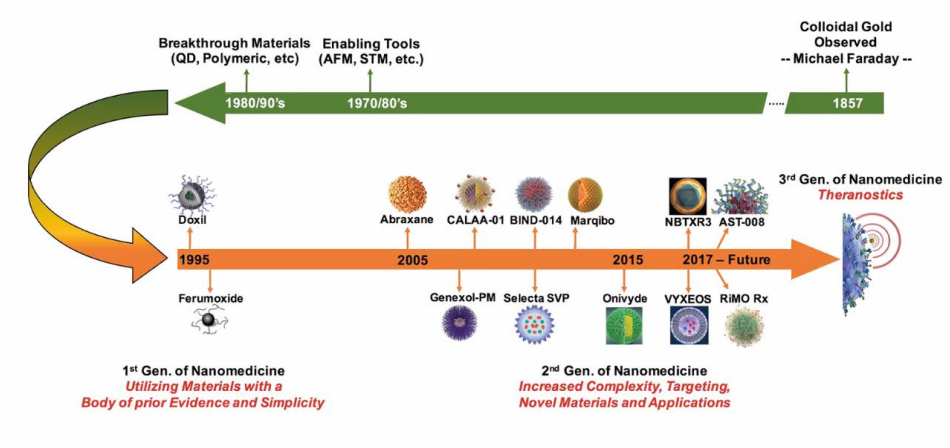

Figure 1.8. Timeline of nanomedicine, important historical events, and examples of nanomedicines currently approved or in clinical trials. Reprinted with permission from "Theranostics: A Historical Perspective of Cancer Nanotechnology Paving the Way for Simultaneous Use Applications" by C. M. Hartshorn, S. A. Morris, 2019, Springer.

However, to move into the clinical stages and, especially, to reach the market,[97] nanomedicines require a comprehensive understanding of their physicochemical parameters.[80,98] All nanomedicine candidates must be characterized by robust, straightforward, and affordable methods to ensure manufacturing quality and information on the undesired/toxic effects of the novel nanomaterials.[95,99] This task can be particularly challenging due to the wealth of parameters to assess (*e.g.*, morphology, size distribution, surface properties, charge, purity, drug encapsulation efficiency, number of conjugated ligands, etc.).[100] In addition, harmonized standards for nanomedicine characterization are still lacking, further complicating this situation. However, some institutions (FDA, EMA, NCL, to name a few) have made great efforts to address such a situation by establishing guidelines and roadmaps that encompass a set of characterization methods to facilitate the subsequent approval of emerging technologies nanomedicines (**Figure 1.9**).

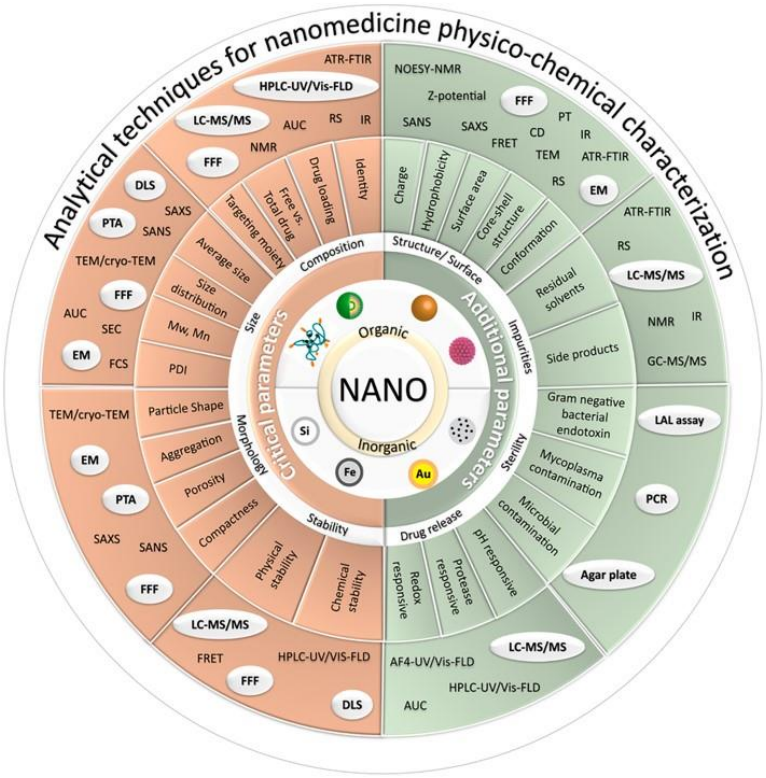

Figure 1.9. An overview of techniques for the physicochemical characterization of nanomedicines. Reprinted with permission from "Current Hurdles to the Translation of Nanomedicines from Bench to the Clinic" by S. Đorđević, M. M. Gonzalez, I. Conejos-Sánchez, B. Carreira, S. Pozzi, R. C. Acúrcio, R. Satchi-Fainaro, H. F. Florindo, M. J. Vicent, 2022, Drug Deliv. and Transl. Res., 12, 500-525.

It is also worth mentioning that most nanomedicines are characterized under controlled and idealized laboratory conditions without considering that their interactions with biological fluids and biomolecules after administration significantly change their properties. Therefore, it would be useful to characterize nanomedicine products under clinically relevant conditions to understand *in vivo* pharmacokinetics, pharmacodynamics, and cytotoxicity.[101]

1.2.1 Nanoparticles

No one can deny that it had not been for the emergence of nanoparticles, the field of nanomedicine would not be what it is. In fact, nanomedicine is often generally defined as the application of nanoparticles in medicine.[102] This statement relies on the fact that the vast majority of nanomedicines are based on nanoparticles if it is considered that any particulate material having a size that ranges from a few nanometres to 500 nm (a nanosphere, a nanorod, a nanowire, a nanotube, etc.) is a nanoparticle.

The relevant contribution of nanoparticles to science and, particularly to biomedical and health research, is reflected by the number of publications regarding nanoparticles in such fields (**Figure 1.10**). While, in the section above, we stated that supra-molecular gels were a significant research field with around 400 publications per year, nanoparticles have surpassed by far all limits. Last year almost 10,000 scientific publications regarding nanoparticles were generated and published in indexed scientific journals of both pure and applied disciplines, representing nearly 0,4 % of the total number of publications in natural sciences. In simple terms, four out of one thousand scientific studies have been using nanoparticles in their studies, astonishing data that emphasizes the importance of nanoparticles to research.

Generally speaking, nanoparticles fall into two main categories, depending on whether nanoparticles are engineered from organic or inorganic materials (**Figure 1.11**). While organic nanoparticles (liposomes, polymeric nanoparticles, micelles, solid-lipid nanoparticles, dendrimers, etc.) are extensively used for therapy and controlled release,[69,103–105] the inorganic counterparts (magnetic nanoparticles, silica and gold nanoparticles, quantum dots, upconversion

nanoparticles, etc.) possess unique properties and exceptional advantages to be applied in bioimaging[106,107] and biosensing.[108,109] Although of interest, deepening the topic of inorganic nanoparticles goes beyond the scope of this thesis.

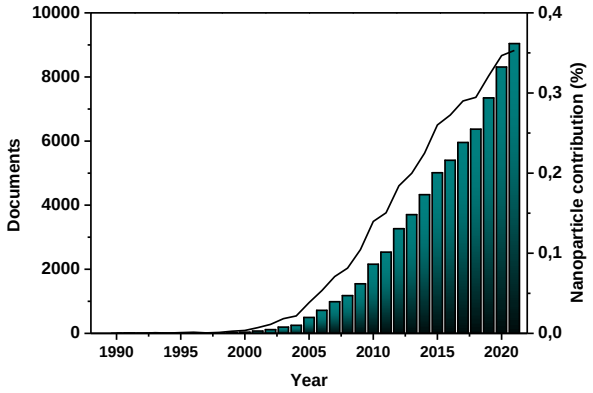

Figure 1.10. A rapid assessment of the field of nanoparticles in nanomedicine area representing the number of publications (histogram, results returned from "*nanoparticles AND *medic*" search in Scopus,) and its contribution (line, nanoparticles regarding publications/total number of publications x 100) over the last three decades.

Many therapeutics (drugs, photosensitizers, peptides, proteins, nucleic acids, antibodies, etc.), imaging probes or contrast agents have their targets in a specific organ, tissue, or even inside the cells.[63] However, these agents frequently do not present good performance properties. Their fate after administration is either degradation or accumulation at undesired sites after the administration of repeated doses, thus producing damage to healthy tissues and off-target toxicity because of the systemic distribution.[110] Nanoparticles, particularly organic nanoparticles, come as the solution to these difficulties providing superior safety and efficacy, in that nanoparticles grant the opportunity to encapsulate bioactive agents through a process known as "nanoencapsulation".[111] Note that hereafter the term nanoparticle is indistinctly renamed as nanocarrier.

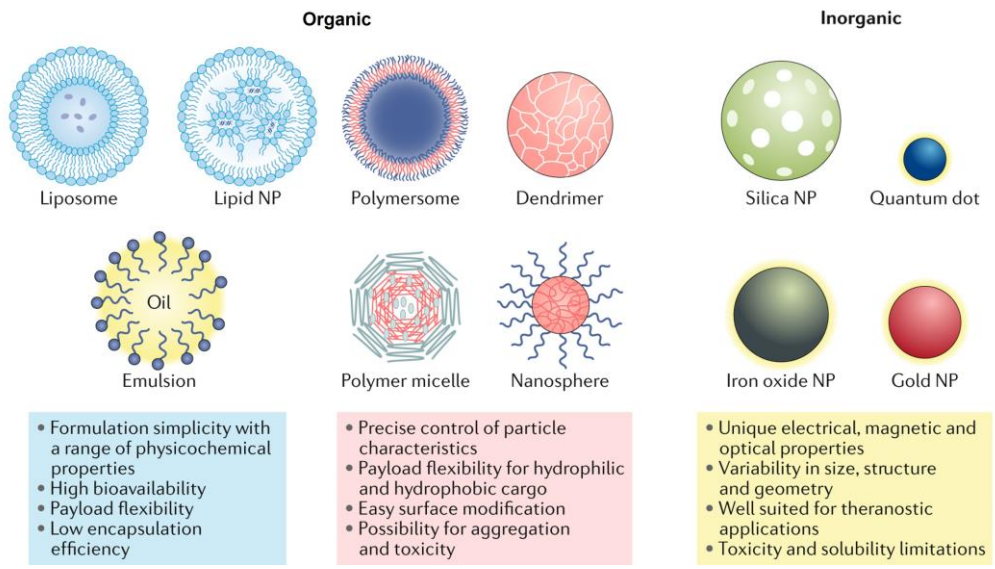

Figure 1.11. The most common classes of nanoparticles in biomedicine. Strengths and weaknesses of each class are also summarized. Adapted with permission from "Engineering Precision Nanoparticles for Drug Delivery" by M. J. Mitchell, M. M. Billingsley, R. M. Haley, M. E. Wechsler, N. A. Peppas, R. Langer, 2021, Nat. Rev. Drug Discov., 20, 101-124.

Nanoparticles (or nanocarriers) offer outstanding advantages by means of the encapsulation process, as explained in the following. Nanocarriers provide stability to active agents that possess poor solubility in aqueous media by "solubilizing" them into the nanoparticle core or surface mainly *via* electrostatic and hydrophobic interactions or physical entrapment.[112] Another intrinsic advantage is that nanocarrier surface can be easily chemically modified, offering protection to the encapsulated agents against degradation mechanisms in biological environments such as enzymatic degradation, immunodegradation, sequestration by the reticuloendothelial system (RES), acid hydrolysis, and so on.[112] Therefore, the protection of therapeutics by nanocarriers increases active concentration, therapeutic longevity and bioavailability. The primary strategy used to control or protect the nanocarriers against degradation by the attack of plasma proteins and opsonization by the reticuloendothelial system (RES) is

utilizing nanoparticle surface engineering. Poly (ethylene glycol) (PEG) is the most resorted procedure among many coating materials. However, it has been demonstrated that anti-PEG antibodies rise after injections of PEG-modified nanoparticles, leading to rapid clearance and thus the inefficient activity of PEGylated nanoparticles in post-injections.[113] Thus, the approach to surface modification of nanoparticles using cell membrane-based coatings is of particular interest. In this approach, the cell membrane layer mimics the antigenic diversity of the source cells and provides relevant functions of the source cell that leads to immune escape and long circulation.[114]

In addition, nanocarriers reduce the overall dose and toxic side effects because nanoparticles target specific body sites. There are two main strategies for targeting: passive and active. Active targeting is achieved by introducing onto the nanoparticle system a moiety (*e.g.*, ligand, antibody, peptide) that targets specific changes, which permits distinguishing between healthy and non-healthy cells and tissues. Passive targeting is a size-dependent mechanism that allows nanoparticle accumulation in sites of high vascular permeability, like sites of inflammation, in a discerning manner *via* the enhanced permeability and retention (EPR) effect (**Figure 1.12**). The EPR effect has been extensively used to treat cancer.[115] This effect is based on specific pathophysiological differences between tumours and healthy tissues. Due to tumour endothelium being fenestrated (with gaps ranging from 100 nm to *ca.* 800 nm) and not possessing an adequate lymphatic drainage system, nanoparticles can selectively penetrate and accumulate in tumours.[116] However, the EPR effect presents limitations because many other parameters in the tumour microenvironment can cause an inefficient penetration (**Figure 1.12**).[117] In addition to that, passive targeting does not prevent accumulation in other fenestrated tissues (such as the liver, the spleen, etc.), as well as EPR effect is an ill-considered approach on many

occasions because EPR-mediated accumulation has only been reported for some tumour types.[117] This highlights that the EPR effect, on which the vast majority of first-generation nanomedicines are based, is insufficient, underscoring the urgent need for further progress.

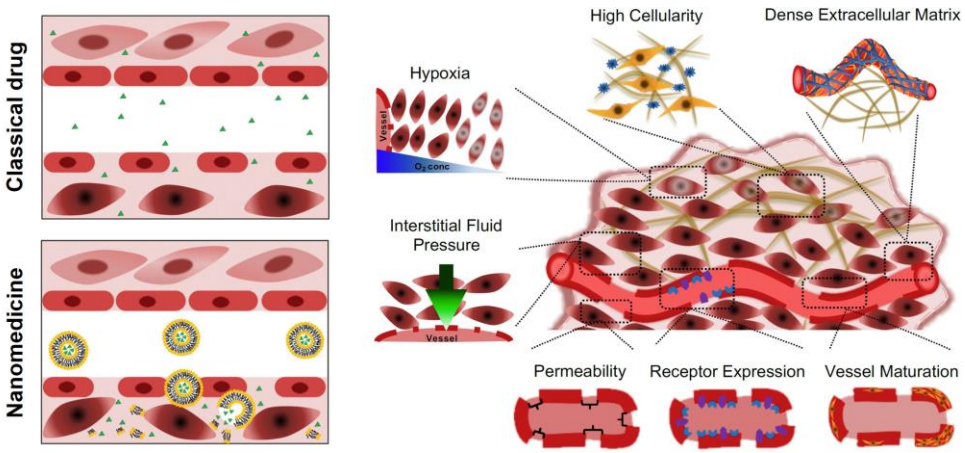

Figure 1.12. (Left) Conventional chemotherapy *vs.* EPR-based nanomedicine therapy. (Right) Tumour microenvironment factors cause inefficient penetration. Adapted with permission from "Tumor Targeting via EPR: Strategies to Enhance Patient Responses" by S. K. Golombek, J. N. May, B. Theek, L. Appold, N. Drude, F. Kiessling, T. Lammers, 2018, Adv. Drug. Deliv. Rev., 130, 17-38.

Active targeting can significantly increase, by means of high-affinity ligands attached to the surface of the nanocarrier, the accumulation of drugs delivered in the location of interest compared to free drug or passively targeted counterparts. This strategy improves the affinities of the nanocarriers for the surface of cancer cells, binding selectively and thus enhancing drug penetration.[118,119] A vast number of cellular receptors have been recognized, and their respective targeting ligands have been successfully synthesized and investigated *in vitro* and *in vivo*, including antibodies and non-antibodies ligands such as proteins, peptides, vitamins and aptamers.[120] Over the past few years, many actively targeted candidates have entered clinical trials. However, the

complex scale-up of the manufacturing process of actively targeted nanosystems often impedes their translation from the bench to the bedside.

In summary, an ideal nanocarrier (**Figure 1.13**) should (1) have no toxicity effects and be safely excreted from the body, (2) achieve both high accumulation in the desired site and enhanced cellular internalization, and (3) be designed for the controlled and on-demand release of drugs and bioactive agents over the desired timescale.[121] In particular, to successfully achieve conditions number 2 and 3, it has recently been stated that the designed nanocarriers must necessarily be able to change their structures when they meet different physiological environments.[122] This innovative programmed specific strategy is based on the so-called stimuli-responsive nanocarriers. Typical triggered actions in responsive materials are depicted in **Figure 1.14**. Here, there are two primary requisites to be fulfilled: one refers to targeting/penetration and the other focuses on the release process. First, nanocarriers should show high stability during blood circulation for efficient passive/active targeting. To promote cellular internalization, they should respond to endogenous or exogenous stimuli in the extracellular environment to transform themselves into a more cell-interactive form.[122] Next, the nanocarrier should be functionalized/modified to deliver, release or activate its cargos in the desired region by responding to internal/external stimuli inside cells to trigger the pharmacological activity of the corresponding cargo.[122] The most convenient and powerful stimuli for use in delivery systems could be external (or exogenous) such as magnetic field, temperature, ultrasound, light and electronic field, etc.,[123–125] or internal (endogenous and bio-chemical) such as pH, ATP, H_2O_2, enzyme, redox, hypoxia, etc.[126–129] (**Figure 1.15**).

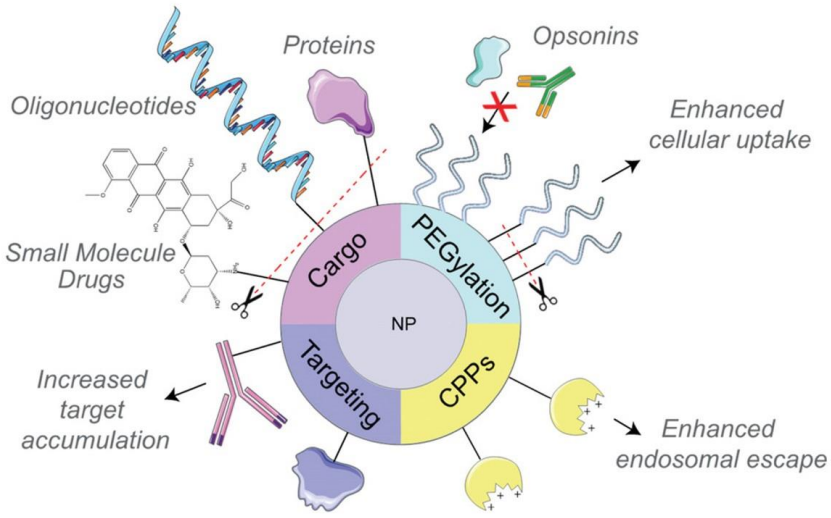

Figure 1.13. Representing an ideal nanocarrier for delivery applications. Adapted with permission from "Nanomaterial Strategies for Delivery of Therapeutic Cargoes" by F. Ledesma, B. Ozcan, X. Sun, S. M. Medina, M. P. Landry, 2022, Adv. Funct. Mater., 32 (4), 2107174.

These stimuli-responsive materials that are sensitive to biological signals or pathological abnormalities and interact with or are actuated by them are appealing therapeutic platforms for developing next-/second-generation nanomedicines.[130] Most of these systems can be described as "smart" as they consist of a therapeutic-loaded nanocarrier, possess a mechanism to target the desired site, and change their structures, compositions or conformations in response to stimuli to release the payloads.[103,131] Stimuli-responsive nanosystems can address the unmet medical needs for non-invasive or minimally invasive approaches, in that stimuli-sensitive nanocarriers enhance specificity, accuracy and efficacy of therapies employing multiple functions such as on-demanded drug delivery, tumour accumulation, targeting/delivery OFF/ON states, and nanoparticle structure, size or charge modifications.[132]

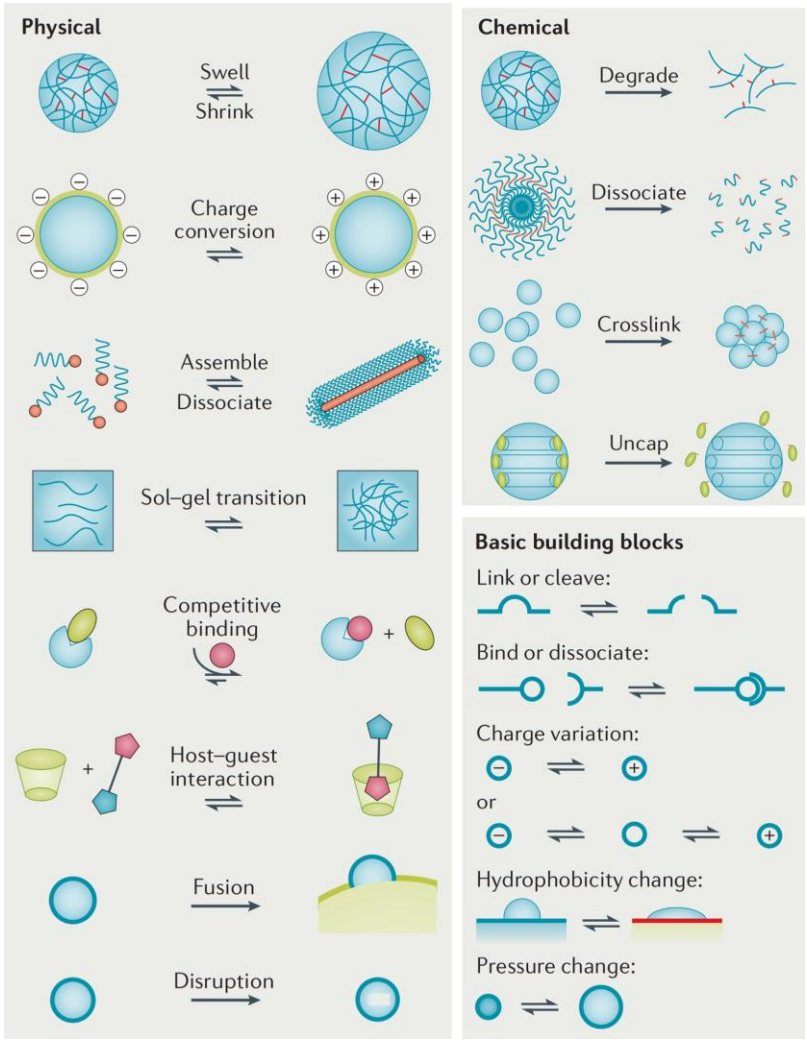

Figure 1.14. Typical triggered actions in responsive materials. Reprinted with permission from "Bioresponsive Materials" by Y. Lu, A. A. Aimetti, R. Langer, Z. Gu, 2017, Nat. Rev. Mater., 2, 16075.

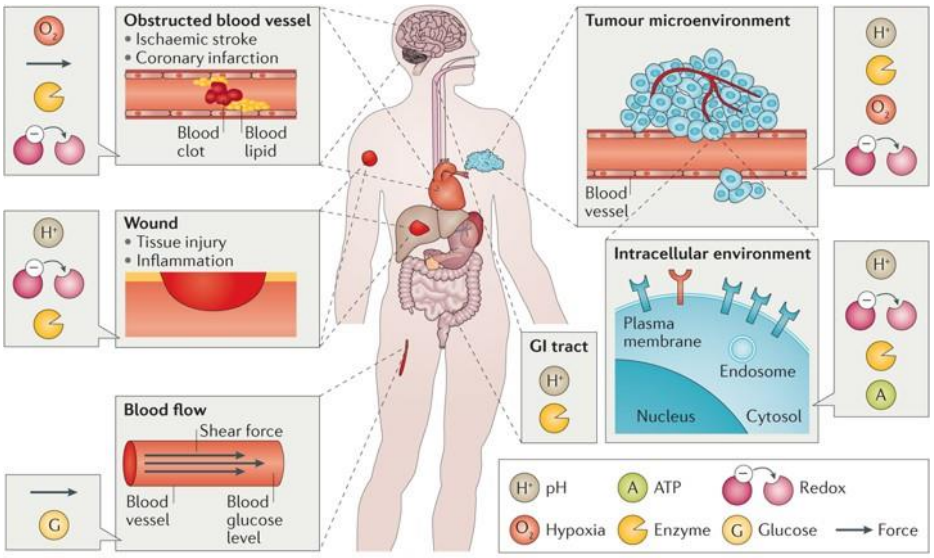

Figure 1.15. Typical physiological environments with associated biological stimuli. Reprinted with permission from "Bioresponsive Materials" by Y. Lu, A. A. Aimetti, R. Langer, Z. Gu, 2017, Nat. Rev. Mater., 2, 16075.

In particular, supramolecular self-assembled nanoparticles could hold great potential in constructing intelligent/smart nanosystems. Supramolecular chemistry allows manipulating molecules and supramolecular building blocks at a molecular level to end up controlling the sizes and morphologies of the resulting supramolecular materials following the "bottom-up" approach.[133] By controlling multiple noncovalent interactions and spatial specificity, supramolecular self-assembled nanoparticles combine bioactive species to promote biocompatibility and achieve accurate targeting and enhanced therapy based on their reversible assembly/disassembly process.[134] Supramolecular synthetic approaches have attracted lots of attention due to their tunability, convenience, responsiveness, biomimicry, and modularity for producing nanoparticles.[135] The self-assembly process provides a reproducible and straightforward way to achieve unique and enhanced nanosystems. Self-assembled materials can offer high levels of precision molecular control that

provide a unique opportunity to generate well-controlled structures and can create design guidelines for new therapeutic strategies, such as triggering responses through selective molecular pathways.[136]

It can be appreciated that nanoparticles provide new opportunities and challenges.[80] The full control over the nanoparticle transport in the body is not achieved yet, so a specific and efficient delivery of nanoparticles to desired sites in the body remains a challenging task to be solved.[137] Thus, more than 99% of the nanoparticles administered *in vivo* are sequestered by the mononuclear phagocytic system (MPS) regardless of whether the active or passive target mechanism has been chosen.[138] Not to mention that when nanoparticles are in contact with the biological milieu, they interact with plasma proteins forming a biomolecular corona, changing nanoparticle properties and functions. At present, nanomedicines still have significant hurdles to overcome as far as their basic mechanisms *in vivo* (*e.g.*, ability to deliver cargo to a specific site, toxicity, enhanced efficacy, etc.). Furthermore, the delivery efficacy of most nanocarriers is still relatively low and requires further improvement.

1.2.2 Organic Fluorophores for Bioimaging

Fluorescence imaging is considered to be one of the most widespread non-destructive tools for biomedical research, as it enables imaging of biomolecules, cellular organelles, and dynamic processes in living organisms due to its high spatiotemporal resolution.[139] As many biological species are scarcely fluorescent or not at all, the use of extrinsic (exogenous) fluorescent agents has therefore become necessary.[140] Bioimaging is defined as the acquisition of images of

biological matter by using such extrinsic synthetic fluorescent agents.[141] Bioimages can be acquired by measuring fluorescence intensity, photo-induced electron transfer (PET) fluorescence, fluorescence lifetime (FLIM), anisotropy/polarization, or fluorescence resonance energy transfer (FRET).[142]

Although many agents such as genetically-encoded fluorescent proteins,[143] fluorescent nanoparticles[144] or fluorescent metal complexes[145] have been explored for fluorescence imaging, small-molecule-organic fluorophores are still the most common agents used in academic and commercial laboratories.[139] Organic fluorophores (or fluorescent dyes) exhibit high versatility due to their attractive photophysical attributes such as small size, easy administration, high sensitivity, flexible design, chemically modifiable, and near-infrared (NIR) emission.[140,146,147] In general, fluorescent dyes fall into two main categories: stains and sensors. Stains are markers for specific subcellular locations or species that return, generally, a constant fluorescence signal, while sensors are actuators that can monitor specific analytes (ions, pH, specific cellular organelles, etc.), returning a fluorescence output that varies in response to this analyte.[148] Based on the response type, there are chromogenic (variation in the colour/emission wavelength) and fluorogenic sensors (variation in the fluorescence intensity).[149] The fluorescent scaffolds for the development and design of fluorescent stains and sensors are manifold, including BODIPYs, coumarin, fluorescein, and cyanine dyes, to name but a few (**Figure 1.16**).

Particularly, it is of paramount importance to bioimage chemical species and processes within individual organelles as physiological and anatomic changes occur when cells become abnormal or diseased.[148] However, to get specific information about organelle environments, stains and sensors must be targeted to the organelle of interest in a selective manner. The distinctive physicochemical

and structural parameters that each subcellular organelle presents could be used for organelle-specific targeting.[150] This ''targeted bioimaging'' is achieved by functionalizing molecular fluorophores with specific moieties such as receptors, ligands, antibodies and so on, which provides fluorescent agents with the desired targeting properties.[141] There is a plethora of strategies for targeting specific subcellular locations. For instance, triphenylphosphonium (TPP) is a chemical moiety that targets mitochondria in that mitochondria attract positively charged moieties due to its negative membrane potential; morpholines and dimethylamines have been extensively used for lysosomal targeting as lysosomes are an acidic organelle that allows weakly basic compounds to be accumulated, or cationic peptides based on lysine and arginine residues enable the subcellular location in the nucleus.[150]

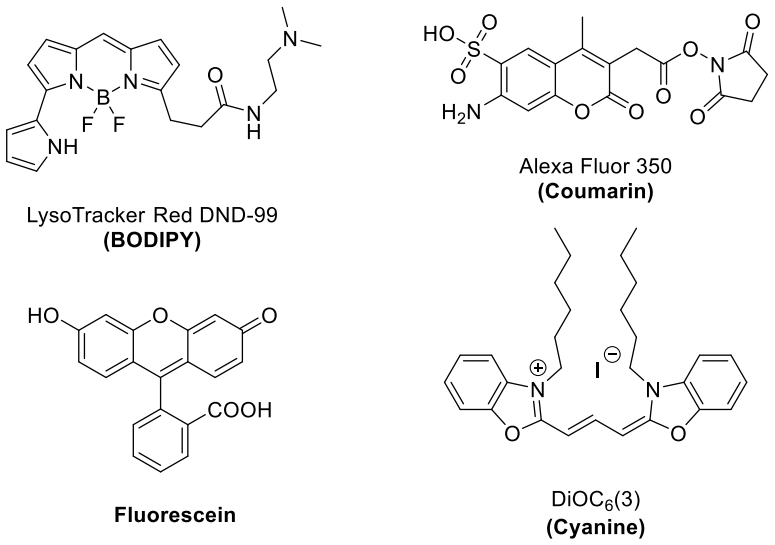

Figure 1.16. Examples of commercially available organic fluorophores.

Among all known molecular probes, the BODIPY family is considered a cornerstone for fluorescence imaging due to their favourable photophysical properties, including large absorption coefficients, high fluorescence quantum yields, narrow emission profiles, nanosecond excited-state lifetimes, excellent thermal and photochemical stability, negligible triplet-state formation, and relative insensitivity to changes in polarity and pH value.[151] In addition, BODIPYs are distinguished by their versatility as minor synthetic modifications to their structures enable tuning of their absorption and fluorescence characteristics, being highly influenced by the extent of electron delocalization around the central cyanine framework.[152] The BODIPY core can be functionalized at the meso, pyrrole, or boron sites and enable to construction of asymmetric dyes.[153] In fact, the potential use of BODIPYs for biological imaging is reflected in the molecular probes market, as several BODIPY-based probes such as ER-Tracker Green or LysoTracker Red are commercially available for the endoplasmic reticulum and lysosomal imaging, respectively. Structural modifications with specific groups for targeting purposes permit obtaining BODIPYs with switchable fluorescence in response to target molecules, analytes, and biological phenomena using the FRET or the PET processes. Indeed, BODIPY dyes are excellent indicators for pH, metal ions, reactive oxygen species, reactive nitrogen species, redox potential or chemical reactions, and are useful in the detection of biomolecules or various physical phenomena.[154,155]

Overall, although further studies are required, particularly on toxicity, bioavailability and bioaccessibility of nanomedicines and nano-enabled techniques, their impact in fighting and diagnosing diseases cannot be understated.[156] Being of utmost importance, not only the (nano)platform design but also the discovery of new multitarget drugs capable of interfering with resistance mechanisms, *e.g.*, in tumours to increase successful treatments.[157]

Fortunately, nanomedicines are in constant advance and progress, leading to an increase in the understanding of human diseases like cancer and many others. It should be noted that this contemporary reality was merely science fiction only 50 years ago, and it is almost certain that nanomedicine and nano-enabled techniques will further revolutionize the healthcare system for the treatment of complex, rare, and incurable diseases.[156] Regarding the fascinating 'nano-world', this thesis reports the design, development and study of amino acid-based compounds as nanocarriers for delivery applications, and as organic fluorophores for bioimaging applications. Organic nanoparticles prepared from a low-molecular-weight bolaamphiphile with responsiveness to a redox environment for enhanced targeted delivery applications are reported in **Chapter 4**. Additionally, the thesis describes the formation of nanotubes from a dipeptide bearing an azobenzene moiety and studies its assembly/disassembly triggered by light in **Chapter 5**. Lastly, structure-performance relationships of BODIPY-based organic dyes bearing diverse monopeptide chains for bioimaging studies are assessed in **Chapter 6**.

References

(1) Weiss, R. G. Chapter 1: Introduction: An Overview of the "What" and "Why" of Molecular Gels. In *Monographs in Supramolecular Chemistry*; 2018; pp 1–27.

(2) Draper, E. R.; Adams, D. J. Low-Molecular-Weight Gels: The State of the Art. *Chem* **2017**, *3* (3), 390–410. https://doi.org/10.1016/j.chempr.2017.07.012.

(3) Du, X.; Zhou, J.; Shi, J.; Xu, B. Supramolecular Hydrogelators and Hydrogels: From Soft Matter to Molecular Biomaterials. *Chem. Rev.* **2015**, *115* (24), 13165–13307. https://doi.org/10.1021/acs.chemrev.5b00299.

(4) Das, T.; Häring, M.; Haldar, D.; Díaz Díaz, D. Phenylalanine and Derivatives as Versatile Low-Molecular-Weight Gelators: Design, Structure and Tailored Function. *Biomater. Sci.* **2018**, *6* (1), 38–59. https://doi.org/10.1039/c7bm00882a.

(5) Mayr, J.; Saldías, C.; Díaz Díaz, D. Release of Small Bioactive Molecules from Physical Gels. *Chem. Soc. Rev.* **2018**, *47* (4), 1484–1515. https://doi.org/10.1039/c7cs00515f.

(6) Chivers, P. R. A.; Smith, D. K. Shaping and Structuring Supramolecular Gels. *Nat. Rev. Mater.* **2019**, *4* (7), 463–478. https://doi.org/10.1038/s41578-019-0111-6.

(7) Okesola, B. O.; Smith, D. K. Applying Low-Molecular Weight Supramolecular Gelators in an Environmental Setting-Self-Assembled Gels as Smart Materials for Pollutant Removal. *Chem. Soc. Rev.* **2016**, *45* (15), 4226–4251. https://doi.org/10.1039/c6cs00124f.

(8) Grover, G.; Weiss, R. G. Luminescent Behavior of Gels and Sols Comprised of Molecular Gelators. *Gels* **2021**, *7* (1), 1–27. https://doi.org/10.3390/GELS7010019.

(9) Van Lommel, R.; De Borggraeve, W. M.; De Proft, F.; Alonso, M. Computational Tools to Rationalize and Predict the Self-Assembly Behavior of Supramolecular Gels. *Gels* **2021**, *7* (3). https://doi.org/10.3390/gels7030087.

(10) Lampel, A.; Ulijn, R. V.; Tuttle, T. Guiding Principles for Peptide Nanotechnology through Directed Discovery. *Chem. Soc. Rev.* **2018**, *47* (10), 3737–3758. https://doi.org/10.1039/c8cs00177d.

(11) Draper, E. R.; Wilbraham, L.; Adams, D. J.; Wallace, M.; Schweins, R.; Zwijnenburg, M. A. Insight into the Self-Assembly of Water-Soluble Perylene Bisimide Derivatives through a Combined Computational and Experimental Approach. *Nanoscale* **2019**, *11* (34), 15917–15928. https://doi.org/10.1039/c9nr03898a.

(12) Hu, X.; Liao, M.; Gong, H.; Zhang, L.; Cox, H.; Waigh, T. A.; Lu, J. R. Recent Advances in Short Peptide Self-Assembly: From Rational Design to Novel Applications. *Curr. Opin. Colloid Interface Sci.* **2020**, *45*, 1–13. https://doi.org/10.1016/j.cocis.2019.08.003.

(13) Dong, R.; Pang, Y.; Su, Y.; Zhu, X. Supramolecular Hydrogels: Synthesis, Properties and Their Biomedical Applications. *Biomater. Sci.* **2015**, *3* (7), 937–954. https://doi.org/10.1039/c4bm00448e.

(14) Li, Z. H.; Yang, H. L.; Adam, K. M.; Yao, H.; Wei, T. B.; Zhang, Y. M.; Lin, Q. Theoretical and Experimental Insights into the Self-Assembly and Ion Response Mechanisms of Tripodal Quinolinamido-Based Supramolecular Organogels. *Chempluschem* **2021**, *86* (1), 146–154. https://doi.org/10.1002/cplu.202000789.

(15) Lan, Y.; Corradini, M. G.; Weiss, R. G.; Raghavan, S. R.; Rogers, M. A. To Gel or Not to Gel: Correlating Molecular Gelation with Solvent Parameters. *Chem. Soc. Rev.* **2015**, *44* (17), 6035–6058. https://doi.org/10.1039/c5cs00136f.

(16) Zurcher, D. M.; Mcneil, A. J. Tools for Identifying Gelator Scaffolds and Solvents. *J. Org. Chem.* **2015**, *80* (5), 2473–2478. https://doi.org/10.1021/jo502915w.

(17) Gupta, J. K.; Adams, D. J.; Berry, N. G. Will It Gel? Successful Computational Prediction of Peptide Gelators Using Physicochemical Properties and Molecular Fingerprints. *Chem. Sci.* **2016**, *7* (7), 4713–4719. https://doi.org/10.1039/c6sc00722h.

(18) Jones, C. D.; Kennedy, S. R.; Walker, M.; Yufit, D. S.; Steed, J. W. Scrolling of

Supramolecular Lamellae in the Hierarchical Self-Assembly of Fibrous Gels. *Chem* **2017**, *3* (4), 603–628. https://doi.org/10.1016/j.chempr.2017.09.001.

(19) Panja, S.; Adams, D. J. Stimuli Responsive Dynamic Transformations in Supramolecular Gels. *Chem. Soc. Rev.* **2021**, *50* (8), 5165–5200. https://doi.org/10.1039/d0cs01166e.

(20) Draper, E. R.; Adams, D. J. Controlling the Assembly and Properties of Low-Molecular-Weight Hydrogelators. *Langmuir* **2019**, *35*, 6506–6521. https://doi.org/10.1021/acs.langmuir.9b00716.

(21) Denzer, B. R.; Kulchar, R. J.; Huang, R. B.; Patterson, J. Advanced Methods for the Characterization of Supramolecular Hydrogels. *Gels* **2021**, *7* (4), 1–29. https://doi.org/10.3390/gels7040158.

(22) Yu, G.; Yan, X.; Han, C.; Huang, F. Characterization of Supramolecular Gels. *Chem. Soc. Rev.* **2013**, *42* (16), 6697–6722. https://doi.org/10.1039/c3cs60080g.

(23) Draper, E. R.; Adams, D. J. How Should Multicomponent Supramolecular Gels Be Characterised? *Chem. Soc. Rev.* **2018**, *47* (10), 3395–3405. https://doi.org/10.1039/c7cs00804j.

(24) Pang, X.; Ge, J.; Yu, X.; Li, Y.; Shen, F.; Wang, Y.; Ren, J. An "off-on" Fluorescent Naphthalimide-Based Sensor for Anions: Its Application in Visual F- and AcO- Discrimination in a Self-Assembled Gel State. *New J. Chem.* **2019**, *43* (26), 10554–10559. https://doi.org/10.1039/c9nj01687b.

(25) Manjunatha Reddy, G. N.; Peters, G. M.; Tatman, B. P.; Rajan, T. S.; Kock, S. M.; Zhang, J.; Frenguelli, B. G.; Davis, J. T.; Marsh, A.; Brown, S. P. Magic-Angle Spinning NMR Spectroscopy Provides Insight into the Impact of Small Molecule Uptake by G-Quartet Hydrogels. *Mater. Adv.* **2020**, *1* (7), 2236–2247. https://doi.org/10.1039/d0ma00475h.

(26) Nonappa; Kolehmainen, E. Solid State NMR Studies of Gels Derived from Low Molecular Mass Gelators. *Soft Matter* **2016**, *12* (28), 6015–6026. https://doi.org/10.1039/c6sm00969g.

(27) Drechsler, S.; Balog, S.; Kilbinger, A. F. M.; Casalini, T. The Influence of Substituents on Gelation and Stacking Order of Oligoaramid-Based Supramolecular Networks. *Soft Matter* **2019**, *15* (36), 7250–7261. https://doi.org/10.1039/c9sm00148d.

(28) Okesola, B. O.; Wu, Y.; Derkus, B.; Gani, S.; Wu, D.; Knani, D.; Smith, D. K.; Adams, D. J.; Mata, A. Supramolecular Self-Assembly to Control Structural and Biological Properties of Multicomponent Hydrogels. *Chem. Mater.* **2019**, *31* (19), 7883–7897. https://doi.org/10.1021/acs.chemmater.9b01882.

(29) Onogi, S.; Shigemitsu, H.; Yoshii, T.; Tanida, T.; Ikeda, M.; Kubota, R.; Hamachi, I. In Situ Real-Time Imaging of Self-Sorted Supramolecular Nanofibres. *Nat. Chem.* **2016**, *8* (8), 743–752. https://doi.org/10.1038/nchem.2526.

(30) Dawn, A.; Mirzamani, M.; Jones, C. D.; Yufit, D. S.; Qian, S.; Steed, J. W.; Kumari, H. Investigating the Effect of Supramolecular Gel Phase Crystallization on Gel Nucleation. *Soft Matter* **2018**, *14* (46), 9489–9497. https://doi.org/10.1039/c8sm01916a.

(31) Draper, E. R.; Dietrich, B.; McAulay, K.; Brasnett, C.; Abdizadeh, H.; Patmanidis, I.; Marrink, S. J.; Su, H.; Cui, H.; Schweins, R.; Seddon, A.; Adams, D. J. Using Small-Angle Scattering and Contrast Matching to Understand Molecular Packing in Low Molecular Weight Gels. *Matter* **2020**, *2* (3), 764–778. https://doi.org/10.1016/j.matt.2019.12.028.

(32) Andrews, J. L.; Pearson, E.; Yufit, D. S.; Steed, J. W.; Edkins, K. Supramolecular Gelation as the First Stage in Ostwald's Rule. *Cryst. Growth Des.* **2018**, *18* (12), 7690–7700. https://doi.org/10.1021/acs.cgd.8b01539.

(33) Angelerou, M. G. F.; Frederix, P. W. J. M.; Wallace, M.; Yang, B.; Rodger, A.; Adams, D. J.; Marlow, M.; Zelzer, M. Supramolecular Nucleoside-Based Gel: Molecular Dynamics Simulation and Characterization of Its Nanoarchitecture and Self-Assembly Mechanism. *Langmuir* **2018**, *34* (23), 6912–6921. https://doi.org/10.1021/acs.langmuir.8b00646.

(34) Dawn, A.; Kumari, H. Low Molecular Weight Supramolecular Gels Under Shear: Rheology as the Tool for Elucidating Structure–Function Correlation. *Chem. - A Eur. J.* **2018**, *24* (4), 762–776. https://doi.org/10.1002/chem.201703374.

(35) Zhang, Y.; Zhang, H.; Zou, Q.; Xing, R.; Jiao, T.; Yan, X. An Injectable Dipeptide-Fullerene Supramolecular Hydrogel for Photodynamic Antibacterial Therapy. *J. Mater. Chem. B* **2018**, *6* (44), 7335–7342. https://doi.org/10.1039/c8tb01487f.

(36) Hashemnejad, S. M.; Kundu, S. Probing Gelation and Rheological Behavior of a Self-Assembled Molecular Gel. *Langmuir* **2017**, *33* (31), 7769–7779. https://doi.org/10.1021/acs.langmuir.7b01531.

(37) Rutgeerts, L. A. J.; Soultan, A. H.; Subramani, R.; Toprakhisar, B.; Ramon, H.; Paderes, M. C.; De Borggraeve, W. M.; Patterson, J. Robust Scalable Synthesis of a Bis-Urea Derivative Forming Thixotropic and Cytocompatible Supramolecular Hydrogels. *Chem. Commun.* **2019**, *55* (51), 7323–7326. https://doi.org/10.1039/c9cc02927c.

(38) Schweitzer-Stenner, R.; Alvarez, N. J. Short Peptides as Tunable, Switchable, and Strong Gelators. *J. Phys. Chem. B* **2021**, *125* (25), 6760–6775. https://doi.org/10.1021/acs.jpcb.1c01447.

(39) Adams, D. J. Does Drying Affect Gel Networks? *Gels* **2018**, *4* (2). https://doi.org/10.3390/gels4020032.

(40) Kubota, R.; Nakamura, K.; Torigoe, S.; Hamachi, I. The Power of Confocal Laser Scanning Microscopy in Supramolecular Chemistry: In Situ Real-Time Imaging of Stimuli-Responsive Multicomponent Supramolecular Hydrogels. *ChemistryOpen* **2020**, *9* (1), 67–79. https://doi.org/10.1002/open.201900328.

(41) Caló, E.; Khutoryanskiy, V. V. Biomedical Applications of Hydrogels: A Review of Patents and Commercial Products. *Eur. Polym. J.* **2015**, *65*, 252–267. https://doi.org/10.1016/j.eurpolymj.2014.11.024.

(42) Andrade, F.; Roca-Melendres, M. M.; Durán-Lara, E. F.; Rafael, D.; Schwartz, S. Stimuli-Responsive Hydrogels for Cancer Treatment: The Role of Ph, Light, Ionic Strength and Magnetic Field. *Cancers (Basel).* **2021**, *13* (5), 1–17.

https://doi.org/10.3390/cancers13051164.

(43) Segarra-Maset, M. D.; Nebot, V. J.; Miravet, J. F.; Escuder, B. Control of Molecular Gelation by Chemical Stimuli. *Chem. Soc. Rev.* **2013**, *42* (17), 7086–7098. https://doi.org/10.1039/C2CS35436E.

(44) Webber, M. J.; Appel, E. A.; Meijer, E. W.; Langer, R. Supramolecular Biomaterials. *Nat. Mater.* **2015**, *15* (1), 13–26. https://doi.org/10.1038/nmat4474.

(45) Skilling, K. J.; Citossi, F.; Bradshaw, T. D.; Ashford, M.; Kellam, B.; Marlow, M. Insights into Low Molecular Mass Organic Gelators: A Focus on Drug Delivery and Tissue Engineering Applications. *Soft Matter* **2014**, *10* (2), 237–256. https://doi.org/10.1039/c3sm52244j.

(46) Lim, J. Y. C.; Lin, Q.; Xue, K.; Loh, X. J. Recent Advances in Supramolecular Hydrogels for Biomedical Applications. *Mater. Today Adv.* **2019**, *3*, 100021. https://doi.org/10.1016/j.mtadv.2019.100021.

(47) Liu, M.; Ouyang, G.; Niu, D.; Sang, Y. Supramolecular Gelatons: Towards the Design of Molecular Gels. *Org. Chem. Front.* **2018**, *5* (19), 2885–2900. https://doi.org/10.1039/c8qo00620b.

(48) Kar, T.; Debnath, S.; Das, D.; Shome, A.; Das, P. K. Organogelation and Hydrogelation of Low-Molecular-Weight Amphiphilic Dipeptides: PH Responsiveness in Phase-Selective Gelation and Dye Removal. *Langmuir* **2009**, *25* (15), 8639–8648. https://doi.org/10.1021/la804235e.

(49) Sheehan, F.; Sementa, D.; Jain, A.; Kumar, M.; Tayarani-Najjaran, M.; Kroiss, D.; Ulijn, R. V. Peptide-Based Supramolecular Systems Chemistry. *Chem. Rev.* **2021**. https://doi.org/10.1021/acs.chemrev.1c00089.

(50) Falcone, N.; Kraatz, H. B. Supramolecular Assembly of Peptide and Metallopeptide Gelators and Their Stimuli-Responsive Properties in Biomedical Applications. *Chem. - A Eur. J.* **2018**, *24* (54), 14316–14328. https://doi.org/10.1002/chem.201801247.

(51) Das, S.; Das, D. Rational Design of Peptide-Based Smart Hydrogels for Therapeutic Applications. *Front. Chem.* **2021**, *9*, 1–30. https://doi.org/10.3389/fchem.2021.770102.

(52) Das, A. K.; Gavel, P. K. Low Molecular Weight Self-Assembling Peptide-Based Materials for Cell Culture, Antimicrobial, Anti-Inflammatory, Wound Healing, Anticancer, Drug Delivery, Bioimaging and 3D Bioprinting Applications. *Soft Matter* **2020**, *16* (44), 10065–10095. https://doi.org/10.1039/d0sm01136c.

(53) Tang, J. D.; Mura, C.; Lampe, K. J. Stimuli-Responsive, Pentapeptide, Nanofiber Hydrogel for Tissue Engineering. *J. Am. Chem. Soc.* **2019**, *141* (12), 4886–4899. https://doi.org/10.1021/jacs.8b13363.

(54) Jeena, M. T.; Jeong, K.; Go, E. M.; Cho, Y.; Lee, S.; Jin, S.; Hwang, S. W.; Jang, J. H.; Kang, C. S.; Bang, W. Y.; Lee, E.; Kwak, S. K.; Kim, S.; Ryu, J. H. Heterochiral Assembly of Amphiphilic Peptides Inside the Mitochondria for Supramolecular Cancer Therapeutics. *ACS Nano* **2019**, *13* (10), 11022–11033. https://doi.org/10.1021/acsnano.9b02522.

(55) Yang, L.; Zhang, C.; Ren, C.; Liu, J.; Zhang, Y.; Wang, J.; Huang, F.; Zhang, L.; Liu, J. Supramolecular Hydrogel Based on Chlorambucil and Peptide Drug for Cancer Combination Therapy. *ACS Appl. Mater. Interfaces* **2019**, *11* (1), 331–339. https://doi.org/10.1021/acsami.8b18425.

(56) Roth-Konforti, M. E.; Comune, M.; Halperin-Sternfeld, M.; Grigoriants, I.; Shabat, D.; Adler-Abramovich, L. UV Light–Responsive Peptide-Based Supramolecular Hydrogel for Controlled Drug Delivery. *Macromol. Rapid Commun.* **2018**, *39* (24). https://doi.org/10.1002/marc.201800588.

(57) Jian, H.; Wang, M.; Dong, Q.; Li, J.; Wang, A.; Li, X.; Ren, P.; Bai, S. Dipeptide Self-Assembled Hydrogels with Tunable Mechanical Properties and Degradability for 3D Bioprinting. *ACS Appl. Mater. Interfaces* **2019**, *11* (50), 46419–46426. https://doi.org/10.1021/acsami.9b13905.

(58) Kumar, N.; Kumbhat, S. *Essentials in Nanoscience and Nanotechnology*; 2016.

(59) Rauscher, H.; Rasmussen, K.; Sokull-Klüttgen, B. Regulatory Aspects of Nanomaterials in the EU. *Chemie-Ingenieur-Technik* **2017**, *89* (3), 224–231. https://doi.org/10.1002/cite.201600076.

(60) Baig, N.; Kammakakam, I.; Falath, W.; Kammakakam, I. Nanomaterials: A Review of Synthesis Methods, Properties, Recent Progress, and Challenges. *Mater. Adv.* **2021**, *2* (6), 1821–1871. https://doi.org/10.1039/d0ma00807a.

(61) Saallah, S.; Lenggoro, I. W. Nanoparticles Carrying Biological Molecules: Recent Advances and Applications. *KONA Powder Part. J.* **2018**, *2018* (35), 89–111. https://doi.org/10.14356/kona.2018015.

(62) Jeevanandam, J.; Barhoum, A.; Chan, Y. S.; Dufresne, A.; Danquah, M. K. Review on Nanoparticles and Nanostructured Materials: History, Sources, Toxicity and Regulations. *Beilstein J. Nanotechnol.* **2018**, *9* (1), 1050–1074. https://doi.org/10.3762/bjnano.9.98.

(63) Liu, C. G.; Han, Y. H.; Kankala, R. K.; Wang, S. Bin; Chen, A. Z. Subcellular Performance of Nanoparticles in Cancer Therapy. *Int. J. Nanomedicine* **2020**, *15*, 675–704. https://doi.org/10.2147/IJN.S226186.

(64) Yang, B.; Chen, Y.; Shi, J. Nanocatalytic Medicine. *Adv. Mater.* **2019**, *31* (39), 1901778. https://doi.org/10.1002/adma.201901778.

(65) Weiss, C.; Carriere, M.; Fusco, L.; Fusco, L.; Capua, I.; Regla-Nava, J. A.; Pasquali, M.; Pasquali, M.; Pasquali, M.; Scott, J. A.; Vitale, F.; Vitale, F.; Unal, M. A.; Mattevi, C.; Bedognetti, D.; Merkoçi, A.; Merkoçi, A.; Tasciotti, E.; Tasciotti, E.; Yilmazer, A.; Yilmazer, A.; Gogotsi, Y.; Stellacci, F.; Delogu, L. G. Toward Nanotechnology-Enabled Approaches against the COVID-19 Pandemic. *ACS Nano* **2020**, *14* (6), 6383–6406. https://doi.org/10.1021/acsnano.0c03697.

(66) Patra, J. K.; Das, G.; Fraceto, L. F.; Campos, E. V. R.; Rodriguez-Torres, M. D. P.; Acosta-Torres, L. S.; Diaz-Torres, L. A.; Grillo, R.; Swamy, M. K.; Sharma, S.; Habtemariam, S.; Shin, H. S. Nano Based Drug Delivery Systems: Recent Developments and Future

Prospects. *J. Nanobiotechnology* **2018**, *16* (1), 1–33. https://doi.org/10.1186/s12951-018-0392-8.

(67) Sung, Y. K.; Kim, S. W. Recent Advances in the Development of Gene Delivery Systems. *Biomater. Res.* **2019**, *23* (1), 1–7. https://doi.org/10.1186/s40824-019-0156-z.

(68) Buck, J.; Grossen, P.; Cullis, P. R.; Huwyler, J.; Witzigmann, D. Lipid-Based DNA Therapeutics: Hallmarks of Non-Viral Gene Delivery. *ACS Nano* **2019**, *13* (4), 3754–3782. https://doi.org/10.1021/acsnano.8b07858.

(69) Mitchell, M. J.; Billingsley, M. M.; Haley, R. M.; Wechsler, M. E.; Peppas, N. A.; Langer, R. Engineering Precision Nanoparticles for Drug Delivery. *Nat. Rev. Drug Discov.* **2021**, *20* (2), 101–124. https://doi.org/10.1038/s41573-020-0090-8.

(70) Lin, H.; Chen, Y.; Shi, J. Nanoparticle-Triggered: In Situ Catalytic Chemical Reactions for Tumour-Specific Therapy. *Chem. Soc. Rev.* **2018**, *47* (6), 1938–1958. https://doi.org/10.1039/c7cs00471k.

(71) Li, M.; Chen, T.; Gooding, J. J.; Liu, J. Review of Carbon and Graphene Quantum Dots for Sensing. *ACS Sensors* **2019**, *4* (7), 1732–1748. https://doi.org/10.1021/acssensors.9b00514.

(72) Shu, T.; Shen, Q.; Zhang, X.; Serpe, M. J. Stimuli-Responsive Polymer/Nanomaterial Hybrids for Sensing Applications. *Analyst* **2020**, *145* (17), 5713–5724. https://doi.org/10.1039/d0an00686f.

(73) Liu, Y.; Bhattarai, P.; Dai, Z.; Chen, X. Photothermal Therapy and Photoacoustic Imaging: Via Nanotheranostics in Fighting Cancer. *Chem. Soc. Rev.* **2019**, *48* (7), 2053–2108. https://doi.org/10.1039/c8cs00618k.

(74) Huang, X.; Song, J.; Yung, B. C.; Huang, X.; Xiong, Y.; Chen, X. Ratiometric Optical Nanoprobes Enable Accurate Molecular Detection and Imaging. *Chem. Soc. Rev.* **2018**, *47* (8), 2873–2920. https://doi.org/10.1039/c7cs00612h.

(75) Eivazzadeh-Keihan, R.; Maleki, A.; de la Guardia, M.; Bani, M. S.; Chenab, K. K.; Pashazadeh-Panahi, P.; Baradaran, B.; Mokhtarzadeh, A.; Hamblin, M. R. Carbon Based Nanomaterials for Tissue Engineering of Bone: Building New Bone on Small Black Scaffolds: A Review. *J. Adv. Res.* **2019**, *18* (March), 185–201. https://doi.org/10.1016/j.jare.2019.03.011.

(76) Hasan, A.; Morshed, M.; Memic, A.; Hassan, S.; Webster, T. J.; Marei, H. E. S. Nanoparticles in Tissue Engineering: Applications, Challenges and Prospects. *Int. J. Nanomedicine* **2018**, *13*, 5637–5655. https://doi.org/10.2147/IJN.S153758.

(77) Xu, L.; Liang, H. W.; Yang, Y.; Yu, S. H. Stability and Reactivity: Positive and Negative Aspects for Nanoparticle Processing. *Chem. Rev.* **2018**, *118* (7), 3209–3250. https://doi.org/10.1021/acs.chemrev.7b00208.

(78) Adepu, S.; Ramakrishna, S. Controlled Drug Delivery Systems: Current Status and Future Directions. *Molecules* **2021**, *26* (19). https://doi.org/10.3390/molecules26195905.

(79) Ehmann, F.; Sakai-Kato, K.; Duncan, R.; Pérez De La Ossa, D. H.; Pita, R.; Vidal, J. M.; Kohli, A.; Tothfalusi, L.; Sanh, A.; Tinton, S.; Robert, J. L.; Silva Lima, B.; Amati, M. P. Next-Generation Nanomedicines and Nanosimilars: EU Regulators' Initiatives Relating to the Development and Evaluation of Nanomedicines. *Nanomedicine* **2013**, *8* (5), 849–856. https://doi.org/10.2217/nnm.13.68.

(80) Bobo, D.; Robinson, K. J.; Islam, J.; Thurecht, K. J.; Corrie, S. R. Nanoparticle-Based Medicines: A Review of FDA-Approved Materials and Clinical Trials to Date. *Pharm. Res.* **2016**, *33* (10), 2373–2387. https://doi.org/10.1007/s11095-016-1958-5.

(81) Hartshorn, C. M.; Morris, S. A. Theranostics: A Historical Perspective of Cancer Nanotechnology Paving the Way for Simultaneous Use Applications. In *Nanotheranostics for Cancer Applications*; P., R., S., M., Eds.; Springer, 2019; pp 91–105. https://doi.org/10.1007/978-3-030-01775-0_5.

(82) Malviya, R.; Fuloria, S.; Verma, S.; Subramaniyan, V.; Sathasivam, K. V.; Kumarasamy, V.; Kumar, D. H.; Vellasamy, S.; Meenakshi, D. U.; Yadav, S.; Sharma, A.; Fuloria, N. K. Commercial Utilities and Future Perspective of Nanomedicines. *PeerJ* **2021**, *9*, 1–30. https://doi.org/10.7717/peerj.12392.

(83) Anselmo, A. C.; Mitragotri, S. Nanoparticles in the Clinic: An Update. *Bioeng. Transl. Med.* **2019**, *4* (3), 1–16. https://doi.org/10.1002/btm2.10143.

(84) Munster, P.; Krop, I. E.; LoRusso, P.; Ma, C.; Siegel, B. A.; Shields, A. F.; Molnár, I.; Wickham, T. J.; Reynolds, J.; Campbell, K.; Hendriks, B. S.; Adiwijaya, B. S.; Geretti, E.; Moyo, V.; Miller, K. D. Safety and Pharmacokinetics of MM-302, a HER2-Targeted Antibody–Liposomal Doxorubicin Conjugate, in Patients with Advanced HER2-Positive Breast Cancer: A Phase 1 Dose-Escalation Study. *Br. J. Cancer* **2018**, *119* (9), 1086–1093. https://doi.org/10.1038/s41416-018-0235-2.

(85) Lim, E. K.; Kim, T.; Paik, S.; Haam, S.; Huh, Y. M.; Lee, K. Nanomaterials for Theranostics: Recent Advances and Future Challenges. *Chem. Rev.* **2015**, *115* (1), 327–394. https://doi.org/10.1021/cr300213b.

(86) Furtado, D.; Björnmalm, M.; Ayton, S.; Bush, A. I.; Kempe, K.; Caruso, F. Overcoming the Blood–Brain Barrier: The Role of Nanomaterials in Treating Neurological Diseases. *Adv. Mater.* **2018**, *30* (46). https://doi.org/10.1002/adma.201801362.

(87) Cicha, I.; Chauvierre, C.; Texier, I.; Cabella, C.; Metselaar, J. M.; Szebeni, J.; Dézsi, L.; Alexiou, C.; Rouzet, F.; Storm, G.; Stroes, E.; Bruce, D.; MacRitchie, N.; Maffia, P.; Letourneur, D. From Design to the Clinic: Practical Guidelines for Translating Cardiovascular Nanomedicine. *Cardiovasc. Res.* **2018**, *114* (13), 1714–1727. https://doi.org/10.1093/cvr/cvy219.

(88) Hammond, P. T. Nano Tools Pave the Way to New Solutions in Infectious Disease. *ACS Infect. Dis.* **2017**, *3* (8), 554–558. https://doi.org/10.1021/acsinfecdis.7b00104.

(89) Zhang, C.; Maruggi, G.; Shan, H.; Li, J. Advances in MRNA Vaccines for Infectious Diseases. *Front. Immunol.* **2019**, *10* (MAR), 1–13. https://doi.org/10.3389/fimmu.2019.00594.

(90) Hare, J. I.; Lammers, T.; Ashford, M. B.; Puri, S.; Storm, G.; Barry, S. T. Challenges and Strategies in Anti-Cancer Nanomedicine Development: An Industry Perspective. *Adv. Drug Deliv. Rev.* **2017**, *108*, 25–38. https://doi.org/10.1016/j.addr.2016.04.025.

(91) Barenholz, Y. Doxil® - The First FDA-Approved Nano-Drug: Lessons Learned. *J. Control. Release* **2012**, *160* (2), 117–134. https://doi.org/10.1016/j.jconrel.2012.03.020.

(92) Beltrán-Gracia, E.; López-Camacho, A.; Higuera-Ciapara, I.; Velázquez-Fernández, J. B.; Vallejo-Cardona, A. A. Nanomedicine Review: Clinical Developments in Liposomal Applications. *Cancer Nanotechnol.* **2019**, *10* (1), 1–40. https://doi.org/10.1186/s12645-019-0055-y.

(93) Zhou, J.; Rao, L.; Yu, G.; Cook, T. R.; Chen, X.; Huang, F. Supramolecular Cancer Nanotheranostics. *Chem. Soc. Rev.* **2021**, *50* (4), 2839–2891. https://doi.org/10.1039/d0cs00011f.

(94) Sainz, V.; Conniot, J.; Matos, A. I.; Peres, C.; Zupančič, E.; Moura, L.; Silva, L. C.; Florindo, H. F.; Gaspar, R. S. Regulatory Aspects on Nanomedicines. *Biochem. Biophys. Res. Commun.* **2015**, *468* (3), 504–510. https://doi.org/10.1016/j.bbrc.2015.08.023.

(95) Đorđević, S.; Gonzalez, M. M.; Conejos-Sánchez, I.; Carreira, B.; Pozzi, S.; Acúrcio, R. C.; Satchi-Fainaro, R.; Florindo, H. F.; Vicent, M. J. Current Hurdles to the Translation of Nanomedicines from Bench to the Clinic. *Drug Deliv. Transl. Res.* **2022**, *12*, 500–525. https://doi.org/10.1007/s13346-021-01024-2.

(96) Farjadian, F.; Ghasemi, A.; Gohari, O.; Roointan, A.; Karimi, M.; Hamblin, M. R. Nanopharmaceuticals and Nanomedicines Currently on the Market: Challenges and Opportunities. *Nanomedicine* **2019**, *14* (1), 93–126. https://doi.org/10.2217/nnm-2018-0120.

(97) Halwani, A. A. Development of Pharmaceutical Nanomedicines: From the Bench to the Market. *Pharmaceutics* **2022**, *14* (1), 1–21. https://doi.org/10.3390/pharmaceutics14010106.

(98) Younis, M. A.; Tawfeek, H. M.; Abdellatif, A. A. H.; Abdel-Aleem, J. A.; Harashima, H. Clinical Translation of Nanomedicines: Challenges, Opportunities, and Keys. *Adv. Drug Deliv. Rev.* **2022**, *181*, 114083. https://doi.org/10.1016/j.addr.2021.114083.

(99) Saydé, T.; Hamoui, O. El; Alies, B.; Gaudin, K.; Lespes, G.; Battu, S. Biomaterials for Three-Dimensional Cell Culture: From Applications in Oncology to Nanotechnology. *Nanomaterials* **2021**, *11* (2), 1–29. https://doi.org/10.3390/nano11020481.

(100) Hua, S.; de Matos, M. B. C.; Metselaar, J. M.; Storm, G. Current Trends and Challenges in the Clinical Translation of Nanoparticulate Nanomedicines: Pathways for Translational Development and Commercialization. *Front. Pharmacol.* **2018**, *9* (JUL), 1–14. https://doi.org/10.3389/fphar.2018.00790.

(101) Wicki, A.; Witzigmann, D.; Balasubramanian, V.; Huwyler, J. Nanomedicine in Cancer Therapy: Challenges, Opportunities, and Clinical Applications. *J. Control. Release* **2015**, *200*, 138–157. https://doi.org/10.1016/j.jconrel.2014.12.030.

(102) Khan, I.; Saeed, K.; Khan, I. Nanoparticles: Properties, Applications and Toxicities. *Arab.*

J. Chem. **2019**, *12* (7), 908–931. https://doi.org/10.1016/j.arabjc.2017.05.011.

(103) Hossen, S.; Hossain, M. K.; Basher, M. K.; Mia, M. N. H.; Rahman, M. T.; Uddin, M. J. Smart Nanocarrier-Based Drug Delivery Systems for Cancer Therapy and Toxicity Studies: A Review. *J. Adv. Res.* **2019**, *15*, 1–18. https://doi.org/10.1016/j.jare.2018.06.005.

(104) Chariou, P. L.; Ortega-Rivera, O. A.; Steinmetz, N. F. Nanocarriers for the Delivery of Medical, Veterinary, and Agricultural Active Ingredients. *ACS Nano* **2020**, *14* (3), 2678–2701. https://doi.org/10.1021/acsnano.0c00173.

(105) Yetisgin, A. A.; Cetinel, S.; Zuvin, M.; Kosar, A.; Kutlu, O. Therapeutic Nanoparticles and Their Targeted Delivery Applications. *Molecules* **2020**, *25* (9), 1–31. https://doi.org/10.3390/molecules25092193.

(106) Kim, D.; Kim, J.; Park, Y. Il; Lee, N.; Hyeon, T. Recent Development of Inorganic Nanoparticles for Biomedical Imaging. *ACS Cent. Sci.* **2018**, *4* (3), 324–336. https://doi.org/10.1021/acscentsci.7b00574.

(107) Zhao, Z.; Li, M.; Zeng, J.; Huo, L.; Liu, K.; Wei, R.; Ni, K.; Gao, J. Recent Advances in Engineering Iron Oxide Nanoparticles for Effective Magnetic Resonance Imaging. *Bioact. Mater.* **2022**, *12* (October 2021), 214–245. https://doi.org/10.1016/j.bioactmat.2021.10.014.

(108) Krishnan, S. K.; Singh, E.; Singh, P.; Meyyappan, M.; Nalwa, H. S. A Review on Graphene-Based Nanocomposites for Electrochemical and Fluorescent Biosensors. *RSC Adv.* **2019**, *9* (16), 8778–8781. https://doi.org/10.1039/c8ra09577a.

(109) Loiseau, A.; Asila, V.; Boitel-Aullen, G.; Lam, M.; Salmain, M.; Boujday, S. Silver-Based Plasmonic Nanoparticles for and Their Use in Biosensing. *Biosensors* **2019**, *9* (2). https://doi.org/10.3390/bios9020078.

(110) Li, D.; van Nostrum, C. F.; Mastrobattista, E.; Vermonden, T.; Hennink, W. E. Nanogels for Intracellular Delivery of Biotherapeutics. *J. Control. Release* **2017**, *259*, 16–28. https://doi.org/10.1016/j.jconrel.2016.12.020.

(111) Kumari, A.; Singla, R.; Guliani, A.; Yadav, S. K. Nanoencapsulation for Drug Delivery. *EXCLI J.* **2014**, *13*, 265–286. https://doi.org/10.17877/DE290R-15592.

(112) Chen, G.; Roy, I.; Yang, C.; Prasad, P. N. Nanochemistry and Nanomedicine for Nanoparticle-Based Diagnostics and Therapy. *Chem. Rev.* **2016**, *116* (5), 2826–2885. https://doi.org/10.1021/acs.chemrev.5b00148.

(113) Zhang, P.; Sun, F.; Liu, S.; Jiang, S. Anti-PEG Antibodies in the Clinic: Current Issues and beyond PEGylation. *J. Control. Release* **2016**, *244*, 184–193. https://doi.org/10.1016/j.jconrel.2016.06.040.

(114) Zhen, X.; Cheng, P.; Pu, K. Recent Advances in Cell Membrane–Camouflaged Nanoparticles for Cancer Phototherapy. *Small* **2019**, *15* (1), 1–19. https://doi.org/10.1002/smll.201804105.

(115) Thakkar, S.; Sharma, D.; Kalia, K.; Tekade, R. K. Tumor Microenvironment Targeted

Nanotherapeutics for Cancer Therapy and Diagnosis: A Review. *Acta Biomater.* **2020**, *101*, 43–68. https://doi.org/10.1016/j.actbio.2019.09.009.

(116) Ding, J.; Chen, J.; Gao, L.; Jiang, Z.; Zhang, Y.; Li, M.; Xiao, Q.; Lee, S. S.; Chen, X. Engineered Nanomedicines with Enhanced Tumor Penetration. *Nano Today* **2019**, *29*, 100800. https://doi.org/10.1016/j.nantod.2019.100800.

(117) Golombek, S. K.; May, J. N.; Theek, B.; Appold, L.; Drude, N.; Kiessling, F.; Lammers, T. Tumor Targeting via EPR: Strategies to Enhance Patient Responses. *Adv. Drug Deliv. Rev.* **2018**, *130*, 17–38. https://doi.org/10.1016/j.addr.2018.07.007.

(118) Attia, M. F.; Anton, N.; Wallyn, J.; Omran, Z.; Vandamme, T. F. An Overview of Active and Passive Targeting Strategies to Improve the Nanocarriers Efficiency to Tumour Sites. *J. Pharm. Pharmacol.* **2019**, *71* (8), 1185–1198. https://doi.org/10.1111/jphp.13098.

(119) Yoo, J.; Park, C.; Yi, G.; Lee, D.; Koo, H. Active Targeting Strategies Using Biological Ligands for Nanoparticle Drug Delivery Systems. *Cancers (Basel).* **2019**, *11* (5). https://doi.org/10.3390/cancers11050640.

(120) Salahpour Anarjan, F. Active Targeting Drug Delivery Nanocarriers: Ligands. *Nano-Structures and Nano-Objects* **2019**, *19*, 100370. https://doi.org/10.1016/j.nanoso.2019.100370.

(121) Ledesma, F.; Ozcan, B.; Sun, X.; Medina, S. M.; Landry, M. P. Nanomaterial Strategies for Delivery of Therapeutic Cargoes. *Adv. Funct. Mater.* **2022**, *32* (4), 1–13. https://doi.org/10.1002/adfm.202107174.

(122) Wang, S.; Huang, P.; Chen, X. Stimuli-Responsive Programmed Specific Targeting in Nanomedicine. *ACS Nano* **2016**, *10* (3), 2991–2994. https://doi.org/10.1021/acsnano.6b00870.

(123) Akimoto, J.; Nakayama, M.; Okano, T. Temperature-Responsive Polymeric Micelles for Optimizing Drug Targeting to Solid Tumors. *J. Control. Release* **2014**, *193*, 2–8. https://doi.org/10.1016/j.jconrel.2014.06.062.

(124) Yang, F.; Cao, Z.; Wang, G. Micellar Assembly of a Photo- and Temperature-Responsive Amphiphilic Block Copolymer for Controlled Release. *Polym. Chem.* **2015**, *6* (46), 7995–8002. https://doi.org/10.1039/c5py01435b.

(125) Li, Y.; Zhang, Y.; Wang, W. Phototriggered Targeting of Nanocarriers for Drug Delivery. *Nano Res.* **2018**, *11* (10), 5424–5438. https://doi.org/10.1007/s12274-018-2132-7.

(126) Cheng, T.; Zhang, Y.; Liu, J.; Ding, Y.; Ou, H.; Huang, F.; An, Y.; Liu, Y.; Liu, J.; Shi, L. Ligand-Switchable Micellar Nanocarriers for Prolonging Circulation Time and Enhancing Targeting Efficiency. *ACS Appl. Mater. Interfaces* **2018**, *10* (6), 5296–5304. https://doi.org/10.1021/acsami.7b18137.

(127) Li, X. X.; Chen, J.; Shen, J. M.; Zhuang, R.; Zhang, S. Q.; Zhu, Z. Y.; Ma, J. B. PH-Sensitive Nanoparticles as Smart Carriers for Selective Intracellular Drug Delivery to Tumor. *Int. J. Pharm.* **2018**, *545* (1–2), 274–285. https://doi.org/10.1016/j.ijpharm.2018.05.012.

(128) Sun, C.; Li, X.; Du, X.; Wang, T. Redox-Responsive Micelles for Triggered Drug Delivery and Effective Laryngopharyngeal Cancer Therapy. *Int. J. Biol. Macromol.* **2018**, *112*, 65–73. https://doi.org/10.1016/j.ijbiomac.2018.01.136.

(129) Thomas, R. G.; Surendran, S. P.; Jeong, Y. Y. Tumor Microenvironment-Stimuli Responsive Nanoparticles for Anticancer Therapy. *Front. Mol. Biosci.* **2020**, *7* (December). https://doi.org/10.3389/fmolb.2020.610533.

(130) Lu, Y.; Aimetti, A. A.; Langer, R.; Gu, Z. Bioresponsive Materials. *Nat. Rev. Mater.* **2017**, *2*, 16075. https://doi.org/10.1038/natrevmats.2016.75.

(131) Ramasamy, T.; Ruttala, H. B.; Gupta, B.; Poudel, B. K.; Choi, H. G.; Yong, C. S.; Kim, J. O. Smart Chemistry-Based Nanosized Drug Delivery Systems for Systemic Applications: A Comprehensive Review. *J. Control. Release* **2017**, *258* (May), 226–253. https://doi.org/10.1016/j.jconrel.2017.04.043.

(132) Mi, P. Stimuli-Responsive Nanocarriers for Drug Delivery, Tumor Imaging, Therapy and Theranostics. *Theranostics* **2020**, *10* (10), 4557–4588. https://doi.org/10.7150/thno.38069.

(133) Ma, X.; Zhao, Y. Biomedical Applications of Supramolecular Systems Based on Host-Guest Interactions. *Chem. Rev.* **2015**, *115* (15), 7794–7839. https://doi.org/10.1021/cr500392w.

(134) Zhao, L.; Xing, Y.; Wang, R.; Yu, F. F.; Yu, F. Self-Assembled Nanomaterials for Enhanced Phototherapy of Cancer. *ACS Appl. Bio Mater.* **2020**, *3* (1), 86–106. https://doi.org/10.1021/acsabm.9b00843.

(135) Prins, T. J. Supramolecular Nanoparticles for Molecular Diagnostics and Therapeutics. In *Supramolecular Chemistry*; John Wiley & Sons, Ltd.: New York, 2012.

(136) Lan, C.; Zhao, S. Self-Assembled Nanomaterials for Synergistic Antitumour Therapy. *J. Mater. Chem. B* **2018**, *6* (42), 6685–6704. https://doi.org/10.1039/c8tb01978a.

(137) Donahue, N. D.; Acar, H.; Wilhelm, S. Concepts of Nanoparticle Cellular Uptake, Intracellular Trafficking, and Kinetics in Nanomedicine. *Adv. Drug Deliv. Rev.* **2019**, *143*, 68–96. https://doi.org/10.1016/j.addr.2019.04.008.

(138) Polo, E.; Collado, M.; Pelaz, B.; Del Pino, P. Advances toward More Efficient Targeted Delivery of Nanoparticles in Vivo: Understanding Interactions between Nanoparticles and Cells. *ACS Nano* **2017**, *11* (3), 2397–2402. https://doi.org/10.1021/acsnano.7b01197.

(139) Li, K.; Ren, T. B.; Huan, S.; Yuan, L.; Zhang, X. B. Progress and Perspective of Solid-State Organic Fluorophores for Biomedical Applications. *J. Am. Chem. Soc.* **2021**, *143* (50), 21143–21160. https://doi.org/10.1021/jacs.1c10925.

(140) Zheng, Q.; Juette, M. F.; Jockusch, S.; Wasserman, M. R.; Zhou, Z.; Altmana, R. B.; Blanchard, S. C. Ultra-Stable Organic Fluorophores for Single-Molecule Research. *Chem Soc Rev.* **2014**, *43*, 1044–1056. https://doi.org/10.1039/c3cs60237k.Ultra-Stable.

(141) Wolfbeis, O. S. An Overview of Nanoparticles Commonly Used in Fluorescent Bioimaging. *Chem. Soc. Rev.* **2015**, *44* (14), 4743–4768. https://doi.org/10.1039/c4cs00392f.

(142) Toseland, C. P. Fluorescent Labeling and Modification of Proteins. *J. Chem. Biol.* **2013**, *6* (3), 85–95. https://doi.org/10.1007/s12154-013-0094-5.

(143) Swedlow, J. R.; Platani, M. Live Cell Imaging Using Wide-Field Microscopy and Deconvolution Cell Engineering for in Vivo Fluorescence Imaging. *Cell Struct. Funct.* **2002**, *341* (5), 335–341.

(144) Ruedas-Rama, M. J.; Walters, J. D.; Orte, A.; Hall, E. A. H. Fluorescent Nanoparticles for Intracellular Sensing: A Review. *Anal. Chim. Acta* **2012**, *751*, 1–23. https://doi.org/10.1016/j.aca.2012.09.025.

(145) Thorp-greenwood, F. L.; Coogan, M. P. Application of d 6 Transition Metal Complexes in Fluorescence Cell Imaging. *Chem. Commun.* **2010**, *46*, 186–202. https://doi.org/10.1039/b917757d.

(146) Klymchenko, A. S. Solvatochromic and Fluorogenic Dyes as Environment-Sensitive Probes: Design and Biological Applications. *Acc. Chem. Res.* **2017**, *50* (2), 366–375. https://doi.org/10.1021/acs.accounts.6b00517.

(147) Heilemann, M.; van de Linde, S.; Mukherjee, A.; Sauer, M. Super-Resolution Imaging with Small Organic Fluorophores. *Angew. Chem. Int. Ed.* **2099**, *48*, 6903–6908.

(148) In, J.; Yang, K.; New, E. J. Strategies for Organelle Targeting of Fluorescent Probes. *Org. Biomol. Chem.* **2021**, *19*, 9339. https://doi.org/10.1039/d1ob01447a.

(149) Martínez-Máñez, R.; Sancenón, F. Fluorogenic and Chromogenic Chemosensors and Reagents for Anions. *Chem. Rev.* **2003**, *103*, 4419–4476. https://doi.org/10.1021/cr010421e.

(150) Choi, N.; Lee, J.; Park, E.; Lee, J.; Lee, J. Recent Advances in Organelle-Targeted Fluorescent Probes. *Molecules* **2021**, *26*, 217. https://doi.org/https://doi.org/10.3390/molecules26010217.

(151) Ziessel, R.; Harriman, A. The Chemistry of Bodipy: A New El Dorado for Fluorescence Tools W. *New J. Chem.* **2007**, *31*, 496–501. https://doi.org/10.1039/b617972j.

(152) Loudet, A.; Burgess, K. BODIPY Dyes and Their Derivatives: Syntheses and Spectroscopic Properties. *Chem. Rev.* **2007**, *107*, 4891–4932.

(153) Ulrich, G.; Ziessel, R.; Harriman, A. The Chemistry of Fluorescent Bodipy Dyes: Versatility Unsurpassed. *Angew. Chem. Int. Ed.* **2008**, *47*, 1184–1201. https://doi.org/10.1002/anie.200702070.

(154) Kowada, T.; Maeda, H.; Kikuchi, K. BODIPY-Based Probes for the Fluorescence Imaging of Biomolecules in Living Cells. *Chem Soc Rev.* **2015**, *44*, 4953. https://doi.org/10.1039/c5cs00030k.

(155) Boens, N.; Leen, V.; Dehaen, W. Fluorescent Indicators Based on BODIPY. *Chem Soc Rev.* **2012**, *41*, 1130–1172. https://doi.org/10.1039/c1cs15132k.

(156) Martins, J. P.; das Neves, J.; de la Fuente, M.; Celia, C.; Florindo, H.; Günday-Türeli, N.; Popat, A.; Santos, J. L.; Sousa, F.; Schmid, R.; Wolfram, J.; Sarmento, B.; Santos, H. A. The Solid Progress of Nanomedicine. *Drug Deliv. Transl. Res.* **2020**, *10* (3), 726–729. https://doi.org/10.1007/s13346-020-00743-2.

(157) Martín-Beltrán, C.; Gil-Edo, R.; Hernández-Ribelles, G.; Agut, R.; Marí-Mezquita, P.; Carda, M.; Falomir, E. Aryl Urea Based Scaffolds for Multitarget Drug Discovery in Anticancer Immunotherapies. *Pharmaceuticals* **2021**, *14*, 337. https://doi.org/10.3390/ph14040337.

Chapter 2

Objectives of the Thesis

The general objective of this Ph.D. thesis is to design, develop and study self-assembled amino acid-based compounds from the standpoint of both fundamental science and applied research for controlled delivery and fluorescence imaging applications.

The specific objectives tackled in each chapter have been:

- To prepare supra-molecular hydrogels containing disulfide and carboxylic units to provide a material with redox and pH responsiveness. These features are initially aimed to be applied in the encapsulation, protection, and release of bioactive species. (**Chapter 3**)

- To prepare nanoparticles (or nanocarriers) from a self-assembled low-molecular-weight bolaamphiphile containing a disulfide unit providing a nanomaterial with responsiveness against naturally present reductants, such as glutathione. (**Chapter 4**)

- To use the novel nanocarriers as vehicles for the transport and release into human cells of compounds of biomedical interest. (**Chapter 4**)

- To study the photocontrolled reversible self-assembly at physiological pH of a dipeptide amphiphile with an appended azobenzene moiety. (**Chapter 5**)

- Preparation of BODIPY derivatives with pendant units to modulate their aggregation and solubility. (**Chapter 6**)

- To assess the structure-performance relationships of new BODIPY derivatives as lysosomal markers for the imaging of cancer cells and a cellular model of lysosomal storage disease. (**Chapter 6**)

Chapter 3

A Dual Stimuli Responsive Supramolecular Gel Provides Insulin Hydrolysis Protection and Redox-Controlled Release of Actives

A Dual Stimuli Responsive Supramolecular Gel Provides Insulin Hydrolysis Protection and Redox-Controlled Release of Actives

Diego Navarro-Barreda, César A. Angulo-Pachón, Begoña Bedrina, Francisco Galindo, and Juan F. Miravet*

Department of Inorganic and Organic Chemistry, University Jaume I, 12071, Castelló de la Plana, Spain.

Accepted Date: 13th January 2020.

Abstract

Two supra-molecular hydrogelators containing a central disulfide moiety and terminal carboxylic acid groups are studied. On the one hand, the hydrogels are responsive to a reductive environment, which transforms the disulfide unit to the corresponding thiols. On the other hand, the hydrogels show pH-response associated with the presence of carboxylic acid units. Gels are formed at pH below *ca.* 4 while at higher pH values, ionization of the gelators provokes gel disassembly.

The properties of the gel are exploited for the release, as a proof of concept, of bromophenol blue in the presence of the reducing species tris(2-carboxyethyl)phosphine hydrochloride (TCEP). Additionally, insulin is loaded into the hydrogels and protected from hydrolysis in a gastric environment using simulated gastric fluid (SGF) containing pepsin. Quantitative release of unaltered insulin, checked with an ELISA colourimetric assay, is observed upon treatment with pH 7.4 buffer. This behaviour would permit the use of these new hydrogels for oral insulin delivery.

3.1 Introduction

The development of smart, stimuli-responsive, materials is undoubtedly a major driving force in chemistry and materials science nowadays. As for soft organic materials, intelligent systems are associated with polymeric gels to a great deal.[1,2] For example, these materials can contract in response to electric fields, light or temperature changes, as revealed in several fundamental reports.[3–6] The potential biomedical application of responsive gels has been explored to a considerable extent. Temperature responsive gels were already used in the 1990s for protein and peptide delivery.[7] Polymeric gel networks permit to design biomedical devices that respond to stimuli such as temperature, pH, or the presence of different molecules such as glucose, glutathione or antigens, among others.[8] In particular, the use of polymeric gel matrices for drug delivery has been extensively studied and reviewed.[9–11]

Molecular (supra-molecular) gels, unlike conventional gels formed by polymers, are constituted by low molecular weight molecules, which self-assemble into solvent percolating fibrillar networks. The interest in these soft supramolecular materials has grown exponentially in the last two decades.[12–14] In particular, molecular hydrogels are receiving much attention due to their potential biomedical applications.[15,16] Distinctive characteristics of supramolecular gels are their intrinsic reversibility and stimuli responsiveness. Due to the supramolecular nature of the interactions, the fibrillar network can usually be reversibly assembled/disassembled by temperature changes or, upon proper design, by different stimuli such as saline effects, light, pH change, enzymes or different chemical species.[17–19] It has to be noted that stimuli-responsiveness in polymeric gels is mostly associated with swelling/shrinking processes, but in molecular gels, the response to the stimulus results commonly in gel disassembly. This

property makes supramolecular gels ideal for stimuli-triggered controlled release as shown, for example, in a recent review on this topic,[20] or for their application in regenerative medicine.[21]

The introduction of ionizable groups in the structure of molecular hydrogelators results in pH-sensitive gels. A relatively large number of pH-sensitive supramolecular gels have been described in the literature. Carboxylic acid moieties are common motifs in pH-responsive molecular gels,[22–24] but a variety of ionizable units have been incorporated such as phenol,[25] histidine,[26] triazole,[27] pyridine[28] or guanidinium,[29] among others. On the other hand, the presence of disulfide moieties in gels affords responsiveness to a reductive environment, like that generated in cells by the presence of glutathione. In this regard, quite a few polymeric gels have been reported containing disulfide linkages, which can be reduced to thiols by glutathione provoking the release of the gel cargo. For example, this approach has been demonstrated for the release of paclitaxel,[30] doxorubicin,[31,32] plasmid DNA,[33] and methotrexate.[34] However, only a reduced number of low molecular weight gelators with disulfide moieties have been described. The most notable case is dibenzoyl-L-cystine, a gelator reported in 1921[35] that was studied in detail in an illuminating paper from Menger et. al.[36] This gelator has been recently used for the preparation of transient supramolecular hydrogels based on the disulfide/thiol interconversion chemistry.[37] Cysteine is also a structural unit for other molecular gelators with disulfide-thiol chemistry,[38–42] but other building blocks have also been used like diphenyldisulfides[43] and commercially available cystamine.[44,45] Interestingly, disulfide reduction, commonly with glutathione,[41,46] dithiothreitol[46,47] or tris(2-carboxyethyl)phosphine hydrochloride (TCEP)[38,48] can result either in gel disassembly[39,40,42–44] or assembly[38,41,45] depending on the system.

A notable application of polymeric gels is their use for the protection of insulin aiming for its oral delivery. The first biological barrier against any orally administered proteins of therapeutic use, such as insulin, is the harsh acidic conditions inside the stomach together with the presence of gastric enzymes, resulting in rapid hydrolysis of peptides and proteins. Different polymeric hydrogels formed, for example, by poly(methacrylic acid) grafted with poly(ethylene glycol),[49] carboxymethylcellulose/poly(acrylic acid)[50] or food gums tragacanth[51] and salecan[52] protected insulin towards hydrolysis in gastric fluids. Nanoparticles or microgels prepared from different biodegradable polymers such as chitosan or poly(lactic-co-glycolic acid), among many others, have also been tested for their use in oral insulin delivery.[53–55] However, up to our knowledge, supra-molecular gels have not been tested for this purpose.

Here we report on two new supramolecular gelator containing both a redox-sensitive disulfide group and pH-responsive carboxylic acid units. The responsiveness of the formed gels towards the disulfide reducing agent TCEP and pH are assayed. As a proof of concept, the release of the entrapped dye bromophenol blue is studied. Additionally, the protection of insulin towards hydrolysis under simulated gastric fluid and later discharge of the protein at simulated intestinal pH is also described.

3.2 Results and Discussion

In previous work, we have described a few amphiphilic and bolaamphiphilic hydrogelators constituted by amino acid units that are N-acylated with succinic anhydride and present alkyl amides formed from the carboxylic acid function

(**Scheme 3.1**, compounds 1 and 2 are given as an example).[24,56,57] Based on that structure and to introduce reduction responsive units, two new isomeric bolaform molecular gelators were built from cystamine (abbr: 'Csa'), and amino acid L-isoleucine (abbr: 'Ile') and succinic anhydride (abbr: 'Suc') for **SucIleCsa**, or L-valine (abbr: 'Val') and glutaric anhydride (abbr: 'Glt') for **GltValCsa** (Scheme 3.1). The preparation of compounds **SucIleCsa** and **GltValCsa** was found to be efficient and straightforward. Acylation of commercially available cystamine with the corresponding C-activated amino acid was followed by N-acylation of the amino acid residue with the corresponding anhydride (Scheme S3.1 and Figure S3.15-S3.18).

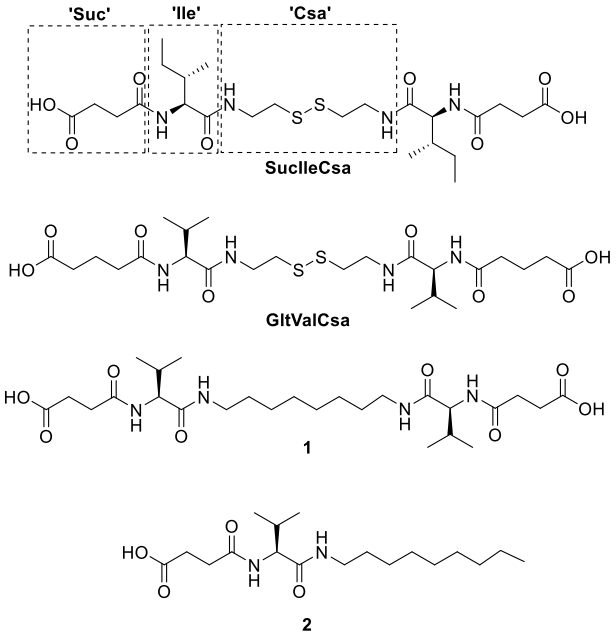

Scheme 3.1. Structure of the studied compounds **SucIleCsa**, **GltValCsa**, and related compounds 1 and 2.

SucIleCsa and **GltValCsa** are pH-sensitive hydrogelators that form gels only in their neutral form at acidic pH. Potentiometric titration of **SucIleCsa** revealed

apparent pK_a values of 4.2 and 5.1 for the first and second deprotonation, respectively. Similar results were obtained for **GltValCsa** with apparent pKa values of 4.3 and 4.6. Apparent pK_a values englobe the thermodynamic balance associated with acid-base and aggregation equilibria.[22,58] **Figure 3.1** shows the calculated species distribution species diagram for **SucIleCsa**, which reveals that neutral species, capable of hydrogelation, are predominant in solution only below pH = 4. At higher pH values, the ionic species are water-soluble, precluding gel formation.

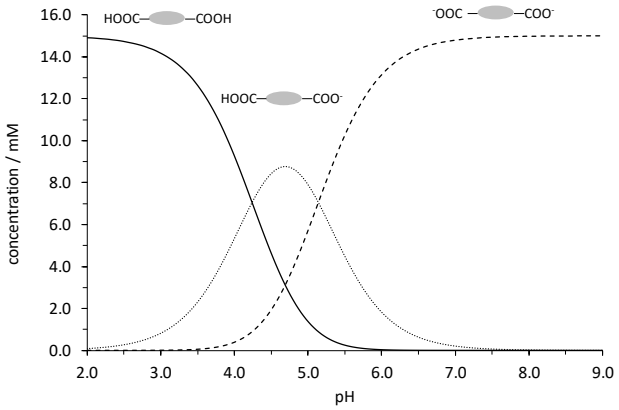

Figure 3.1. Calculated species distribution diagram for **SucIleCsa** (15 mM).

The study of the hydrogelation capabilities was performed at room temperature by addition of 0.1 M HCl to a 0.1 M NaOH solution of the gelator. Opaque hydrogels were formed with minimum gelation concentration (mgc) values of 15 mM, determined by vial inversion methodology, for both **SucIleCsa** and **GltValCsa**. Thermal stability (T_{gel}) was tested with the vial inversion test for 18 mM gels, as those used in the experiments reported below. A T_{gel} value of 80 ± 5 ºC was measured for **GltValCsa** while the gel formed by **SucIleCsa** was not diassembled even at 95 ºC. Rheology studies confirmed the gel-like nature of the soft materials formed, being the elastic modulus, *G'*, considerably higher than

the viscous modulus, *G''*(see Figure S3.1). For gels at a concentration of 18 mM, the elastic moduli showed significative differences between **SucIleCsa** (24,500 Pa) and **GltValCsa** (2,500 Pa). Probably the different morphology of the self-assembled networks, discussed in the next lines, could account for such differences. Transmission electron microscopy (TEM) images of the corresponding xerogels revealed an entanglement of self-assembled fibrillar objects observed commonly in molecular gels (**Figure 3.2** and Figure S3.12). Noticeably, the fibers formed by **SucIleCsa** are thinner and more curved than those found for **GltValCsa** which are flatter and straighter. Additionally, the addition of the fluorescent dye Nile red, that is adsorbed on the fibers, permitted to obtain images by confocal scanning laser microscopy (CSLM) of the unaltered fibrillar structure, without removal of the solvent (**Figure 3.2** and Figure S3.13-S3.14).

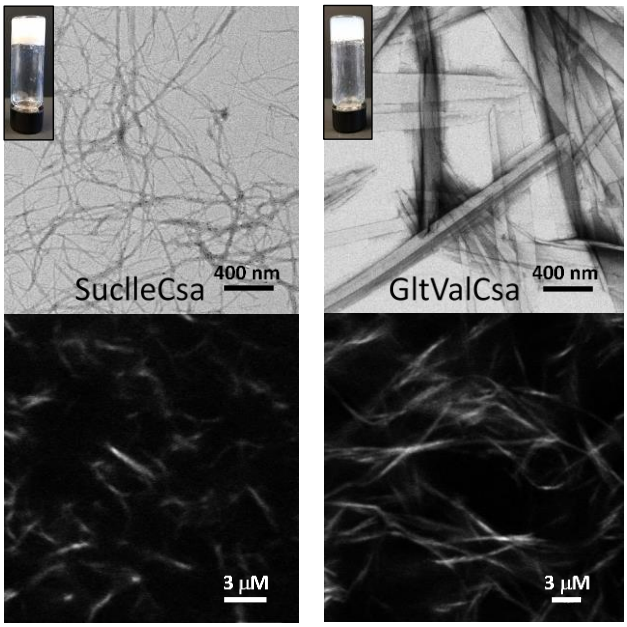

Figure 3.2. Top: TEM images of the xerogels of **SucIleCsa** and **GltValCsa** (18 mM). Bottom: CSLM images of the hydrogels stained with nile red (10 μM).

Gels of **SucIleCsa** and **GltValCsa** (18 mM for both of them) were treated with TCEP at 37.4 °C to evaluate their stability in a reducing environment (Figure S3.2-S3.3). Gel disassembly could be monitored by NMR taking advantage of the fact that the fibrillar network is NMR silent,[59] but the reduced thiols obtained are NMR visible (see **Figure 3.3** and Figure S3.4 for data on **SucIleCsa**, similar results were obtained for **GltValCsa**, shown at Figure S3.5). The NMR integration data collected at different time intervals (see Figure S3.6, S3.7) were fitted to first-order kinetics. It has to be noted that the fibrillar network is solid-like and therefore does not intervene in the kinetic constant. Additionally, the amount of free gelator in equilibrium with the gel network is constant because of the solubility equilibrium present. Half-life times, $t_{1/2}$, of 10.7 and 7.5 hours were calculated for **SucIleCsa** and **GltValCsa**, respectively. As can be seen in **Figure 3.3**, after 18 hours, the gel was transformed into a clear solution of the corresponding thiol. Control experiments with compounds without the disulfide moiety such as **1** and **2** in Scheme 3.1, as expected, revealed that those gels were unaffected by the addition of TCEP (data not shown).

From an applied point of view, the lability of the molecular hydrogelators could find application for the controlled release of actives. It was envisaged that disulfide bond reduction could potentially be used for the controlled, progressive discharge of species entrapped in the hydrogels. To test this idea, bromophenol blue was loaded in hydrogels of **SucIleCsa** and **GltValCsa**. A solution of TCEP was deposited on top of the gel, and the release of bromophenol blue was monitored by UV–Vis at 37.4 ºC, λ_{max}= 437 nm. As shown in **Figure 3.4**, the gel of **SucIleCsa** showed a steady release of the dye for 24 h, resulting from progressive gel disassembly. The control experiment in the absence of TCEP showed a partial liberation of bromophenol blue, which corresponds to the fraction of the dye that is loosely adsorbed on the fibrillary

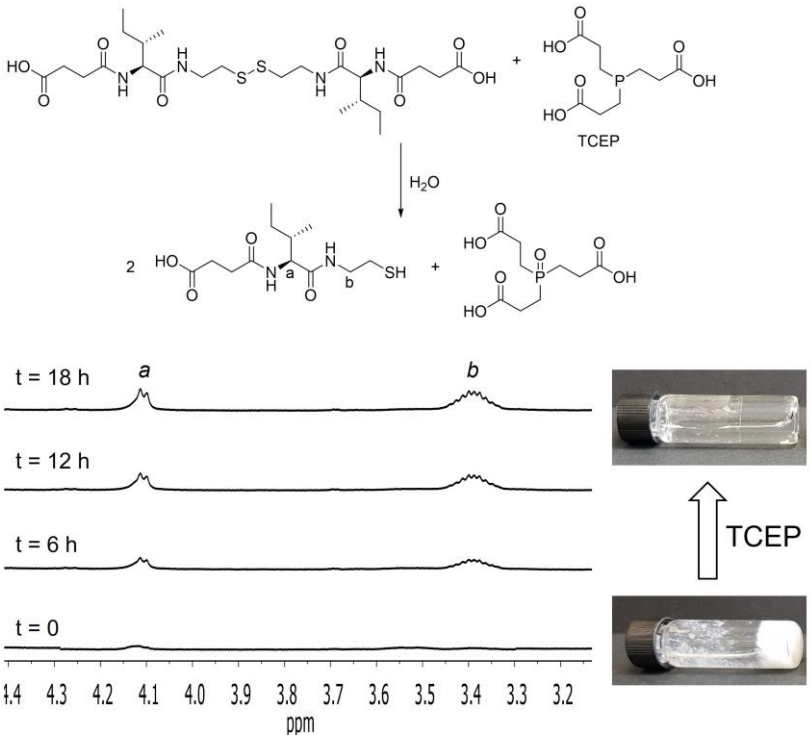

Figure 3.3. Selected ^{1}H-NMR spectra from the kinetic study of **SucIleCsa** gel (18 mM) disassembly in the presence of TCEP (40 mM).

network and leaches out by diffusion. Similar results were obtained in the case of **GltValCsa** although in this case, the amount of dye released by diffusion out of the fibrillary network in the absence of TCEP was higher (see Figure S3.10, S3.11). This behaviour is probably the result of the differences in the morphology of the gel networks pointed by electron microscopy, presenting that of **SucIleCsa** has a higher aspect ratio and better adsorption capabilities.

Finally, the pH responsiveness nature of the gels was exploited for entrapment and later liberation of insulin. Gels were prepared in the presence of insulin (0.25 mg/mL) and incubated keeping contact with a simulated gastric fluid (SGF, pH 1.2) containing pepsin. Under these conditions, free insulin would be hydrolyzed

rapidly, precluding its oral administration. The system was incubated for 2 hours and then, phosphate buffer pH 7.4 was deposited on the top of the gel provoking its disassembly to yield solutions (**Scheme 3.2**). Noteworthy, the pH is rapidly changed from highly acid in the stomach to pH 6.4-7.4 in different areas of the intestine.[60]

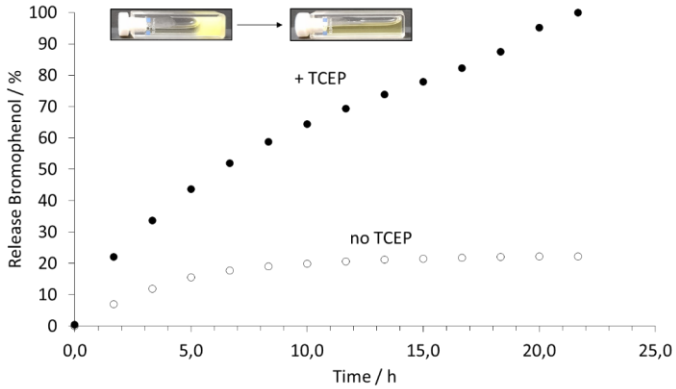

Figure 3.4. UV–Vis evaluation of the liberation of bromophenol blue (0.1 mM) entrapped in the hydrogel formed by **SucIleCsa** in the presence (solid circles) and absence of TCEP (empty circles).

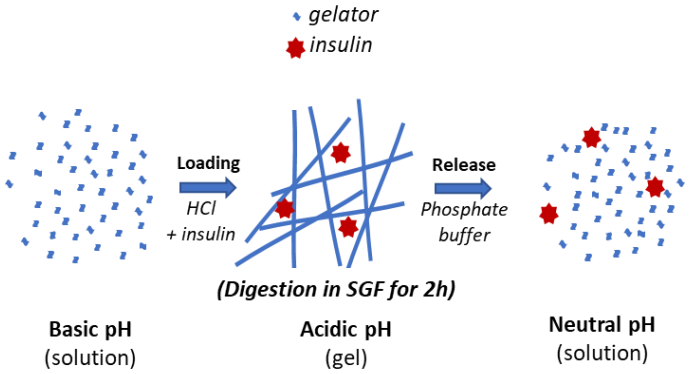

Scheme 3.2. Pictorial representation of entrapment of insulin in a supra-molecular gel and its pH change promoted liberation.

As can be observed in **Figure 3.5**, left, notable differences in the gel solubilization kinetics were noted, being the gel formed by **GltValCsa** fully solubilized after 30 min while that of **SucIleCsa** required more than 2 hours for its complete disaggregation (see NMR study in Figure S3.8-S3.9). An enzyme-linked immunosorbent assay (ELISA), using colourimetric detection of insulin, revealed that after gel disaggregation at pH 7.4 insulin was recovered quantitatively from gel protected insulin samples. On the other hand, no insulin was detected in control samples because of its hydrolysis (**Figure 3.5**, right).

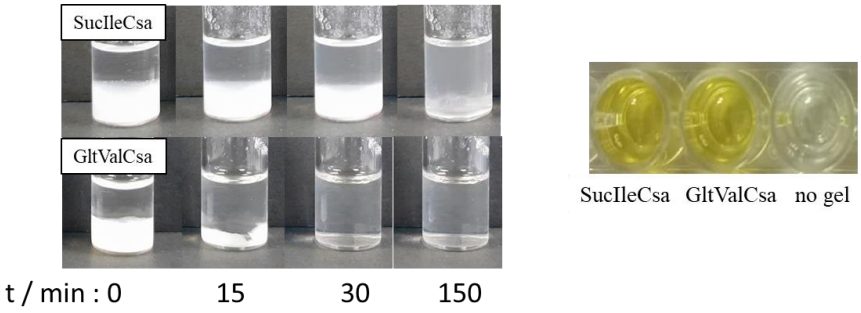

Figure 3.5. Left: images of insulin-loaded hydrogels in the presence of 0.2 M phosphate buffer (pH 7.4) at different time intervals. Right: wells used in the ELISA evaluation of insulin concentration. The yellow colour indicates the presence of unaltered insulin.

3.3 Conclusions

The compounds **SucIleCsa** and **GltValCsa** form supra-molecular hydrogels in acidic media which are constituted by fibrillar networks visualized by electron and confocal microscopy. Despite being **SucIleCsa** and **GltValCsa** isomers, their fibrillar network morphology differs notably. The gels of **GltValCsa** are formed by flat and straight fibres whereas in **SucIleCsa** gels, the fibres are curved and

thinner. The rationalization of these differences is far from trivial nowadays, being the prediction of aggregate morphology based on the structure of the molecule involved a significant challenge.

The studied gelators present two stimuli-responsive groups, disulfide, and carboxylic acid. The presence of a reducing agent capable of breaking disulfide bonds into thiol units, such as TCEP, provokes gel disassembly and subsequent release of the entrapped dye, bromophenol blue, which is used to prove the validity of the stimuli-driven release system devised. The presence of the carboxylic acid moiety in the gelators limits the pH range of hydrogel existence to acidic pH. For pH values higher than *ca.* 4 the gelators are ionized and soluble. This property precludes the use of bioactive reduction molecules such as glutathione for gel disassembly, whose reducing characteristics are halted at acidic pH. The present work highlights how the structural motif used in the preparation of the gelators, a cystamine core coupled to amino acids provides the desired gelation and stimuli responsiveness. For application in biological media, the substitution of a carboxylic acid by other functionalities that permit gel formation at neutral pH should be designed in future work.

On the other hand, the stability of the gels in acidic media and their smooth disassembly at neutral pH permits their use for insulin protection. The insulin loaded into the gels resist degradation in the presence of simulated gastric fluid containing pepsin, a medium that hydrolyzes almost instantly free insulin. The fibrillar network of the gel protects insulin from pepsin that, due to its macromolecular nature, probably diffuses very slowly into the gel. Changing pH from acidic to neutral (pH 7.4), as occurs in the gastrointestinal tract, results in gelator solubilization and insulin release. ELISA analysis shows that insulin released from the gel is recovered quantitatively, while in the absence of gel is

completely hydrolyzed. Therefore, the described hydrogelators show successful results in the proof of concept experiment of protection and release of insulin, overcoming the primary barrier for oral administration of drugs, the harsh conditions of pH and the presence of hydrolytic enzymes along the gastrointestinal tract.[61]

Overall, relatively simple molecules, which can be prepared quickly on a grams scale, form hydrogels that show the sought stimuli responsiveness. The modular nature of their skeleton paves the way for improved properties based on different amino acid building blocks and terminal units.

3.4 Experimental Section

3.4.1 General considerations

^{1}H-NMR and ^{13}C-NMR spectra were recorded on Agilent VNMR System spectrometer (500 MHz for ^{1}H-NMR, 125 MHz ^{13}C-NMR) or Bruker Avance III HD spectrometers (400 MHz and 300 MHz for ^{1}H-NMR, 101 MHz and 75 MHz for ^{13}C-NMR) in the indicated solvent at 30 ºC. Reactions that required an inert atmosphere were carried out under N_2. Commercially available reagents and HPLC grade solvents were used as received. Masses spectra were recorded at Mass Spectrometry triple Quadrupole Q-TOF Premier (Waters) with simultaneous Electrospray and APCI Probe. Rheology studies were done on a Discovery HR-1 (TA Instrument) system, 40 mm parallel plates were used during the experiment at the gap of 500 µm. The gels were characterized by the dynamic frequency sweep test in the region of 1-50 Hz with 0.1% strain at 25 ºC. Before the dynamic sweep, a dynamic strain sweep was performed to find out the linear

viscoelastic region. The UV/Vis absorption measurements were recorded on a JASCO V-630 spectrophotometer. The measurements were carried out using 4 mL SUPRASIL quartz cells with a 10 mm light path from Hellma Analytics. Transmission electron microscopy (TEM) was performed using a JEOL 2100 microscope equipped with a camera CCD (11 MP). The corresponding fresh gels were applied directly onto 200 mesh carbon-coated copper grids and stained with one drop of phosphotungstic acid 1 % for 1 min. Solvent and stain excess were carefully removed by capillary action. Confocal laser scanning microscopy (CLSM) was performed using an inverted confocal microscope Leica TCS SP8. The corresponding fresh gels were stained with Nile red (10 uM) and loaded onto a sterilized Ibidi µ-Slide 8 Well Glass Bottom: # 1.5H (170 mm +/- 5 mm) Schott glass. Excitation of samples was done with a diode laser (514 nm), and images were captured at 63x magnification with HCxPL APO 40.0 x 1.32 oil objective.

3.4.2 Synthesis of SucIleCsa and GltValCsa

See synthetic procedures and characterization in Appendix: Supporting Information.

3.4.3 Hydrogel formation

In a representative example, 10 mg of the hydrogelator were placed in a cylindrical glass vial (diameter = 1.5 cm) and dissolved with 500 µL of aqueous 0.1 M NaOH. Then 600 µL of aqueous 0.1 M HCl were added, and the closed vial was allowed to stand at room temperature until the formation of gel (*ca.* 10 min).

3.4.4 Gel disassembly with TCEP

SucIleCsa and **GltValCsa** hydrogels (1.1 mL, 18 mM) were prepared as described above. Then, 1 mL of aqueous 40 mM TCEP was deposited over the gel, and the closed vial was let to stand at 37.4 °C in a thermostatic bath overnight. At this point, gel disassembly into a solution was observed. Water was removed by lyophilization, and the residue was dissolved in DMSO-d_6 to record the ^{1}H-NMR spectrum. For the kinetic study of the gelator reduction with TCEP, the gels (18 mM, 550 mL) were mixed (vortex) with 500 mL of 40 mM TCEP solution and then sonicated for 1 min to remove air bubbles. The mixture was placed inside an NMR tube, and ^{1}H-NMR spectra were recorded at one-hour intervals at 37 ºC.

The release of bromophenol blue was studied by preparing 1.1 mL of the hydrogels (18 mM) in the presence of bromophenol blue (0.1 mM) in a UV-Vis spectroscopy cuvette (1 cm optical path). Then, 1 mL of the TCEP solution (40 mM, 2.2 eq.) in water was placed over the gels, and the cuvette was sealed and allocated inside the spectrophotometer at 37 ºC. The variation of absorbance with time was monitored at 437 nm. Control experiments with distilled water, instead of the 40 mM TCEP solution, were carried out.

3.4.5 Gel disassembly triggered by the change of pH

1 mL of the hydrogels at a concentration of gelator of 18 mM were prepared as described above. Then, 1 mL of 0.2 M phosphate buffer pH 7.4 was deposited over the gel, and the closed vial was let to stand at room temperature. Gel disassembly was monitored visually by photographs taken during the experiment. At the end of the experiment, the hydrogel network was completely disrupted which yield a clear solution.

For the NMR study of pH-triggered disassembly, 250 µL of hydrogels of the **SucIleCsa** and **GltValCsa** (18 mM for both compounds) were prepared inside an NMR tube. Then, 250 µL of 0.2 M phosphate buffer pH 7.4 were added. The tubes were sealed. The successive ^{1}H-NMR spectra were recorded at intervals of 10 minutes at 30 °C. All solutions were prepared using deuterium oxide (D_2O) as solvent.

3.4.6 Insulin loading and release

All the experiments were carried out at 37 ºC. Hydrogels (1mL, 18 mM) were made in the presence of human recombinant insulin (0.25 mg/mL). Then, 1 mL of simulated gastric fluid (SGF; 0.2 % w/w sodium chloride and 0.32 % w/w pepsin in 0.08 M aqueous HCl, pH 1.2) was placed over the gel. After 2 h, the supernatant SGF solution was withdrawn and then, 1 mL of 0.2 M phosphate buffer, pH 7.4, was added. After several minutes the hydrogel network was utterly disrupted. Control experiments were carried out analogously for aqueous solutions of insulin in the absence of hydrogel. To check the release of undamaged insulin, duplicated ELISA tests were performed with Human Insulin ELISA Kit (RAB0327, Sigma), monitoring colour appearance with a Labtech LT-4000 microplate reader at a wavelength of 450 nm.

Acknowledgements

The authors acknowledge financial support from Ministerio de Economía y Competitividad of Spain (grant CTQ2015-71004-R) and Universitat Jaume I (grants UJI-B2018-54; UJI-B2018-30).

References

(1) Stuart, M. A. C.; Huck, W. T. S.; Genzer, J.; Müller, M.; Ober, C.; Stamm, M.; Sukhorukov, G. B.; Szleifer, I.; Tsukruk, V. V.; Urban, M.; Winnik, F.; Zauscher, S.; Luzinov, I.; Minko, S. Emerging Applications of Stimuli-Responsive Polymer Materials. *Nat. Mater.* **2010**, *9* (2), 101–113. https://doi.org/10.1038/nmat2614.

(2) Pasparakis, G.; Vamvakaki, M. Multiresponsive Polymers: Nano-Sized Assemblies, Stimuli-Sensitive Gels and Smart Surfaces. *Polym. Chem.* **2011**, *2* (6), 1234–1248. https://doi.org/10.1039/c0py00424c.

(3) Tanaka, T.; Nishio, I.; Sun, S. T.; Ueno-Nishio, S. Collapse of Gels in an Electric Field. *Science (80-.).* **1982**, *218*, 467–469.

(4) Suzuki, A.; Tanaka, T. Phase Transition in Polymer Gels Induced by Visible Light. *Nature* **1990**, *346* (6282), 345–347. https://doi.org/10.1038/346345a0.

(5) Osada, Y.; Okuzaki, H.; Hori, H. A Polymer Gel with Electrically Driven Motility. *Nature* **1992**, *355*, 242–244.

(6) Yoshida, R.; Uchida, K.; Kaneko, Y.; Sakai, K.; Kikuchi, A.; Sakurai, Y.; Okano, T. Comb-Type Grafted Hydrogels with Rapid Deswelling Response to Temperature Changes. *Nature* **1995**, *374* (6519), 240–242. https://doi.org/10.1038/374240a0.

(7) Bromberg, L. E.; Ron, E. S. Temperature-Responsive Gels and Thermogelling Polymer Matrices for Protein and Peptide Delivery. *Adv. Drug Deliv. Rev.* **1998**, *31*, 197–221.

(8) Chaterji, S.; Kwon, I. K.; Park, K. Smart Polymeric Gels: Redefining the Limits of Biomedical Devices. *Prog Polym Sci.* **2007**, *32*, 1083–1122.

(9) Gu, D.; O'Connor, A. J.; G.H. Qiao, G.; Ladewig, K. Hydrogels with Smart Systems for Delivery of Hydrophobic Drugs. *Expert Opin. Drug Deliv.* **2017**, *14* (7), 879–895. https://doi.org/10.1080/17425247.2017.1245290.

(10) Narayanaswamy, R.; Torchilin, V. P. Hydrogels and Their Applications in Targeted Drug Delivery. *Molecules* **2019**, *24* (3). https://doi.org/10.3390/molecules24030603.

(11) Bolla, P. K.; Rodriguez, V. A.; Kalhapure, R. S.; Kolli, C. S.; Andrews, S.; Renukuntla, J. A Review on PH and Temperature Responsive Gels and Other Less Explored Drug Delivery Systems. *J. Drug Deliv. Sci. Technol.* **2018**, *46* (March), 416–435. https://doi.org/10.1016/j.jddst.2018.05.037.

(12) Weiss, R. G. The Past, Present, and Future of Molecular Gels. What Is the Status of the Field, and Where Is It Going? *J. Am. Chem. Soc.* **2014**, *136* (21), 7519–7530. https://doi.org/10.1021/ja503363v.

(13) Draper, E. R.; Adams, D. J. Low-Molecular-Weight Gels: The State of the Art. *Chem* **2017**, *3* (3), 390–410. https://doi.org/10.1016/j.chempr.2017.07.012.

(14) Amabilino, D. B.; Smith, D. K.; Steed, J. W. Supramolecular Materials. *Chem. Soc. Rev.* **2017**, *46* (9), 2404–2420. https://doi.org/10.1039/c7cs00163k.

(15) Du, X.; Zhou, J.; Shi, J.; Xu, B. Supramolecular Hydrogelators and Hydrogels: From Soft Matter to Molecular Biomaterials. *Chem. Rev.* **2015**, *115* (24), 13165–13307. https://doi.org/10.1021/acs.chemrev.5b00299.

(16) Webber, M. J.; Dankers, P. Y. W. Supramolecular Hydrogels for Biomedical Applications. *Macromol. Biosci.* **2019**, *19* (1), 1–4. https://doi.org/10.1002/mabi.201800452.

(17) Jones, C. D.; Steed, J. W. Gels with Sense: Supramolecular Materials That Respond to Heat, Light and Sound. *Chem. Soc. Rev.* **2016**, *45* (23), 6546–6596. https://doi.org/10.1039/c6cs00435k.

(18) Dolores Segarra-Maset, M.; Nebot, V. J.; Miravet, J. F.; Escuder, B. Control of Molecular Gelation by Chemical Stimuli. *Chem. Soc. Rev* **2013**, *42*, 7086. https://doi.org/10.1039/c2cs35436e.

(19) Sun, Z.; Huang, Q.; He, T.; Li, Z.; Zhang, Y.; Yi, L. Multistimuli-Responsive Supramolecular Gels: Design Rationale, Recent Advances, and Perspectives. *ChemPhysChem* **2014**, *15* (12), 2421–2430. https://doi.org/10.1002/cphc.201402187.

(20) Mayr, J.; Saldías, C.; Díaz Díaz, D. Release of Small Bioactive Molecules from Physical Gels. *Chem. Soc. Rev.* **2018**, *47* (4), 1484–1515. https://doi.org/10.1039/c7cs00515f.

(21) Hoque, J.; Sangaj, N.; Varghese, S. Stimuli-Responsive Supramolecular Hydrogels and Their Applications in Regenerative Medicine. *Macromol. Biosci.* **2019**, *19* (1), 1–16. https://doi.org/10.1002/mabi.201800259.

(22) Tang, C.; Smith, A. M.; Collins, R. F.; Ulijn, R. V.; Saiani, A. Fmoc-Diphenylalanine Self-ASsembly Mechanism Induces Apparent PK a Shifts. *Langmuir* **2009**, *25* (16), 9447–9453. https://doi.org/10.1021/la900653q.

(23) Adams, D. J.; Butler, M. F.; Frith, W. J.; Kirkland, M.; Mullen, L.; Sanderson, P. A New Method for Maintaining Homogeneity during Liquid-Hydrogel Transitions Using Low Molecular Weight Hydrogelators. *Soft Matter* **2009**, *5* (9), 1856–1862. https://doi.org/10.1039/b901556f.

(24) Angulo-Pachon, C. A.; Miravet, J. F. Sucrose-Fueled, Energy Dissipative, Transient Formation of Molecular Hydrogels Mediated by Yeast Activity. *Chem. Commun.* **2016**, *52* (31), 5398–5401. https://doi.org/10.1039/C6CC01183G.

(25) Verdejo, B.; Rodríguez-Llansola, F.; Escuder, B.; Miravet, J. F.; Ballester, P. Sodium and PH Responsive Hydrogel Formation by the Supramolecular System Calix[4]Pyrrole Derivative/Tetramethylammonium Cation. *Chem. Commun.* **2011**, *47* (7), 2017–2019. https://doi.org/10.1039/c0cc04051g.

(26) Lange, S. C.; Unsleber, J.; Drücker, P.; Galla, H. J.; Waller, M. P.; Ravoo, B. J. PH Response and Molecular Recognition in a Low Molecular Weight Peptide Hydrogel. *Org. Biomol. Chem.* **2015**, *13* (2), 561–569. https://doi.org/10.1039/c4ob02069c.

(27) Okafor, I. S.; Wang, G. Synthesis and Gelation Property of a Series of Disaccharide Triazole Derivatives. *Carbohydr. Res.* **2017**, *451*, 81–94. https://doi.org/10.1016/j.carres.2017.09.008.

(28) Wang, W. Z.; Gao, C.; Zhang, Q.; Ye, X. H.; Qu, D. H. Supramolecular Helical Nanofibers Formed by Achiral Monomers and Their Reversible Sol–Gel Transition. *Chem. - An Asian J.* **2017**, *12* (4), 410–414. https://doi.org/10.1002/asia.201601733.

(29) Externbrink, M.; Riebe, S.; Schmuck, C.; Voskuhl, J. A Dual PH-Responsive Supramolecular Gelator with Aggregation-Induced Emission Properties. *Soft Matter* **2018**, *14* (30), 6166–6170. https://doi.org/10.1039/c8sm01190g.

(30) Sun, K. H.; Sohn, Y. S.; Jeong, B. Thermogelling Poly(Ethylene Oxide-b-Propylene Oxide-b-Ethylene Oxide) Disulfide Multiblock Copolymer as a Thiol-Sensitive Degradable Polymer. *Biomacromolecules* **2006**, *7* (10), 2871–2877. https://doi.org/10.1021/bm060512r.

(31) Chacko, R. T.; Ventura, J.; Zhuang, J.; Thayumanavan, S. Polymer Nanogels: A Versatile Nanoscopic Drug Delivery Platform. *Adv. Drug Deliv. Rev.* **2012**, *64* (9), 836–851. https://doi.org/10.1016/j.addr.2012.02.002.

(32) Zhang, X.; Achazi, K.; Steinhilber, D.; Kratz, F.; Dernedde, J.; Haag, R. A Facile Approach for Dual-Responsive Prodrug Nanogels Based on Dendritic Polyglycerols with Minimal Leaching. *J. Control. Release* **2014**, *174* (1), 209–216. https://doi.org/10.1016/j.jconrel.2013.11.005.

(33) Cai, X.; Dong, C.; Dong, H.; Wang, G.; Pauletti, G. M.; Pan, X.; Wen, H.; Mehl, I.; Li, Y.; Shi, D. Effective Gene Delivery Using Stimulus-Responsive Catiomer Designed with Redox-Sensitive Disulfide and Acid-Labile Imine Linkers. *Biomacromolecules* **2012**, *13* (4), 1024–1034. https://doi.org/10.1021/bm2017355.

(34) Feng, N.; Yang, M.; Feng, X.; Wang, Y.; Chang, F.; Ding, J. Reduction-Responsive Polypeptide Nanogel for Intracellular Drug Delivery in Relieving Collagen-Induced Arthritis. *ACS Biomater. Sci. Eng.* **2018**, *4* (12), 4154–4162. https://doi.org/10.1021/acsbiomaterials.8b00738.

(35) Gortner, R. A.; Hoffman, W. F. THE ACTION OF HYDROGEN PHOSPHIDE ON FORMALDEHYDE. **1921**, *43*, 2199–2202.

(36) Menger, F. M.; Caran, K. L. Anatomy of a Gel. Amino Acid Derivatives That Rigidify Water at Submillimolar Concentrations. *J. Am. Chem. Soc.* **2000**, *122* (47), 11679–11691. https://doi.org/10.1021/ja0016811.

(37) Wojciechowski, J. P.; Martin, A. D.; Thordarson, P. Kinetically Controlled Lifetimes in Redox-Responsive Transient Supramolecular Hydrogels. *J. Am. Chem. Soc.* **2018**, *140* (8), 2869–2874. https://doi.org/10.1021/jacs.7b12198.

(38) Bowerman, C. J.; Nilsson, B. L. A Reductive Trigger for Peptide Self-Assembly and Hydrogelation. *J. Am. Chem. Soc.* **2010**, *132* (28), 9526–9527. https://doi.org/10.1021/ja1025535.

(39) Sadownik, J. W.; Ulijn, R. V. Locking an Oxidation-Sensitive Dynamic Peptide System in the Gel State. *Chem. Commun.* **2010**, *46* (20), 3481–3483. https://doi.org/10.1039/c001982h.

(40) Chen, J.; Wu, W.; McNeil, A. J. Detecting a Peroxide-Based Explosive via Molecular

Gelation. *Chem. Commun.* **2012**, *48* (58), 7310–7312. https://doi.org/10.1039/c2cc33486k.

(41) Liu, S.; Tang, A.; Xie, M.; Zhao, Y.; Jiang, J.; Liang, G. Oligomeric Hydrogels Self-Assembled from Reduction-Controlled Condensation. *Angew. Chemie - Int. Ed.* **2015**, *54* (12), 3639–3642. https://doi.org/10.1002/anie.201409952.

(42) Rasale, D. B.; Maity, I.; Konda, M.; Das, A. K. Peptide Self-Assembly Driven by Oxo-Ester Mediated Native Chemical Ligation. *Chem. Commun.* **2013**, *49* (42), 4815–4817. https://doi.org/10.1039/c3cc41475b.

(43) Ge, Y.; Gong, H.; Shang, J.; Jin, L.; Pan, T.; Zhang, Q.; Dong, S.; Wang, Y.; Qi, Z. Supramolecular Gel Based on Crown-Ether-Appended Dynamic Covalent Macrocycles. *Macromol. Rapid Commun.* **2019**, *40* (17), 1–7. https://doi.org/10.1002/marc.201800731.

(44) Gao, Y.; Lu, J.; Wu, J.; Hu, J.; Ju, Y. Water Tuned Nano/Micro-Structures in a Redox-Responsive Supramolecular Gel. *RSC Adv.* **2014**, *4* (108), 63539–63543. https://doi.org/10.1039/c4ra12247j.

(45) Chen, G.; Li, J.; Cai, Y.; Zhan, J.; Gao, J.; Song, M.; Shi, Y.; Yang, Z. A Glycyrrhetinic Acid-Modified Curcumin Supramolecular Hydrogel for Liver Tumor Targeting Therapy. *Sci. Rep.* **2017**, *7* (November 2016), 1–8. https://doi.org/10.1038/srep44210.

(46) Milanesi, L.; Hunter, C. A.; Tzokova, N.; Waltho, J. P.; Tomas, S. Versatile Low-Molecular-Weight Hydrogelators: Achieving Multiresponsiveness through a Modular Design. *Chem. - A Eur. J.* **2011**, *17* (35), 9753–9761. https://doi.org/10.1002/chem.201100640.

(47) Yu, J.; Fan, H.; Huang, J.; Chen, J. Fabrication and Evaluation of Reduction-Sensitive Supramolecular Hydrogel Based on Cyclodextrin/Polymer Inclusion for Injectable Drug-Carrier Application. *Soft Matter* **2011**, *7* (16), 7386–7394. https://doi.org/10.1039/c1sm05426k.

(48) Rasale, D. B.; Maity, I.; Das, A. K. In Situ Generation of Redox Active Peptides Driven by Selenoester Mediated Native Chemical Ligation. *Chem. Commun.* **2014**, *50*, 11397–11400. https://doi.org/10.1039/c4cc03835e.

(49) Yamagata, T.; Morishita, M.; Kavimandan, N. J.; Nakamura, K.; Fukuoka, Y.; Takayama, K.; Peppas, N. A. Characterization of Insulin Protection Properties of Complexation Hydrogels in Gastric and Intestinal Enzyme Fluids. *J. Control. Release* **2006**, *112* (3), 343–349. https://doi.org/10.1016/j.jconrel.2006.03.005.

(50) Gao, X.; Cao, Y.; Song, X.; Zhang, Z.; Zhuang, X.; He, C.; Chen, X. Biodegradable, PH-Responsive Carboxymethyl Cellulose/Poly(Acrylic Acid) Hydrogels for Oral Insulin Delivery. *Macromol. Biosci.* **2014**, *14* (4), 565–575. https://doi.org/10.1002/mabi.201300384.

(51) Cikrikci, S.; Mert, B.; Oztop, M. H. Development of PH Sensitive Alginate/Gum Tragacanth Based Hydrogels for Oral Insulin Delivery. *J. Agric. Food Chem.* **2018**, *66* (44), 11784–11796. https://doi.org/10.1021/acs.jafc.8b02525.

(52) Qi, X.; Yuan, Y.; Zhang, J.; Bulte, J. W. M.; Dong, W. Oral Administration of Salecan-Based Hydrogels for Controlled Insulin Delivery. *J. Agric. Food Chem.* **2018**, *66* (40), 10479–10489. https://doi.org/10.1021/acs.jafc.8b02879.

(53) Damgé, C.; Reis, C. P.; Maincent, P. Nanoparticle Strategies for the Oral Delivery of Insulin. *Expert Opin. Drug Deliv.* **2008**, *5* (1), 45–68. https://doi.org/10.1517/17425247.5.1.45.

(54) Liu, L.; Zhang, Y.; Yu, S.; Yang, Z.; He, C.; Chen, X. Dual Stimuli-Responsive Nanoparticle-Incorporated Hydrogels as an Oral Insulin Carrier for Intestine-Targeted Delivery and Enhanced Paracellular Permeation. *ACS Biomater. Sci. Eng.* **2018**, *4* (8), 2889–2902. https://doi.org/10.1021/acsbiomaterials.8b00646.

(55) Liu, L.; Zhang, Y.; Yu, S.; Zhang, Z.; He, C.; Chen, X. PH- and Amylase-Responsive Carboxymethyl Starch/Poly(2-Isobutyl-Acrylic Acid) Hybrid Microgels as Effective Enteric Carriers for Oral Insulin Delivery. *Biomacromolecules* **2018**, *19* (6), 2123–2136. https://doi.org/10.1021/acs.biomac.8b00215.

(56) Fontanillo, M.; Angulo-Pachón, C. A.; Escuder, B.; Miravet, J. F. In Situ Synthesis-Gelation at Room Temperature vs. Heating-Cooling Procedure. Fine Tuning of Molecular Gels Derived from Succinic Acid and L-Valine. *J. Colloid Interface Sci.* **2013**, *412*, 65–71. https://doi.org/10.1016/j.jcis.2013.08.055.

(57) Angulo-Pachón, C. A.; Navarro-Barreda, D.; Rueda, C. M.; Galindo, F.; Miravet, J. F. Deamidation of Pseudopeptidic Molecular Hydrogelators and Its Application to Controlled Release. *J. Colloid Interface Sci.* **2017**, *505*, 1111–1117. https://doi.org/10.1016/j.jcis.2017.07.003.

(58) Tena-Solsona, M.; Escuder, B.; Miravet, J. F.; Casttelleto, V.; Hamley, I. W.; Dehsorkhi, A. Thermodynamic and Kinetic Study of the Fibrillization of a Family of Tetrapeptides and Its Application to Self-Sorting. What Takes so Long? *Chem. Mater.* **2015**, *27* (9), 3358–3365. https://doi.org/10.1021/acs.chemmater.5b00580.

(59) Escuder, B.; LLusar, M.; Miravet, J. F. Insight on the NMR Study of Supramolecular Gels and Its Application to Monitor Molecular Recognition on Self-Assembled Fibers. *J. Org. Chem.* **2006**, *71* (20), 7747–7752. https://doi.org/10.1021/jo0612731.

(60) Pye, G.; Evans, D. F.; Ledingham, S.; Hardcastle, J. D. Gastrointestinal Intraluminal PH in Normal Subjects and Those with Colorectal Adenoma or Carcinoma. *Gut* **1990**, *31* (12), 1355–1357. https://doi.org/10.1136/gut.31.12.1355.

(61) Homayun, B.; Lin, X.; Choi, H. J. Challenges and Recent Progress in Oral Drug Delivery Systems for Biopharmaceuticals. *Pharmaceutics* **2019**, *11* (3). https://doi.org/10.3390/pharmaceutics11030129.

(62) Becerril, J.; Bolte, M.; Burguete, M. I.; Galindo, F.; Luis, S. V; Miravet, J. F. Efficient Macrocyclization of U-Turn Preorganized Peptidomimetics: The Role of Intramolecular H-Bond and Solvophobic Effects. **2003**, No. 5, 6677–6686. https://doi.org/10.1021/ja0284759.

Appendix: Supporting Information

1. Synthesis

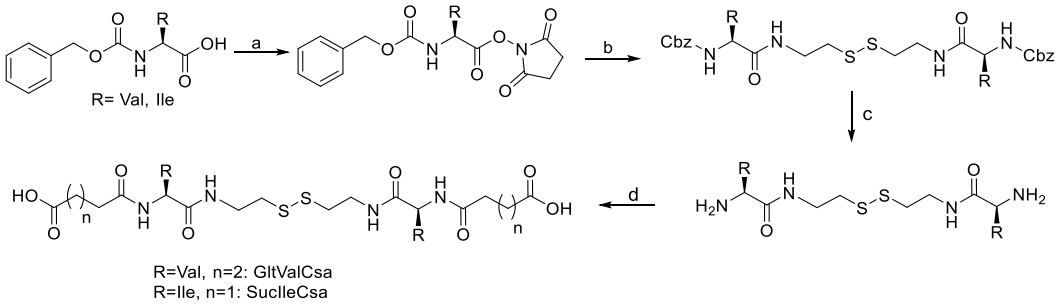

Scheme S3.1. Reagents and conditions: a) DCC, *N*-hydroxisuccinimide, THF, 2 h, 95 – 97%; b) cystamine dihydrochloride, Et_3N, DMF, 16 h, 93%; c) HBr 33 wt. % in acetic acid, 2 h, 90 – 98%; d) Succinic or glutaric anhydride, Na_2CO_3, THF, 16 h, 70 - 85%.

A. General procedure for activation of amino acid: A solution of commercially available carbobenzyloxy-*L*-amino acid (40 mmol, 1 eq.) and *N*-hydroxysuccinimide (40 mmol, 1.0 eq.) in THF (150 mL) was added dropwise by using a dropping funnel to a solution of *N,N*′-dicyclohexylcarbodiimide (10.9 mmol, 1.01 eq.) in THF (75 mL) under N_2 atmosphere at 0 ºC. The mixture was further stirred for 1 h at 0 ºC. The solution was then allowed to stand in the refrigerator for 2 h, which caused precipitation of *N,N*′-dicyclohexylurea. After this time, the mixture was filtered under vacuum, the filtrate was evaporated under reduced pressure and the crude residue was purified by crystallization in isopropanol to yield the corresponding activated ester.

2,5-dioxopyrrolidin-1-yl ((benzyloxy)carbonyl)-L-valinate (ZValOSu): A white solid was obtained (yield 97%); the NMR spectra were consistent with those described in the literature.[62]

2,5-dioxopyrrolidin-1-yl ((benzyloxy)carbonyl)-L-isoleucinate (ZIleOSu): A white solid was obtained (yield 95%); the NMR spectra were consistent with those described in the literature.[62]

B. General procedure for coupling between activated ester and amine: A solution of activated ester (8.3 mmol, 2.1 eq.) in dry dimethylformamide (DMF, 45 mL) was added dropwise under N_2 atmosphere at room temperature by using a dropping funnel to a solution of cystamine dihydrochloride (3.94, 1 eq.) in DMF (20 mL). The mixture was stirred for 1 h at 60 ºC. After this time, Et_3N (1.1 mL, 2 eq.) was added dropwise to the mixture. The resulting mixture was further stirred at 60 ºC overnight. Afterwards, the solution was allowed to cool down to room temperature and water was added dropwise to the reaction solution, precipitating a solid that was filtered, washed with water twice and dried in vacuum at 50 ºC for 24 hours.

Benzyl ((5R,16S)-5-isopropyl-17-methyl-3,6,15-trioxo-1-phenyl-2-oxa-10,11 dithia-4,7,14-triazaoctadecan-16-yl)carbamate (ZValCsa): Compound **ZValCsa** was obtained (yield 93%) as a white solid. **^{1}H-NMR (400 MHz, DMSO-*d*$_6$, *δ*)**: 8.10 (t, *J* = 5.3 Hz, 2H), 7.47 – 7.28 (m, 10H), 7.21 (d, *J* = 8.8 Hz, 2H), 5.11 – 4.94 (s, 4H), 3.90 – 3.71 (m, 2H), 3.49 – 3.34 (m, 4H), 2.87 – 2.67 (m, 4H), 2.02-1.85 (m, 2H), 0.92-0.80 (m, 12H). **^{13}C-NMR (101 MHz, DMSO-*d*$_6$, *δ*)**: 171.3, 156.1, 137.1 , 128.3, 127.7, 127.6, 65.4, 60.3, 37.8, 37.1, 30.2, 19.2, 18.1. **HRMS (ESI-TOF) m/z:** $[M+H]^+$ calcd for $C_{30}H_{42}N_4O_6S_2$ 619.2624; found, 619.2621.

Benzyl ((5R,16S,17S)-5-((S)-sec-butyl)-17-methyl-3,6,15-trioxo-1-phenyl-2-oxa-10,11-dithia-4,7,14-triazanonadecan-16-yl)carbamate (ZIleCsa): Compound **ZIleCsa** was obtained (yield 72%) as a white solid. **^{1}H-NMR**

(400 MHz, DMSO-*d*$_6$, *δ*): 8.11 (t, *J* = 5.2 Hz, 2H), 7.42 – 7.25 (m, 10H), 7.23 (d, *J* = 8.8 Hz, 2H), 5.02 (s, 4H), 3.84 (t, *J* = 8.2 Hz, 2H), 3.47 – 3.32 (m, 4H), 2.87 – 2.67 (m, 4H), 1.78-1.61 (m, 2H), 1.49 – 1.33 (m, 2H), 1.22 – 1.01 (m, 2H), 0.87 - 0.74 (m, 12H). **^{13}C-NMR (101 MHz, DMSO-*d*$_6$, *δ*)**: 171.3, 156.0, 137.1, 128.3, 127.7, 127.6, 65.4, 59.2, 37.84, 37.05, 36.32, 24.36, 15.40, 10.89. **HRMS (ESI-TOF) m/z:** $[M+H]^+$ calcd for $C_{32}H_{46}N_4O_6S_2$ 647.2937; found, 647.2936.

C. General procedure for deprotection of carbobenzyloxy group: Carbobenzyloxy amino compounds (1.55 mmol, 1 eq.) were added to HBr/AcOH (33 wt. %) (5 mL, 18 eq.) and the mixture was stirred at room temperature until CO_2 evolution ceased. At this point, diethyl ether was added to the clear solution, which led to the deposition of a white precipitate. This was filtered off, washed with additional ether and dissolved in distilled water. Solid NaOH was then added up to a pH value of 12 and the resulting solution was saturated with NaCl and extracted with chloroform (30 mL, x3). The organic phase was dried over Na_2SO_4 and evaporated under vacuum to obtain a yellow oil. The compound was used in crude form for the next reaction.

(S)-2-amino-N-(2-((2-((R)-2-amino-3-methylbutanamido)ethyl)-disulfaneyl)-ethyl)-3-methylbutanamide (HValCsa): Yellow oil was obtained (yield 98%). **^{1}H-NMR (300 MHz, DMSO-*d*$_6$, *δ*)**: 8.04 (t, *J* = 5.6 Hz, 2H), 3.43 – 3.34 (m, 4H), 2.93 (d, *J* = 5.1 Hz, 2H), 2.79 (t, *J* = 6.8 Hz, 4H), 1.96 – 1.79 (m, 2H), 0.86 (d, *J* = 6.9 Hz, 6H), 0.78 (d, *J* = 6.8 Hz, 6H). **^{13}C-NMR (101 MHz, DMSO-*d*$_6$, *δ*)**: 174.6, 60.0, 37.6, 37.3, 31.5, 19.5, 17.0. **HRMS (ESI-TOF) m/z:** $[M+H]^+$ calcd for $C_{14}H_{30}N_4O_2S_2$ 351.1888; found, 351.1888.

(2S,3S)-2-amino-N-(2-((2-((2R,3S)-2-amino-3-methylpentanamido)ethyl)-disulfaneyl) ethyl)-3-methylpentanamide (HIleCsa): Yellow oil was obtained (yield 90%). **^{1}H-NMR (300 MHz, DMSO-*d*$_6$, *δ*)**: 8.05 (t, *J* = 5.5 Hz, 2H), 3.44 – 3.33 (m, 4H), 2.97 (d, *J* = 5.4 Hz, 2H), 2.79 (t, *J* = 6.8 Hz, 4H), 1.70 – 1.51 (m, 2H), 1.51 – 1.32 (m, 2H), 1.17 – 0.97 (m, 2H), 0.91 – 0.73 (m, 12H). **^{13}C-NMR (101 MHz, DMSO-*d*$_6$, *δ*)**: 174.6, 59.3, 38.3, 37.6, 37.3, 23.7, 15.8, 11.5. **HRMS (ESI-TOF) m/z:** $[M+H]^+$ calcd for $C_{16}H_{34}N_4O_2S_2$ 379.2201; found, 379.2206.

D. General procedure for anhydride coupling: A solution of the respective unprotected amine (1.55 mmol, 1 eq.) in THF (65 mL) was treated at 0 ºC under N_2 atmosphere with solid Na_2CO_3 (6.2 mmol, 4 eq.). After 15 minutes at 0 ºC, a solution of commercially available succinic anhydride or glutaric anhydride (6.2 mmol, 4.0 eq.) in THF (50mL) was added dropwise. The mixture was further stirred vigorously for 16 h at room temperature. After this time, the solution was concentrated under reduced pressure and the crude residue was dissolved in water (40 mL); then concentrated hydrochloric acid (HCl) was added dropwise at 0 ºC until the formation of a white precipitate was complete. The solid obtained was filtered under vacuum, and the residue was washed with water (30 mL, x3). The compound was dried under reduced pressure at 60 ºC overnight.

(7R,18S)-7,18-diisopropyl-5,8,17,20-tetraoxo-12,13-dithia-6,9,16,19-tetraaza-tetracosanedioic acid (GltValCsa): A white solid was obtained (yield 85%). **^{1}H-NMR (500 MHz, DMSO-*d*$_6$, *δ*)**: 8.12 (t, *J* = 5.1 Hz, 2H), 7.81 (d, *J* = 8.8 Hz, 2H), 4.18 – 4.03 (m, 2H), 3.53 – 3.33 (m, 4H), 2.77 (t, *J* = 6.6 Hz, 4H), 2.30 – 2.12 (m, 8H), 2.01-1.86 (m, 2H), 1.78 – 1.61 (m, 4H), 0.95 - 0.70 (m, 12H). **^{13}C-NMR (126 MHz, DMSO-*d*$_6$, *δ*)**: 174.1, 171.7, 171.2, 57.7, 37.9, 37.1, 34.2, 33.1, 30.3, 20.8, 19.2, 18.2. **HRMS (ESI-TOF) m/z:** $[M-H]^-$ calcd for $C_{24}H_{42}N_4O_8S_2$ 577.2360; found, 577.2366.

(6R,17S)-6,17-di((S)-sec-butyl)-4,7,16,19-tetraoxo-11,12-dithia-5,8,15,18-tetraazadocosanedioic acid (SucIleCsa): A white solid was obtained (yield 70%). **^{1}H-NMR (400 MHz, DMSO-*d*$_6$, *δ*)**: 8.12 (t, J = 5.6 Hz, 2H), 7.90 (d, J = 8.9 Hz, 2H), 4.12 (dd, J = 8.8, 7.3 Hz, 2H), 3.43 – 3.27 (m, 4H), 2.77 (t, J = 6.8 Hz, 4H), 2.46 – 2.38 (m, 8H), 1.78 – 1.65 (m, 2H), 1.46 – 1.39 (m, 2H), 1.16 – 1.01 (m, 2H), 0.87 – 0.73 (m, 12H). **^{13}C-NMR (101 MHz, DMSO-*d*$_6$, *δ*)**: 173.8, 171.2, 171.0, 56.9, 37.9, 37.0, 36.6, 29.9, 29.2, 24.3, 15.4, 11.1. **HRMS (ESI-TOF) m/z:** $[M+Na]^+$ calcd for $C_{24}H_{42}N_4O_8S_2$ 601.2342; found, 601.2343.

2. Rheology

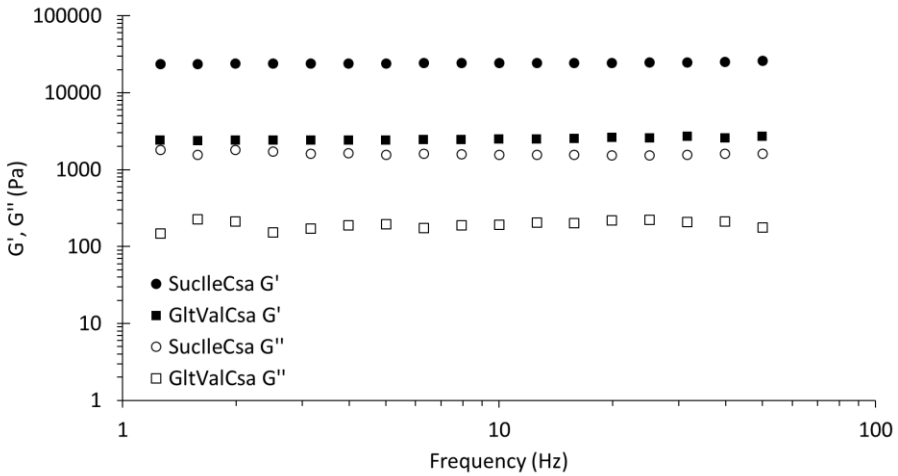

Figure S3.1. Dynamic frequency sweep test results of **GltValCsa** (18mM) and **SucIleCsa** (18mM) hydrogels at a strain of 0.1% at 25 °C.

3. NMR studies of Gel Disassembly

Gel disassembly with TCEP

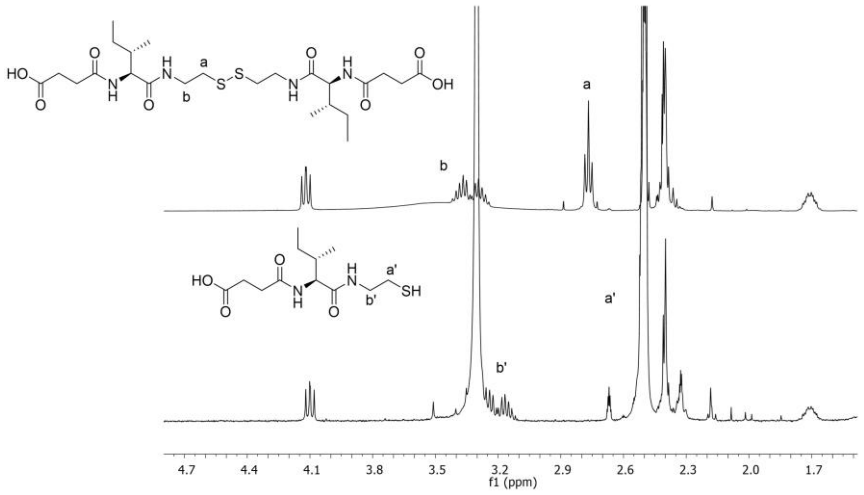

Figure S3.2. (Top) ^{1}H-NMR spectrum of compound **SucIleCsa** in DMSO-d_6 before treatment with TCEP. (Bottom) ^{1}H-NMR spectrum after treatment. Total disulfide bond reduction was observed.

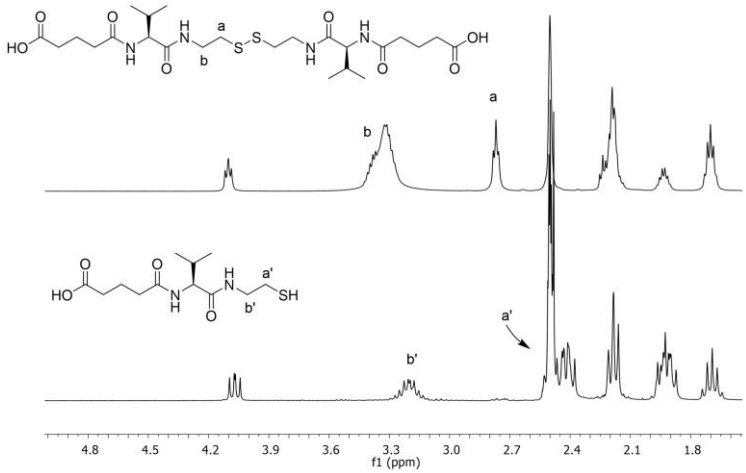

Figure S3.3. (Top) ^{1}H-NMR spectrum of compound **GltValCsa** in DMSO-d_6 before treatment with TCEP. (Bottom) ^{1}H-NMR spectrum after treatment. Total disulfide bond reduction was observed.

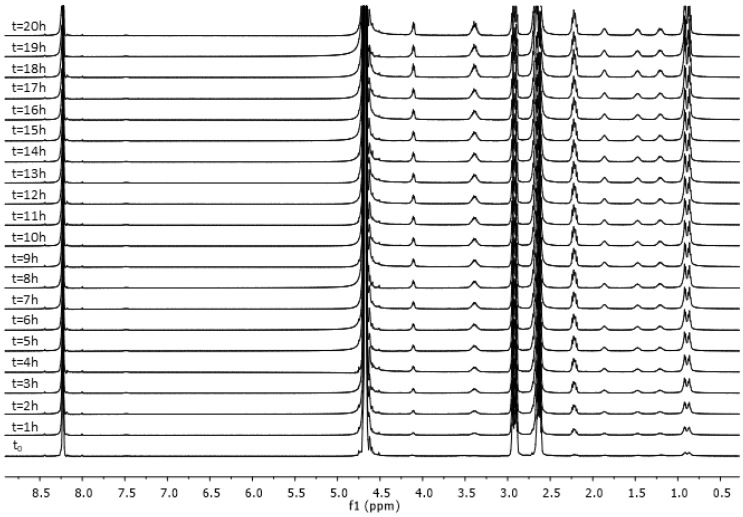

Figure S3.4. Stack-plot of 500 MHz ^{1}H-NMR spectra recorded over 20 h, showing the reaction of compound **SucIleCsa** with TCEP.

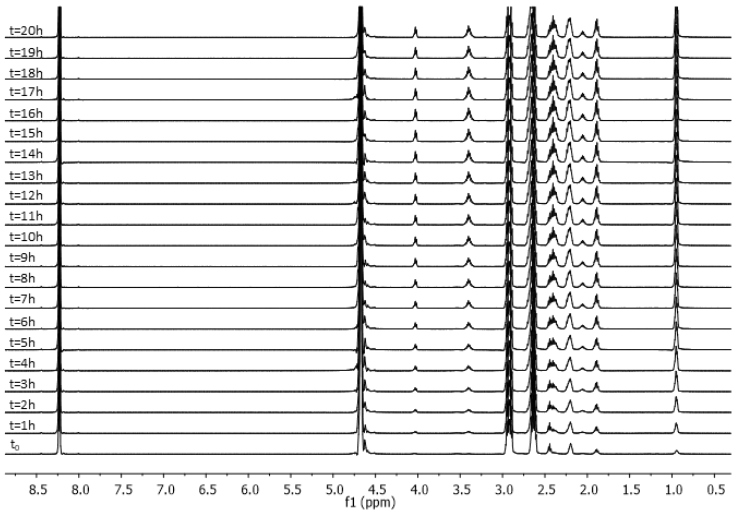

Figure S3.5. Stack-plot of 500 MHz ^{1}H-NMR spectra recorded over 20 h, showing the reaction of compound **GltValCsa** with TCEP.

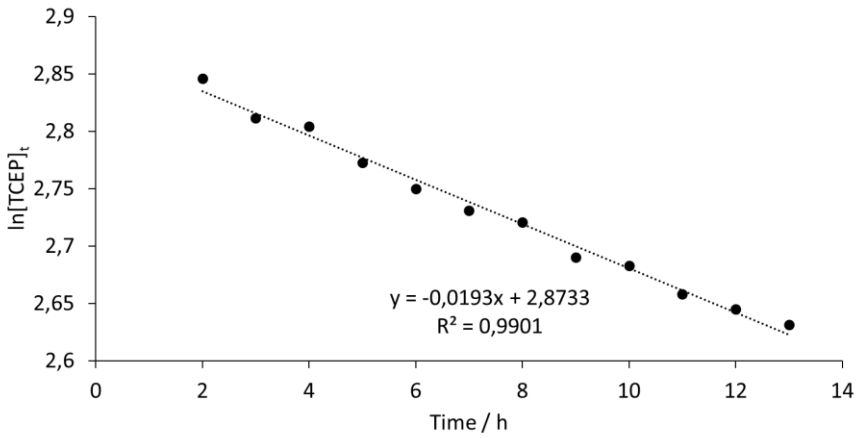

Figure S3.6. Linear regression curves of data obtained by means of NMR in **SucIleCsa** fitting with pseudo-first kinetic mode.

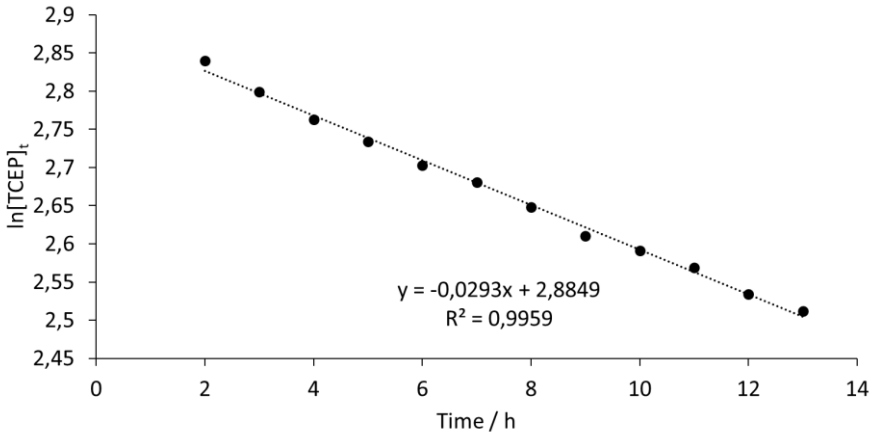

Figure S3.7. Linear regression curves of data obtained by means of NMR in **GltValCsa** fitting with pseudo-first kinetic mode.

Gel disassembly triggered by the change in pH

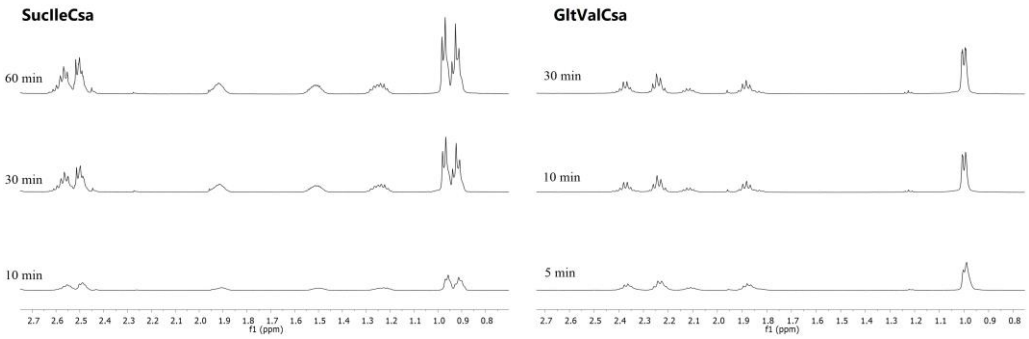

Figure S3.8. Selected ^{1}H-NMR spectra from the study of disassembly of **SucIleCsa** (left) and **GltValCsa** (right) gel into 0.2 M phosphate buffer pH 7.4.

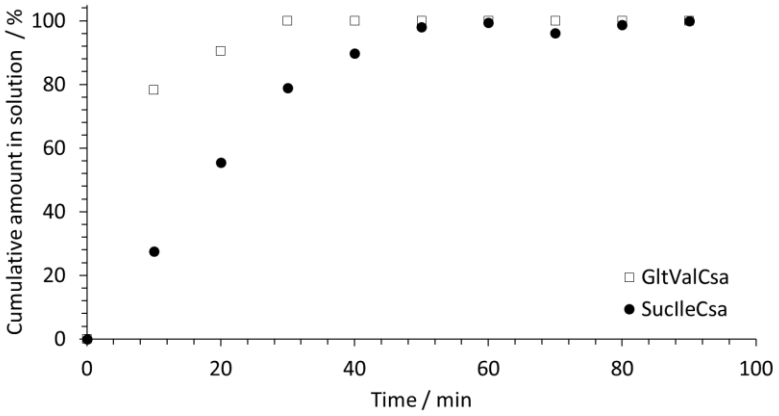

Figure S3.9. The gradual disintegration of **GltValCsa** and **SucIleCsa** hydrogels under the condition of 0.2 M phosphate buffer solution pH 7.4.

4. UV-Vis Spectroscopy study of bromophenol release

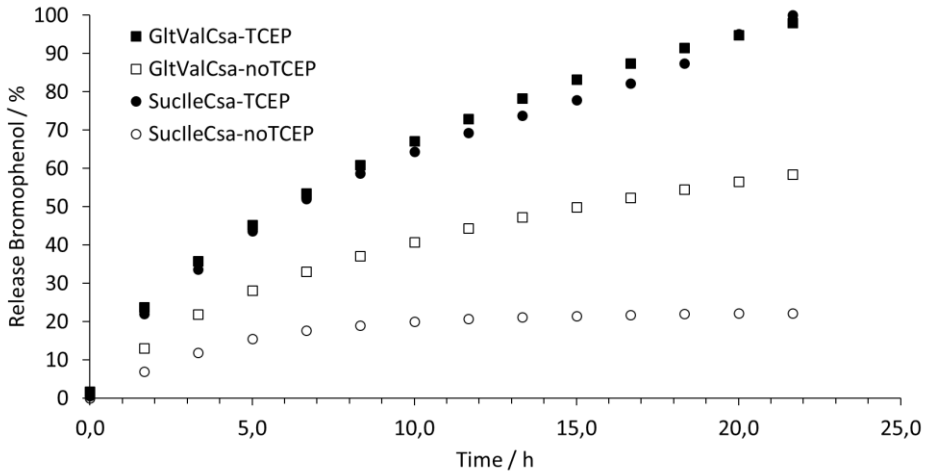

Figure S3.10. UV–Vis evaluation of the liberation of bromophenol blue (0.1 mM) entrapped in the hydrogel formed by **SucIleCsa** and **GltValCsa**.

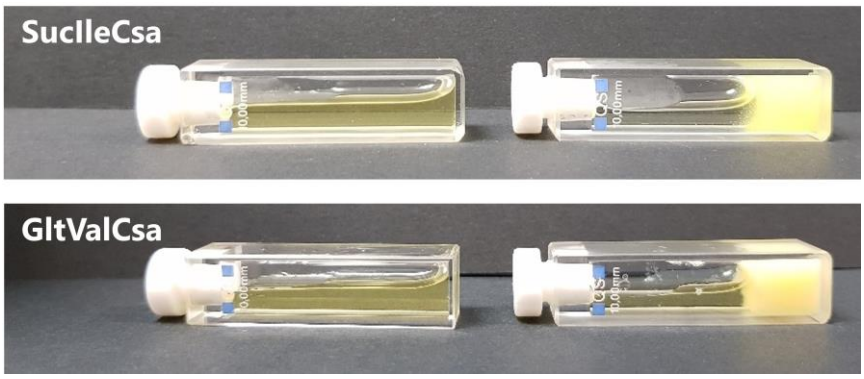

Figure S3.11. Blank experiment, heating at 37.4ºC: **GltValCsa** and **SucIleCsa** gels are not affected (Right). After 40 mM TCEP addition, heating at 37.4ºC: **GltValCsa** and **SucIleCsa** gels are completely dissolved (Left).

5. Transmission Electron Microscopy (TEM)

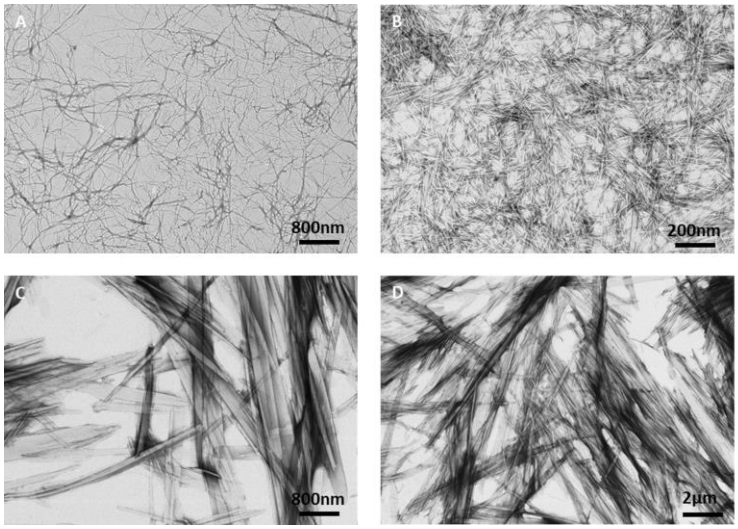

Figure S3.12. Electron microscopy (TEM) images obtained from gels of compounds prepared by the NaOH/HCl precipitation method. **A - B SucIleCsa** (18 mM); **C - D GltValCsa** (18 mM).

6. Confocal Laser Scanning Microscopy (CLSM)

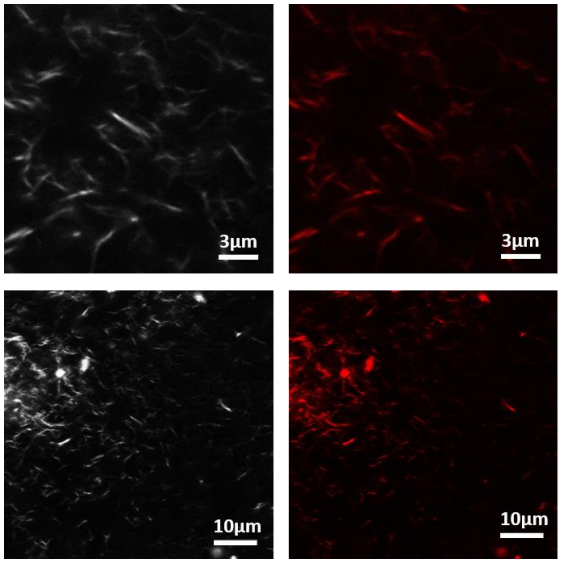

Figure S3.13. Confocal laser scanning microscopy (CLSM) images obtained from gels of **SucIleCsa** (18 mM) stained with Nile red.

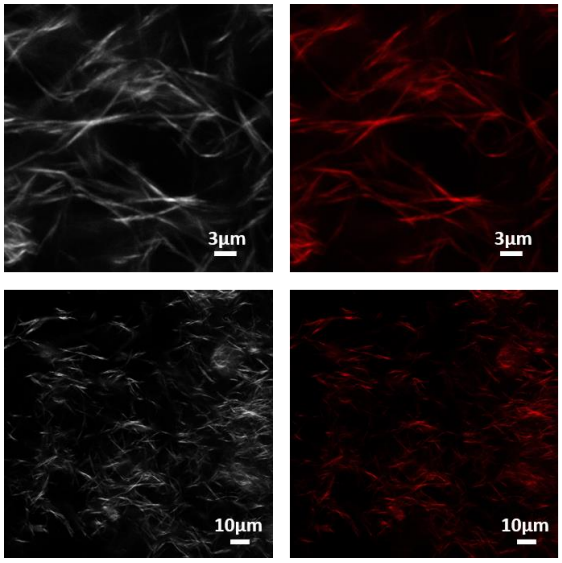

Figure S3.14. Confocal laser scanning microscopy (CLSM) images obtained from gels of **GltValCsa** (18 mM) stained with Nile red.

7. NMR Spectra

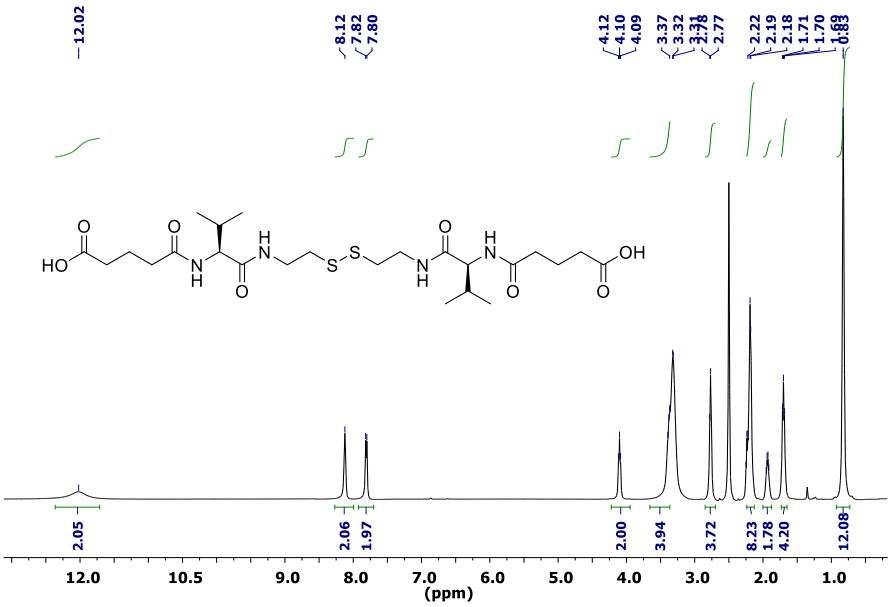

Figure S3.15. ^{1}H-NMR spectrum of compound **GltValCsa.**

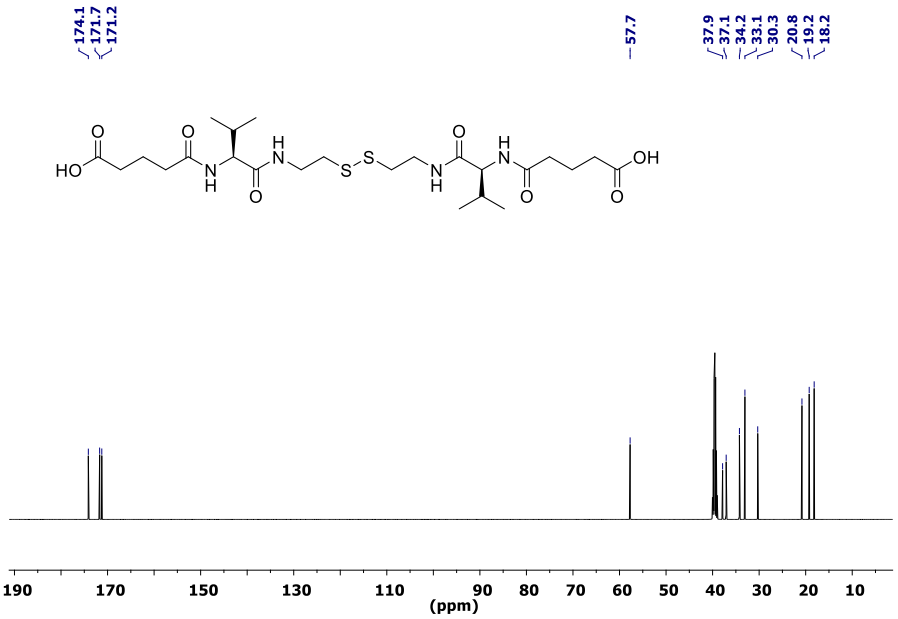

Figure S3.16. ^{13}C-NMR spectrum of compound **GltValCsa.**

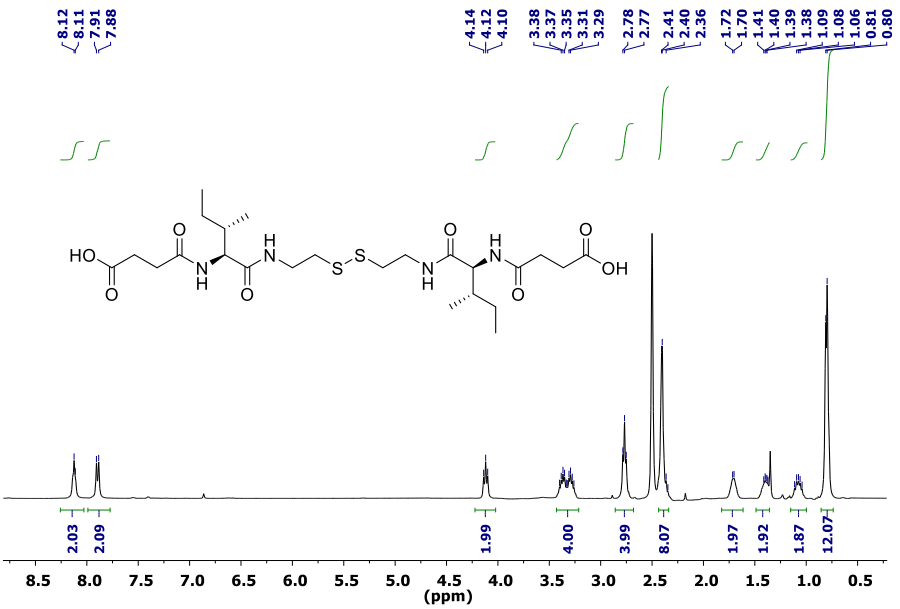

Figure S3.17. ^{1}H-NMR spectrum of compound **SucIleCsa.**

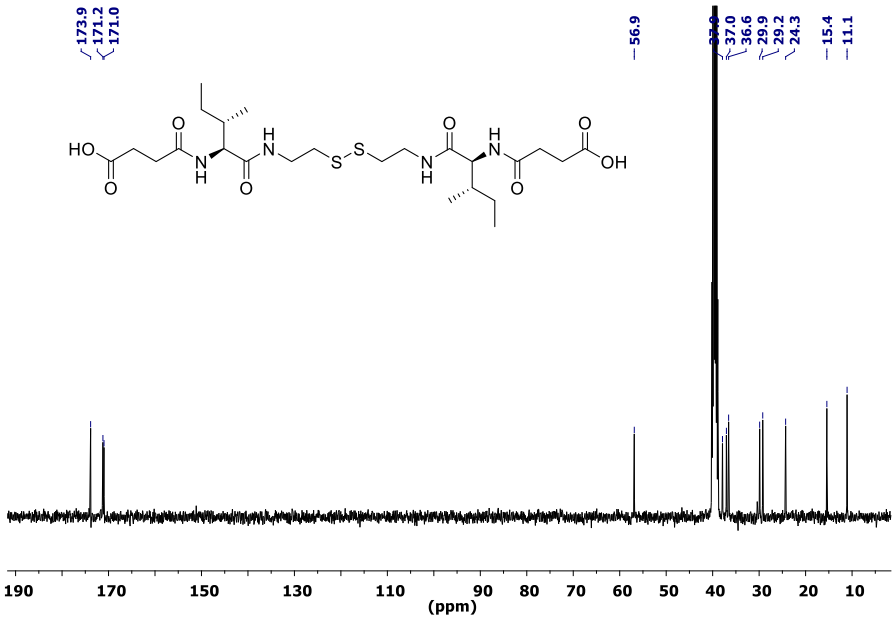

Figure S3.18. ^{13}C-NMR spectrum of compound **SucIleCsa.**

Chapter 4

Glutathione-responsive molecular nanoparticles from a dianionic bolaamphiphile and their use as carriers for targeted delivery

Glutathione-responsive molecular nanoparticles from a dianionic bolaamphiphile and their use as carriers for targeted delivery

Diego Navarro-Barreda, Begoña Bedrina, Francisco Galindo, and Juan F. Miravet*

Department of Inorganic and Organic Chemistry, University Jaume I, 12071, Castelló de la Plana, Spain.

Accepted Date: 24th October 2021.

Abstract

The formation in aqueous media of molecular nanoparticles from a bolaamphiphile (**SucIleCsa**) incorporating a disulfide moiety is described. The nanoparticles can be loaded efficiently with the lipophilic mitochondrial marker $DiOC_6(3)$, quenching its fluorescence, which is recovered upon reductive particle disassembly. $DiOC_6(3)$ transport into human colorectal adenocarcinoma cells (HT-29) is demonstrated by using flow cytometry and confocal scanning fluorescence microscopy. A significant increase in intracellular fluorescence is observed when the cells are stimulated to produce glutathione (GSH). These new molecular nanoparticles could be considered a theranostic tool as the nanoparticles simultaneously achieves targeted delivery of lipophilic substances and signals high levels of GSH.

4.1 Introduction

The development of nanocarriers, also called nano-drug delivery systems, is a very active area in the intersection of chemistry and biomedicine. These vehicles provide some relevant advantages in drug administration, such as increased aqueous solubility, improved stability, and extended duration of drug action.[1,2] Additionally, nanocarriers can show both passive and active targeted delivery activity. In the former case, they take advantage of the enhanced permeability and retention (EPR) effect. On the other hand, active targeting strategies commonly imply the incorporation of affinity ligand fragments on the surface of the nanoparticles.[3,4] Diverse families of nanocarriers have been studied, such as solid-lipid nanoparticles,[5] liposomes,[6] albumin[7] or silica nanoparticles.[8] In many cases, nanocarriers are built from either natural or synthetic high molecular weight polymers, forming polymeric micelles[9,10] or nanogel particles.[11,12]

An essential issue in using nanocarriers is to avoid the premature and non-specific release of the encapsulated actives. For this reason, there is a growing interest in developing stimuli-responsive nanocarriers that can respond to specific microenvironments, such as altered conditions of the pathological tissues, releasing their load in a spatiotemporally controlled fashion. The stimuli can be exogenous, such as temperature, ultrasound or light, or endogenous, such as pH, red-ox species or enzymes.[13,14] In particular, the introduction of disulfide moieties represents a customary strategy for preparing reduction-sensitive nanoparticles, which release their load upon reaction with glutathione (GSH).[15–17] Several intracellular compartments such as cytosol, mitochondria, and cell nucleus contain a high concentration of GSH (about 2.0 – 10.0 mM), 100 to 1000 times higher than that of the extracellular fluids and circulation (about 2.0 – 20.0 μM). GSH levels tend to be 2-10 times higher in breast, ovarian, head,

neck, and lung cancers than in healthy cells.[18] Consequently, GSH has been recognized as an ideal and ubiquitous internal stimulus for the rapid destabilization of nanocarriers inside cells to accomplish efficient drug release.[15,19–22] Among many examples, recently, nanogel particles were prepared with crosslinking disulfide units realizing GSH-triggered tumor microenvironment-controlled drug release.[23] Polymeric micelles with disulfide moieties have been used in fast drug release in cancer cells under the effect of a high level of GSH,[24] or as GSH scavengers.[25] Non-ionic gemini amphiphiles with disulfide and lipase-responsive ester units were shown to encapsulate lipophilic guests.[26] Disulfide linkages also have been used in polymer-protein conjugates.[27]

Here we report a study on the aggregation of the compound **SucIleCsa** (**Scheme 4.1**) into glutathione-responsive nanometric particles. In addition, this work studies the transport into a human colorectal adenocarcinoma cell line (HT-29) of the lipophilic mitochondrial dye 3,3'-dihexyloxacarbocyanine iodide, abbreviated as $DiOC_6(3)$ (**Scheme 4.1**), which is presented as a test for the nanocarrier capabilities of **SucIleCsa**. Although recently bolaamphiphiles derived from lactobionic acid have been applied for curcumin delivery to cancer cells *in vitro*,[28] the use of bolaamphiphilic molecules as building blocks of nanocarriers is an almost unexplored are of research. The molecular (non-polymeric) nature of the GSH-responsive nanovehicle studied here represents a key novelty compared to the precedents in the literature cited above. It has to be noted that a critical consideration when using polymeric carriers in biomedicine is the batch-to-batch reproducibility of the polymer preparation and its proper characterization. Issues such as variability in the polydispersity index or crosslinking degree of the materials and the analysis of side products incorporated in the polymers should not be neglected.[29,30] Molecular nanocarriers are envisaged to benefit from the reproducible synthesis and

characterization of their components and to present improved biodisposition compared to polymeric particles. Indeed, recently we have studied the preparation of molecular nanoparticles from hydrogelators and their use as nanocarriers.[31–34] As for compound **SucIleCsa,** we have reported the formation of hydrogels in acidic media which are capable of entrapping insulin, preventing its enzymatic degradation.[35]

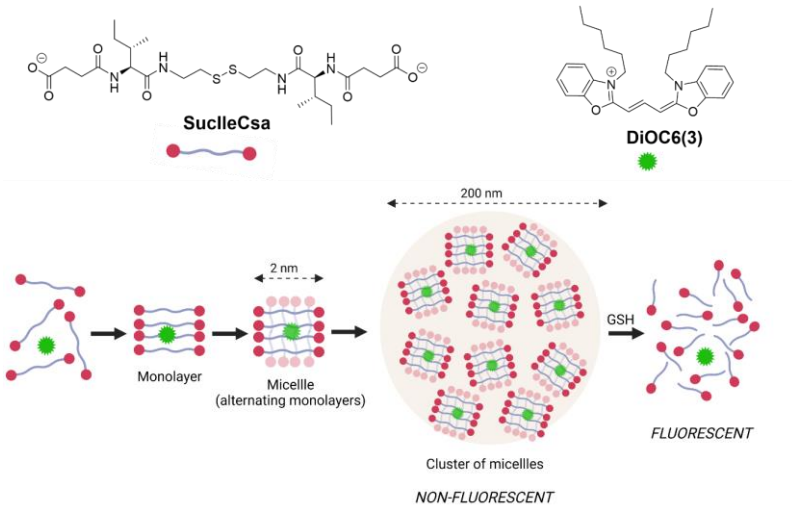

Scheme 4.1. Structure of the bolaamphiphile molecule **SucIleCsa** in its dianionic form and lipophilic dye **DiOC$_6$(3)**. Pictorial representation nanoparticle formation and GSH-promoted release of the fluorescent dye.

4.2 Results and Discussion

The preparation of **SucIleCsa** was previously reported by us, using cystamine, *N*-Boc-L-Isoleucine and succinic anhydride as building blocks, all of them commercially available.[35] The critical aggregation point of **SucIleCsa** in HEPES buffer (0.2 M, pH 7.4) was determined by monitoring the absorbance of 1,6-

diphenyl-1,3,5-hexatriene (DPH).[36] As shown in **Figure 4.1**, a critical aggregation concentration of *ca.* 1.0 mM was obtained in this way. A similar value was obtained by measurement of the intensity of scattered light (Figure S4.1). Bolaamphiphilic species (molecules with two polar heads separated by a hydrophobic moiety) can form micelles by adopting either from U-shaped or extended conformations.[37–40] Molecular modeling of the monosodium salt of **SucIleCsa** (AM1 calculations, Figure S4.10) confirms the feasibility of a U-shaped conformation, but it does not show a sufficient separation of the hydrophobic and hydrophilic moieties to justify the formation of the micelles. In the case of extended conformations, micelles can be formed from alternating monolayers of straight bolas.[37] Based on these considerations, micelle formation is proposed and pictorially represented in Scheme 4.1.

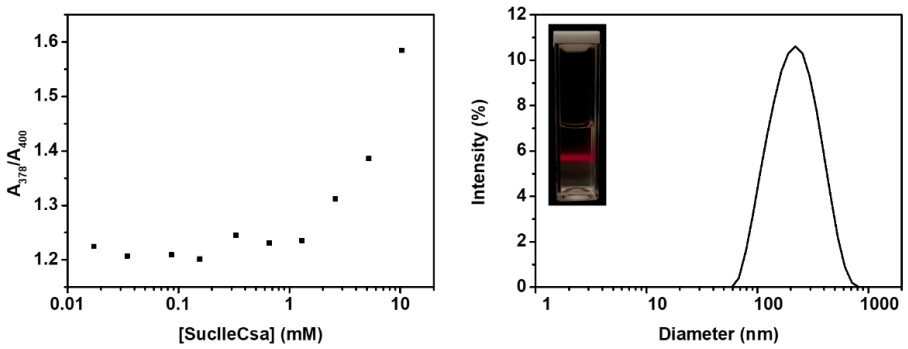

Figure 4.1. Left: Variation of the absorbance ratio (378nm/400nm) of DPH (5.0 μM) with the concentration of **SucIleCsa**. Right: Diameter distribution of the nanoparticles formed by **SucIleCsa** (5.0 mM) determined by DLS. Inset: Tyndall effect observed for nanoparticle dispersion. The measurements were carried out at pH 7.4 (0.2 M HEPES).

The size of the particles formed by **SucIleCsa** in 0.2 M HEPES at pH 7.4 was analysed by dynamic light scattering (DLS), as shown in **Figure 4.1** and Figure S4.2. An intensity averaged diameter (Di) of 190 nm was obtained (std dev = 20,

polydispersity index = 0.21). The Zeta potential of the particles was determined to be -46.5 mV (std dev = 1.7, see Figure S4.3). The value is negative as expected from the anionic nature of **SucIleCsa** at the studied pH and is within the range of values that are considered to impart colloidal stability.[41] Accordingly, the particles were found to exhibit a similar size distribution by DLS after 24 h of preparation (Figure S4.3).

The particle size pointed out by DLS, *ca.* 200 nm, is much larger than expected for discrete micelles (*ca.* 2 nm). TEM pictures in **Figure 4.2** show spherical objects with sizes ranging from *ca.* 50 nm to 650 nm. The particles present a granular appearance, suggesting that the combination of smaller units forms them. Similar objects were observed by SEM (Figure S4.4). Confocal laser scanning microscopy images of the particles could also be captured after loading them with Nile red, a hydrophobic dye whose fluorescence in water is switched on upon its incorporation in hydrophobic domains (Figure S4.4).[42] It could be proposed that **SucIleCsa** micelles evolve into micellar clusters, acting the cations in the medium as intermicellar bridges. Further aggregation into macroscopic particles is precluded, probably being the negative Z-potential mentioned before a critical factor for the colloidal stability. In agreement with this interpretation, a significant two-fold reduction of scattering intensity was observed by DLS (data not shown) when HEPES buffer (ammonium-type cations) was replaced by PBS (sodium cations). Micellar clusters originating from polymeric micelles or surfactants have been reported previously.[43–46]

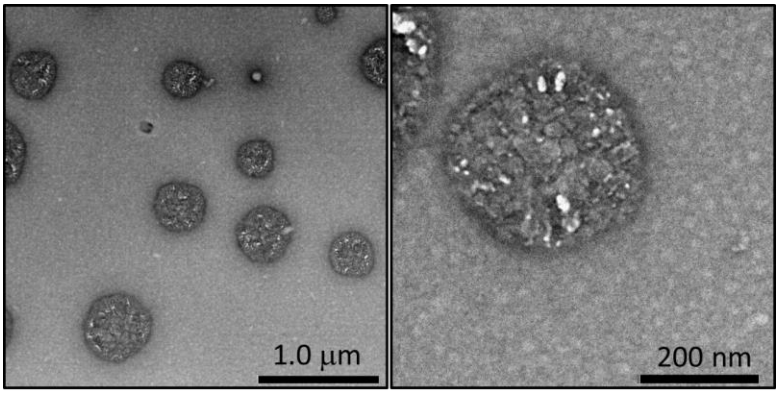

Figure 4.2. TEM images of the nanoparticles formed by **SucIleCsa** (5.0 mM) in 0.2 M HEPES, pH 7.4.

The responsiveness of the nanoparticles to reducing agents was confirmed by DLS and ^{1}H-NMR measurements (**Figure 4.3**). DLS studies revealed that the addition of dithiothreitol (DTT), a well-known agent used, for example, to reduce disulfide bonds in proteins,[47] produced a notable decrease in the intensity of scattered light, ascribed to particle disassembly. Similar results are obtained in the presence GSH (Figure S4.11). The intensity changes of dispersed light upon particle disaggregation have not been analyzed in similar DLS experiments reported for polymeric nanocarriers. Only size distribution and polydispersity changes (PdI) were reported, revealing that the remaining particles generally show a broader size distribution and increased PdI.[48–51] ^{1}H-NMR could be used to monitor the reduction process following the shift of the amide proton signals (**Figure 4.3**). Unfortunately, the other ^{1}H-NMR signals are masked by the presence of HEPES and DTT. The ^{1}H-NMR experiment indicates a complete reduction of **SucIleCsa** after three hours, but the DLS observation of the process reveals a slower reaction rate. A possible rationale for this apparent contradiction would be that the particles are NMR-silent,[52] and the reduction process observed by this technique affects the fraction of free molecules and small aggregates

present in the sample, which are observable by NMR. To evaluate this possibility, spectra from samples of accurately measured concentration were recorded, and the integration of the signals was evaluated using an electronic signal as reference (ERETIC).[53] As a result, it was found that the NMR-observed concentration is identical to the nominal one, discarding the presence of NMR-silent species and indicating that the molecules in the assemblies present enough mobility to be NMR-observable. Therefore, it is proposed that the different kinetic patterns measured by DLS, and NMR arise because disulfide reduction does not result in immediate particle disassembly. The addition of DTT would afford, after a few minutes, reduced nanoparticles which most likely are metastable, kinetically trapped, and evolve slowly, after some hours, to free molecules. Further confirmation of the successful reduction was obtained by mass spectrometry which showed the absence of the molecular peak of **SucIleCsa** and the formation of the corresponding thiol (Figure S4.5).

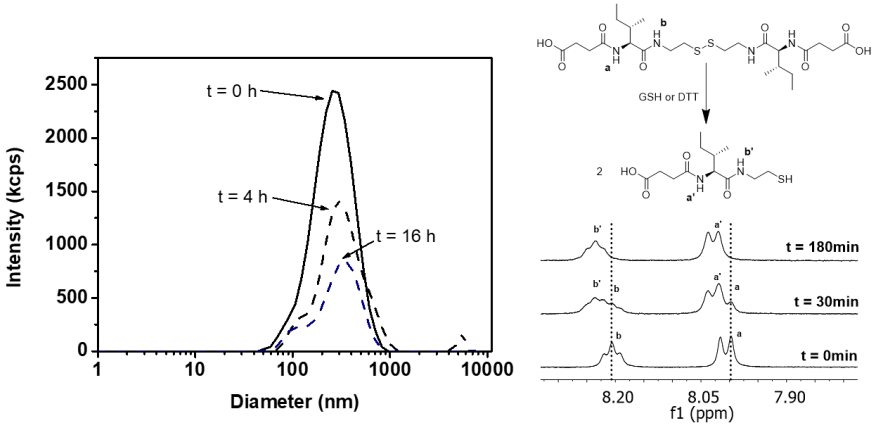

Figure 4.3. Left: Variation of the intensity of scattered light measured by DLS for a sample of nanoparticles of **SucIleCsa** (5.0 mM, pH 7.4, 0.2 M HEPES) upon addition of DTT (20.0 mM) at 37 °C. Right: Fragment of the ^{1}H-NMR spectra obtained at different time intervals for the same system (solvent contains 10% of D_2O in this case).

Assays with the mitochondrial marker **DiOC$_6$(3)** were carried out to test the performance of the nanoparticles as nanocarriers of hydrophobic substances. Mitochondrial-targeting nanotherapeutics represents a challenging and active field in biomedicine.[54] **DiOC$_6$(3)** is a lipophilic carbocyanine dye whose absorption and emission maxima in methanol are 484 nm and 501 nm. It is weakly fluorescent in water but becomes highly fluorescent when incorporated in non-polar environments. **DiOC$_6$(3)** has been used for the staining of the endoplasmatic reticulum and mitochondria.[55,56] In practice, due to its low solubility in water, commonly, a stock solution of the dye in DMSO is diluted in an aqueous buffer to yield a final concentration below 1.0 μM.[57] It has to be noted that although both positively and negatively charged nanocarriers can transport actives into the cell,[58] the use of anionic vehicles such as **SucIleCsa** could be advantageous in this case given the cationic nature of **DiOC$_6$(3)**.

The absorption maxima of **DiOC$_6$(3)** shows a significant red-shift from 484 to 496 upon addition of **SucIleCsa**, indicating incorporation of the dye (encapsulation efficiency > 80 %) in the hydrophobic areas of the nanoparticles. On the other hand, a dramatic reduction of **DiOC$_6$(3)** fluorescent emission occurred upon its loading into the particles, which should most likely be ascribed to a fluorescence quenching process caused by the disulfide group of **SucIleCsa** (**Figure 4.4**).[59,60] The interaction of the dye with the carrier most likely has a predominant hydrophobic character considering the results described previously for the study of the interaction of several DiOCn dyes with SDS anionic micelles.[61] However, it must be kept in mind that in general the interaction of cationic dyes with anionic micelles can result in a competition between electrostatic interactions with the head groups of the surfactant and hydrophobic ones inside the aggregates.[62]

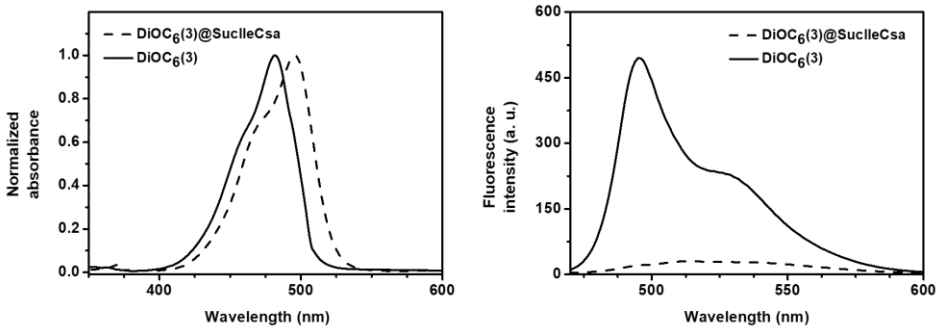

Figure 4.4. Absorption and fluorescence (λ_{ex} = 465 nm) spectra of **DiOC$_6$(3)** (5.0 μM) in the presence and the absence of **SucIleCsa** nanoparticles (5.0 mM). 0.2 M HEPES, pH 7.4.

SucIleCsa particles increase notably the solubility of lipophilic **DiOC$_6$(3)** in an aqueous medium. As shown in **Figure 4.5**, in a biphasic system consisting of an aqueous solution of **DiOC$_6$(3)** and dichloromethane, the dye is fully transferred to the organic phase after *ca.* 1 h when nanoparticles are absent. On the contrary, for the system **DiOC$_6$(3)@SucIleCsa**, the transport is radically halted. No phase transfer is observed after 1 h, and only *ca.* 20% of the dye is present in the organic phase after 24 h. The addition of GSH provokes progressive particle disassembly and the transport of the dye to the dichloromethane phase (*ca.* 20 % after 1 h and 80% after 24 h).

The use of the nanoparticles as carriers of **DiOC$_6$(3)** was studied with human colorectal adenocarcinoma cells (HT-29). In the first place, cell viability in the presence of **SucIleCsa** was determined using the MTT assay. The results revealed that for high concentrations (up to 600 μM), more than 80% of the cell population was viable (Figure S4.6), making **SucIleCsa** suited to being applied in living cells.

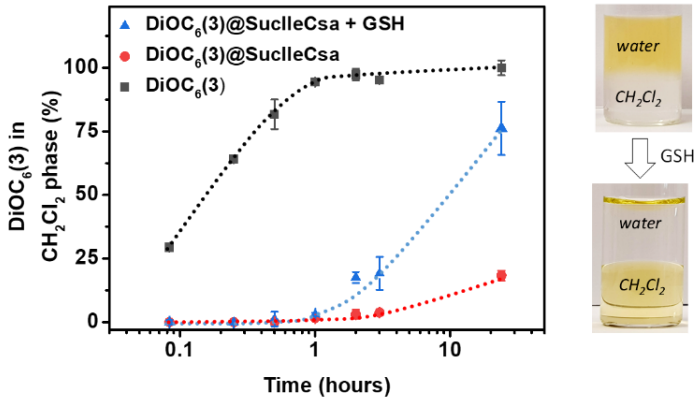

Figure 4.5. Effect of the presence of **SucIleCsa** nanoparticles (5.0 mM) and their reduction with GSH (20 mM) in the rate of transfer of **DiOC$_6$(3)** (5.0 μM) from water (0.2 M HEPES, pH 7.4) to dichloromethane. Dotted lines as used as a guide to the eye.

Transport of **DiOC$_6$(3)** into HT-29 cells was studied in the presence and absence of the nanoparticles. Flow cytometry analysis showed that **DiOC$_6$(3)** fluorescent emission in the cells is significantly higher when it is carried by the nanoparticles (**Figure 4.6** and Figure S4.7). After incubation for 16 h, the fluorescence is approximately twice in the system with **SucIleCsa**. As mentioned above, incorporation of the dye in the nanoparticles results in fluorescence quenching; therefore, the data in **Figure 4.6** would indicate that the particles are disassembled in the cellular medium. The improved signal using **SucIleCsa** is manifested after 4 h of incubation but not after 1 h. This fact would be in accordance with a relatively slow intracellular nanoparticle disassembly process and/or a different mechanism of cell internalization. The GSH-responsive nature of the nanoparticles in the cells was confirmed by stimulating GSH production with *N*-acetylcysteine ethyl ester (NACET).[63] **Figure 4.6** (and Figure S4.8) shows how when HT-29 cells were preincubated with NACET, a significant enhancement of **DiOC$_6$(3)** cellular fluorescence was measured by flow cytometry. This result supports that **DiOC$_6$(3)** is introduced in the cell with the help of **SucIleCsa** and

that a progressive disassembly of the nanoparticle is taking place, accelerated by an increased concentration of GSH. The results of the flow cytometry experiments cited above are in agreement with those obtained by confocal microscopy. The images in **Figure 4.7** reveal qualitatively that NACET-stimulated cells present a higher intensity of fluorescence than that observed for non-stimulated cells. Also, in the absence of the nanocarrier, the fluorescence in the cells is significantly reduced. Quantification of the emission intensity is shown in the graph of **Figure 4.7**, presenting the stimulated cells *ca.* twice the fluorescence intensity of those with normal GSH levels. Also, a six-fold increase of emission is observed compared to cells incubated with **DiOC$_6$(3)** without the nanocarrier.

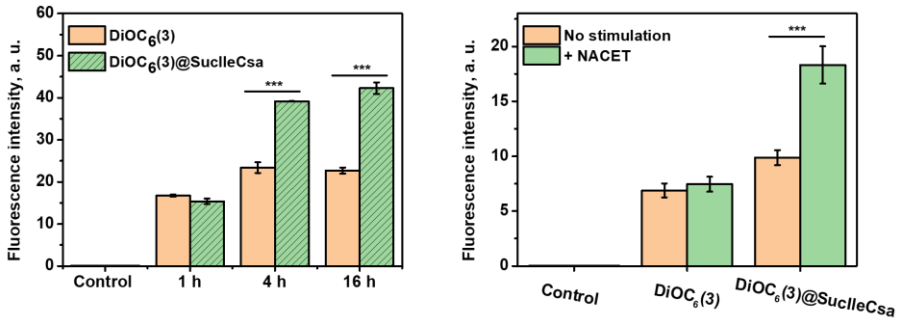

Figure 4.6. Flow cytometry studies. Left: Incorporation of **DiOC$_6$(3)** (1.0 μM) in the presence of **SucIleCsa** nanoparticles (5.0 mM) into HT-29 cells. Right: Effect of cellular stimulation with NACET (0.5 mM, preincubation 16 h). 0.2 M HEPES, pH 7.4. Statistical analysis was performed by one-way ANOVA followed by Tukey's multiple comparisons test (*** indicates a p-value ≤ 0.001).

Finally, confocal analysis of the superposition of fluorescence of **DiOC$_6$(3)** and Mitotracker Red,[64] shows an excellent correlation, revealing that the dye is preferentially located in the mitochondria, as expected for a delocalized lipophilic cation (DLC) (Figure S4.9). The fact that **DiOC$_6$(3)** stains efficiently the mitochondria is remarkable considering that nanoparticles of

DiOC$_6$(3)@SucIleCsa should enter the cell via endocytosis, endolysosomal pathway, due to their size,[65,66] and this implies that at some point, the dye can escape from endolysosomal sequestration, reaching the expected organelle (details to be investigated). This trapping effect is suffered by many encapsulated drugs, which hampers the efficient therapeutic action at the desired site (for instance, the nucleus or the mitochondria for some antiproliferative compounds). In this regard, nanoparticles able to cross the plasmatic membrane and deliver the cargo to the targeted subcellular structure, avoiding the lysosomes as dead ends, are very valuable.[67,68]

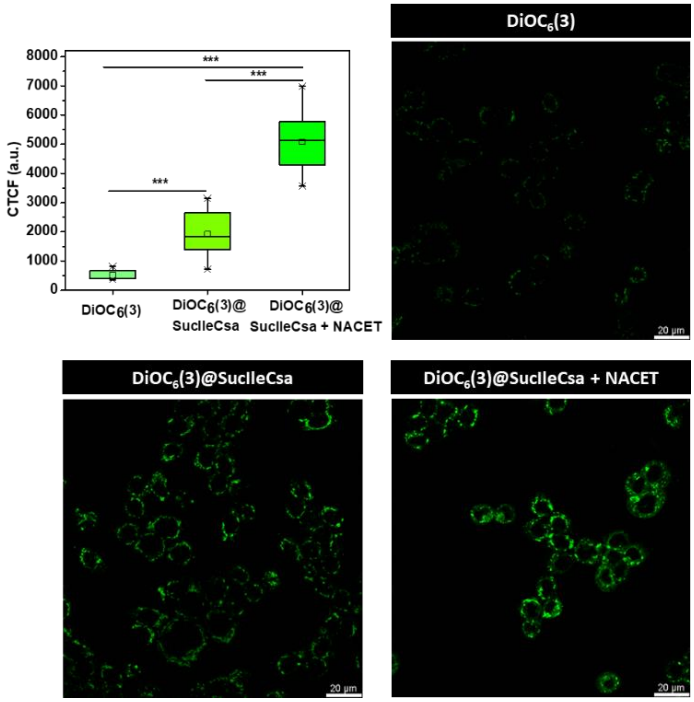

Figure 4.7. Representative confocal microscopy images showing the cellular fluorescence of **DiOC$_6$(3)** obtained in HT-29 cells. The stimulation with NACET (0.5 mM) was carried by preincubation for 16 h. Quantification of the green fluorescent signal (CTCF, corrected total cell fluorescence) is also shown in the graph. Data are shown as median ± (interquartile range) IQR, n=3. Statistical analysis was performed by one-way ANOVA followed by Tukey's multiple comparisons test (*** indicates a p-value ≤ 0.001). [**DiOC$_6$(3)**] = 1.0 µM, [**SucIleCsa**] = 5.0 mM.

4.3 Conclusions

Currently, there is widespread interest in developing stimuli-responsive nanocarriers[13,14] and, in particular, GSH-sensitive nanoparticles.[15,19–22] This work has demonstrated the preparation of molecular nanoparticles from the bolamphihphile **SucIleCsa**, which contains a reduction sensitive disulfide bond. This molecule is shown to form negatively charged nanoparticles, seemingly constituted by micelle clusters with an averaged diameter of *ca.* 200 nm.

Reduction responsiveness to DTT and GSH was observed. ^{1}H-NMR, DLS and mass spectrometry could monitor the fragmentation of the molecule. The capability of the nanoparticles to entrap hydrophobic substances is revealed by the loading of the mithocondrila dye **DiOC$_6$(3)**, which is accompanied by a red shift in its absorption spectrum. In a biphasic system **DiOC$_6$(3)@SucIleCsa** is kept in the aqueous phase, but the addition of GSH provokes disassembly of the nanoparticles and rapid migration of the lipophilic dye into the organic phase.

The described system is especially interesting because the fluorescence of **DiOC$_6$(3)** is quenched when loaded into the particles, most likely because of the proximity of the disulfide groups. Based on this property, three findings should be highlighted in the study of **DiOC$_6$(3)** transport into HT-29 cells. Firstly, the use of the nanocarrier significantly improves the incorporation of the dye into the cells. Secondly, the increased fluorescence observed using the nanoparticles must be linked to particle disassembly. Finally, the study with cells stimulated for overproduction of GSH shows a higher fluorescence, confirming that reductive nanoparticle disassembly is a crucial step in the process.

Overall, the self-assembled nanoparticles presented show promising properties for their use in theranostics, providing simultaneously targeted delivery and signaling on cells with overexpression of GSH, like those associated with different malignant processes.[18]

4.4 Experimental Section

4.4.1 Materials

All chemicals used were of analytical grade, purchased from MERK/SIGMA/ALDRICH and used without further purification.

4.4.2 Synthesis of SucIleCsa

SucIleCsa was synthesized as previously reported.[35]

4.4.3 Characterization

NMR spectra were recorded on an Agilent VNMR System spectrometer (500 MHz for ^{1}H-NMR) or Bruker Avance III HD spectrometers (400 MHz and 300 MHz for ^{1}H-NMR) in the indicated solvent at 30 °C. Mass spectra were recorded with a mass spectrometry triple quadrupole Q-TOF Premier spectrometer (Waters) with simultaneous Electrospray and APCI Probe. The ultraviolet-visible (UV-Vis) absorption spectra and the fluorescence intensity were measured with a JASCO V-630 UV–Vis spectrophotometer and a JASCO FP-8300 fluorometer, respectively. DLS size distribution and Zeta-potential measurements were recorded using a Zetasizer Nano-ZS90 (Malvern Instruments, UK). Automatic optimization of beam focusing and attenuation was applied for each sample.

Samples from independent batches were tested and the data used are the averaged data for three consecutive measurements. Transmission electron microscopic (TEM) images were obtained using a JEOL 2100 electron microscope with thermionic gun LaB6 100 kV equipped with a GatanOrius high-resolution CCD camera. TEM samples were prepared over carbon formvar copper grids. Scanning electron microscopic (SEM) images were obtained using a JEOL 7001F microscope equipped with a digital camera, operated at an accelerating voltage of 5.0 kV. The samples were coated with a fine layer of platinum using a standard SEM sputter coater (Baltec SCD 500) for 30 s. The MTT assay was performed by using a microplate reader (Thermo Scientific™ Multiskan™ FC). CLSM images were obtained using an inverted confocal microscope Leica TCS SP8. The corresponding fresh samples were loaded onto a sterilized Ibidi® µ-Slide 8 Well Glass Bottom. Excitation of samples was done with a diode (405 nm), argon (488 nm) or DPSS (561 nm) laser, and images were captured at 63× magnification with HCxPL APO 40.0 × 1.32 oil objective. Flow cytometry measurements were conducted using BD Accuri™ C6 flow cytometer with excitation at 488 nm. The mean fluorescence was determined by counting 10,000 events.

4.4.4 Preparation of SucIleCsa nanoparticles

In a representative example, 6.0 mg (0.01 mmol) of **SucIleCsa** in 2.0 mL of HEPES buffer (0.2 M, pH 7.4) were ultrasonicated (37 kHz) for 25 min at room temperature. The HEPES buffer solution was previously filtered through a 0.22 µm nylon filter membrane.

4.4.5 Stability and reduction-responsiveness of SucIleCsa nanoparticles

The stability and reduction-responsiveness of **SucIleCsa** nanoparticles were investigated in HEPES buffer solution (0.2 M, pH 7.4) with or without 20 mM DTT, respectively. The particle size, polydispersity (PdI), and the variation of the intensity of scattered light were measured by DLS at different times (0, 4 and 16 h), keeping the samples in a thermostatic bath at 37 °C. The breakage of the disulfide bond was also evaluated by mass spectrometry (MS) and nuclear magnetic resonance (NMR). For MS analysis, the nanoparticles (5.0 mM) were kept in a thermostatic bath at 37 °C for 24 hours in the presence of DTT (20 mM). Then, the samples were evaporated to dryness, and the residue was dissolved in MeOH and analysed by mass spectrometry. For NMR analysis, nanoparticles (5 mM) were prepared in 9:1 HEPES buffer:D2O in the presence of DTT (20 mM) and ^{1}H-NMR spectra were recorded at different time intervals (0, 0.5 and 3 h).

4.4.6 Preparation of DiOC$_6$(3)-loaded nanoparticles

A **DiOC$_6$(3)** dispersion (5.0 μM, 2.0 mL) was prepared in HEPES buffer (0.2 M, pH 7.4). Then, 6.0 mg (0.01 mmol) of **SucIleCsa** were added and ultrasonicated (37 kHz) for 25 min at room temperature. The obtained nanoparticles (denoted as **DiOC$_6$(3)@SucIleCsa**) were analysed by UV−Vis and fluorescence spectrophotometry. The encapsulation efficiency was assessed measuring the amount of free **DiOC$_6$(3)** obtained by removal of nanoparticles using an inorganic membrane filter (Anotop 25 Plus, 0.02 μm, Whatman).

4.4.7 Reduction-triggered release of $DiOC_6(3)$

The **$DiOC_6(3)$** release profile from **SucIleCsa** nanoparticles was investigated using a biphasic dissolution test. In a representative example, 3 mL of a solution **$DiOC_6(3)$**-loaded nanoparticles and 3.0 mL of dichloromethane were gently stirred with a magnetic bar. The organic phase was withdrawn, and the absorbance at 488 nm was measured at the corresponding time interval. Next, the organic phase was put back into the chamber for the subsequent measurement. The experiments were carried out in triplicate, and the results are shown as mean ± std dev (n = 3).

4.4.8 Determination of cell viability (MTT assay test)

The cytotoxic effects of **SucIleCsa** were assessed using the assy based on the use of the tetrazolium salt of 3-[4,5-dimethylthiazol-2-yl]-2-5 diphenyltetrazolium bromide (MTT). HT-29 cells were seeded into a 96-well plate at a density of 1 x 10^4 cells per well for 24 h at 37 °C. The culture medium was replaced with 100 µL fresh growth medium containing **SucIleCsa** nanoparticles at serial concentrations. After 48 h of incubation (37 °C, 5% CO_2 in a humid atmosphere), MTT solution (final concentration 0.5 mg/ml) was added into each well, and the cells were incubated for a further 3 h period at 37 °C. The supernatant was discarded, and the blue formazan crystals, formed through MTT metabolism, were dissolved in 100 µL DMSO. Optical densities were measured at 550 nm using a microplate reader. The relative cell viability was determined by comparing the absorbance of treated cells to non-treatment control wells. Data are presented as mean ± std dev (n = 3).

4.4.9 Cellular uptake

The cellular uptake of **$DiOC_6$(3)** was determined by flow cytometry (FCM) and confocal laser scanning microscopy (CLSM). For FCM analysis, HT-29 cells were seeded into 6-well plates at a density of 1×10^4 cells per well and treated with **$DiOC_6$(3)**-loaded nanoparticles (1.0 μM and 5.0 mM, respectively) and unencapsulated **$DiOC_6$(3)** (1.0 μM) for 1h, 4 h and 16 h at 37 °C. Then, cell suspensions were collected and washed with PBS. After centrifugation, the cells were re-suspended in PBS for cytometry analysis. For CLSM analysis, HT-29 cells were seeded into an Ibidi® μ-dish chamber at a density of 1×10^4 cells per well. After 24 h incubation, the cells were treated with the above-mentioned formulations and further incubated for 2 h at 37 °C. Finally, the cells were observed by CLSM (excitation wavelength 488 nm, emission 505-575 nm). For experiments carried out with *N*-acetylcysteine ethyl ester (NACET), cells were pre-incubated with 0.5 mM NACET for 16 h before **$DiOC_6$(3)** incubation. The quantification of the green fluorescent signal (CTCF, corrected total cell fluorescence) was calculated using Image J.

4.4.10 Subcellular localization of $DiOC_6$(3)@SucIleCsa

The subcellular localization of **$DiOC_6$(3)** after internalization through **SucIleCsa** nanoparticles was determined by CLSM analysis. HT-29 cells were seeded into an Ibidi® μ-dish chamber at a density of 1×10^4 cells per well for 24 h. Then, the cells were treated with **$DiOC_6$(3)@SucIleCsa** (1.0 μM and 5.0 mM, respectively) for 2 h at 37 °C. According to the standard protocol, after washing with PBS cells were stained with MitoTracker™ Red FM (MTR) and Hoechst 33342 aming for the mitochondria and the cell nucleus, respectively. Then, the cells were washed with PBS and imaged immediately by confocal laser scanning microscope. The excitation wavelength was fixed at 405 nm for Hoechst (emission recorded from

455 to 495 nm), at 488 nm for **DiOC$_6$(3)** (emission recorded from 500 to 565 nm) and at 561 nm for MTR (emission recorded from 570 to 660 nm). For colocalization analysis, Coloc2 plugin in ImageJ was employed.

Acknowledgements

The authors acknowledge the financial support from the Spanish Ministry of Science and Innovation co-funded by the European Regional Development Fund of the European Union (grants RTI2018-101675-B-I00), Generalitat Valenciana (grant AICO/2020/322) and Universitat Jaume I (grant UJI-B2018-30).

References

(1) Chariou, P. L.; Ortega-Rivera, O. A.; Steinmetz, N. F. Nanocarriers for the Delivery of Medical, Veterinary, and Agricultural Active Ingredients. *ACS Nano* **2020**, *14* (3), 2678–2701. https://doi.org/10.1021/acsnano.0c00173.

(2) Patra, J. K.; Das, G.; Fraceto, L. F.; Campos, E. V. R.; Rodriguez-Torres, M. D. P.; Acosta-Torres, L. S.; Diaz-Torres, L. A.; Grillo, R.; Swamy, M. K.; Sharma, S.; Habtemariam, S.; Shin, H. S. Nano Based Drug Delivery Systems: Recent Developments and Future Prospects. *J. Nanobiotechnology* **2018**, *16* (1), 1–33. https://doi.org/10.1186/s12951-018-0392-8.

(3) Majumder, J.; Taratula, O.; Minko, T. Nanocarrier-Based Systems for Targeted and Site Specific Therapeutic Delivery. *Adv. Drug Deliv. Rev.* **2019**, *144*, 57–77. https://doi.org/10.1016/j.addr.2019.07.010.

(4) Rosenblum, D.; Joshi, N.; Tao, W.; Karp, J. M.; Peer, D. Progress and Challenges towards Targeted Delivery of Cancer Therapeutics. *Nat. Commun.* **2018**, *9* (1), 1410. https://doi.org/10.1038/s41467-018-03705-y.

(5) Tapeinos, C.; Battaglini, M.; Ciofani, G. Advances in the Design of Solid Lipid Nanoparticles and Nanostructured Lipid Carriers for Targeting Brain Diseases. *J. Control. Release* **2017**, *264*, 306–332. https://doi.org/10.1016/j.jconrel.2017.08.033.

(6) Pattni, B. S.; Chupin, V. V.; Torchilin, V. P. New Developments in Liposomal Drug

Delivery. *Chem. Rev.* **2015**, *115* (19), 10938–10966. https://doi.org/10.1021/acs.chemrev.5b00046.

(7) Bhushan, B.; Khanadeev, V.; Khlebtsov, B.; Khlebtsov, N.; Gopinath, P. Impact of Albumin Based Approaches in Nanomedicine: Imaging, Targeting and Drug Delivery. *Adv. Colloid Interface Sci.* **2017**, *246*, 13–39. https://doi.org/10.1016/j.cis.2017.06.012.

(8) Baeza, A.; Colilla, M.; Vallet-Regí, M. Advances in Mesoporous Silica Nanoparticles for Targeted Stimuli-Responsive Drug Delivery. *Expert Opin. Drug Deliv.* **2015**, *12* (2), 319–337. https://doi.org/10.1517/17425247.2014.953051.

(9) Ghosh, B.; Biswas, S. Polymeric Micelles in Cancer Therapy: State of the Art. *J. Control. Release* **2021**, *332*, 127–147. https://doi.org/10.1016/j.jconrel.2021.02.016.

(10) Torchilin, V. P. Micellar Nanocarriers: Pharmaceutical Perspectives. *Pharm. Res.* **2007**, *24* (1), 1–16. https://doi.org/10.1007/s11095-006-9132-0.

(11) Kabanov, A. V.; Vinogradov, S. V. Nanogels as Pharmaceutical Carriers: Finite Networks of Infinite Capabilities. *Angew. Chemie - Int. Ed.* **2009**, *48* (30), 5418–5429. https://doi.org/10.1002/anie.200900441.

(12) Mauri, E.; Perale, G.; Rossi, F. Nanogel Functionalization: A Versatile Approach to Meet the Challenges of Drug and Gene Delivery. *ACS Appl. Nano Mater.* **2018**, *1* (12), 6525–6541. https://doi.org/10.1021/acsanm.8b01686.

(13) Devnarain, N.; Osman, N.; Fasiku, V. O.; Makhathini, S.; Salih, M.; Ibrahim, U. H.; Govender, T. Intrinsic Stimuli-Responsive Nanocarriers for Smart Drug Delivery of Antibacterial Agents—An in-Depth Review of the Last Two Decades. *Wiley Interdiscip. Rev. Nanomedicine Nanobiotechnology* **2021**, *13* (1), e1664. https://doi.org/10.1002/wnan.1664.

(14) Majumder, J.; Minko, T. Multifunctional and Stimuli-Responsive Nanocarriers for Targeted Therapeutic Delivery. *Expert Opin. Drug Deliv.* **2021**, *18* (2), 205–227. https://doi.org/10.1080/17425247.2021.1828339.

(15) Chen, M.; Liu, D.; Liu, F.; Wu, Y.; Peng, X.; Song, F. Recent Advances of Redox-Responsive Nanoplatforms for Tumor Theranostics. *J. Control. Release* **2021**, *332*, 269–284. https://doi.org/10.1016/j.jconrel.2021.02.030.

(16) Ding, Y.; Dai, Y.; Wu, M.; Li, L. Glutathione-Mediated Nanomedicines for Cancer Diagnosis and Therapy. *Chem. Eng. J.* **2021**, *426*, 128880. https://doi.org/10.1016/j.cej.2021.128880.

(17) Hsu, P. H.; Almutairi, A. Recent Progress of Redox-Responsive Polymeric Nanomaterials for Controlled Release. *J. Mater. Chem. B* **2021**, *9* (9), 2179–2188. https://doi.org/10.1039/d0tb02190c.

(18) Gamcsik, M. P.; Kasibhatla, M. S.; Teeter, S. D.; Colvin, O. M. Glutathione Levels in Human Tumors. *Biomarkers* **2012**, *17* (8), 671–691. https://doi.org/10.3109/1354750X.2012.715672.

(19) Kgesa, T.; Choonara, Y.; Tyagi, C.; Tomar, L.; Kumar, P.; du Toit, L.; Pillay, V. Disulphide-

Thiol Chemistry: A Multi-Faceted Tool for Macromolecular Design and Synthesis of Polyfunctional Materials for Specialized Drug Delivery. *Curr. Drug Deliv.* **2015**, *12* (3), 282–298. https://doi.org/10.2174/1567201812666150120161952.

(20) Cheng, R.; Feng, F.; Meng, F.; Deng, C.; Feijen, J.; Zhong, Z. Glutathione-Responsive Nano-Vehicles as a Promising Platform for Targeted Intracellular Drug and Gene Delivery. *J. Control. Release* **2011**, *152* (1), 2–12. https://doi.org/10.1016/j.jconrel.2011.01.030.

(21) Adamo, G.; Grimaldi, N.; Campora, S.; Sabatino, M. A.; Dispenza, C.; Ghersi, G. Glutathione-Sensitive Nanogels for Drug Release. *Chem. Eng. Trans.* **2014**, *38*, 457–462. https://doi.org/10.3303/CET1438077.

(22) Deng, Z.; Liu, S. Controlled Drug Delivery with Nanoassemblies of Redox-Responsive Prodrug and Polyprodrug Amphiphiles. *J. Control. Release* **2020**, *326*, 276–296. https://doi.org/10.1016/j.jconrel.2020.07.010.

(23) Wang, Y.; Zu, M.; Ma, X.; Jia, D.; Lu, Y.; Zhang, T.; Xue, P.; Kang, Y.; Xu, Z. Glutathione-Responsive Multifunctional "Trojan Horse" Nanogel as a Nanotheranostic for Combined Chemotherapy and Photodynamic Anticancer Therapy. *ACS Appl. Mater. Interfaces* **2020**, *12* (45), 50896–50908. https://doi.org/10.1021/acsami.0c15781.

(24) Wan, D.; Li, C.; Pan, J. Polymeric Micelles with Reduction-Responsive Function for Targeted Cancer Chemotherapy. *ACS Appl. Bio Mater.* **2020**, 3–10. https://doi.org/10.1021/acsabm.9b01070.

(25) Xia, H.; Liang, Y.; Chen, K.; Guo, C.; Wang, M.; Cao, J.; Han, S.; Ma, Q.; Sun, Y.; He, B. Reduction-Sensitive Polymeric Micelles as Amplifying Oxidative Stress Vehicles for Enhanced Antitumor Therapy. *Colloids Surfaces B Biointerfaces* **2021**, *203*, 111733. https://doi.org/10.1016/j.colsurfb.2021.111733.

(26) Rashmi; Singh, A. K.; Achazi, K.; Ehrmann, S.; Böttcher, C.; Haag, R.; Sharma, S. K. Stimuli-Responsive Non-Ionic Gemini Amphiphiles for Drug Delivery Applications. *Polym. Chem.* **2020**, *11* (42), 6772–6782. https://doi.org/10.1039/d0py01040e.

(27) Talelli, M.; Vicent, M. J. Reduction Sensitive Poly(l-Glutamic Acid) (PGA)-Protein Conjugates Designed for Polymer Masked-Unmasked Protein Therapy. *Biomacromolecules* **2014**, *15* (11), 4168–4177. https://doi.org/10.1021/bm5011883.

(28) Habib, S. M.; Jawad-ur-Rehman; Maharjan, R.; Kanwal, T.; Althagafi, I. I.; Saifullah, S.; Ullah, S.; Simjee, S. U.; Shah, M. R. Synthesis of Lactobionic Acid Based Bola-Amphiphiles and Its Application as Nano-Carrier for Curcumin Delivery to Cancer Cell Cultures in-Vitro. *Int. J. Pharm.* **2020**, *590*, 119897. https://doi.org/10.1016/j.ijpharm.2020.119897.

(29) Vinogradov, S. V. Nanogels in the Race for Drug Delivery. *Nanomedicine* **2010**, *5* (2), 165–168. https://doi.org/10.2217/nnm.09.103.

(30) Gaspar, R.; Duncan, R. Polymeric Carriers: Preclinical Safety and the Regulatory Implications for Design and Development of Polymer Therapeutics. *Adv. Drug Deliv. Rev.* **2009**, *61* (13), 1220–1231. https://doi.org/10.1016/j.addr.2009.06.003.

(31) Felip-León, C.; Cejudo-Marín, R.; Peris, M.; Galindo, F.; Miravet, J. F. Sizing Down a Supramolecular Gel into Micro- and Nanoparticles. *Langmuir* **2017**, *33* (39), 10322–10328. https://doi.org/10.1021/acs.langmuir.7b02440.

(32) Torres-Martínez, A.; Bedrina, B.; Falomir, E.; Marín, M. J.; Angulo-Pachón, C. A.; Galindo, F.; Miravet, J. F. Non-Polymeric Nanogels as Versatile Nanocarriers: Intracellular Transport of the Photosensitizers Rose Bengal and Hypericin for Photodynamic Therapy. *ACS Appl. Bio Mater.* **2021**, *4* (4), 3658–3669. https://doi.org/10.1021/acsabm.1c00139.

(33) Torres-Martínez, A.; Angulo-Pachón, C. A.; Galindo, F.; Miravet, J. F. In between Molecules and Self-Assembled Fibrillar Networks: Highly Stable Nanogel Particles from a Low Molecular Weight Hydrogelator. *Soft Matter* **2019**, *15* (17), 3565–3572. https://doi.org/10.1039/C9SM00252A.

(34) Torres-Martínez, A.; Angulo-Pachón, C. A.; Galindo, F.; Miravet, J. F. Liposome-Enveloped Molecular Nanogels. *Langmuir* **2019**, *35* (41), 13375–13381. https://doi.org/10.1021/acs.langmuir.9b02282.

(35) Navarro-Barreda, D.; Angulo-Pachón, C. A.; Bedrina, B.; Galindo, F.; Miravet, J. F. A Dual Stimuli Responsive Supramolecular Gel Provides Insulin Hydrolysis Protection and Redox-Controlled Release of Actives. *Macromol. Chem. Phys.* **2020**, *221* (4), 1–6. https://doi.org/10.1002/macp.201900419.

(36) Bae, J.; Maurya, A.; Shariat-Madar, Z.; Murthy, S. N.; Jo, S. Novel Redox-Responsive Amphiphilic Copolymer Micelles for Drug Delivery: Synthesis and Characterization. *AAPS J.* **2015**, *17* (6), 1357–1368. https://doi.org/10.1208/s12248-015-9800-2.

(37) Fuhrhop, J. H.; Wang, T. Bolaamphiphiles. *Chem. Rev.* **2004**, *104* (6), 2901–2937. https://doi.org/10.1021/cr030602b.

(38) Brisset, F. Synthesis of New Sugar-Based Bolaamphiphilic Compounds Physicochemical Study of Their Molecular Aggregation in Aqueous Solution. *New J. Chem.* **1996**, *20* (5), 595–605.

(39) Jürgen-Hinrich, F.; Wang, T. Bolaamphiphiles. *Chem. Rev.* **2004**, *104*, 2901–2937.

(40) Yan, Y.; Huang, J.; Li, Z.; Zhao, X.; Zhu, B.; Ma, J. Surface Properties of Cationic Bolaamphiphiles and Their Mixed Systems with Oppositely Charged Conventional Surfactant. *Colloids Surfaces A Physicochem. Eng. Asp.* **2003**, *215*, 263–275. https://doi.org/10.1016/S0927-7757(02)00486-7.

(41) Midekessa, G.; Godakumara, K.; Ord, J.; Viil, J.; Lättekivi, F.; Dissanayake, K.; Kopanchuk, S.; Rinken, A.; Andronowska, A.; Bhattacharjee, S.; Rinken, T.; Fazeli, A. Zeta Potential of Extracellular Vesicles: Toward Understanding the Attributes That Determine Colloidal Stability. *ACS Omega* **2020**, *5* (27), 16701–16710. https://doi.org/10.1021/acsomega.0c01582.

(42) Kurniasih, I. N.; Liang, H.; Mohr, P. C.; Khot, G.; Rabe, J. P.; Mohr, A. Nile Red Dye in Aqueous Surfactant and Micellar Solution. *Langmuir* **2015**, *31* (9), 2639–2648. https://doi.org/10.1021/la504378m.

(43) Gao, L.; Shi, L.; Zhang, W.; An, Y.; Jiang, X. Expulsion of Unimers from Polystyrene-Block-Poly(Acrylic Acid) Micelles. *Macromol. Chem. Phys.* **2006**, *207* (5), 521–527. https://doi.org/10.1002/macp.200500496.

(44) Xie, D.; Bai, W.; Xu, K.; Bai, R.; Zhang, G. Polymeric Micelles Formed by Splitting of Micellar Cluster. *J. Phys. Chem. B* **2007**, *111* (28), 8034–8037. https://doi.org/10.1021/jp072329d.

(45) Razuvaeva, E. V.; Kulebyakina, A. I.; Streltsov, D. R.; Bakirov, A. V.; Kamyshinsky, R. A.; Kuznetsov, N. M.; Chvalun, S. N.; Shtykova, E. V. Effect of Composition and Molecular Structure of Poly(l -Lactic Acid)/Poly(Ethylene Oxide) Block Copolymers on Micellar Morphology in Aqueous Solution. *Langmuir* **2018**, *34* (50), 15470–15482. https://doi.org/10.1021/acs.langmuir.8b03379.

(46) Solomonov, A. V.; Marfin, Y. S.; Rumyantsev, E. V.; Ragozin, E.; Zahavi, T. S.; Gellerman, G.; Tesler, A. B.; Muench, F.; Kumagai, A.; Miyawaki, A. Self-Assembled Micellar Clusters Based on Triton-X-Family Surfactants for Enhanced Solubilization, Encapsulation, Proteins Permeability Control, and Anticancer Drug Delivery. *Mater. Sci. Eng. C* **2019**, *99*, 794–804. https://doi.org/10.1016/j.msec.2019.02.016.

(47) Cleland, W. W. Dithiothreitol, a New Protective Reagent for SH Groups. *Biochemistry* **1964**, *3* (4), 480–482. https://doi.org/10.1021/bi00892a002.

(48) Yang, X.; Cai, X.; Yu, A.; Xi, Y.; Zhai, G. Redox-Sensitive Self-Assembled Nanoparticles Based on Alpha-Tocopherol Succinate-Modified Heparin for Intracellular Delivery of Paclitaxel. *J. Colloid Interface Sci.* **2017**, *496*, 311–326. https://doi.org/10.1016/j.jcis.2017.02.033.

(49) Li, J.; Huo, M.; Wang, J.; Zhou, J.; Mohammad, J. M.; Zhang, Y.; Zhu, Q.; Waddad, A. Y.; Zhang, Q. Redox-Sensitive Micelles Self-Assembled from Amphiphilic Hyaluronic Acid-Deoxycholic Acid Conjugates for Targeted Intracellular Delivery of Paclitaxel. *Biomaterials* **2012**, *33* (7), 2310–2320. https://doi.org/10.1016/j.biomaterials.2011.11.022.

(50) Wang, J.; Yang, G.; Guo, X.; Tang, Z.; Zhong, Z.; Zhou, S. Redox-Responsive Polyanhydride Micelles for Cancer Therapy. *Biomaterials* **2014**, *35* (9), 3080–3090. https://doi.org/10.1016/j.biomaterials.2013.12.025.

(51) Cai, Z.; Zhang, H.; Wei, Y.; Wei, Y.; Xie, Y.; Cong, F. Reduction- and PH-Sensitive Hyaluronan Nanoparticles for Delivery of Iridium(III) Anticancer Drugs. *Biomacromolecules* **2017**, *18* (7), 2102–2117. https://doi.org/10.1021/acs.biomac.7b00445.

(52) Escuder, B.; LLusar, M.; Miravet, J. F. Insight on the NMR Study of Supramolecular Gels and Its Application to Monitor Molecular Recognition on Self-Assembled Fibers. *J. Org. Chem.* **2006**, *71* (20), 7747–7752. https://doi.org/10.1021/jo0612731.

(53) Akoka, S.; Barantin, L.; Trierweiler, M. Concentration Measurement by Proton NMR Using the ERETIC Method. *Anal. Chem.* **1999**, *71* (13), 2554–2557. https://doi.org/10.1021/ac981422i.

(54) Liew, S. S.; Qin, X.; Zhou, J.; Li, L.; Huang, W.; Yao, S. Q. Smart Design of Nanomaterials for Mitochondria-Targeted Nanotherapeutics. *Angew. Chemie - Int. Ed.* **2021**, *60* (5), 2232–2256. https://doi.org/10.1002/anie.201915826.

(55) Korchak, H. M.; Rich, A. M.; Wilkenfeld, C.; Rutherford, L. E.; Weissmann, G. A CARBOCYANINE DYE, DiOC6(3) , ACTS AS A MITOCHONDRIAL PROBE IN HUMAN NEUTROPHILS. *Biochem. Biophys. Res. Commun.* **1982**, *108* (4), 1495–1501.

(56) Sabnis, R. W.; Deligeorgiev, T. G.; Jachak, M. N.; Dalvi, T. S. DiOC6(3): A Useful Dye for Staining the Endoplasmic Reticulum. *Biotech. Histochem.* **1997**, *72* (5), 253–258. https://doi.org/10.3109/10520299709082249.

(57) Zamzami, N.; Métivier, D.; Kroemer, G. Quantitation of Mitochondrial Transmembrane Potential in Cells and in Isolated Mitochondria. *Methods Enzymol.* **2000**, *322*, 208–213. https://doi.org/10.1016/s0076-6879(00)22021-1.

(58) Bannunah, A. M.; Vllasaliu, D.; Lord, J.; Stolnik, S. Mechanisms of Nanoparticle Internalization and Transport across an Intestinal Epithelial Cell Model: Effect of Size and Surface Charge. *Mol. Pharm.* **2014**, *11* (12), 4363–4373. https://doi.org/10.1021/mp500439c.

(59) Hennecke, J.; Sillen, A.; Huber-Wunderlich, M.; Engelborghs, Y.; Glockshuber, R. Quenching of Tryptophan Fluorescence by the Active-Site Disulfide Bridge in the DsbA Protein from Escherichia Coli. *Biochemistry* **1997**, *36* (21), 6391–6400. https://doi.org/10.1021/bi963017w.

(60) Cowgill, R. W. Fluorescence and the Structure of Proteins. 18. Spatial Requirements for Quenching by Disulfide Groups. *Biochim. Biophys. Acta* **1970**, *207* (3), 556–559. https://doi.org/10.1016/s0005-2795(70)80019-8.

(61) Lebed, A. S.; Yefimova, S. L.; Guralchuk, G. Y.; Sorokin, A. V.; Borovoy, I. A.; Malyukin, Y. V. Effect of Hydrophobicity of Cationic Carbocyanine Dyes DiOCn on Their Binding to Anionic Surfactant Micelles. *J. Appl. Spectrosc.* **2010**, *77* (2), 183–188. https://doi.org/10.1007/s10812-010-9312-x.

(62) Freire, S.; Bordello, J.; Granadero, D.; Al-Soufi, W.; Novo, M. Role of Electrostatic and Hydrophobic Forces in the Interaction of Ionic Dyes with Charged Micelles. *Photochem. Photobiol. Sci.* **2010**, *9* (5), 687–696. https://doi.org/10.1039/b9pp00198k.

(63) Giustarini, D.; Galvagni, F.; Dalle Donne, I.; Milzani, A.; Severi, F. M.; Santucci, A.; Rossi, R. N-Acetylcysteine Ethyl Ester as GSH Enhancer in Human Primary Endothelial Cells: A Comparative Study with Other Drugs. *Free Radic. Biol. Med.* **2018**, *126*, 202–209. https://doi.org/10.1016/j.freeradbiomed.2018.08.013.

(64) Rubi, B.; Del Arco, A.; Bartley, C.; Satrustegui, J.; Maechler, P. The Malate-Aspartate NADH Shuttle Member Aralar1 Determines Glucose Metabolic Fate, Mitochondrial Activity, and Insulin Secretion in Beta Cells. *J. Biol. Chem.* **2004**, *279* (53), 55659–55666. https://doi.org/10.1074/jbc.M409303200.

(65) Patel, S.; Kim, J.; Herrera, M.; Mukherjee, A.; Kabanov, A. V.; Sahay, G. Brief Update on Endocytosis of Nanomedicines. *Adv. Drug Deliv. Rev.* **2019**, *144*, 90–111.

https://doi.org/10.1016/j.addr.2019.08.004.

(66) He, W.; Xing, X.; Wang, X.; Wu, D.; Wu, W.; Guo, J.; Mitragotri, S. Nanocarrier-Mediated Cytosolic Delivery of Biopharmaceuticals. *Adv. Funct. Mater.* **2020**, *30* (37), 1–22. https://doi.org/10.1002/adfm.201910566.

(67) Van de Vyver, T.; Bogaert, B.; De Backer, L.; Joris, F.; Guagliardo, R.; Van Hoeck, J.; Merckx, P.; Van Calenbergh, S.; Ramishetti, S.; Peer, D.; Remaut, K.; De Smedt, S. C.; Raemdonck, K. Cationic Amphiphilic Drugs Boost the Lysosomal Escape of Small Nucleic Acid Therapeutics in a Nanocarrier-Dependent Manner. *ACS Nano* **2020**, *14* (4), 4774–4791. https://doi.org/10.1021/acsnano.0c00666.

(68) Dong, K.; Wang, Z.; Zhang, Y.; Ren, J.; Qu, X. Metal-Organic Framework-Based Nanoplatform for Intracellular Environment-Responsive Endo/Lysosomal Escape and Enhanced Cancer Therapy. *ACS Appl. Mater. Interfaces* **2018**, *10* (38), 31998–32005. https://doi.org/10.1021/acsami.8b11972.

Appendix: Supporting Information

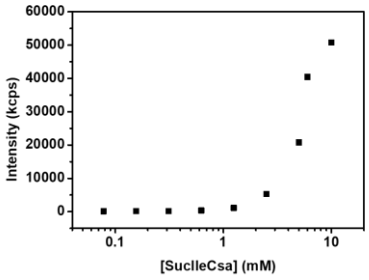

Figure S4.1. Plot of the intensity of scattered light determined by DLS as a function of the concentration of **SucIleCsa**. (kcps = kilocounts per second, 0.2 M HEPES, pH 7.4).

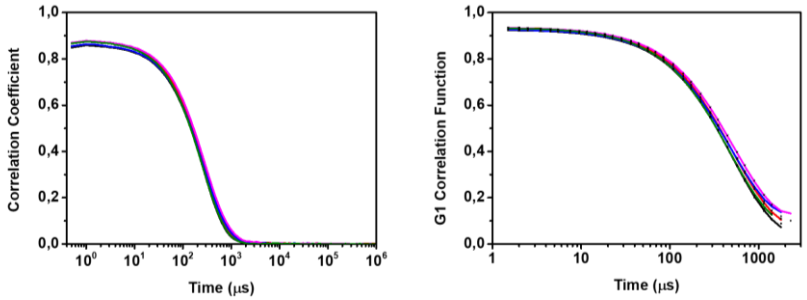

Figure S4.2. Left: Representative examples of raw correlation data for **SucIleCsa** nanoparticle dispersions (5.0 mM in 0.2 M HEPES, pH 7.4); right: data and fits obtained by the Cumulants Analysis.

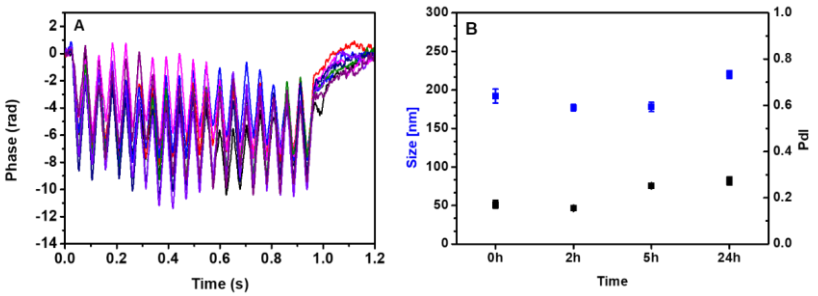

Figure S4.3. A: Representative Z-potential phase plots of **SucIleCsa** nanoparticles (5.0 mM in 0.2 M HEPES pH 7.4) obtained by a monomodal measurement (FFR mode); B: Stability of **SucIleCsa** nanoparticles (5 mM) for 24 hours at 25 ºC (0.2 M HEPES, pH 7.4).

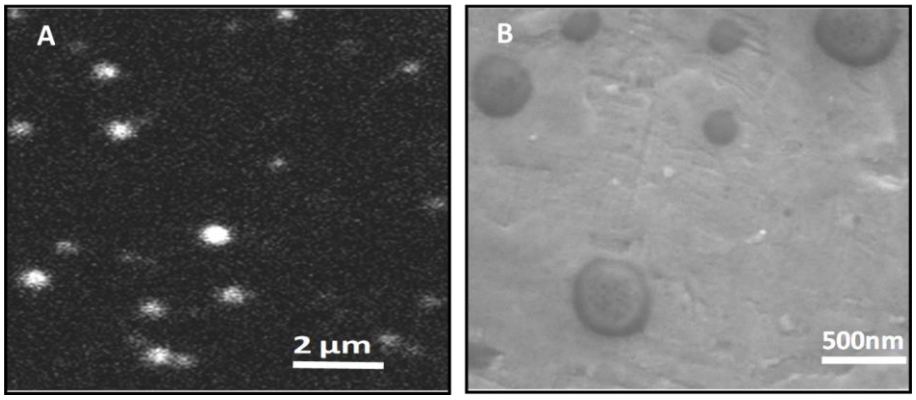

Figure S4.4. CLSM (A) and SEM (B) images obtained for the nanoparticles formed by **SucIleCsa** (5.0 mM in 0.2 M HEPES pH 7.4). CLSM image corresponds to the fluorescence of entrapped Nile red (10 µM, λ_{ex} = 488 nm).

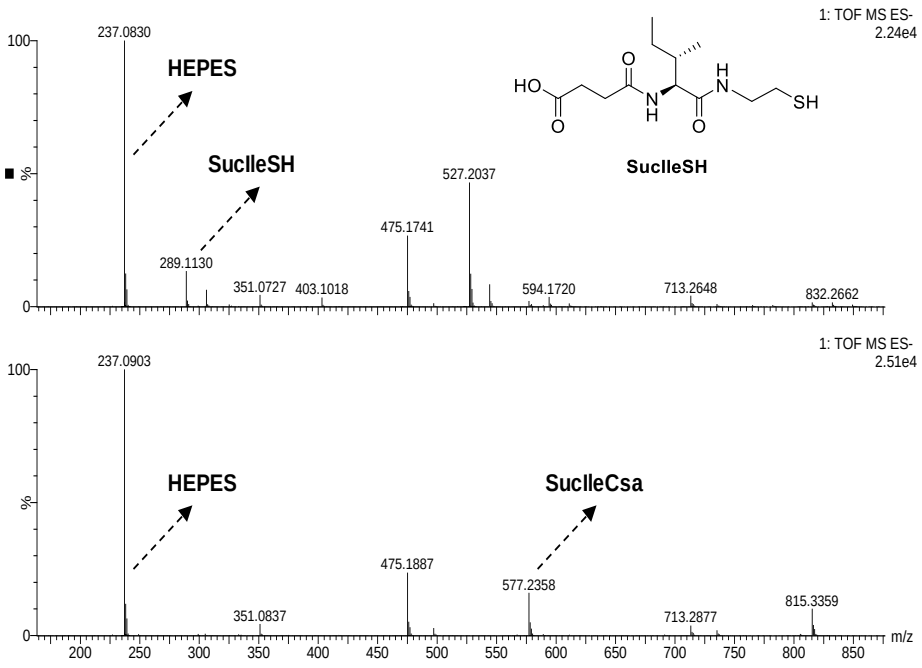

Figure S4.5. Mass spectra (ESI, TOF, negative mode) for a representative sample of **SucIleCsa** nanoparticles (5.0 mM in 0.2 M HEPES) with (top; incubating 16 h) and without (bottom) treatment using DTT (20 mM).

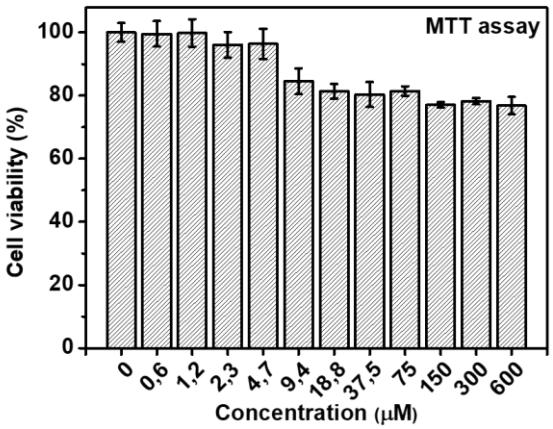

Figure S4.6. MTT assay analysis of cell viability of HT-29 cells treated with serial dilutions of **SucIleCsa** concentrations (0, 0.6, 1.2, 2.3, 4.7, 9.4, 18.8, 37.5, 75.0, 150.0, 300.0 or 600.0 μM) for 48 hours.

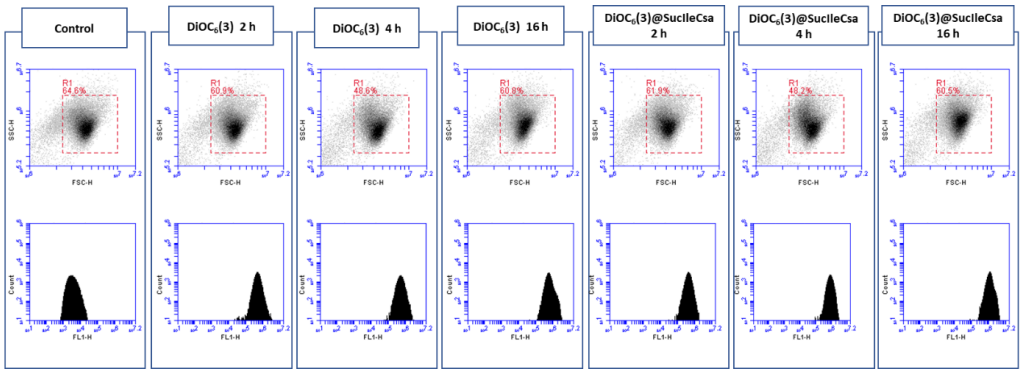

Figure S4.7. Flow cytometry data of HT-29 cells exposed to **$DiOC_6(3)$** and **$DiOC_6(3)$@SucIleCsa** for 2, 4 and 16 hours. Scatter plots (cell size/granularity) showing typical HT-29 cells distribution (FSC corresponds to cell size and SSC to cell granularity) and green cell fluorescence intensity distributions (signal collected in the FL1 detector, 533/30 nm) are displayed.

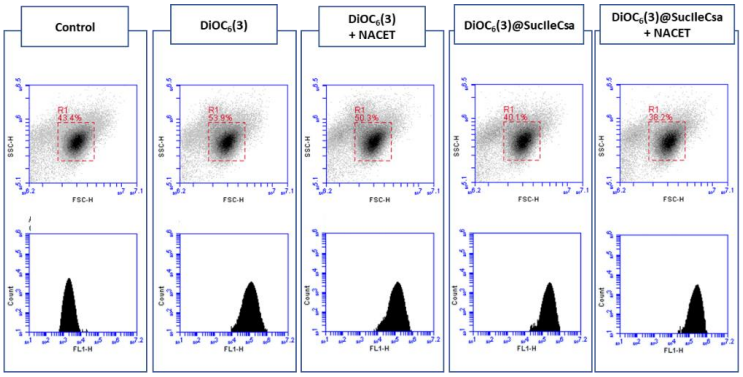

Figure S4.8. Flow cytometry data of HT-29 cells exposed to **$DiOC_6(3)$** and **$DiOC_6(3)$@SucIleCsa** for 2 hours with and without pre-treatment with 0.5 mM NACET. Scatter plots (cell size/granularity) showing typical HT-29 cells distribution (FSC corresponds to cell size and SSC to cell granularity) and green cell fluorescence intensity distributions (signal collected in the FL1 detector, 533/30 nm) are displayed.

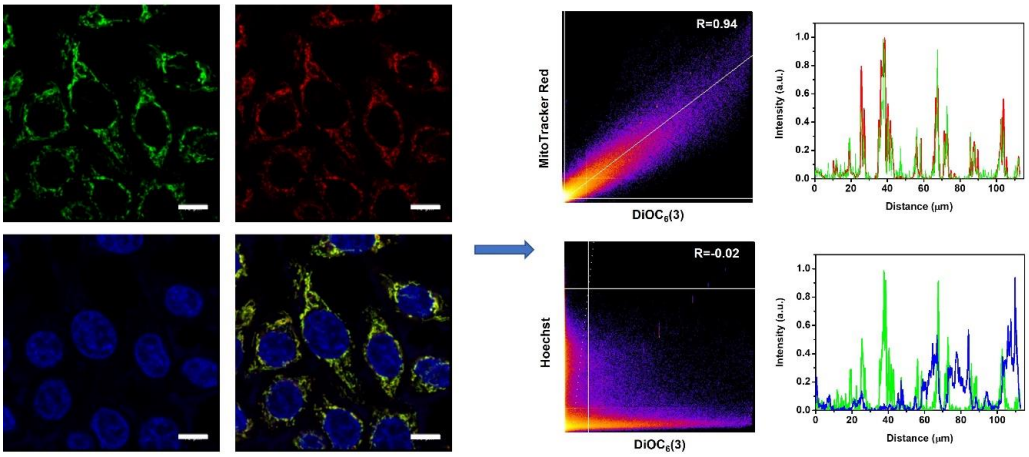

Figure S4.9. Fluorescence assessment of co-stained HT-29 cells. Confocal fluorescence microscope images were obtained after cells were 30-min-exposed to **$DiOC_6(3)$@SucIleCsa** (green) and stained with Hoechst 33342 (blue) and MitoTracker Red (red). Representative images and correlation between the green and the red and blue fluorescence signal are displayed (Pearson´s coefficient). Scale bars = 10 μm.

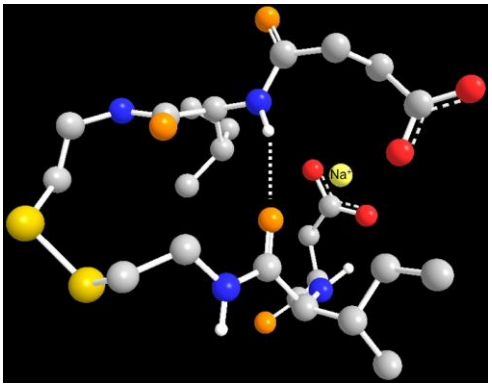

Figure S4.10. Molecular model of a folded conformation of **SucIleCsa** complexed with a sodium cation. The structure corresponds to an energy minimum obtained with semiempirical calculations with AM1 parametrization**.** Non-polar hydrogen atoms have been omitted for clarity.

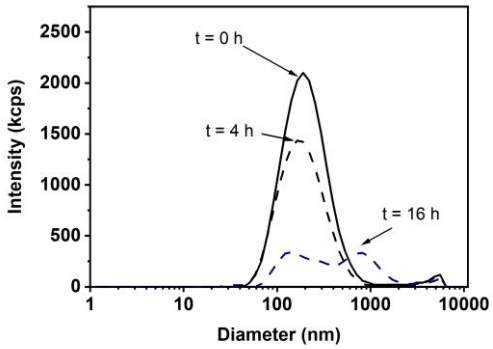

Figure S4.11. Variation of the intensity of scattered light measured by DLS for a sample of nanoparticles of **SucIleCsa** (5.0 mM, pH 7.4, 0.2 M HEPES) upon addition of GSH (20.0 mM) at 37 °C.

Chapter 5

Photoreversible formation of nanotubes in water from an amphiphilic azobenzene derivative

Photoreversible formation of nanotubes in water from an amphiphilic azobenzene derivative

Diego Navarro-Barreda, César A. Angulo-Pachón, Francisco Galindo, and Juan F. Miravet*

Department of Inorganic and Organic Chemistry, University Jaume I, 12071, Castelló de la Plana, Spain.

Accepted Date: 13th October 2021.

Abstract

An anionic azobenzene-appended derivative of L-ValylGlycine self-assembles into nanotubes in water. Irradiation with 365 nm light provokes *trans-cis* isomerization of the azobenzene unit and subsequent tube disassembly. Thermal or photoinduced (457 nm light) recovery of the trans isomer restores the nanotubes.

5.1 Introduction

Responsive and adaptive organic molecular (nano)materials are used, among other fascinating applications, as actuators and in targeted drug release.[1–3] The use of light as a stimulus is especially attractive because it provides spatial and temporal control without direct contact. Thus, controlled delivery of bioactive molecules in a given microenvironment with a good time and position resolution is of utmost interest for biomedical applications.[4,5]

Amphiphilic molecules are a preferred building block for preparing functional molecular materials in aqueous environments.[6] Particularly, photoresponsive amphiphiles afford materials whose formation and function are light-controlled.[7] Examples of units that can undergo light-induced reversible changes in their structure and that have been incorporated into amphiphiles include derivatives of diarylethene,[8] spiropyran[9] and, mostly, azobenzene.[10,11]Azobenzenes show outstanding properties for their use as a photoswitch, such as excellent reversibility and *trans-cis* isomerization cycles endurance.[12,13] Photocontrollable self-assembly has been mainly studied using molecules with azobenzene moieties.[14] Examples include the formation or size regulation of micelles,[15] vesicles,[16–19] organic nanoparticles,[20,21] molecular hydrogels[22,23] and the reversible conversion between nanotubes and nanoparticles.[24] With a biomedical perspective, azobenzene isomerization permits photocontrol of complex biological systems,[25,26] and an azobenzene-modified diphenylalanine derivative has been used for photocontrolled targeted delivery of siRNA biomolecules.[27]

Peptide-derived nanotubes have received much attention focused on understanding their self-assembly mechanism and exciting properties.[28–30] Aside

from cyclic peptides,[31] many of the studies on peptide nanotubes are based on the self-assembly of dipeptide derivatives. Remarkably, the diphenylalanine motif is prone to self-assemble into tubular structures, and many studies have been carried out in this direction.[32] Peptide nanotubes are studied in the context of different applications in areas such as electronics, sensors, and biomedical materials, among others.[33] Noticeably, peptidic nanostructures can be used for targeted drug delivery.[34,35]

Here we report on the light-controlled reversible formation of nanotubes from a derivative of L-ValGly with an appended azobenzene moiety (**SucValGlyAzo**, **Scheme 5.1**). Up to our knowledge, these results are unprecedented. In related work, a diphenylalanine moiety with a pendant azo-group formed fibrils that evolved to vesicles upon photoisomerization.[36] The insertion of an azobenzene moiety in a decapeptide permitted photoregulated fibrilization.[37] A diglycine-based molecule containing an azobenzene unit changed its aggregation upon irradiation from nanoribbons to a hydrogel.[38]

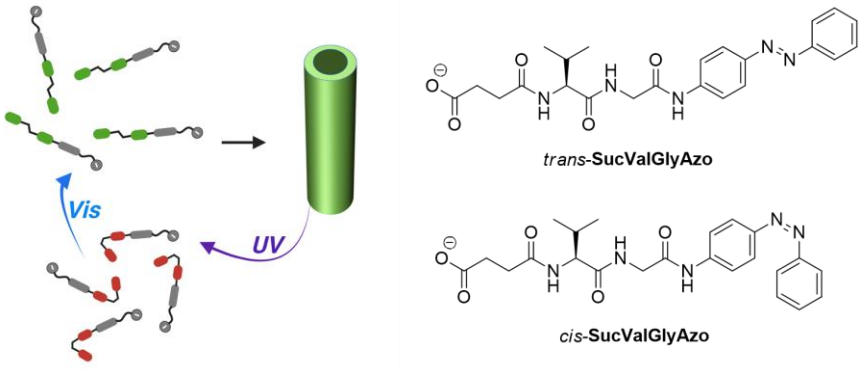

Scheme 5.1. Structure of **SucValGlyAzo**, and pictorial representation of its photoisomerization and the nanotube formation.

5.2 Results and Discussion

SucValGlyAzo was prepared from L-ValGly by N-acylation with succinic anhydride (abbr: 'Suc') at the N-terminus and amide formation with 4-aminoazobenzene (abbr: 'Azo') at the C-terminus, using the corresponding N-protection and C-activation strategies (see SI for details). The introduction of a succinic acid moiety has been explored several times in our previous work to produce molecules that can aggregate in water to yield gels formed by fibrillar networks[39–41] or nanoparticles.[42]

SucValGlyAzo showed, as expected, a reversible *trans-cis* photoisomerization. **Figure 5.1** shows that upon irradiation with UV light, the absorption band at *ca.* 340 nm diminishes in parallel with the increase of the band of the *cis*-isomer at *ca.* 440 nm. The measurements were carried out in tris(hydroxymethyl)aminomethane (Tris) buffer at pH 7.4, where the predominant species of **SucValGlyAzo** is the carboxylate (the pK_a of the conjugated acid is 6.1). The photoisomerization process was found to be fully reversible. Several cycles of *trans-cis* interconversion could be performed by alternative irradiation at 365 nm and 457 nm, without significant alteration of the chromophore (**Figure 5.1**). As usual for the azobenzene unit, thermal energy also permits a progressive *cis-trans* transformation, which is significantly slower for this molecule. For example, the absorption spectrum of the *cis* isomer is almost unchanged after 10 minutes of thermal equilibration at 25 ºC. It requires more than one hour to recover the *trans* form (Figure S5.1) fully. However, after irradiating the *cis* isomer with visible light, the *trans* form is obtained immediately (Figure S5.2).

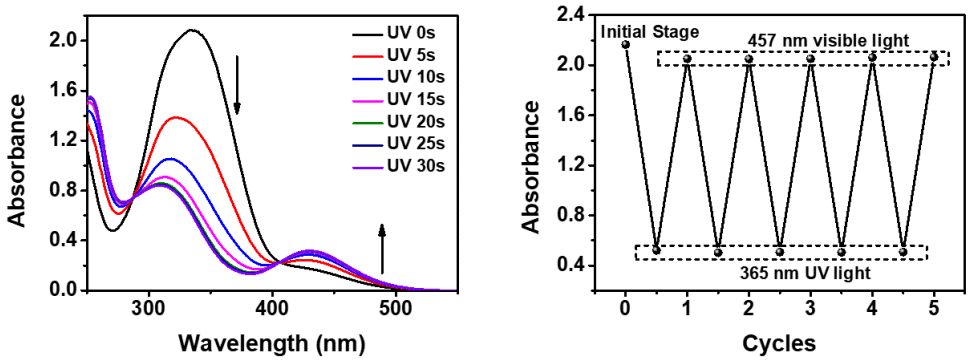

Figure 5.1. Left: UV-Vis spectra of **SucValGlyAzo** as a function of time upon 365 nm UV light irradiation Right: Absorbance changes at 340 nm observed during five cycles of consecutive irradiation for 30 seconds with 365 nm UV light and 457 nm visible light. [**SucValGlyAzo**] = 1.7 mM, 0.1 M Tris buffer, pH 7.4, 25 ºC.

The aggregation of **SucValGlyAzo** was monitored by dynamic light scattering (DLS). The plot of the intensity of scattered light *vs.* concentration of the azo derivative reveals a scattering onset at *ca.* 0.6 mM, ascribable to the critical aggregation concentration (**Figure 5.2**). The analysis of the size distribution obtained by DLS is also shown in **Figure 5.2**. A broad distribution was obtained with an intensity averaged apparent diameter (Di) of 334 ± 49 nm and a polydispersity index (PdI) of 0.50 ± 0.09. Filtration through a 0.45 µm mesh nylon filter to remove large particles afforded a monomodal symmetrical size distribution, with Di = 107.0 ± 1.0 nm and PdI = 0.203 ± 0.012. The nanometric objects showed reasonable temporal stability, being the size distribution very similar after storage for 16 hours of the sample at 4 ºC (Figure S5.4). It has to be noted that DLS results are commonly presented as a particle diameter distribution, obtained from the Stokes-Einstein equation assuming spherical particles.[43] However, for rods or cylindrical objects, as those described below, the analysis is much more complex.[44] For this reason, the plot in **Figure 5.2** shows

the distribution of diffusion coefficients and the apparent diameter, namely, that obtained assuming spherical particles.

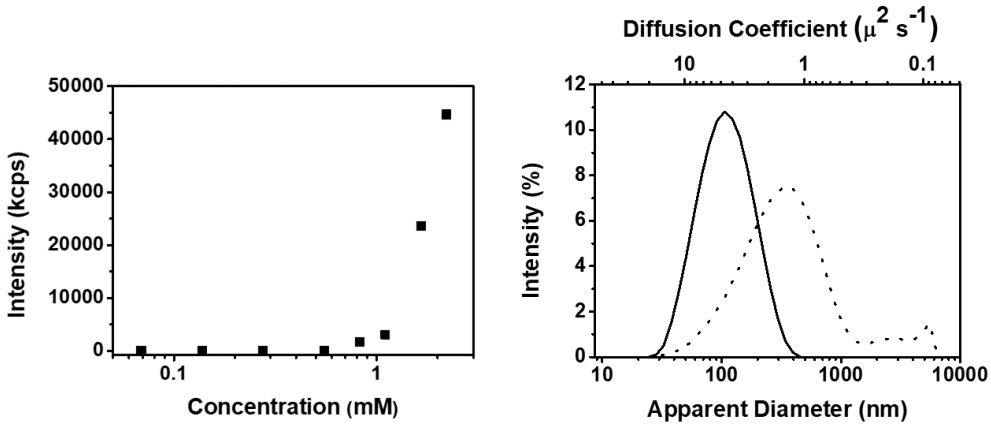

Figure 5.2. Left: Variation of the intensity of scattered light with the concentration of **SucValGlyAzo** determined by DLS. Right: Diffusion coefficient and apparent diameter particle distribution determined by DLS for a 1.7 mM sample of **SucValGlyAzo** before (dashed line) and after (solid line) filtration through a 0.45 μm mesh filter. All the measurements were carried out in 0.1 M Tris buffer, pH 7.4, 25 ºC.

Given the anionic nature of **SucValGlyAzo** at neutral pH values, it was expected that its aggregation could be influenced by the concentration and nature of the cations present in the medium. For this reason, a comparison of dispersing media was made by DLS in 0.1 M Tris, phosphate (PB) and 4-(2-hydroxyethyl)-1-piperazineethanesulfonic acid (HEPES) buffers (Figure S5.5). Significant differences were found. The sample in PB shows a broad bimodal distribution of sizes (D_i *ca.* 400 and 2000 nm). For the case of HEPES buffer, also a bimodal distribution of smaller objects is obtained (D_i *ca.* 40 and 200 nm). These results differ from the monomodal size distribution previously obtained for the aggregation of **SucValGlyAzo** in Tris (**Figure 5.2**). Seemingly, the different characteristics of the cations present in the buffers affect the aggregation

according to these preliminary assays, but further studies would be required taking into account variables such a pH or ionic strength. It is worth noting that PB contains mainly the spherical and relatively small cation sodium, which presumably promotes larger aggregated species. HEPES buffer preparation requires neutralization with sodium hydroxide, affording sodium and ammonium species as cations. However, Tris buffer contains exclusively organic ammonium-type cations. This behavior is directly related to the Hofmeister (lyotropic) series, where the sodium cation presents a significantly higher aggregation-promoting effect than ammonium derivatives.[45]

Electron microscopy revealed that the objects detected by DLS correspond to nanotubes. The images in **Figure 5.3** correspond to a sample treated with a 0.45 µm mesh nylon filter, but similar nanotubes were observed for unfiltered samples (Figure S5.6). Transmission electron microscopy (TEM) images show the extensive formation of nanotubes with a monodisperse diameter distribution of 23 nm and a wall thickness of 9 nm (Figure 5.3 A-C). Cryo-TEM showed the formation of nanotubes that coexist with twisted tapes (Figure 5.3 D). It could be argued that **SucValGlyAzo** forms an amphiphilic bilayer that originates a tape that twists into nanotubes, as reported in related systems.[29,46–48]

The light-controlled nanotube assembly/diassembly processes were studied by DLS measurements (**Figure 5.4**). After UV irradiation, almost no scattering is measured by DLS, revealing that the *trans-cis* isomerization results in nanotube disassembly, with a residual number of aggregates. TEM images (Figure S5.7) show that most nanotubes have disappeared compared to the images previous to irradiation shown in **Figure 5.3**. Noticeably, TEM also reveals that some blurred structures reminiscent of the nanotubes are still present. The thermal equilibration of the system shows that the intensity of scattered light increases

with time. Also, after 60 min the size distribution shifts towards smaller apparent diameters. This behaviour can be ascribed to the progressive growth of nanotubes, which in the initial stages are smaller than the residual ones remaining after UV irradiation. Finally, a monomodal size distribution like the initial one, but broader, is achieved after two hours.

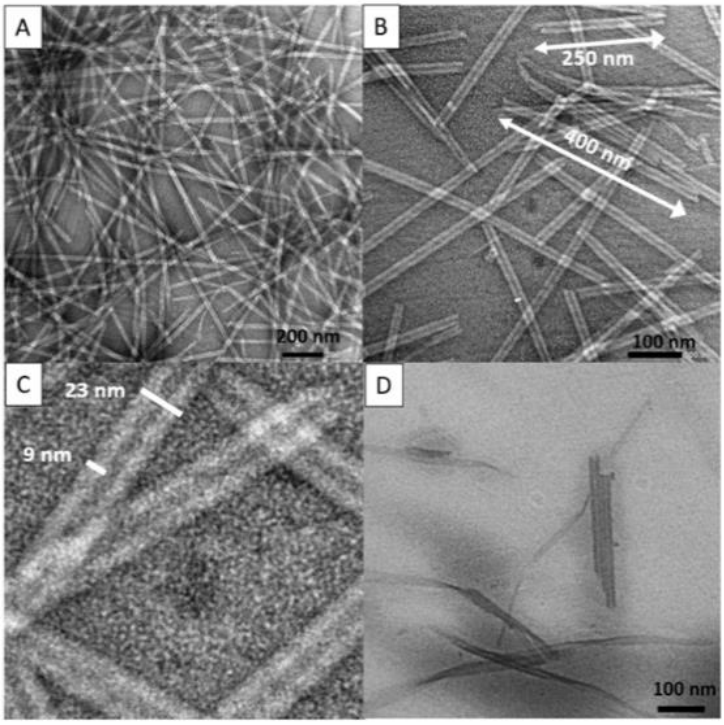

Figure 5.3. TEM (A-C) and cryo-TEM (D) images of the nanotubes formed by **SucValGlyAzo** (1.7 mM, 0.1 M Tris buffer, pH 7.4; uranyl acetate was used as a staining agent for the TEM images).

The UV-promoted nanotube disassembly can be rationalized considering that *trans*-azobenzene is almost flat and has no dipole moment, whereas the *cis* isomer presents an angular geometry and a dipole moment.[49] This dramatic change would affect intermolecular interactions like aromatic stacking, which are responsible for the self-assembly process.

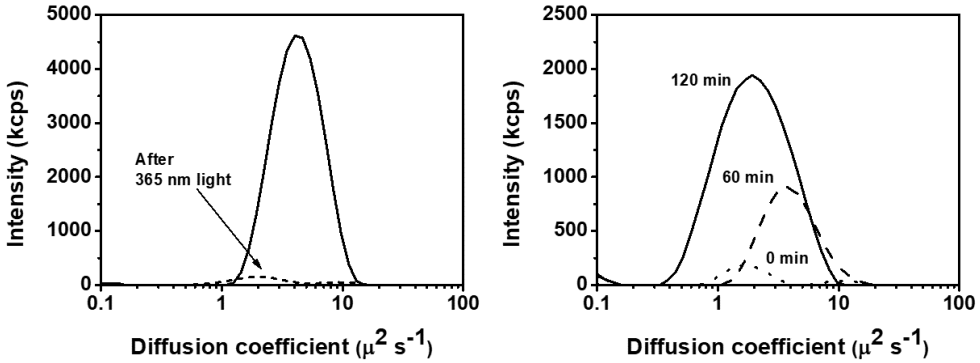

Figure 5.4. DLS measurements of a **SucValGlyAzo** solution (1.7 mM, 0.1 M Tris buffer, pH 7.4) Left: Scattering intensity distribution before (solid line) and after (dashed line) irradiation with 365 nm light. Right: Temporal evolution of the scattering intensity distribution for the UV-irradiated sample upon resting in the darkness at 25 ºC.

It is interesting to note that the UV-vis spectra of the sample before UV irradiation and immediately after visible irradiation differ in the shape of the band assigned to the *trans* isomer at *ca.* 340 nm (Figure S5.3). Most likely, irradiation with visible light initially affords free (non-aggregated) *trans* molecules whose absorption spectrum is more symmetric and slightly red-shifted compared to nanotubes.

The photoisomerization-controlled self-assembly process can also be monitored using the fluorescent probe Nile red. This dye shows a very weak fluorescence in water that is dramatically boosted upon its incorporation into hydrophobic environments.[50] In the presence of **SucValGlyAzo,** Nile red shows an intense emission (λ_{max} = 625 nm), indicating the incorporation of the dye in hydrophobic regions of the nanotubes (**Figure 5.5** and Figure S5.8). Irradiation with UV light results in fluorescence quenching and peak shift to 660 nm, indicating the exposition of Nile red to the aqueous solvent due to light-promoted nanotube

disaggregation. Then, irradiation with 457 nm light (30 seconds) provokes a notable fluorescence recovery after 30 min (**Figure 5.5**).

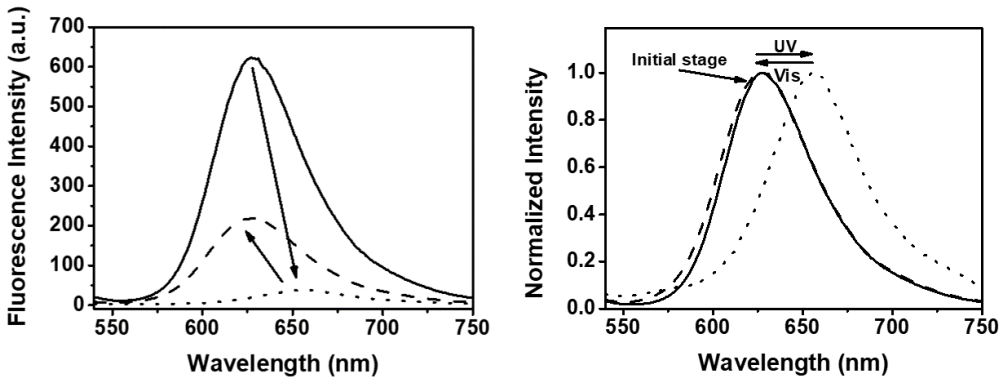

Figure 5.5. Emission intensity (λ_{ex} = 520 nm) of a solution of **SucValGlyAzo** containing Nile red (10 μM) at the initial stage (solid line), after irradiation with 365 nm light for 30 seconds (dotted line), and after subsequent irradiation with 457 nm light for 30 seconds and then resting for 30 minutes (dashed line). Left: Absolute emission intensities. Right: Normalized emission intensities. ([**SucValGlyAzo**] = 1.7 mM, in 0.1 M Tris buffer, pH 7.4 at 25 ºC).

5.3 Conclusions

Summarizing, **SucValGlyAzo** shows photocontrolled reversible self-assembly into nanotubes of monodisperse diameter in aqueous media at physiological pH values. It should be highlighted that **SucValGlyAzo** is a small, synthetically simple molecule. This represents a considerable advantage for envisaged practical applications. Additionally, the reported self-assembly into nanotubes comes from a dipeptide that does not contain a phenylalanine unit. Instead, it seems that the azobenzene unit imparts the required hydrophobic and presumably aromatic stacking interactions for the self-assembly. The blue-shift

and broadening observed in the absorption spectrum of the aggregates would support such interactions.

Overall, the reported photocontrolled nanotube formation in water is unprecedented and could constitute a relevant tool for developing smart systems with biomedical applications. For example, UV light-mediated drug delivery can be applied to organs that can be directly illuminated, such as the skin, or to targets that can be reached by endoscopic techniques.[51] Also, this type of system could be used as an actuator to convert light to mechanical work.[52]

Acknowledgements

The authors acknowledge the financial support from the Spanish Ministry of Science and Innovation co-funded by the European Regional Development Fund of the European Union (grants RTI2018-101675-B-I00), Generalitat Valenciana (grant AICO/2020/322) and Universitat Jaume I (grant UJI-B2018-30).

References

(1) Fang, Z.; Shen, Y.; Gao, D. Stimulus-Responsive Nanocarriers for Targeted Drug Delivery. *New J. Chem.* **2021**, *45* (10), 4534–4544. https://doi.org/10.1039/D0NJ05169A.

(2) Mamuti, M.; Zheng, R.; An, H.-W.; Wang, H. In Vivo Self-Assembled Nanomedicine. *Nano Today* **2021**, *36*, 101036. https://doi.org/10.1016/j.nantod.2020.101036.

(3) Zhu, P.; Chen, R.; Zhou, C.; Aizenberg, M.; Aizenberg, J.; Wang, L. Bioinspired Soft Microactuators. *Adv. Mater.* **2021**, *33* (21), 2008558. https://doi.org/10.1002/adma.202008558.

(4) Xiong, Q.; Lim, Y.; Li, D.; Pu, K.; Liang, L.; Duan, H. Photoactive Nanocarriers for Controlled Delivery. *Adv. Funct. Mater.* **2020**, *30* (2), 1903896.

https://doi.org/10.1002/adfm.201903896.

(5) Tao, Y.; Chan, H. F.; Shi, B.; Li, M.; Leong, K. W. Light: A Magical Tool for Controlled Drug Delivery. *Adv. Funct. Mater.* **2020**, *30* (49), 2005029. https://doi.org/https://doi.org/10.1002/adfm.202005029.

(6) Luk, Y. Y.; Abbott, N. L. Applications of Functional Surfactants. *Curr. Opin. Colloid Interface Sci.* **2002**, *7*, 267–275. https://doi.org/10.1016/S1359-0294(02)00067-5.

(7) Chen, S.; Costil, R.; Leung, F. K. C.; Feringa, B. L. Self-Assembly of Photoresponsive Molecular Amphiphiles in Aqueous Media. *Angew. Chemie - Int. Ed.* **2021**, *60* (21), 11604–11627. https://doi.org/10.1002/anie.202007693.

(8) Hirose, T.; Matsuda, K.; Irie, M. Self-Assembly of Photochromic Diarylethenes with Amphiphilic Side Chains: Reversible Thermal and Photochemical Control. *J. Org. Chem.* **2006**, *71* (20), 7499–7508. https://doi.org/10.1021/jo060505t.

(9) Sakata, T.; Yan, Y.; Marriott, G. Optical Switching of Dipolar Interactions on Proteins. *Proc. Natl. Acad. Sci. U. S. A.* **2005**, *102* (13), 4759–4764. https://doi.org/10.1073/pnas.0405265102.

(10) Wang, X. R.; Li, M. P.; Xu, W. R.; Kuck, D. Photo and PH Dual-Responsive Supramolecular Vesicles Based on a Water-Soluble Tribenzotriquinacene and an Azobenzene-Containing Amphiphile in Water. *Asian J. Org. Chem.* **2021**, *10* (3), 567–570. https://doi.org/10.1002/ajoc.202000683.

(11) Cheng, Q.; Duan, H.; Hao, A.; Xing, P. Photoregulated "Breathing" Vesicle with Inversed Supramolecular Chirality. *ACS Appl. Mater. Interfaces* **2021**, *13* (1), 2091–2099. https://doi.org/10.1021/acsami.0c20211.

(12) Beharry, A. A.; Woolley, G. A. Azobenzene Photoswitches for Biomolecules. *Chem. Soc. Rev.* **2011**, *40* (8), 4422–4437. https://doi.org/10.1039/c1cs15023e.

(13) Xie, X.; Wang, L.; Liu, X.; Du, Z.; Li, Y.; Li, B.; Wu, L.; Li, W. Light-Powered and Transient Peptide Two-Dimensional Assembly Driven by Trans-to-Cis Isomerization of Azobenzene Side Chains. *Chem. Commun.* **2020**, *56* (12), 1867–1870. https://doi.org/10.1039/C9CC09448B.

(14) Yagai, S.; Karatsu, T.; Kitamura, A. Photocontrollable Self-Assembly. *Chem. - A Eur. J.* **2005**, *11* (14), 4054–4063. https://doi.org/10.1002/chem.200401323.

(15) Nan, Y. Q.; Liu, J. X.; Zhang, S. S.; Chen, D. J.; Ye, Q. X.; Yuan, C.; Hao, L. S. Photo-Responsive Wormlike Micellar Systems Based on Mixed Cationic/Anionic Surfactants and Mixed Photo-Sensitive Additives. *Colloids Surfaces A Physicochem. Eng. Asp.* **2020**, *601*, 124988. https://doi.org/10.1016/j.colsurfa.2020.124988.

(16) Nam, S. H.; Choi, Y. J.; Kim, Y. W.; Jun, K.; Jeong, N. H.; Oh, S. G.; Kang, H. C. Syntheses and Characterization of New Photoresponsive Surfactants, N-(Azobenzene-4-Oxy-2-Hydroxypropyl)-N-(Alkyloxy-2-Hydroxypropyl) Aminopropyl Sulfonic Acid Sodium Salt. *J. Ind. Eng. Chem.* **2020**, *90*, 203–213. https://doi.org/10.1016/j.jiec.2020.07.013.

(17) Kang, H. C.; Lee, B. M.; Yoon, J.; Yoon, M. Synthesis and Surface-Active Properties of

New Photosensitive Surfactants Containing the Azobenzene Group. *J. Colloid Interface Sci.* **2000**, *231* (2), 255–264. https://doi.org/10.1006/jcis.2000.7158.

(18) Sakai, H.; Matsumura, A.; Yokoyama, S.; Saji, T.; Abe, M. Photochemical Switching of Vesicle Formation Using an Azobenzene-Modified Surfactant. *J. Phys. Chem. B* **1999**, *103* (49), 10737–10740. https://doi.org/10.1021/jp9927505.

(19) Wang, Y.; Han, P.; Xu, H.; Wang, Z.; Zhang, X.; Kabanov, A. V. Photocontrolled Self-Assembly and Disassembly of Block Ionomer Complex Vesicles: A Facile Approach toward Supramolecular Polymer Nanocontainers. *Langmuir* **2010**, *26* (2), 709–715. https://doi.org/10.1021/la9023844.

(20) Kwangmettatam, S.; Kudernac, T. Light-Fuelled Reversible Expansion of Spiropyran-Based Vesicles in Water. *Chem. Commun.* **2018**, *54* (42), 5311–5314. https://doi.org/10.1039/c8cc01780h.

(21) Zhang, C.-C.; Li, S.-H.; Zhang, C.-F.; Liu, Y. Size Switchable Supramolecular Nanoparticle Based on Azobenzene Derivative within Anionic Pillar[5]Arene. *Sci. Rep.* **2016**, *6* (1), 37014. https://doi.org/10.1038/srep37014.

(22) Muraoka, T.; Koh, C. Y.; Cui, H.; Stupp, S. I. Light-Triggered Bioactivity in Three Dimensions. *Angew. Chemie - Int. Ed.* **2009**, *48* (32), 5946–5949. https://doi.org/10.1002/anie.200901524.

(23) Tamesue, S.; Takashima, Y.; Yamaguchi, H.; Shinkai, S.; Harada, A. Photoswitchable Supramolecular Hydrogels Formed by Cyclodextrins and Azobenzene Polymers. *Angew. Chemie - Int. Ed.* **2010**, *49* (41), 7461–7464. https://doi.org/10.1002/anie.201003567.

(24) Sun, H.-L.; Chen, Y.; Zhao, J.; Liu, Y. Photocontrolled Reversible Conversion of Nanotube and Nanoparticle Mediated by β-Cyclodextrin Dimers. *Angew. Chemie Int. Ed.* **2015**, *54* (32), 9376–9380. https://doi.org/10.1002/ANIE.201503614.

(25) Szymański, W.; Beierle, J. M.; Kistemaker, H. A. V.; Velema, W. A.; Feringa, B. L. Reversible Photocontrol of Biological Systems by the Incorporation of Molecular Photoswitches. *Chem. Rev.* **2013**, *113* (8), 6114–6178. https://doi.org/10.1021/cr300179f.

(26) Song, X.; Perlstein, J.; Whitten, D. G. Supramolecular Aggregates of Azobenzene Phospholipids and Related Compounds in Bilayer Assemblies and Other Microheterogeneous Media: Structure, Properties, and Photoreactivity. *J. Am. Chem. Soc.* **1997**, *119* (39), 9144–9159. https://doi.org/10.1021/ja971291n.

(27) Li, F.-Q.; Yu, Q.-L.; Liu, Y.-H.; Yu, H.-J.; Chen, Y.; Liu, Y. Highly Efficient Photocontrolled Targeted Delivery of SiRNA by a Cyclodextrin-Based Supramolecular Nanoassembly. *Chem. Commun.* **2020**, *56* (27), 3907–3910. https://doi.org/10.1039/D0CC00629G.

(28) Scanlon, S.; Aggeli, A. Self-Assembling Peptide Nanotubes. *Nano Today* **2008**, *3* (3–4), 22–30. https://doi.org/10.1016/S1748-0132(08)70041-0.

(29) Valéry, C.; Artzner, F.; Paternostre, M. Peptide Nanotubes: Molecular Organisations, Self-Assembly Mechanisms and Applications. *Soft Matter* **2011**, *7* (20), 9583–9594.

https://doi.org/10.1039/c1sm05698k.

(30) Hamley, I. W. Peptide Nanotubes. *Angew. Chemie - Int. Ed.* **2014**, *53* (27), 6866–6881. https://doi.org/10.1002/anie.201310006.

(31) Rodríguez-Vázquez, N.; Amorín, M.; Granja, J. R. Recent Advances in Controlling the Internal and External Properties of Self-Assembling Cyclic Peptide Nanotubes and Dimers. *Org. Biomol. Chem.* **2017**, *15* (21), 4490–4505. https://doi.org/10.1039/c7ob00351j.

(32) Yan, X.; Zhu, P.; Li, J. Self-Assembly and Application of Diphenylalanine-Based Nanostructures. *Chem. Soc. Rev.* **2010**, *39* (6), 1877–1890. https://doi.org/10.1039/b915765b.

(33) Gazit, E. Self-Assembled Peptide Nanostructures: The Design of Molecular Building Blocks and Their Technological Utilization. *Chem. Soc. Rev.* **2007**, *36*, 1263–1269. https://doi.org/10.1039/b605536m.

(34) Habibi, N.; Kamaly, N.; Memic, A.; Shafiee, H. Self-Assembled Peptide-Based Nanostructures: Smart Nanomaterials toward Targeted Drug Delivery. *Nano Today* **2016**, *11* (1), 41–60. https://doi.org/10.1016/j.nantod.2016.02.004.

(35) Porter, S. L.; Coulter, S. M.; Pentlavalli, S.; Laverty, G. Pharmaceutical Formulation and Characterization of Dipeptide Nanotubes for Drug Delivery Applications. *Macromol. Biosci.* **2020**, *20* (7), 2000115. https://doi.org/10.1002/mabi.202000115.

(36) Johny, M.; Vijayalakshmi, K.; Das, A.; Roy, P.; Mishra, A.; Dasgupta, J. Modulating the Phe-Phe Dipeptide Aggregation Landscape via Covalent Attachment of an Azobenzene Photoswitch †. *Chem. Commun* **2017**, *53*, 9348. https://doi.org/10.1039/c7cc04106c.

(37) Deeg, A. A.; Schrader, T. E.; Kempter, S.; Pfizer, J.; Moroder, L.; Zinth, W. Light-Triggered Aggregation and Disassembly of Amyloid-like Structures. *ChemPhysChem* **2011**, *12* (3), 559–562. https://doi.org/10.1002/cphc.201001012.

(38) Lin, Y.; Qiao, Y.; Tang, P.; Li, Z.; Huang, J. Controllable Self-Assembled Laminated Nanoribbons from Dipeptide-Amphiphile Bearing Azobenzene Moiety. *Soft Matter* **2011**, *7* (6), 2762–2769. https://doi.org/10.1039/c0sm01050b.

(39) Fontanillo, M.; Angulo-Pachón, C. A.; Escuder, B.; Miravet, J. F. In Situ Synthesis-Gelation at Room Temperature vs. Heating-Cooling Procedure. Fine Tuning of Molecular Gels Derived from Succinic Acid and L-Valine. *J. Colloid Interface Sci.* **2013**, *412*, 65–71. https://doi.org/10.1016/j.jcis.2013.08.055.

(40) Angulo-Pachón, C. A.; Miravet, J. F. Sucrose-Fueled, Energy Dissipative, Transient Formation of Molecular Hydrogels Mediated by Yeast Activity. *Chem. Commun.* **2016**, *52* (31). https://doi.org/10.1039/c6cc01183g.

(41) Navarro-Barreda, D.; Angulo-Pachón, C. A.; Bedrina, B.; Galindo, F.; Miravet, J. F. A Dual Stimuli Responsive Supramolecular Gel Provides Insulin Hydrolysis Protection and Redox-Controlled Release of Actives. *Macromol. Chem. Phys.* **2020**, *221* (4), 1900419. https://doi.org/10.1002/macp.201900419.

(42) Torres-Martínez, A.; Angulo-Pachón, C. A.; Galindo, F.; Miravet, J. F. In between Molecules and Self-Assembled Fibrillar Networks: Highly Stable Nanogel Particles from a Low Molecular Weight Hydrogelator. *Soft Matter* **2019**, *15* (17), 3565–3572. https://doi.org/10.1039/C9SM00252A.

(43) Hassan, P. A.; Rana, S.; Verma, G. Making Sense of Brownian Motion: Colloid Characterization by Dynamic Light Scattering. *Langmuir* **2015**, *31* (1), 3–12. https://doi.org/10.1021/la501789z.

(44) Liu, T.; Xiao, Z. Dynamic Light Scattering of Rigid Rods - A Universal Relationship on the Apparent Diffusion Coefficient as Revealed by Numerical Studies and Its Use for Rod Length Determination. *Macromol. Chem. Phys.* **2012**, *213* (16), 1697–1705. https://doi.org/10.1002/macp.201200154.

(45) Kang, B.; Tang, H.; Zhao, Z.; Song, S. Hofmeister Series: Insights of Ion Specificity from Amphiphilic Assembly and Interface Property. *ACS Omega* **2020**, *5* (12), 6229–6239. https://doi.org/10.1021/acsomega.0c00237.

(46) Morris, K. L.; Zibaee, S.; Chen, L.; Goedert, M.; Sikorski, P.; Serpell, L. C. The Structure of Cross-β Tapes and Tubes Formed by an Octapeptide, Aβ1. *Angew. Chemie - Int. Ed.* **2013**, *52* (8), 2279–2283. https://doi.org/10.1002/anie.201207699.

(47) Jean, B.; Oss-Ronen, L.; Terech, P.; Talmon, Y. Monodisperse Bile-Salt Nanotubes in Water: Kinetics of Formation. *Adv. Mater.* **2005**, *17* (6), 728–731. https://doi.org/10.1002/ADMA.200401125.

(48) Reches, M.; Gazit, E. Designed Aromatic Homo-Dipeptides: Formation of Ordered Nanostructures and Potential Nanotechnological Applications. *Phys. Biol.* **2006**, *3* (1), 10–19. https://doi.org/10.1088/1478-3975/3/1/S02.

(49) Robertson, J. M. 47. Crystal Structure and Configuration of the Isomeric Azobenzenes. *J. Chem. Soc.* **1939**, No. 0, 232–236. https://doi.org/10.1039/JR9390000232.

(50) Greenspan, P.; Mayer, E. P.; Fowler, S. D. Nile Red: A Selective Fluorescent Stain for Intracellular Lipid Droplets. *J. Cell Biol.* **1985**, *100* (3), 965–973. https://doi.org/10.1083/jcb.100.3.965.

(51) Barhoumi, A.; Liu, Q.; Kohane, D. S. Ultraviolet Light-Mediated Drug Delivery: Principles, Applications, and Challenges. *J. Control. Release* **2015**, *219*, 31–42. https://doi.org/10.1016/j.jconrel.2015.07.018.

(52) Halabi, J. M.; Ahmed, E.; Sofela, S.; Naumov, P. Performance of Molecular Crystals in Conversion of Light to Mechanical Work. *Proc. Natl. Acad. Sci. U. S. A.* **2021**, *118* (5), e2020604118. https://doi.org/10.1073/pnas.2020604118.

(53) Schönberger, M.; Trauner, D. A Photochromic Agonist for μ-Opioid Receptors. *Angew. Chemie - Int. Ed.* **2014**, *53* (12), 3264–3267. https://doi.org/10.1002/anie.201309633.

Appendix: Supporting Information

1. General methods

NMR spectra were recorded on an Agilent VNMR System spectrometer (500 MHz for ^{1}H-NMR, 125 MHz ^{13}C-NMR) or Bruker Avance III HD spectrometers (400 MHz and 300 MHz for ^{1}H-NMR, 101 MHz and 75 MHz for ^{13}C-NMR) in the indicated solvent at 30 °C. Mass spectra were recorded with a mass spectrometry triple quadrupole Q-TOF Premier spectrometer (Waters) with simultaneous Electrospray and APCI Probe. The ultraviolet-visible (UV-Vis) absorption spectra and the fluorescence intensity were measured with a JASCO V- 630 UV–vis spectrophotometer and a JASCO FP-8300 fluorometer, respectively. Dynamic Light Scattering (DLS) measurements were recorded using a Zetasizer Nano ZS (Malvern Instruments, UK), using 3 mL disposable poly(methyl methacrylate) cuvettes (10 mm optical path length). Analyses were carried out using a He-Ne laser (633 nm) at a fixed scattering angle of 173°. Automatic optimization of beam focusing and attenuation was applied for each sample. The results were reported as the average of three measurements. Transmission electron microscopic (TEM) images were obtained using a JEOL 2100 electron microscope with thermionic gun LaB6 100 kV equipped with a GatanOrius high-resolution CCD camera. TEM samples were prepared over carbon formvar copper grids. Cryogenic transmission electron microscopic (Cryo-TEM) images were examined using a a Gatan 626 cryo-holder (Gatan Company, California, USA) on a FEI Tecnai G2 Spirit BioTwin (ThermoFisher Scientific company, Oregon, USA). The images were recorded digitally with a Xarosa camera (EMSIS GmbH, Münster, Germany) under low-dose conditions. Samples were irradiated with UV and visible light using three 365 nm UV LEDs (1200 mW flux output at 2.7 W power dissipation, LZ1- 00UV00) and three 457 nm Blue LEDs (50 lumen nominal flux

at 3.3W power dissipation, LZ1-00B202), respectively. LEDs were placed at 8 cm from the cuvette. Ultrasonication was carried out in a Elmasonic S 60 H device.

2. Preparation of the nanotubes

In a representative example, 2.0 mg (0.0044 mmol) of **SucValGlyAzo** in 1.0 mL of Tris buffer (0.1 M, pH 7.4) were sonicated (37 kHz, Elmasonic S 60 H, 220-240 V) for 25 minutes at room temperature. Subsequently, 1.66 mL of additional buffer was added (final concentration of **SucValGlyAzo** = 1.7 mM) and the mixture was sonicated again for 25 minutes at room temperature. Finally, the resulting mixture was filtered through a 0.45 μm nylon filter membrane to afford a monomodal size distribution.

3. UV-Vis spectroscopic studies

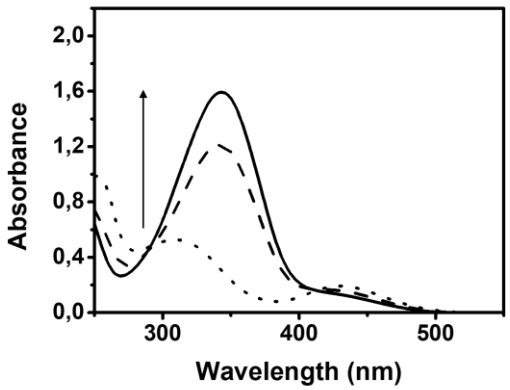

Figure S5.1. Absorption spectra of **SucValGlyAzo** (1.3 mM, 0.1 M Tris buffer, pH 7.4, 25 ºC) obtained in the study of the thermal *cis-trans* conversion at 25 ºC. Dotted line: irradiation for 30 seconds with 365 nm light. Dashed line: 60 minutes of thermal equilibration at 25 ºC. Solid line: 120 minutes of thermal equilibration.

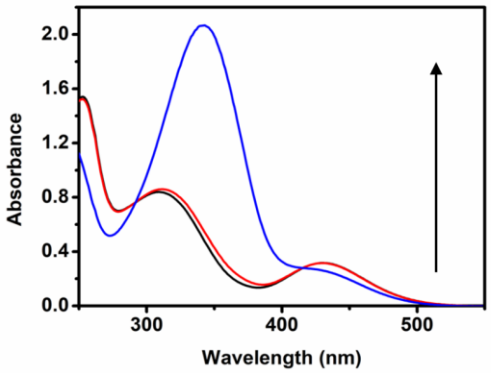

Figure S5.2. Absorption spectra of **SucValGlyAzo** (1.7 mM, 0.1 M Tris buffer, pH 7.4, 25 ºC) obtained in the study of the Vis light promoted *cis-trans* conversion at 25 ºC. Black line: irradiation of the initial sample for 30 seconds with 365 nm light. Red line: After resting in the dark for 10 minutes. Blue line: After irradiation for 30 seconds with 457 nm light.

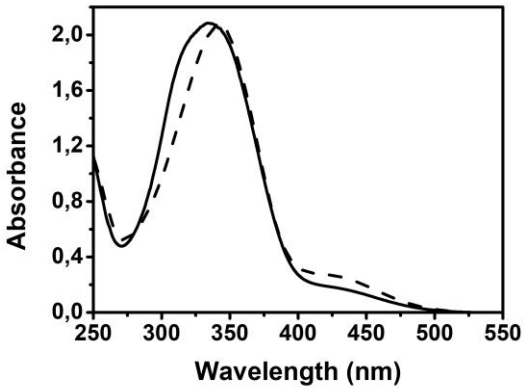

Figure S5.3. Absorption spectra of **SucValGlyAzo** (1.7 mM, 0.1 M Tris buffer, pH 7.4, 25 ºC) obtained before irradiation with UV light (solid line) and after *trans-cis-trans* conversion process triggered by successive irradiation for 30 seconds with 365 UV-light and 457 nm Vis-light (dashed line).

4. DLS studies

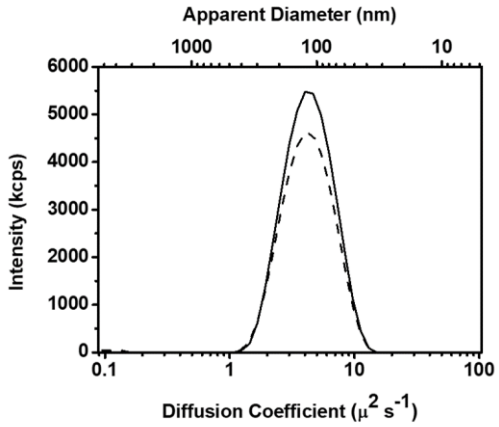

Figure S5.4. Diffusion coefficient and apparent particle diameter distribution obtained by DLS for **SucValGlyAzo** (1.7 mM, 0.1 M Tris buffer, pH 7.4, 25 ºC). Solid line: fresh sample. Dashed line: Sample stored for 16 h at 4 ºC.

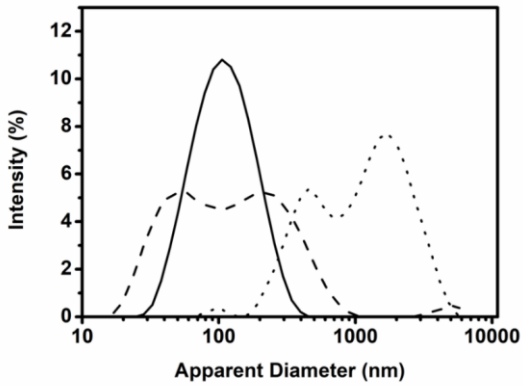

Figure S5.5. Apparent diameter distribution obtained by DLS for **SucValGlyAzo** in different aqueous buffers (1.7 mM, 0.1 M buffer, pH 7.4, 25 ºC). Dotted line: phosphate buffer; dashed line: HEPES; solid line: Tris. The apparent hydrodynamic diameters given are collected after filtration (0.45 μm mesh filter).

5. Electronic microscopy (TEM) studies

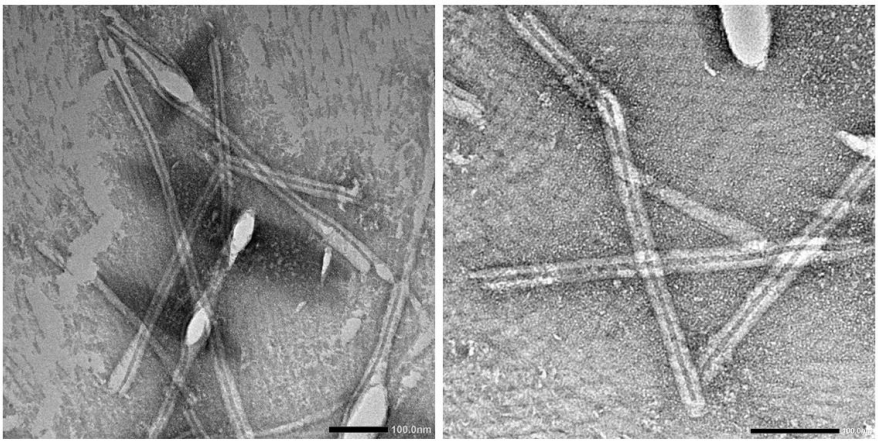

Figure S5.6. TEM images of the nanotubes formed by **SucValGlyAzo** collected before filtration (1.7 mM, 0.1 M Tris buffer, pH 7.4; uranyl acetate was used as a staining agent). Scale bars: 100 nm.

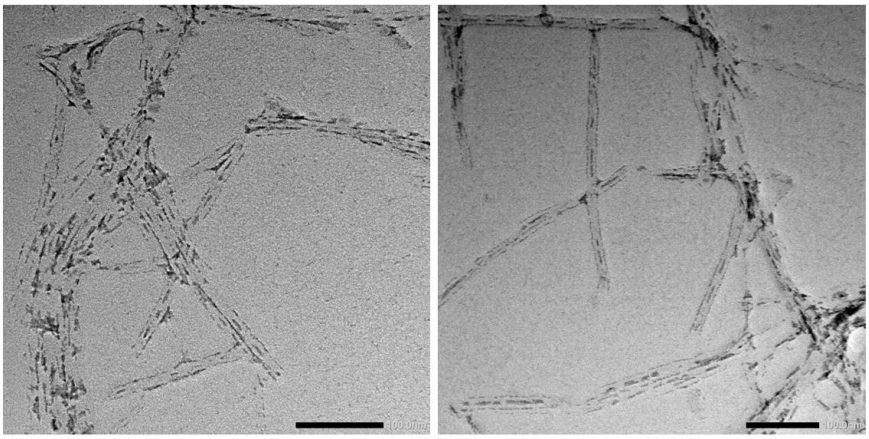

Figure S5.7. TEM images of the nanotubes formed by **SucValGlyAzo** collected after UV light (1.7 mM, 0.1 M Tris buffer, pH 7.4; uranyl acetate was used as a staining agent). Scale bars: 100 nm.

6. Fluorescence studies – Nile red dye

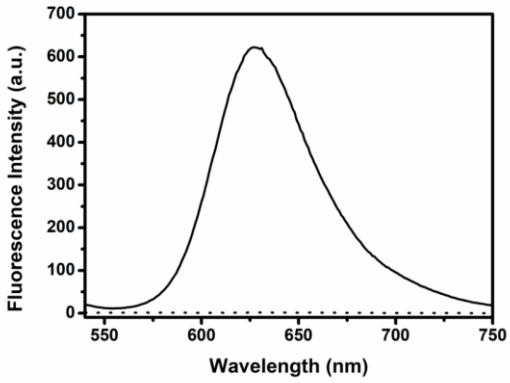

Figure S5.8. Fluorescence emission spectra of Nile red (10 μM) in the presence (solid line) and absence (dotted line) of **SucValGlyAzo** nanotubes (1.7 mM, 0.1 M Tris buffer, pH 7.4, 25 ºC).

7. Synthesis of SucValGlyAzo

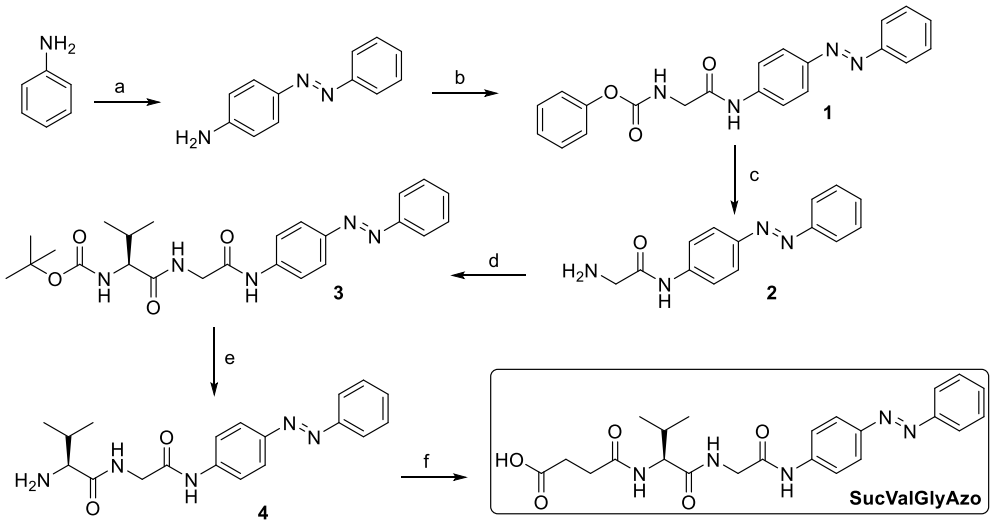

Scheme S5.1. Synthesis of **SucValGlyAzo**. Reagents: a) $NaNO_3$, HCl, NH_3, H_2O; b) *N*-carbobenzyloxyglycine, $(CO)_2Cl_2$, Et_3N; c) HBr 33 wt.% in acetic acid; d) BocValOH, DIPEA, EDCI, ethyl (hydroxyimino)cyanoacetate; e) TFA; f) Succinic anhydride, Na_2CO_3.

A. Synthesis of 4-aminoazobenzene

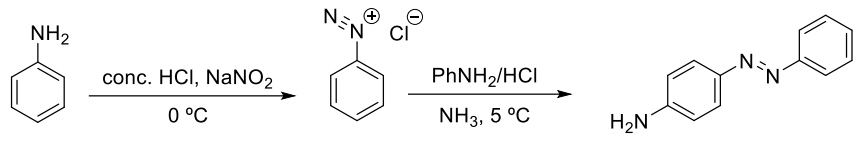

Aniline (0.92 g, 10 mmol) was added dropwise to a solution of concentrated hydrochloric acid (HCl 37%, 3 mL) in deionized water (30 mL) at 0 °C. Then, a sodium nitrite solution (0.70 g, 10.1 mmol) in water (5 mL) was added slowly for 10 min. The mixture was stirred at 0 °C for 60 min to further a yellow transparent diazonium salt solution. Aniline (0.93 g, 10.1 mmol) and 1 M HCl (10 mL) was dissolved in water (30 mL) under vigorous stirring at 0 °C. Then, to this resulting mixture, the diazonium salt solution previously obtained was added dropwise at 0 °C. The system was kept being stirred at 5°C for 3 h. Once, 1 M NH_3 (30 mL) was added slowly, precipitating an orange solid. The precipitate was filtered off and washed with sodium hydrogen carbonate solution (pH≈8). The precipitate was collected by filtration, washed with deionized water three times, and dried under vacuum, yielding the product as an orange crystalline solid. Yield 72%; **^{1}H-NMR** and **^{13}C-NMR** spectra were consistent with those described in the literature;[53] **HRMS (ESI-TOF) m/z**: $[M+H]^+$ calcd for $C_{12}H_{11}N_3$ 198.1031; found, 198.1034.

B. Synthesis of benzyl (E)-(2-oxo-2-((4-(phenyldiazenyl) phenyl)amino)-ethyl) carbamate - (1)

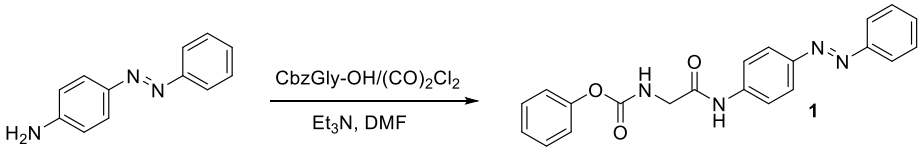

Commercially available *N*-carbobenzyloxyglycine (2.34 g, 11 mmol, 1.08 eq) was dissolved in anhydrous dichloromethane (37 mL) in a two-neck flask. Then, oxalyl chloride (5.6 mL; 11.2 mmol, 1.098 eq) and DMF (90 µL, 8.0 µL/mmol oxalyl chloride) were added dropwise. The mixture was stirred at 0 °C for 2 hours under N_2 atmosphere. After that, 4-aminoazobenzene (2.0 g, 10.2 mmol, 1 eq) in anhydrous dichloromethane (100 mL) was added dropwise at room temperature. Then, triethylamine (1.64 mL, 11 mmol, 1.08 eq) was added and the mixture reaction was stirred overnight under N_2 atmosphere. Then, the solvent was removed under reduced pressure, yielding a dark red slurry. The crude was washed with 1 M HCl (200 mL), 0.1 M NaOH (200 mL) and finally, with destilled water until neutral pH. The product was dried in vacuum at 30 °C for 24 h. The compound **1** was obtained as an orange solid (yield 83%); **^{1}H-NMR (500 MHz, DMSO-*d*$_6$, *δ*)**: 10.29 (s, 1H), 7.93-7.80 (m, 4H), 7.63 – 7.47 (m, 6H), 7.46 – 7.21 (m, 5H), 5.07 (s, 2H), 3.88 (d, J = 5.9 Hz, 2H); **^{13}C-NMR (101 MHz, DMSO-*d*$_6$, *δ*)**: 168.5, 156.6, 152.0, 147.5, 142.0, 137.0, 131.0, 129.4, 128.3, 127.8, 127.7, 123.7, 122.3, 119.3, 65.5, 44.2; **HRMS (ESI-TOF) m/z**: $[M+H]^+$ calcd for $C_{22}H_{20}N_4O_3$ 389.1613; found, 389.1614.

C. Synthesis of (E)-2-amino-N-(4-(phenyldiazenyl)phenyl)acetamide - (2)

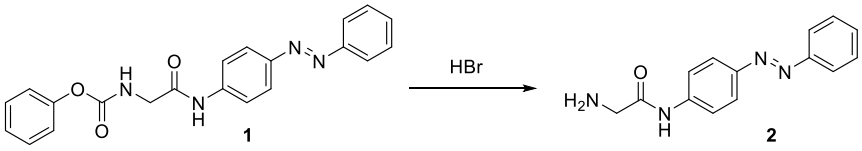

Hydrogen bromide solution, 33 wt.% in acetic acid (27.4 mL, 3.3 mL/ mmol Cbz), was added to **1** (3.22 g, 8.29 mmol). The reaction was stirred under N_2 atmosphere at 0 °C for 30 minutes. After that, the mixture reaction was further stirred at room temperature overnight. Diethyl ether was added dropwise until

the formation of a red precipitate. The reddish solid obtained was filtered off under vacuum, and the residue was dissolved in water (100 mL). The resulting solution was basified with solid sodium hydroxide at 0 °C and the precipitate filtered off and washed with water (300 mL) twice. The compound **2** was dried under reduced pressure at 50 °C overnight. The crude, as orange solid, was used for the next step without further purification. **^{1}H-NMR (300 MHz, DMSO-d_6, δ)**: 9.98 (s, 1H), 7.95 – 7.81 (m, 4H), 7.64 – 7.53 (m, 3H), 7.46 – 7.18 (m, 4H), 3.78 (d, *J* = 9.2 Hz, 2H); **^{13}C-NMR (101 MHz, DMSO-d_6, δ)**: 172.5, 152.0, 147.5, 141.9, 131.0, 129.4, 123.7, 122.3, 119.2, 45.6.

D. Synthesis of Tert-butyl (S,E)-(3-methyl-1-oxo-1-((2-oxo-2-((4-(phenyldiazenyl)phenyl)-amino)ethyl)amino) butan-2-yl) carbamate - (3)

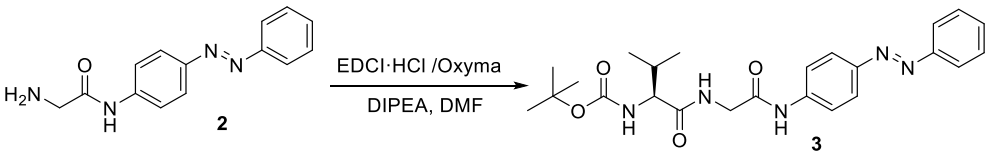

Amine **2** (1.45 g, 5.70 mmol, 1 eq.), DIPEA (1.19 mL, 6.84 mmol, 1.2 eq.) and comercially available *N*-(*tert*-butoxycarbonyl)-L-valine (1.24 g, 5.70 mmol, 1 eq.) were dissolved in anhydrous DMF (150 mL) at room temperature. Then, 1-Ethyl-3-(3-dimethylaminopropyl)carbodiimide hydrochloride (EDCI, 1.19 g, 6.21 mmol, 1.09 eq.) and ethyl (hydroxyimino)cyanoacetate (0.91 g, 6.21 mmol, 1.09 eq.) were added and the reaction was stirred at room temperature overnight. Once, water was added until the total precipitation of a solid occurred. The orange solid obtained was filtered under vacuum and the residue was washed with 1 M HCl (200 mL) and 0.1 M NaOH (200 mL). Finally, the solid was washed with distilled water (400 mL) until neutral pH and dried under reduced pressure at 50 °C overnight. The compound **3** was obtained as an orange-brown solid (yield 82%).

^{1}H-NMR (400 MHz, DMSO-d_6, δ, signals for the *E* isomer): 10.20 (s, 1H), 8.29 (t, J= 4.8 Hz, 1H), 7.95 – 7.80 (m, 6H), 7.64 – 7.49 (m, 3H), 3.96 (m, 1H), 3.85 (m, 2H), 1.97 (m, 1H), 1.40 (s,1H), 0.92– 0.88(dd, J= 7.6 Hz, 6.4 Hz, 3H); **^{13}C-NMR (101 MHz, DMSO-d_6, δ,** signals for the *E* isomer): 172.2, 168.3, 155.9, 152.2, 147.8, 142.0, 131.2, 129.6, 123.9, 122.5, 119.5, 78.4, 60.1, 43.0, 30.4, 28.4, 19.4, 18.39; **HRMS (ESI-TOF) m/z**: $[M+H]^+$ calcd for $C_{24}H_{31}N_5O_4$ 454.2454; found, 454.2447.

E. Synthesis of (S,E)-2-amino-3-methyl-N-(2-oxo-2-((4-(phenyldiazenyl)-phenyl)amino)-ethyl)butanamide - (4)

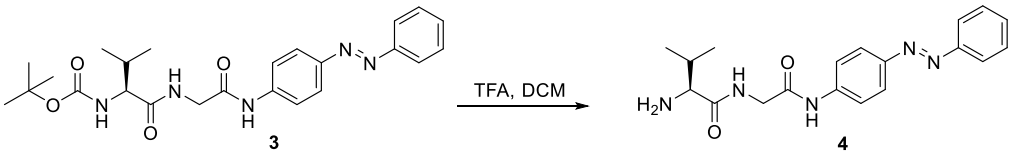

To a solution of **3** (1.83 g, 4.04 mmol, 1 eq.) in dichloromethane (40 mL), trifluoroacetic acid (8.1 mL, 2 mL/mmol Boc) were added dropwise and stirred at room temperature under N_2 atmosphere overnight. Then, solvent was removed under reduced pressure and the residue (dark oil liquid) was dissolved with 0.2 M NaOH (200 mL) and extracted three times with chloroform (200 mL). The organic phase was concentrated until dryness. The compound **4** was obtained as an orange solid (yield 90%); **^{1}H-NMR (500 MHz, DMSO-d_6, δ,** signals for the *E* isomer): 10.33 (s, 1H), 8.24 (s, 1H), 7.92 – 7.78 (m, 6H), 7.60 – 7.48 (m, 3H) 3.97 (m, 2H), 3.06 (d, *J*= 5.0 Hz, 1H), 1.97 (m, 1H), 0.93 (d, *J*= 7.0 Hz, 6H); **^{13}C-NMR (126 MHz DMSO-d_6, δ,** signals for the *E* isomer): 175.1, 168.3, 152.5, 147.6, 142.0, 131.0, 129.4, 123.7, 122.3, 119.2, 59.9, 42.7, 31.4, 19.6; **HRMS (ESI-TOF) m/z**: $[M+H]^+$ calcd for $C_{19}H_{23}N_5O_2$ 354.1930; found, 354.1926.

F. Synthesis of (S,E)-4-((3-methyl-1-oxo-1-((2-oxo-2-((4-(phenyldiazenyl)-phenyl) amino)ethyl) amino)butan-2-yl)amino)-4-oxobutanoic acid – (SucValGlyAzo)

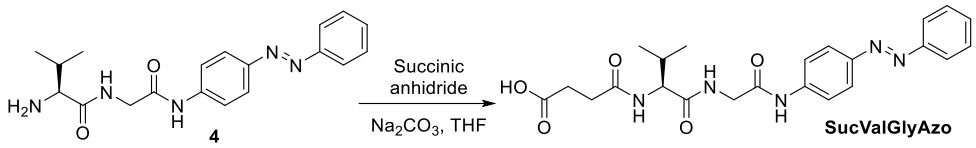

A solution of **4** (1.42 g, 4.04 mmol, 1 eq.) in THF (120 mL) was treated with solid Na_2CO_3 (1.50 g,14.14 mmol, 3.5 eq.) at room temperature under N_2 atmosphere. Succinic anhydride (808 mg, 8.08 mmol, 2 eq.) dissolved in THF (60 mL) was added dropwise at room temperature. The resulting mixture was stirred overnight. Then, the solution was concentrated under reduced pressure and the crude residue was dissolved in water (100 mL). After that, hydrochloric acid (concentrated grade) was added dropwise at 0 °C until complete precipitation occurred. The solid obtained was filtered off under vacuum, and the residue was washed with water (300 mL) until neutral pH. The compound was dried under reduced pressure at 50 °C overnight. The compound **SucValGlyAzo** was obtained as an orange brown solid (yield 85%); **^{1}H-NMR (400 MHz, DMSO-*d*$_6$, *δ*,** signals for the *E* isomer): 12.07 (s, 1H), 10.11 (s, 1H), 8.36 (s, 1H), 8.02 (d, J= 7.2 Hz, 1H), 7.95 – 7.82 (m, 6H) , 7.62 – 7.53 (m, 3H), 4.14 (t, J= 6.4 Hz, 1H), 3.94 (d, J= 4.4 Hz, 2H), 2.49 (s, 4H), 2.03 (m, 1H), 0.92 (d, J= 6.0 Hz, 6H). **^{13}C-NMR (101 MHz, DMSO-*d*$_6$, *δ*,** signals for the *E* isomer): 173.9, 171.8, 171.7, 168.2, 152.0, 147.6, 141.7, 131.0, 129.4, 123.7, 122.3, 119.3, 58.5, 42.8, 30.0, 29.9 , 29.2, 19.2; **HRMS (ESI-TOF) m/z**: $[M-H]^-$ calcd for $C_{23}H_{27}N_5O_5$ 452.1934; found, 452.1937.

8. NMR spectra

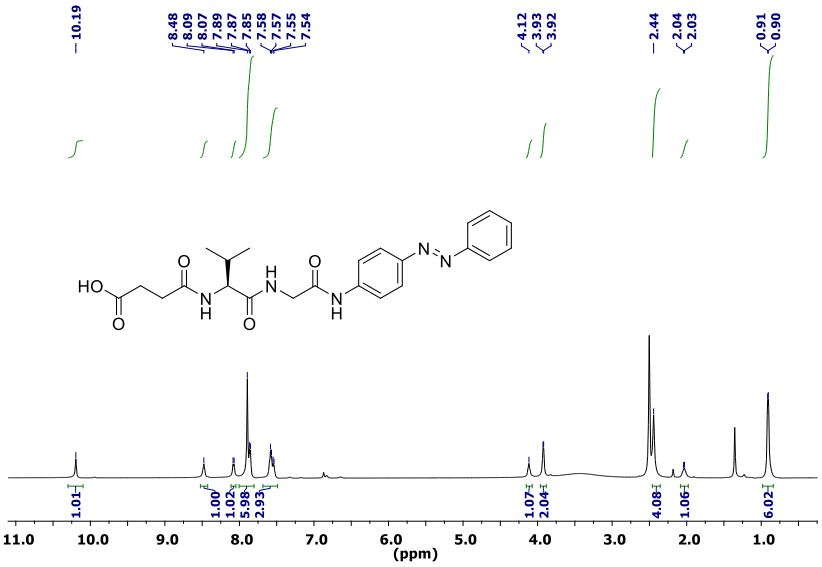

Figure S5.9. ^{1}H-NMR of **SucValGlyAzo**.

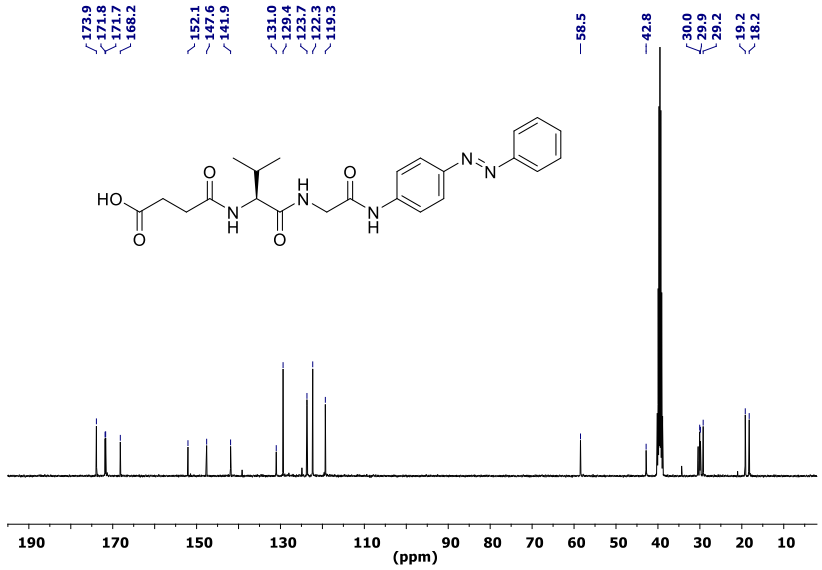

Figure S5.10. ^{13}C-NMR of **SucValGlyAzo**.

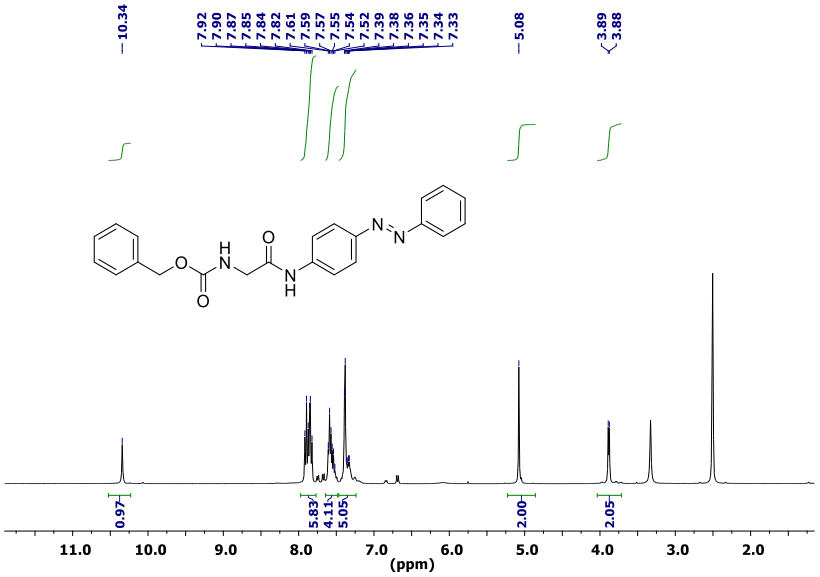

Figure S5.11. ^{1}H-NMR of **1**.

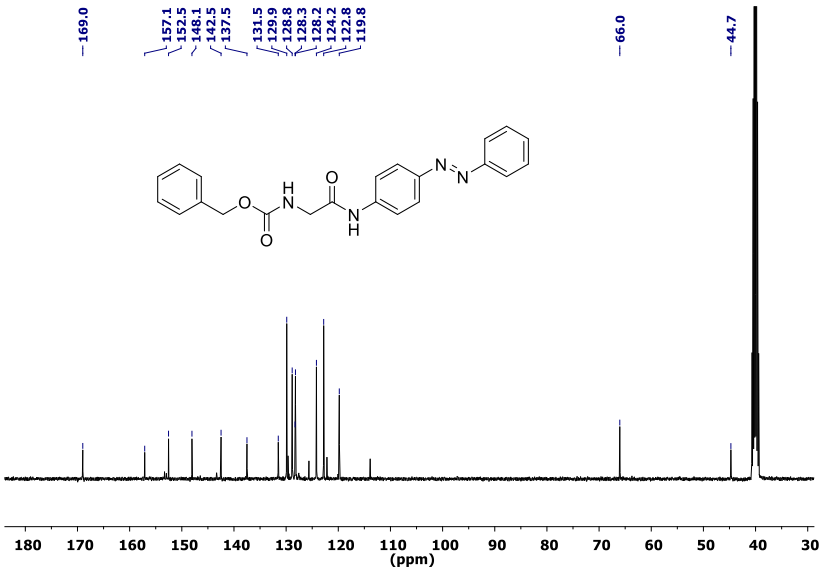

Figure S5.12. ^{13}C-NMR of **1**.

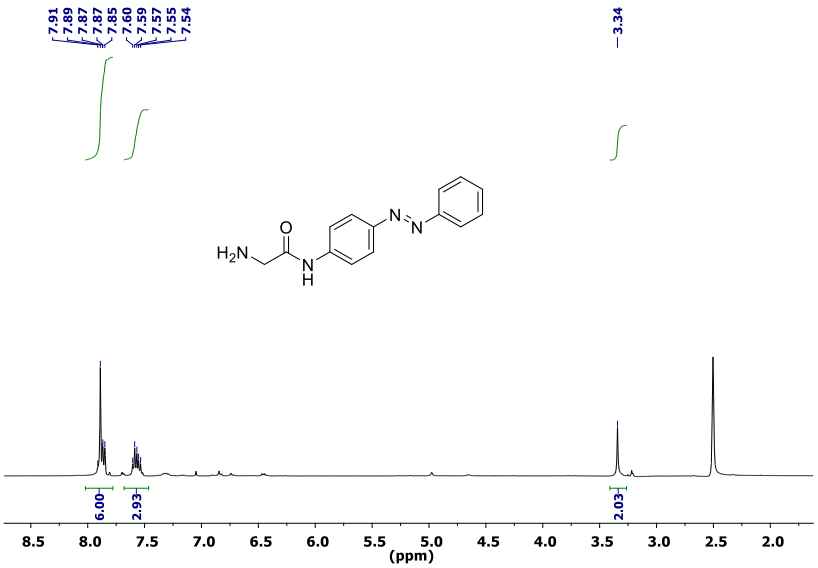

Figure S5.13. ^{1}H-NMR of **2**.

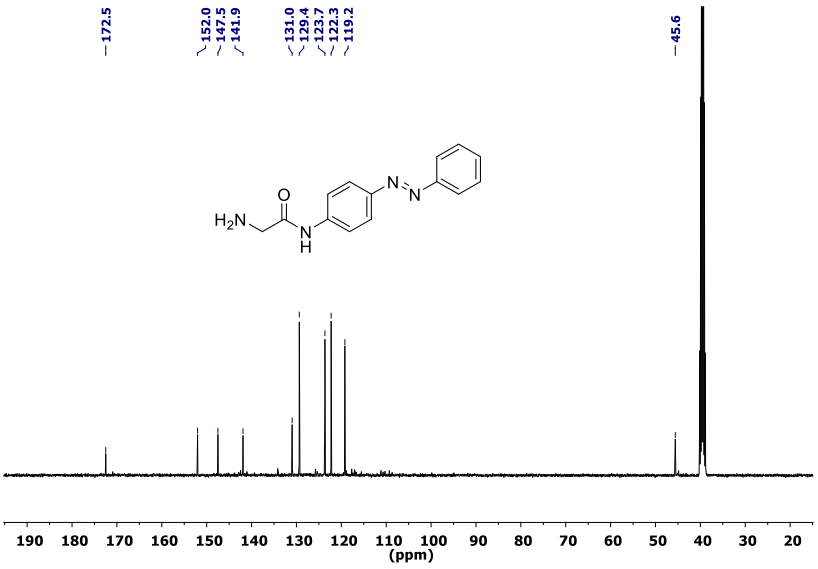

Figure S5.14. ^{13}C-NMR of **2**.

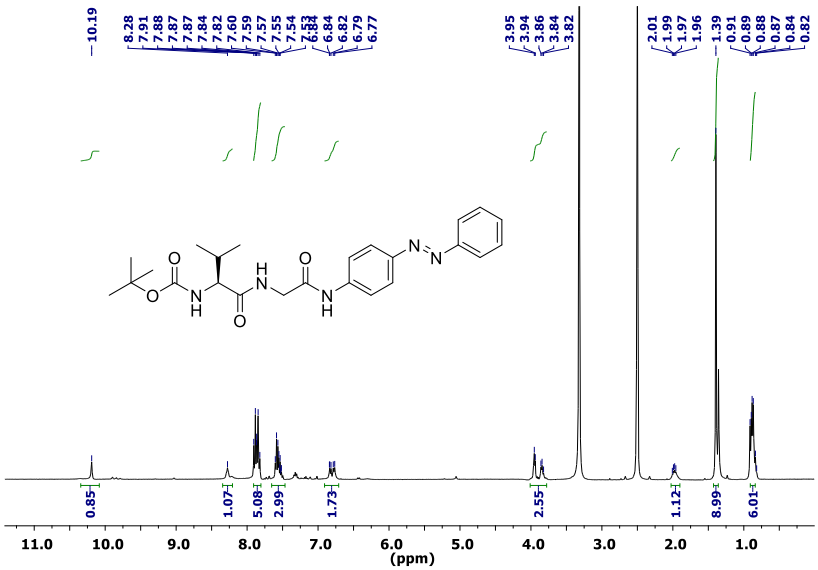

Figure S5.15. ^{1}H-NMR of **3**.

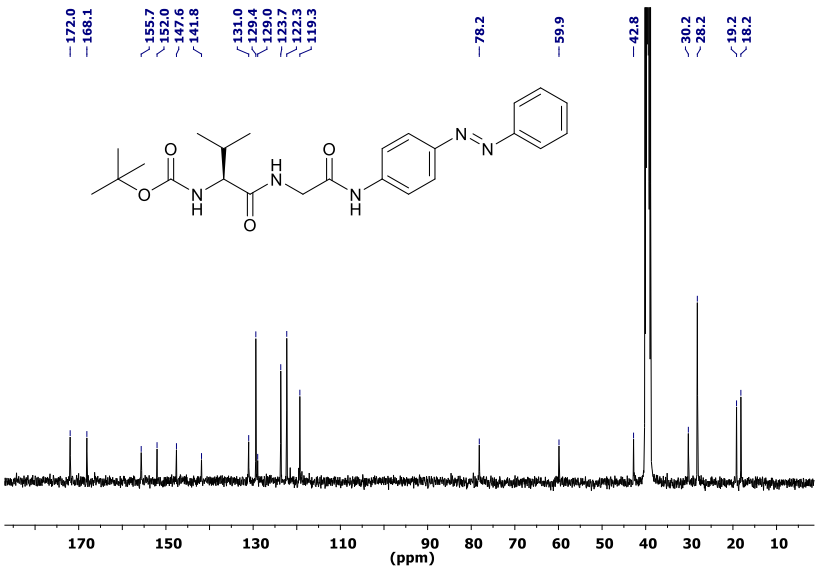

Figure S5.16. ^{13}C-NMR of **3**.

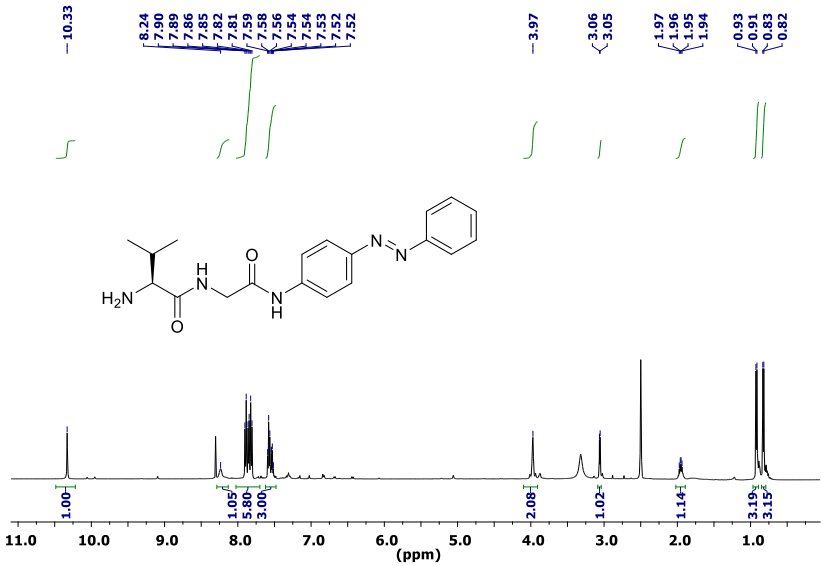

Figure S5.17. ^{1}H-NMR of **4**.

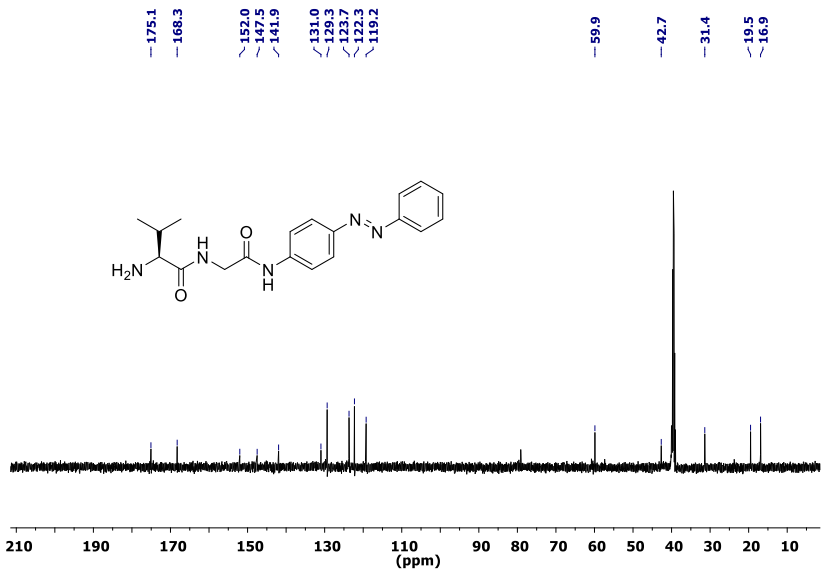

Figure S5.18. ^{13}C-NMR of **4**.

Chapter 6

Structure-performance relationships of four lysosomal markers used for the imaging of HT-29 cancer cells and a cellular model of lysosomal storage disease (Niemann-Pick C)

Structure-performance relationships of four lysosomal markers used for the imaging of HT-29 cancer cells and a cellular model of lysosomal storage disease (Niemann-Pick C)

Diego Navarro-Barreda,[a] Begoña Bedrina,[a] César A. Angulo-Pachón,[a] Juan F. Miravet,[a] Dolores Pérez-Sala,[b] Francisco Galindo[a,*]

[a]Departamento de Química Inorgánica y Orgánica, Universitat Jaume I, Avda. Sos Baynat s/n, 12071, Castelló de la Plana, Spain

[b]Departamento de Biología Estructural y Química, Centro de Investigaciones Biológicas Margarita Salas (CSIC), Ramiro de Maeztu, 9, 28040, Madrid, Spain

Accepted Date: 7th March 2022.

Abstract

Four new BODIPY derivatives with a potential tendency to aggregation have been synthesized and characterized by means of NMR techniques, mass spectrometry and UV-Vis/fluorescence spectroscopies. The objective of this study is to determine which structural factors of the new molecules influence most notably the cellular uptake, intracellular location and fluorescence imaging abilities. The behaviour of the compounds in organic solvent and aqueous solution has been studied. In organic solvents (DMSO, ethanol and toluene), the photophysical properties of the new molecules are almost independent of the building blocks used to synthesize the pendant moieties (non-fluorogenic parts). In an aqueous environment (HEPES Buffer Solution, pH 7), at 10 μM, three of the compounds (**1**, **2** and **4**) tend to form weakly emissive nanoparticles (DLS determination) whereas one of them (**3**) remains soluble and highly fluorescent. In the nanomolar range of concentration, all the compounds are aqueous soluble. The cellular internalization of the compounds (10 nM) has been studied in human colon adenocarcinoma HT-29 cells by means of flow cytometry and confocal laser scanning microscopy. All the compounds were uptaken by HT-29 cells, but notably molecule **3** (made with lysine as a building block) was the one displaying a higher loading and a more clear lysosomal location (0.88 Pearson's correlation coefficient in colocalization assays using lysosomal fluorescent probe LysoTracker DND-99). Molecule **3** also performed better than the valine derivative **1** as a lysosomal marker in a cellular model (human adrenal carcinoma SW13/cl.2 cells) of lysosomal storage disease (Niemann-Pick type C).

6.1 Introduction

Lysosomes are acidic organelles responsible for vital functions in living cells, such as degradation of waste products or defensive action against pathogenic microorganisms.[1] Inadequate functioning of these organelles is associated with common pathologies such as cancer[2] and Alzheimer's disease.[3] Consequently, the proper knowledge of their internal biochemistry is important to design drugs to treat such disorders. In a different context, the endo-lysosomal pathway constitutes the entrance door for viral pathogens like influenza virus, West Nile virus and others. Thus, antiviral drugs like chloroquine and hydroxychloroquine and other lysosomotropic drugs work increasing the pH of these organelles and hence hindering the entrance of some viral pathogens.[4] More recently, the lysosome has been the centre of the debate regarding potential therapeutic approaches to fight SARS-CoV-2.[5] In another realm, one group of specific diseases linked to lysosomes, known as lysosomal storage disorders, involves the accumulation of intracellular waste products in these organelles.[6,7] An example is the Niemann-Pick type C disease[8] which is characterized by the accumulation of cholesterol inside lysosomes.

Fluorescence probes targeting the lysosome have been the key to understanding its functions, and a vast number of molecules have been designed, synthesized and tested in living cells, allowing much of the current knowledge on this cellular structure. The variety of fluorophores used in the design of such intracellular reporters is overwhelming: xanthenes,[9,10] BODIPYs,[11–13] naphthalimides,[13,14] and others.[15–18,19–25] Recently, a series of reviews have been published dealing with probes targeted to specific organelles.[26,27] The great part of the publications described so far report the fine tuning of well-known fluorophores such as those mentioned above, introducing substituents of diverse nature, length, and

branching that affect directly their photophysical properties like absorption or emission wavelengths, fluorescence quantum yields or lifetimes, photostability, etc. Sometimes, combinations of two fluorophores give rise to interesting intramolecular phenomena such as energy or electron transfer processes. Less attention has been paid to the part of the molecule not strictly participating in the emissive event, normally having a secondary role in modulating properties such as membrane translocation ability or resistance to enzyme degradation or to photobleaching. For instance, Urano et al. studied the structure-property relationships of four BODIPY dyes, which differ only in the substitution of the peripheral aniline bearing different combinations of methyl, ethyl and hydrogen substituents at the nitrogen, finding notable differences in the performance of such probes as lysosomal imaging molecules in bovine pulmonary artery endothelial cells.[28] In another example, Rong et al. studied the lysosomal imaging capabilities of a series of bis-naphthalimide derivatives differing only in the substitution at the terminal end of the dyads (including subtle changes such as the number of methylenes in a pendant group) in HeLa cells.[14] In a more dramatic case, Zhou et al. reported two seemingly identical phosphinate xanthenic derivatives differing only in the substitution of the peripheral nitrogen atoms (methyl *vs.* fused cycloalkyl) which locate intracellularly in HeLa cells in a very different manner (lysosome *vs.* mitochondria, respectively).[18] But less attention has been paid to relationships between the tendency to aggregation and the imaging performance in the cellular milieu.

Much effort has been put to answer the question of which architectural motif is best suited for the targeting of a certain fluorophore towards a specific organelle.[29–31] However, the theoretical answers, although valuable, do not take into account apparently secondary phenomena like self-assembly into nanostructures. The present research advocates for the experimental assay of

batteries of compounds showing chemical diversity, including molecules displaying a marked tendency to aggregation.

Here we describe the synthesis and characterization of four molecules (**1 – 4, Figure 6.1**) bearing the same BODIPY emitting core but differing in the pendant chain accompanying the fluorophore. Their ability as fluorescent cell markers has been evaluated using confocal microscopy and flow cytometry as bioanalytical tools. Significant differences have been found in the uptake of the studied compounds, which reinforces the idea that the non-emissive part of the probe is as important as the fluorogenic core to achieve proper cellular internalisation and fluorescence imaging. One of the compounds (**3**), with a low tendency to form aggregates in an aqueous environment, has been especially effective for the fluorescence staining of lysosomes of a human colorectal adenocarcinoma cell line (HT-29). In addition to this cellular type, the ability of this compound for imaging has been confirmed in a pharmacological cellular model of Niemann-Pick type C disease, showing an excellent internalisation and lysosomal staining reflecting the impact of the disorder.

6.2 Results and Discussion

The structures of **1** - **4** were designed following the model of analogous architectures described by us in the past. The combination of amino acid moieties and long alkyl chains has led to compounds with marked self-assembling properties.[32–34] This study aims to determine which structural factors of the pendant chain influence most notably the cellular uptake, intracellular location and fluorescence imaging performance. The synthesis of **1** - **4**, bearing

a BODIPY fluorophore and amino acid-derived chains, was carried out following a convergent route, as illustrated in the Supporting Information (SI) appendix.

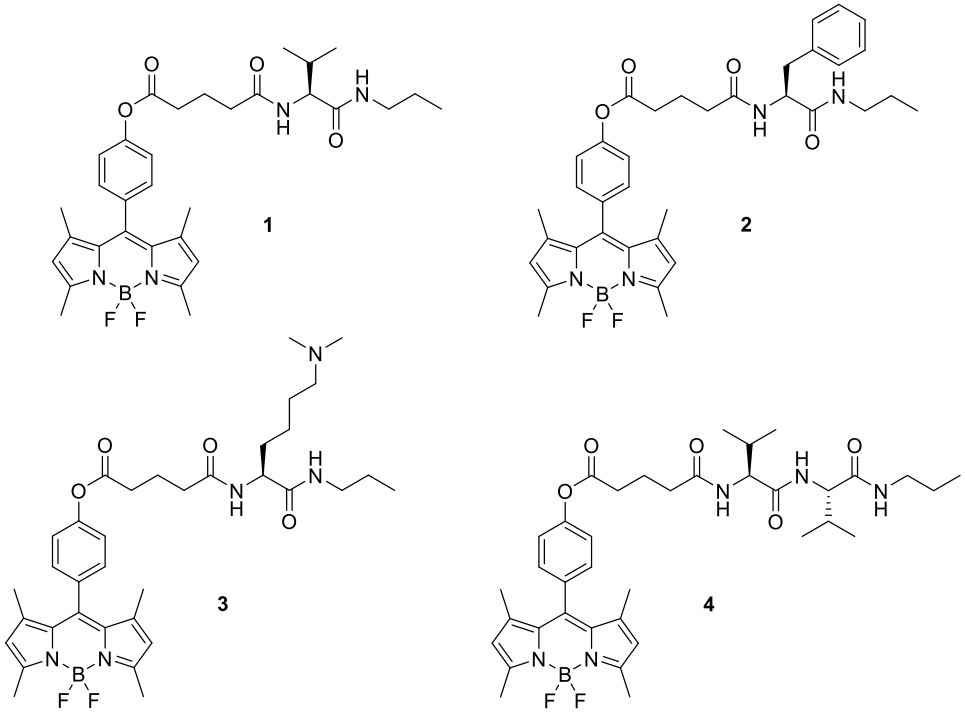

Figure 6.1. Synthetic BODIPY probes with amino acid residues **1** – **4**.

All the compounds were chemically characterized by means of mono- and bi-dimensional NMR techniques and mass spectrometry. Before the biological assays, the photophysical features of all the compounds were determined. The absorption and emission spectra of all the compounds are very similar in organic solvents such as DMSO, ethanol and toluene (**Figure 6.2A**). **Table 1** shows the complete photophysical data of all molecules, including emission quantum yields, fluorescence lifetimes and radiative (k_r) and non-radiative (k_{nr}) decay constants.

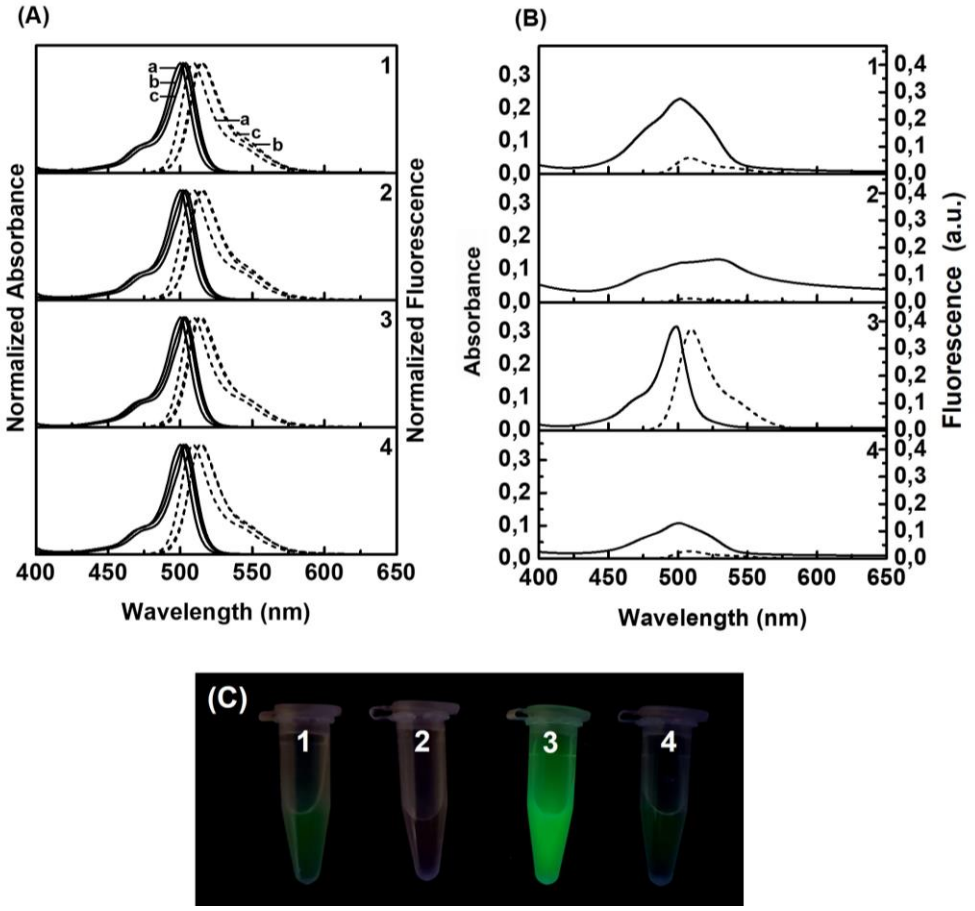

Figure 6.2. A: Normalized absorption (solid line) and emission spectra (dashed line, λ_{exc} = 475 nm) of **1 - 4** (10 μM) in (a) ethanol, (b) DMSO and (c) toluene; B: Absorption (solid line) and emission (dashed line, λ_{exc} = 475 nm) of **1** - **4** in aqueous solution (0.1 M HEPES buffer, pH 7.00); C: Photograph of aqueous solutions of **1** - **4** under UV excitation (365 nm).

The position of the absorption and emission maxima of the spectra of **1** - **4** does not change notably with solvent polarity nor depends on the pendant chain of the compound. The emission quantum yields (ϕ_F) of **1** - **4** in organic solvents lie within the range 0.50-0.63 and the monoexponential fluorescence lifetimes (τ_F) recorded are from 3.2 to 3.8 ns (Figure S6.1 and Figure S6.2).

Table 6.1. Overview of the photophysical properties of the synthesized BODIPY dyes measured in different solvents.

	Solvent	λ_{abs} (log ε) [nm]	λ_{em} [nm]	ϕ_F[a]	τ_F [ns][b]	k_r [ns^{-1}][c]	k_{nr} [ns^{-1}][c]
1	DMSO	502 (4.84)	515	ND	ND	ND	ND
	Ethanol	500 (4.86)	509	0.54	3.5	0.15	0.13
	Toluene	504 (4.89)	515	0.58	3.3	0.18	0.13
	H_2O[d]	502	509	ND	ND	ND	ND
2	DMSO	502 (4.83)	515	ND	ND	ND	ND
	Ethanol	500 (4.84)	509	0.57	3.4	0.17	0.13
	Toluene	504 (4.85)	515	0.63	3.3	0.19	0.11
	H_2O[d]	528	507	ND	ND	ND	ND
3	DMSO	502 (4.80)	513	ND	ND	ND	ND
	Ethanol	500 (4.79)	509	0.53	3.3	0.16	0.14
	Toluene	504 (4.80)	515	0.55	3.2	0.17	0.14
	H_2O[d]	498 (4.70)	510	0.50	3.8	0.13	0.13
4	DMSO	502 (4.67)	514	ND	ND	ND	ND
	Ethanol	500 (4.68)	509	0.57	3.4	0.17	0.13
	Toluene	504 (4.71)	514	0.62	3.3	0.19	0.12
	H_2O[d]	501	508	ND	ND	ND	ND

Abbreviation: ND; not determined

[a]Using fluorescein as a standard in 0.1 M NaOH solution (ϕ_F = 0.91, λ_{exc} = 470 nm)

[b]Mono-exponential fit, $I(t) = I_0 \exp(-t/\tau)$.

[c]$k_r = \phi_F/\tau_F$ and $k_{nr} = (1 - \phi_F)/\tau_F$.

[d]0.1 M HEPES buffered solution, pH 7.00 (reliable fluorescence measurements only possible for 3; 1, 2 and 4 form aggregates)

All the described values are similar to the parameters described in organic solvents for other BODIPY tagged molecules described in the literature.[35] For instance, the group of Resch-Genger has described comprehensive families of BODIPY dyes displaying values of ϕ_F in the range of 0.5-0.9 and τ_F of about 3-6 nanoseconds both in polar solvents.[36,37] Calculated radiative and non-radiative decay constants for **1 - 4** are also in the range of reported values in the literature[36,37] (k_r = 0.13-0.19 ns^{-1} and k_{nr} = 0.11-0.14 ns^{-1}), irrespective of the solvent and the chemical structure of the probe. The independency of ϕ_F and τ_F

on the architecture of the studied molecules implies that the fluorogenic structure and the rest of the molecule behave almost independently in organic solvents. A potential photoinduced electron transfer (PET) process between the dimethylamino group and the bodipy photoactive part in **3** is also absent, according to the invariant values of ϕ_F and τ_F presented by **3** in comparison to the other systems under consideration.

In contrast, in an aqueous solution (0.1 M HEPES, pH 7.00, the spectral features of **1 - 4**), at a concentration of 10 μM, depend largely on the nature of the architecture of the pendant moiety. The absorption spectra of **1**, **2** and **4** are clearly broadened, whereas that of **3** remains sharp (**Figure 6.2B**). This type of spectral feature has been described frequently for BODIPY derivatives showing aggregation.[38] Specific differences can be found between phenylalanine derivative **2** and valine derivatives **1** and **4** since the former displays an absorption band clearly red-shifted (maximum at 528 nm) relative to the positions of the bands of **1** and **4** (maxima at 502 and 501 nm, respectively). The group of Johansson has studied in detail the formation of ground state dimers of BODIPY derivatives and has suggested two types of ensembles:[39] D_I-type dimers (fluorophores stacked) with absorptions around 447 nm, hence below the maximum of the monomeric form (*ca.* 500 nm) and D_{II}-type dimers (fluorophores in the same plane) with absorptions around 580 nm. None of the dimeric forms can be observed in the case of **3**, thus it can be assumed that it remains solvated in an aqueous solution. Regarding the fluorescence properties, the dimethyllysine derivative **3** remains highly emissive in aqueous solution (neutral pH), with ϕ_F = 0.50 and τ_F = 3.8 ns, whereas the emissive properties of **1**, **2** and **4** can be hardly measured (estimated ϕ_F < 0.05). Visually, emission performance differences between the molecules described here can be seen in

Figure 6.2C. The stability of solutions of **1** - **4** (0.1 M HEPES, pH 7.00) overtime was also checked, as can be seen in Figure S6.3.

The formation of nanostructures at a concentration of 10 μM is supported by Dynamic Light Scattering (DLS) measurements (Figure S6.6). Whereas samples of **1**, **2** and **4** in 0.1 M HEPES, pH 7.00 yielded clearly signal dispersion compatible with nanoparticles of *ca.* 100 nm, molecule **3** afforded only some background noise, which can be ascribed to the complete solubilisation of this probe. Notably, among the self-associating molecules **1**, **2** and **4**, the one showing the highest derived count rate in DLS was phenylalanine derivative **2**. It must be recalled that this species is also the one displaying the most distorted absorption spectrum as can be seen in **Figure 6.2B**. In the normalized fluorescence spectra of **1** - **4**, it can also be appreciated a different behaviour between soluble **3** and aggregated **1**, **2** and **4** (shoulder at 530-540 nm) (Figure S6.4, left). However, at a much lower concentration (10 nM) of **1** - **4**, the optical properties of all the molecules are similar, which points to complete solubilisation of them (Figure S6.4, right). In addition, despite the ability of **3** to remain in solution at 10 μM, when the concentration is increased to 100 μM the formation of aggregates is also evident from the fluorescence spectrum (Figure S6.5). To summarize, at a very low concentration (10 nM) all the compounds remain soluble in aqueous solution, at an intermediate concentration (10 μM) **1, 2** and **4** form nanoparticles whereas **3** remains soluble, and at a very high concentration (100 μM) all the molecules form aggregates.

The ability of **1** - **4** to be incorporated intracellularly was tested using human colon adenocarcinoma HT-29 cells by flow cytometry as a bioanalytical technique. Solutions of **1** - **4** at 10 nM were incubated with HT-29 cells for 20 min at 37 ºC. After this time, the fluorescence of samples was measured and it

became clear that **1** and **3** were the compounds marking the cells with higher intensity, especially **3**, which provides a signal about 8-fold more intense than the average of the other molecules (**Figure 6.3)**.

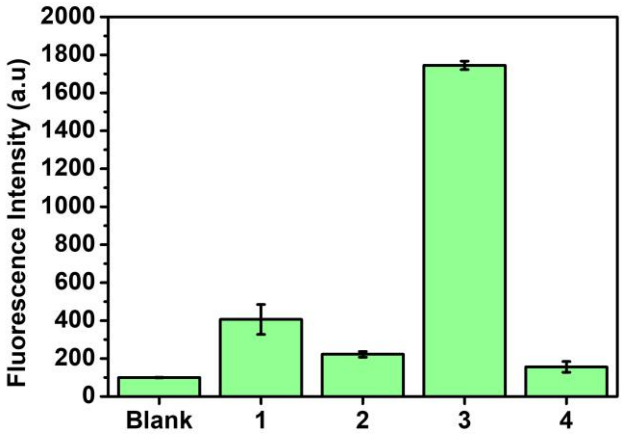

Figure 6.3. Analysis by flow cytometry of samples of HT-29 cells incubated with **1 – 4**. The bar graph shows the mean of fluorescence intensities of selected areas within the scatter plot, which are representative of the uptake of the probes into the cells (see Figure S6.8). All values are presented as the mean ± standard deviation, compared with the blank group (no probe added).

Next, **1 - 4** were studied in more detail and used to image HT-29 cells using confocal laser scanning microscopy (CLSM). As it can be observed in **Figure 6.4**, all the compounds internalized in the cells but with notable differences. Molecule **3** accumulates giving higher intensity signal and a more clear punctate pattern (green colour), which was tentatively assigned to the lysosomes. This hypothesis was confirmed by a colocalization assay using the lysosomal marker LysoTracker DND-99 (red colour in **Figure 6.4**). Merging the images for the emissions of **1-4** and Lysotracker DND-99 gives a better matching (yellow colour) for **3** (Pearson's

correlation coefficient of 0.88; Figure S6.7) than for **1, 2** and **4** (Pearson's correlation coefficients 0.63, 0.53 and 0.56, respectively, Figure S6.7).

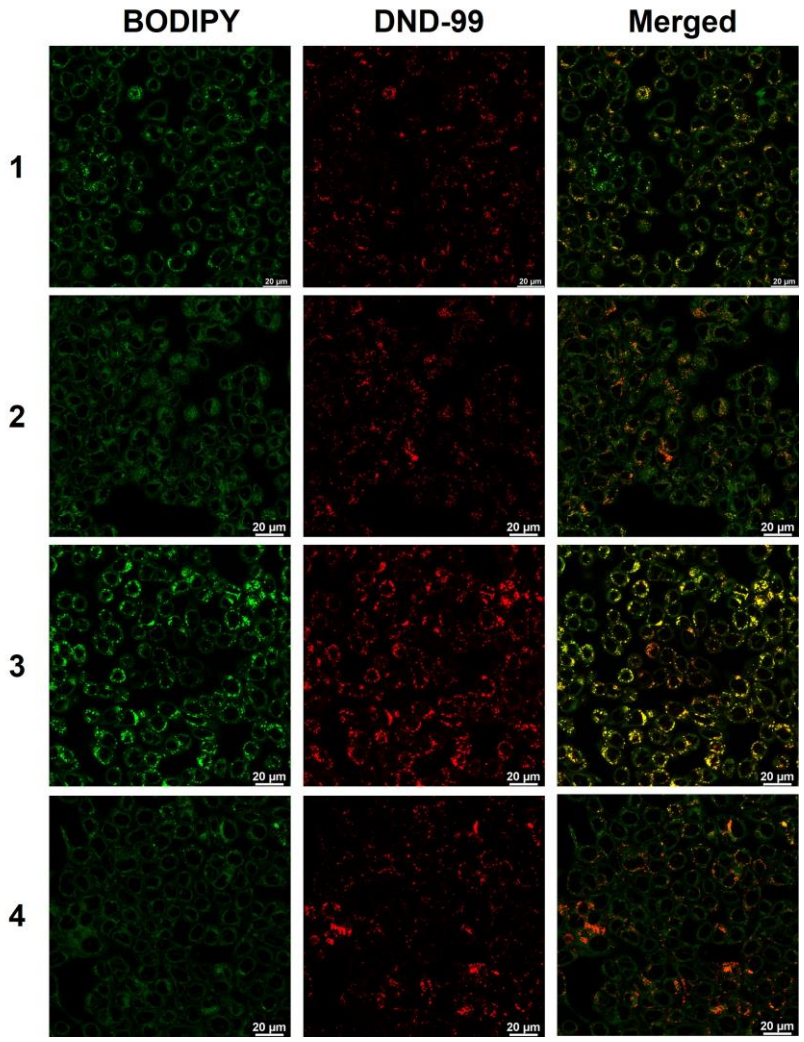

Figure 6.4. Colocalization of **1 - 4** with LysoTracker DND-99 in HT-29 cells. HT-29 cells were preincubated with **1 - 4** (10 nM) for 20 min, followed by incubation with LysoTracker DND-99 (100 nM) for 30 min. Bars, 20 µm.

To expand the scope of application of the studied cellular probes, and considering the excellent lysosomal accumulation of **3**, its distribution was studied in another cell line, the adrenal carcinoma cell line SW13. In particular, SW13/cl.2 cells lack the cytoplasmic intermediate filament vimentin, which impairs the perinuclear distribution of lysosomes leading to their preferential localization at one side of the nucleus.[40,41] Cultures of SW13/cl.2 cells were incubated with **1** or **3**. In this cell type, **1** did not generate a specific lysosome staining (**Figure 6.5**, upper panels). Some vesicles without the typical appearance of lysosomes, *i.e.*, larger than expected (see enlarged image at the right) stand out in some cells on a non-negligible, mainly cytoplasmic background, in which other apparently membranous structures can be seen. In contrast, **3** yielded a more typical pattern with small vesicles accumulated at one side of the nucleus (**Figure 6.5**, lower panels). In cells of patients affected by Niemann Pick C disease the lysosomes are abnormally enlarged due to the accumulation of cholesterol.[7] A correct visualization of this defective process is fundamental to carry out reliable metabolic studies, and thus we used this context to validate the superior ability of **3** over **1** to obtain images of the lysosomes with enough quality. Hence, cultures of SW13/cl.2 human adrenal carcinoma cells were treated with the inhibitor of lysosomal cholesterol export U18666A, which leads to the enlargement of the lysosomes due to the accumulation of the aforementioned lipid[42] and incubated with **1** or **3**. This approach has been used in the past to create valid pharmacological models of the Niemann-Pick C disease.[40,43] As it can be seen in **Figure 6.5**, in cells treated with U18666A and incubated with **1**, a non-specific staining pattern was obtained, with a moderate increase in the intensity of the juxtanuclear structures, but persistence of the cytoplasmic background. In contrast, **3** reveals the typical clustering of lysosomes into larger and better-defined vesicles in a juxtanuclear

distribution, indicating that the distribution of this probe reflects the alterations in lysosomal dynamics.

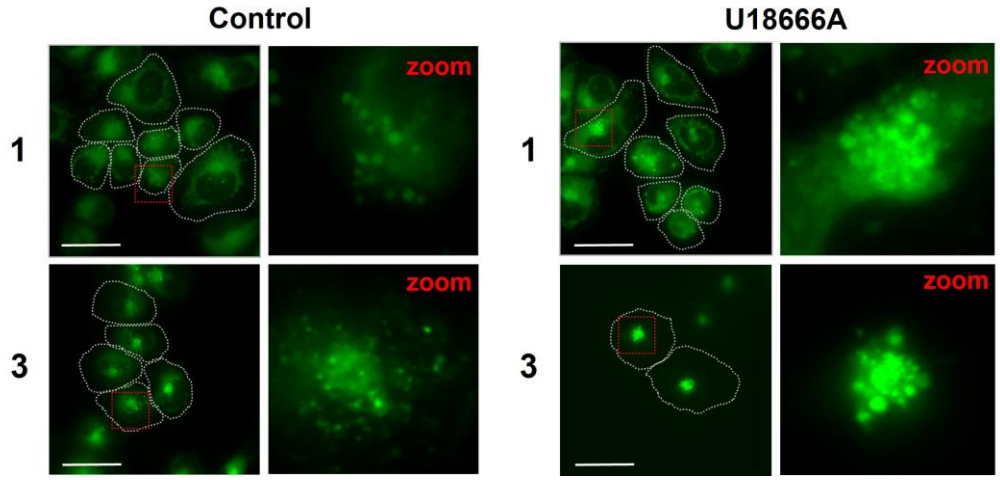

Figure 6.5. Fluorescent signals generated by **1** and **3** in SW13/cl.2 cells. Cells were treated with vehicle (control) or U18666A, and subsequently incubated with **1** or **3**, as indicated. Fluorescence was monitored in live cells. The cell contour is marked by dotted lines. The square regions of interest are enlarged in the panels at the right (zoom). Bars, 40 μm.

Additionally, we were interested in assessing the behaviour of these fluorescent molecules after fixation. In control fixed cells (**Figure 6.6**), the signals from both **1** and **3** displayed a non-specific pattern with some background and scattered vesicular staining. Only U18666A-treated cells stained with **3** retained an apparently specific staining of juxtanuclear lysosome accumulations. Thus, live cell visualization of **3** appears to be superior, and further optimization would be required for the preservation of the fluorescent signal.

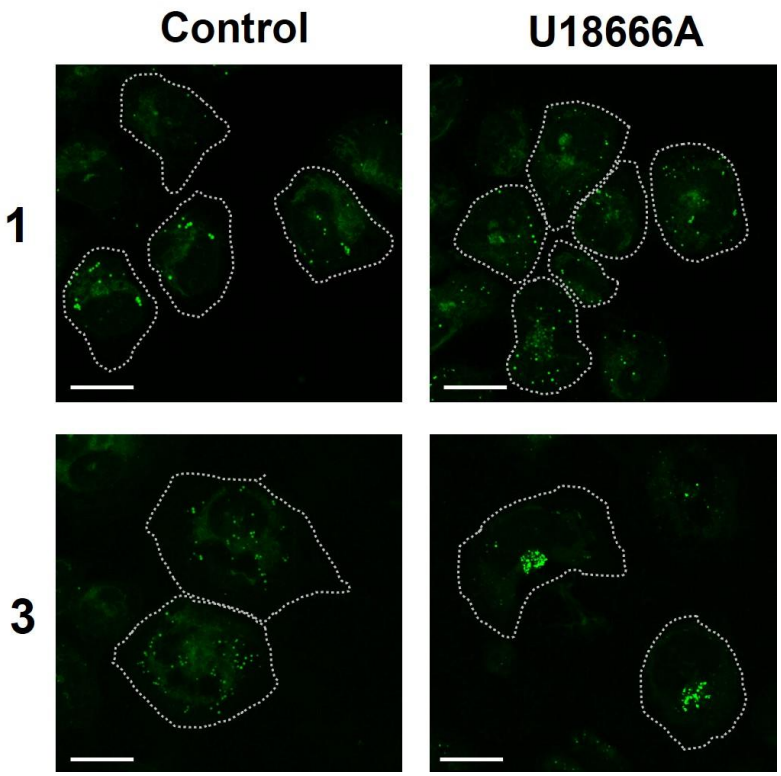

Figure 6.6. Detection of **1** and **3** after cell fixation. SW13/cl.2 cells were treated and incubated with molecules **1** or **3** as described in Figure 6.5. Subsequently, cells were fixed with 4% (w/v) paraformaldehyde and fluorescent signals detected by confocal microscopy. Bars, 20 μm.

The high contrast obtained by **3** makes this compound potentially useful in combination with other probes marking specific molecules inside the lysosome, like filipin, which is able to stain deposits of cholesterol in Niemann-Pick C cells.[44,45] It remains to be determined whether **3** stains any particular biomolecule within the organelle or just accumulates in this acidic organelle in response to protonation. This latter mechanism of internalisation is the most likely occurring since the dialkylamino substitution is found in many fluorescent probes[13,15,16,46,47] and numerous lysosomotropic drugs increasing the pH of the lysosome.[48,49]

6.3 Conclusions

In summary, a series of four BODIPY derivatives made with amino acid building blocks have been synthesized and characterized (NMR techniques, mass spectrometry and UV-Vis/fluorescence spectroscopies). In 0.1 M HEPES, pH 7.00, at a concentration of 10 μM, three of the compounds (**1**, **2** and **4**) form weakly emissive nanoparticles (DLS studies) whereas one of them (**3**), containing lysine as a building block, remains solubilized being highly fluorescent. The tendency to aggregation is also important for **3** at high concentration (100 μM), whereas at 10 nM this phenomenon is absent for all the compounds.

The cellular uptake of **1 - 4** has been studied in human colon adenocarcinoma cells HT-29 by means of flow cytometry and confocal laser scanning microscopy. All the compounds were efficiently internalized, but with a notable preference by molecule **3**. The lysosomal location of all the molecules has been demonstrated by means of colocalization assays using lysosomal fluorescent probe LysoTracker DND-99. In this regard, the soluble compound **3** was the one showing a more specific lysosomal location (Pearson's correlation coefficient 0.88). Molecules **3** and **1** were also tested in a cellular model of lysosomal storage disease (SW13/cl.2 human adrenal carcinoma). In this case, **3** showed a clear better performance in fluorescence microscopy assays, marking the lysosomes of cells treated with the inhibitor of lysosomal cholesterol export U18666A with a higher definition than **1**. We hope that these studies will shed light on the structural factors causing the aggregation of these derivatives and the influence of such self-assembly process on the microscopic imaging of lysosomal vesicles.

6.4 Experimental Section

6.4.1 Materials and instrument

Commercially available reagents and HPLC grade solvents were purchased from commercial suppliers and used without further purification. Reactions that required an inert atmosphere were carried out under a nitrogen atmosphere. NMR spectra were recorded on an Agilent VNMR System spectrometer (500 MHz for ^{1}H-NMR, 125 MHz for ^{13}C-NMR) or Bruker Advance III HD spectrometers (400 MHz and 300 MHz for ^{1}H-NMR, 101 MHz and 75 MHz for ^{13}C-NMR) in the indicated solvent at 30 ºC. All chemical shifts (δ) are quoted in parts per million (ppm) downfield from tetramethylsilane (TMS) and coupling constants (J) are quoted in Hertz (Hz). Mass spectra were recorded at Mass Spectrometry triple Quadrupole Q-TOF Premier (Waters) with simultaneous Electrospray and APCI Probe. The photophysical properties were measured with a JASCO FP-8300 fluorometer and a JASCO V-630 UV–Vis spectrophotometer. Lifetime measurements were recorded using the time-correlated single-photon counting (TCSPC) technique. The excitation source was a nanoLED of 464 nm (1.4 ns pulse width) and the fitting analysis was done using the software provided by IBH. All dynamic light scattering (DLS) measurements were recorded using a Zetasizer Nano ZS (Malvern Instruments, UK). Automatic optimization of beam focusing and attenuation was applied for each sample.

6.4.2 Synthesis

To a stirred solution of **B** (see appendix: supporting information) (0.22 mmol, 1.0 eq.) in $CHCl_3$ (50 mL) at room temperature, DIPEA (0.24 mmol, 1.1 eq.) and TBTU (0.24 mmol, 1.1 eq.) were added, and the mixture is stirred for 25 minutes. Then, the appropriate *N*-unprotected amino acid (0.22 mmol, 1.0 eq.) was added, and

the reaction mixture was stirred overnight. After that, the reaction mixture was evaporated to dryness under reduced pressure. The residue was dissolved in $CHCl_3$ (50 mL) and washed twice with 1.0 M HCl (30 mL), twice with saturated $NaHCO_3$ (30 mL) and once with brine (30 mL). The organic phase is dried over Na_2SO_4 and evaporated under reduced pressure. The solid obtained is washed with petroleum ether and dried to afford **1 – 4**.

4-(5,5-difluoro-1,3,7,9-tetramethyl-5H-4λ4,5λ4-dipyrrolo[1,2-c:2',1'-f][1,3,2]-diazaborinin-10-yl)phenyl (S)-5-((3-methyl-1-oxo-1-(propyl-amino)butan-2-yl)-amino)-5-oxopentanoate (1). Yield: 73%; **^{1}H-NMR (300 MHz, $CDCl_3$, *δ*)**: 7.35 – 7.28 (m, 2H), 7.26 – 7.19 (m, 2H), 6.18 (d, J = 8.5 Hz, 1H), 5.99 (s, 2H), 5.85 (s, 1H), 4.18 (dd, J = 8.7, 7.1 Hz, 1H), 3.36 – 3.09 (m, 2H), 2.67 (t, J = 7.2 Hz, 2H), 2.55 (s, 6H), 2.40 (t, J = 7.0 Hz, 2H), 2.14 – 2.02 (m, 3H), 1.56 – 1.47 (m, 2H), 1.42 (s, 6H), 1.03 – 0.85 (m, 9H); **^{13}C-NMR (101 MHz, $CDCl_3$, *δ*)**: 172.1, 171.4, 171.2, 155.9, 151.4, 143.3, 140.8, 132.6, 131.6, 129.4, 122.6, 121.5, 58.9, 41.4, 35.3, 33.5, 31.3, 22.9, 20.8, 19.4, 18.5, 14.7, 11.5; **HRMS (ESI-TOF) m/z**: $[M+H]^+$ calcd for $C_{32}H_{41}BF_2N_4O_4$ 594.3309; found, 594.3304.

4-(5,5-difluoro-1,3,7,9-tetramethyl-5H-4λ4,5λ4-dipyrrolo[1,2-c:2',1'-f][1,3,2]-diazaborinin-10-yl)phenyl (S)-5-oxo-5-((1-oxo-3-phenyl-1-(propylamino)-propan-2-yl)amino)pentanoate (2). Yield: 51%; **^{1}H-NMR (400 MHz, $CDCl_3$, *δ*)**: 7.42 – 7.15 (m, 9H), 6.29 (d, J = 7.5 Hz, 1H), 5.99 (s, 2H), 5.52 (t, J = 4.9 Hz, 1H), 4.71 – 4.36 (m, 1H), 3.23 – 2.90 (m, 4H), 2.70 – 2.46 (m, 8H), 2.35 (t, J = 7.2 Hz, 2H), 2.19 – 1.97 (m, 2H), 1.50 – 1.17 (m, 8H), 0.78 (t, J = 7.4 Hz, 3H); **^{13}C-NMR (101 MHz, $CDCl_3$, *δ*)**: 171.8, 171.4, 170.7, 155.9, 151.3, 143.3, 140.8, 136.9, 132.6, 131.6, 129.4, 128.9, 127.2, 122.6, 121.5, 55.0, 41.4, 39.1, 35.2, 33.4, 22.7, 20.6, 14.7, 11.4; **HRMS (ESI-TOF) m/z**: $[M+Na]^+$ calcd for $C_{36}H_{41}BF_2N_4O_4$ 664.3123; found, 664.3121.

4-(5,5-difluoro-1,3,7,9-tetramethyl-5H-4 λ4,5 λ4-dipyrrolo[1,2-c:2',1'-f][1,3,2]-diazaborinin-10-yl)phenyl 5-((6-(dimethylamino)-1-oxo-1-(propylamino)hexan-2-yl)amino)-5-oxopentanoate (3). Yield: 26%; **^{1}H-NMR (400 MHz, $CDCl_3$, *δ*)**: 7.50 (d, J = 7.3 Hz, 1H), 7.33 – 7.25 (m, 4H), 7.05 (t, J = 5.5 Hz, 1H), 5.98 (s, 2H), 4.48 (dd, J = 13.8, 7.1 Hz, 1H), 3.25 – 3.08 (m, 3H), 3.04 – 2.93 (m, 1H), 2.84 (d, J = 4.9 Hz, 3H), 2.80 (d, J = 4.9 Hz, 3H), 2.68 (t, J = 7.4 Hz, 2H), 2.55 (s, 6H), 2.51 (t, J = 7.3 Hz, 2H), 2.22 – 2.03 (m, 2H), 1.99 – 1.81 (m, 5H), 1.79 – 1.66 (m, 1H), 1.57 – 1.49 (m, 2H), 1.42 (s, J = 7.1 Hz, 6H), 0.90 (t, J = 7.4 Hz, 3H); **^{13}C-NMR (101 MHz, $CDCl_3$, *δ*)**: 173.2, 171.7, 171.5, 155.8, 151.4, 143.3, 140.9, 132.5, 131.6, 129.3, 122.7, 121.5, 56.9, 53.1, 43.7, 42.8, 41.4, 35.1, 33.7, 31.1, 30.6, 23.9, 22.8, 21.9, 20.9, 14.7, 11.6; **HRMS (ESI-TOF) m/z**: $[M+H]^+$ calcd for $C_{35}H_{48}BF_2N_5O_4$ 651.3883; found, 651.3881.

4-(5,5-difluoro-1,3,7,9-tetramethyl-5H-4λ4,5λ4-dipyrrolo[1,2-c:2',1'-f][1,3,2]-diazaborinin-10-yl)phenyl 5-(((S)-3-methyl-1-(((S)-3-methyl-1-oxo-1-(propyl-amino)butan-2-yl)amino)-1-oxobutan-2-yl)amino)-5-oxopentanoate (4). Yield: 64%; **^{1}H-NMR (300 MHz, MeOD, *δ*)**: 7.44 – 7.27 (m, 4H), 6.08 (s, J = 10.3 Hz, 2H), 4.28 – 4.04 (m, 2H), 3.22 – 3.04 (m, 2H), 2.68 (t, J = 7.5 Hz, 2H), 2.57 – 2.36 (m, 8H), 2.13 – 1.95 (m, 4H), 1.61 – 1.39 (m, 8H), 1.07 – 0.76 (m, 15H); **HRMS (ESI-TOF) m/z**: $[M+Na]^+$ calcd for $C_{37}H_{50}BF_2N_5O_5$ 715.3807; found, 715.3815. Due to its limited solubility, the ^{13}C-NMR spectrum could not be recorded.

6.4.3 Cells and treatments

Human colon adenocarcinoma HT-29 cells were from the American Type Culture Collection and were cultured in FluoroBrite™ DMEM (Gibco™ A1896701, Thermo Fisher Scientific). SW13/cl.2 were the generous gift from Dr A. Sarriá (University

of Zaragoza, Spain),[50] and were cultured as previously described.[51] For pharmacological induction of the Niemann-Pick phenotype,[42] cells were cultured for 24 h in the presence of 10 μM U18666A or vehicle (0.1% (v/v) DMSO), as previously described,[52] before incubation with the lysosomal probes **1** and **3**.

6.4.4 Fluorescence Microscopy

HT-29 cells (grown to 50-60% confluence) in a sterilized Ibidi® μ-Slide (4 well glass bottom) were preincubated with **1** - **4** (10 nM) for 20 min at 37 ºC, followed by incubation with LysoTracker DND-99 (100 nM, a commercial lysosomal indicator) for 30 min at 37 ºC. After washing with PBS, cells were kept in FluoroBrite DMEM medium and visualized under the confocal microscope. Cells were imaged live on an inverted confocal microscope Leica TCS SP8. Images were obtained with an HC PL APO CS2 63×/1.40 oil immersion objective. The **1** – **4** excitation wavelengths and the LysoTracker DND-99 were set at 488 nm and 561 nm, respectively. The fluorescent emissions wavelength was recorded from 500 to 550 nm for **1** – **4** and from 620 to 680 nm for LysoTracker DND-99. For colocalization analysis, the fluorescence intensity profiles were traced along an arbitrary line using LasX software (Leica Microsystems); the Pearson's correlation coefficients were calculated from the whole image using the Coloc2 plugin in ImageJ.

Incubation of SW13/cl.2 cells with lysosomal probes was carried out as above. Cells were imaged live on a Leica AF6000 LX with excitation and emission wavelengths at 488 and 563, respectively. Subsequently, cells were fixed with 4% (w/v) paraformaldehyde and observed in a Leica SP8 confocal microscope. Images were acquired every 0.5 μm and overall projections are shown.

6.4.5 Flow cytometry assay

HT-29 cells in a 6-/12-well plate (grown to 70−80% confluence) were incubated with **1** - **4** (10 nM) for 20 min at 37 ºC. Cells were washed with PBS (1.5 mL/well) twice and detached from the culture dishes by incubation with 0.25 % trypsin + EDTA. After centrifugation at 5000 rpm for 5 min, cells were washed again with PBS to remove away any dye excess. Cells were re-suspended in PBS (1 mL) and analyzed on a BD Accuri™ C6 flow cytometer. After exclusion of the cellular debris by appropriate gating on the SSC versus FSC plots, fluorescence intensity was analyzed on channel FL-1 (excitation at 488 nm; emission collected at 533/30 nm) measuring at least 20,000 cells for each sample. The results are reported as the mean fluorescence intensity from the flow cytometry histograms comparing with the blank group (unstained cells).

Acknowledgements

The authors acknowledge the financial support from the Spanish Ministry of Science and Innovation co-funded by the European Regional Development Fund of the European Union (grant RTI2018-101675-B-I00 to FG and RTI2018-097624-B-I00 to DPS). Technical support by SCIC-UJI is acknowledged.

References

(1) Lawrence, R. E.; Zoncu, R. The Lysosome as a Cellular Centre for Signalling, Metabolism and Quality Control. *Nat. Cell Biol.* **2019**, *21* (2), 133–142. https://doi.org/10.1038/s41556-018-0244-7.

(2) Ma, Z.; Li, J.; Lin, K.; Ramachandran, M.; Zhang, D.; Showalter, M.; De Souza, C.; Lindstrom, A.; Solano, L. N.; Jia, B.; Urayama, S.; Duan, Y.; Fiehn, O.; Lin, T. yin; Li, M.; Li, Y. Pharmacophore Hybridisation and Nanoscale Assembly to Discover Self-Delivering Lysosomotropic New-Chemical Entities for Cancer Therapy. *Nat. Commun.* **2020**, *11* (1), 4615. https://doi.org/10.1038/s41467-020-18399-4.

(3) Whyte, L. S.; Lau, A. A.; Hemsley, K. M.; Hopwood, J. J.; Sargeant, T. J. Endo-Lysosomal and Autophagic Dysfunction: A Driving Factor in Alzheimer's Disease? *J. Neurochem.* **2017**, *140* (5), 703–717. https://doi.org/10.1111/jnc.13935.

(4) Savarino, A.; Boelaert, J. R.; Cassone, A.; Majori, G.; Cauda, R. Effects of Chloroquine on Viral Infections: An Old Drug against Today's Diseases? *Lancet Infect. Dis.* **2003**, *3* (11), 722–727. https://doi.org/10.1016/S1473-3099(03)00806-5.

(5) Khan, N.; Chen, X.; Geiger, J. D. Role of Endolysosomes in Severe Acute Respiratory Syndrome Coronavirus-2 Infection and Coronavirus Disease 2019 Pathogenesis: Implications for Potential Treatments. *Front. Pharmacol.* **2020**, *11* (October), 595888. https://doi.org/10.3389/fphar.2020.595888.

(6) Fukuda, T.; Ewan, L.; Bauer, M.; Mattaliano, R. J.; Zaal, K.; Ralston, E.; Plotz, P. H.; Raben, N. Dysfunction of Endocytic and Autophagic Pathways in a Lysosomal Storage Disease. *Ann. Neurol.* **2006**, *59* (4), 700–708. https://doi.org/10.1002/ana.20807.

(7) Parenti, G.; Medina, D. L.; Ballabio, A. The Rapidly Evolving View of Lysosomal Storage Diseases. *EMBO Mol. Med.* **2021**, *13* (2), e12836. https://doi.org/10.15252/emmm.202012836.

(8) Vanier, M. T. Niemann-Pick Disease Type C. *Orphanet J. Rare Dis.* **2010**, *5*, 16.

(9) Zhu, H.; Fan, J.; Xu, Q.; Li, H.; Wang, J.; Gao, P.; Peng, X. Imaging of Lysosomal PH Changes with a Fluorescent Sensor Containing a Novel Lysosome-Locating Group. *Chem. Commun.* **2012**, *48* (96), 11766–11768. https://doi.org/10.1039/c2cc36785h.

(10) Lv, H. S.; Huang, S. Y.; Xu, Y.; Dai, X.; Miao, J. Y.; Zhao, B. X. A New Fluorescent PH Probe for Imaging Lysosomes in Living Cells. *Bioorganic Med. Chem. Lett.* **2014**, *24* (2), 535–538. https://doi.org/10.1016/j.bmcl.2013.12.025.

(11) Ying, L. Q.; Branchaud, B. P. Selective Labeling and Monitoring PH Changes of Lysosomes in Living Cells with Fluorogenic PH Sensors. *Bioorganic Med. Chem. Lett.* **2011**, *21* (12), 3546–3549. https://doi.org/10.1016/j.bmcl.2011.04.137.

(12) Loudet, A.; Ueno, Y.; Wu, L.; Jose, J.; Barhoumi, R.; Burghardt, R.; Burgess, K. Organelle-Selective Energy Transfer: A Fluorescent Indicator of Intracellular Environment. *Bioorganic Med. Chem. Lett.* **2011**, *21* (6), 1849–1851. https://doi.org/10.1016/j.bmcl.2011.01.040.

(13) Zheng, X.; Zhu, W.; Ni, F.; Ai, H.; Gong, S.; Zhou, X.; Sessler, J. L.; Yang, C. Simultaneous Dual-Colour Tracking Lipid Droplets and Lysosomes Dynamics Using a Fluorescent Probe. *Chem. Sci.* **2019**, *10* (8), 2342–2348. https://doi.org/10.1039/C8SC04462G.

(14) Rong, R. X.; Wang, S. S.; Liu, X.; Li, R. F.; Wang, K. R.; Cao, Z. R.; Li, X. L. Lysosomes-Targeting Imaging and Anticancer Properties of Novel Bis-Naphthalimide Derivatives. *Bioorganic Med. Chem. Lett.* **2018**, *28* (4), 742–747. https://doi.org/10.1016/j.bmcl.2018.01.008.

(15) Kim, H. M.; An, M. J.; Hong, J. H.; Jeong, B. H.; Kwon, O.; Hyon, J. Y.; Hong, S. C.; Lee, K. J.; Cho, B. R. Two-Photon Fluorescent Probes for Acidic Vesicles in Live Cells and Tissue. *Angew. Chemie - Int. Ed.* **2008**, *47* (12), 2231–2234. https://doi.org/10.1002/anie.200704586.

(16) Lim, C. S.; Hong, S. T.; Ryu, S. S.; Kang, D. E.; Cho, B. R. Two-Photon Probes for Lysosomes and Mitochondria: Simultaneous Detection of Lysosomes and Mitochondria in Live Tissues by Dual-Color Two-Photon Microscopy Imaging. *Chem. - An Asian J.* **2015**, *10* (10), 2240–2249. https://doi.org/10.1002/asia.201500314.

(17) Zacharioudakis, E.; Cañeque, T.; Custodio, R.; Müller, S.; Cuadro, A. M.; Vaquero, J. J.; Rodriguez, R. Quinolizinium as a New Fluorescent Lysosomotropic Probe. *Bioorganic Med. Chem. Lett.* **2017**, *27* (2), 203–207. https://doi.org/10.1016/j.bmcl.2016.11.074.

(18) Zhou, X.; Fang, Y.; Lesiak, L.; Stains, C. I. A Phosphinate-Containing Fluorophore Capable of Selectively Inducing Apoptosis in Cancer Cells. *ChemBioChem* **2019**, *20* (13), 1712–1716. https://doi.org/10.1002/cbic.201800811.

(19) Galindo, F.; Burguete, M. I.; Vigara, L.; Luis, S. V.; Kabir, N.; Gavrilovic, J.; Russell, D. A. Synthetic Macrocyclic Peptidomimetics as Tunable PH Probes for the Fluorescence Imaging of Acidic Organelles in Live Cells. *Angew. Chemie Int. Ed.* **2005**, *44* (40), 6504–6508. https://doi.org/10.1002/anie.200501920.

(20) Burguete, M. I.; Galindo, F.; Izquierdo, M. A.; O'Connor, J. E.; Herrera, G.; Luis, S. V.; Vigara, L. Synthesis and Evaluation of Pseudopeptidic Fluorescence PH Probes for Acidic Cellular Organelles: In Vivo Monitoring of Bacterial Phagocytosis by Multiparametric Flow Cytometry. *European J. Org. Chem.* **2010**, No. 31, 5967–5979. https://doi.org/10.1002/ejoc.201000854.

(21) Marín, M. J.; Galindo, F.; Thomas, P.; Russell, D. A. Localized Intracellular PH Measurement Using a Ratiometric Photoinduced Electron-Transfer-Based Nanosensor. *Angew. Chemie Int. Ed.* **2012**, *51* (38), 9657–9661. https://doi.org/10.1002/anie.201203866.

(22) Wadhavane, P. D.; Izquierdo, M. Á.; Lutters, D.; Burguete, M. I.; Marín, M. J.; Russell, D. A.; Galindo, F.; Luis, S. V. Fluorescent Macrocyclic Probes with Pendant Functional Groups as Markers of Acidic Organelles within Live Cells. *Org. Biomol. Chem.* **2014**, *12* (5), 823–831. https://doi.org/10.1039/c3ob41773e.

(23) Saura, A. V.; Marín, M. J.; Burguete, M. I.; Russell, D. A.; Galindo, F.; Luis, S. V. The Synthesis of New Fluorescent Bichromophoric Compounds as Ratiometric PH Probes for Intracellular Measurements. *Org. Biomol. Chem.* **2015**, *13* (28), 7736–7749. https://doi.org/10.1039/c5ob00704f.

(24) Vanessa Saura, A.; Isabel Burguete, M.; Galindo, F.; Luis, S. V. Novel Fluorescent Anthracene-Bodipy Dyads Displaying Sensitivity to PH and Turn-on Behaviour towards Cu(II) Ions. *Org. Biomol. Chem.* **2017**, *15* (14), 3013–3024. https://doi.org/10.1039/C7OB00274B.

(25) Izquierdo, M. A.; Wadhavane, P. D.; Vigara, L.; Burguete, M. I.; Galindo, F.; Luis, S. V. The Interaction of Amino Acids with Macrocyclic PH Probes of Pseudopeptidic Nature. *Photochem. Photobiol. Sci.* **2017**, *16* (8), 1320–1326. https://doi.org/10.1039/c7pp00167c.

(26) Xu, W.; Zeng, Z.; Jiang, J. H.; Chang, Y. T.; Yuan, L. Discerning the Chemistry in Individual Organelles with Small-Molecule Fluorescent Probes. *Angew. Chemie - Int. Ed.* **2016**, *55* (44), 13658–13699. https://doi.org/10.1002/anie.201510721.

(27) Gao, P.; Pan, W.; Li, N.; Tang, B. Fluorescent Probes for Organelle-Targeted Bioactive Species Imaging. *Chem. Sci.* **2019**, *10* (24), 6035–6071. https://doi.org/10.1039/c9sc01652j.

(28) Urano, Y.; Asanuma, D.; Hama, Y.; Koyama, Y.; Kamiya, M.; Nagano, T.; Watanabe, T.; Hasegawa, A.; Peter, L.; Kobayashi, H. Selective Molecular Imaging of Viable Cancer Cells with PH-Activatable Fluorescence Probes. *Nat Med.* **2009**, *15* (1), 104–109. https://doi.org/10.1038/nm.1854.Selective.

(29) Trapp, S.; Rosania, G. R.; Horobin, R. W.; Kornhuber, J. Quantitative Modeling of Selective Lysosomal Targeting for Drug Design. *Eur. Biophys. J.* **2008**, *37* (8), 1317–1328. https://doi.org/10.1007/s00249-008-0338-4.

(30) Horobin, R. W.; Stockert, J. C.; Rashid-Doubell, F. Uptake and Localisation of Small-Molecule Fluorescent Probes in Living Cells: A Critical Appraisal of QSAR Models and a Case Study Concerning Probes for DNA and RNA. *Histochem. Cell Biol.* **2013**, *139* (5), 623–637. https://doi.org/10.1007/s00418-013-1090-0.

(31) Yang, H.; Li, X.; Cai, Y.; Wang, Q.; Li, W.; Liu, G.; Tang, Y. In Silico Prediction of Chemical Subcellular Localization via Multi-Classification Methods. *Medchemcomm* **2017**, *8* (6), 1225–1234. https://doi.org/10.1039/c7md00074j.

(32) Navarro-Barreda, D.; Angulo-Pachón, C. A.; Bedrina, B.; Galindo, F.; Miravet, J. F. A Dual Stimuli Responsive Supramolecular Gel Provides Insulin Hydrolysis Protection and Redox-Controlled Release of Actives. *Macromol. Chem. Phys.* **2020**, *221* (4), 1–6. https://doi.org/10.1002/macp.201900419.

(33) Navarro-Barreda, D.; Angulo-Pachón, C. A.; Galindo, F.; Miravet, J. F. Photoreversible Formation of Nanotubes in Water from an Amphiphilic Azobenzene Derivative. *Chem. Commun.* **2021**, *57* (87), 11545–11548. https://doi.org/10.1039/d1cc04319f.

(34) Navarro-Barreda, D.; Bedrina, B.; Galindo, F.; Miravet, J. F. Glutathione-Responsive Molecular Nanoparticles from a Dianionic Bolaamphiphile and Their Use as Carriers for Targeted Delivery. *J. Colloid Interface Sci.* **2022**, *608*, 2009–2017. https://doi.org/10.1016/j.jcis.2021.10.142.

(35) Loudet, A.; Burgess, K. BODIPY Dyes and Their Derivatives: Syntheses and Spectroscopic Properties. *Chem. Rev.* **2007**, *107* (11), 4891–4932. https://doi.org/10.1021/cr078381n.

(36) Radunz, S.; Tschiche, H. R.; Moldenhauer, D.; Resch-Genger, U. Broad Range ON/OFF PH Sensors Based on PKa Tunable Fluorescent BODIPYs. *Sensors Actuators, B Chem.* **2017**, *251*, 490–494. https://doi.org/10.1016/j.snb.2017.05.080.

(37) Radunz, S.; Kraus, W.; Bischoff, F. A.; Emmerling, F.; Tschiche, H. R.; Resch-Genger, U. Temperature- And Structure-Dependent Optical Properties and Photophysics of BODIPY Dyes. *J. Phys. Chem. A* **2020**, *124* (9), 1787–1797. https://doi.org/10.1021/acs.jpca.9b11859.

(38) Bergström, F.; Mikhalyov, I.; Hägglöf, P.; Wortmann, R.; Ny, T.; Johansson, L. B. . Dimers of Dipyrromethene boron Difluoride (BODIPY) with Light Spectroscopic Applications in Chemistry and Biology. *J. Am. Chem. Soc.* **2002**, *124* (2), 196–204. https://doi.org/10.1021/ja010983f.

(39) Mikhalyov, I.; Gretskaya, N.; Bergström, F.; Johansson, L. B. . Electronic Ground and Excited State Properties of Dipyrromethene boron Difluoride (BODIPY): Dimers with Application to Biosciences. *Phys. Chem. Chem. Phys.* **2002**, *4* (22), 5663–5670. https://doi.org/10.1039/b206357n.

(40) Styers, M. L.; Salazar, G.; Love, R.; Peden, A. A.; Kowalczyk, A. P.; Faundez, V. The Endo-Lysosomal Sorting Machinery Interacts with the Intermediate Filament Cytoskeleton. *Mol Biol Cell* **2004**, *15* (December), 5369–5382. https://doi.org/10.1091/mbc.E04.

(41) Pérez-Sala, D.; Oeste, C. L.; Martínez, A. E.; Carrasco, M. J.; Garzón, B.; Cañada, F. J. Vimentin Filament Organization and Stress Sensing Depend on Its Single Cysteine Residue and Zinc Binding. *Nat. Commun.* **2015**, *6*. https://doi.org/10.1038/ncomms8287.

(42) Lu, F.; Liang, Q.; Abi-Mosleh, L.; Das, A.; de Brabander, J. K.; Goldstein, J. L.; Brown, M. S. Identification of NPC1 as the Target of U18666A, an Inhibitor of Lysosomal Cholesterol Export and Ebola Infection. *Elife* **2015**, *4* (December2015), e12177. https://doi.org/10.7554/eLife.12177.

(43) Pérez-Sala, D.; Boya, P.; Ramos, I.; Herrera, M.; Stamatakis, K. The C-Terminal Sequence of RHoB Directs Protein Degradation through an Endo-Lysosomal Pathway. *PLoS One* **2009**, *4* (12), e8117. https://doi.org/10.1371/journal.pone.0008117.

(44) Pipalia, N. H.; Huang, A.; Ralph, H.; Rujoi, M.; Maxfield, F. R. Automated Microscopy Screening for Compounds That Partially Revert Cholesterol Accumulation in Niemann-Pick C Cells. *J. Lipid Res.* **2006**, *47* (2), 284–301. https://doi.org/10.1194/jlr.M500388-JLR200.

(45) Sitarska, D.; Ługowska, A. Laboratory Diagnosis of the Niemann-Pick Type C Disease: An Inherited Neurodegenerative Disorder of Cholesterol Metabolism. *Metab. Brain Dis.* **2019**, *34* (5), 1253–1260. https://doi.org/10.1007/s11011-019-00445-w.

(46) Zhao, X.; Wang, C.; Yuan, G.; Ding, H.; Zhou, L.; Liu, X.; Lin, Q. A Dual-Site Modulated FRET-Based Two-Photon Ratiometric Fluorescent Probe for Tracking Lysosomal PH Changes in Living Cells, Tissues and Zebrafish. *Sensors Actuators, B Chem.* **2019**, *290*, 79–86. https://doi.org/10.1016/j.snb.2019.03.122.

(47) Sun, S. G.; Ding, H.; Yuan, G.; Zhou, L. An Efficient TP-FRET-Based Lysosome-Targetable Fluorescent Probe for Imaging Peroxynitrite with Two Well-Resolved Emission Channels in Living Cells, Tissues and Zebrafish. *Anal. Chim. Acta* **2020**, *1100*, 200–207. https://doi.org/10.1016/j.aca.2019.11.065.

(48) Villamil Giraldo, A. M.; Appelqvist, H.; Ederth, T.; Öllinger, K. Lysosomotropic Agents: Impact on Lysosomal Membrane Permeabilization and Cell Death. *Biochem. Soc. Trans.* **2014**, *42* (5), 1460–1464. https://doi.org/10.1042/BST20140145.

(49) Norinder, U.; Tuck, A.; Norgren, K.; Munic Kos, V. Existing Highly Accumulating Lysosomotropic Drugs with Potential for Repurposing to Target COVID-19. *Biomed. Pharmacother.* **2020**, *130*, 110582. https://doi.org/10.1016/j.biopha.2020.110582.

(50) Sarria, A. J.; Lieber, J. G.; Nordeen, S. K.; Evans, R. M. The Presence or Absence of a Vimentin-Type Intermediate Filament Network Affects the Shape of the Nucleus in Human SW-13 Cells. *J. Cell Sci.* **1994**, *107* (6), 1593–1607. https://doi.org/10.1242/jcs.107.6.1593.

(51) Duarte, S.; Viedma-Poyatos, Á.; Navarro-Carrasco, E.; Martínez, A. E.; Pajares, M. A.; Pérez-Sala, D. Vimentin Filaments Interact with the Actin Cortex in Mitosis Allowing Normal Cell Division. *Nat. Commun.* **2019**, *10* (1), 1–19. https://doi.org/10.1038/s41467-019-12029-4.

(52) Oeste, C. L.; Pinar, M.; Schink, K. O.; Martínez-Turrión, J.; Stenmark, H.; Penalva, M. A.; Pérez-Sala, D. An Isoprenylation and Palmitoylation Motif Promotes Intraluminal Vesicle Delivery of Proteins in Cells from Distant Species. *PLoS One* **2014**, *9* (9), e107190. https://doi.org/10.1371/journal.pone.0107190.

(53) Felip-León, C.; Martínez-Arroyo, O.; Díaz-Oltra, S.; Miravet, J. F.; Apostolova, N.; Galindo, F. Synthesis, Spectroscopic Studies and Biological Evaluation of Acridine Derivatives: The Role of Aggregation on the Photodynamic Efficiency. *Bioorganic Med. Chem. Lett.* **2018**, *28* (5), 869–874. https://doi.org/10.1016/j.bmcl.2018.02.005.

(54) Berdugo, C.; Escuder, B.; Miravet, J. F. Structural Insight into the Aggregation of L-Prolyl Dipeptides and Its Effect on Organocatalytic Performance. *Org. Biomol. Chem.* **2015**, *13* (2), 592–600. https://doi.org/10.1039/c4ob02003k.

Appendix: Supporting Information

1. Fluorescence decay curves

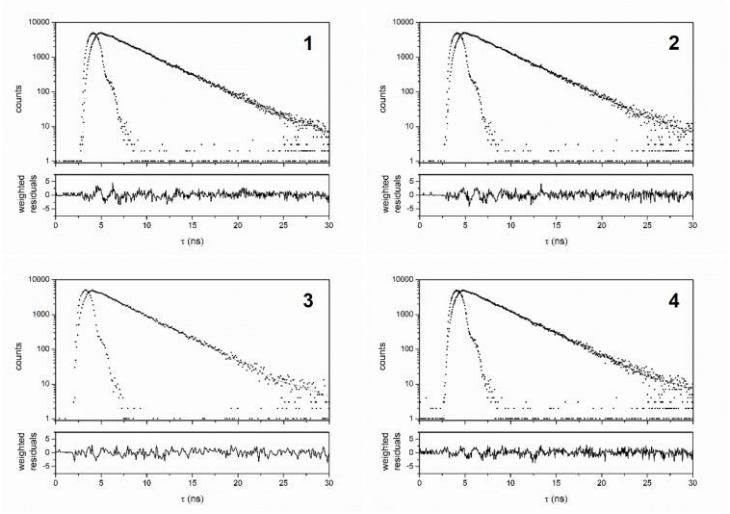

Figure S6.1. Fluorescence decay curves of **1 – 4** (5 μM) in ethanol, (λ_{exc}=464 nm / λ_{em}=500 nm). The incident light pulse and the residuals are also shown.

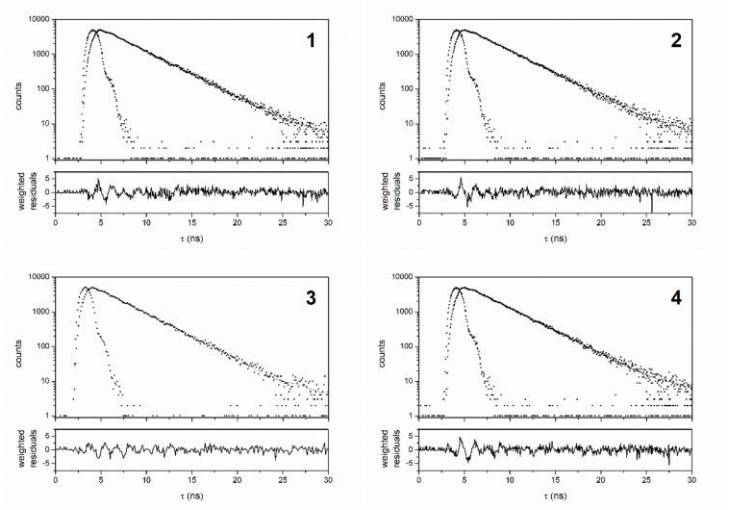

Figure S6.2. Fluorescence decay curves of **1 – 4** (5 μM) in toluene, (λ_{exc}=464 nm / λ_{em}=500 nm). The incident light pulse and the residuals are also shown.

2. Fluorescence studies in aqueous solution

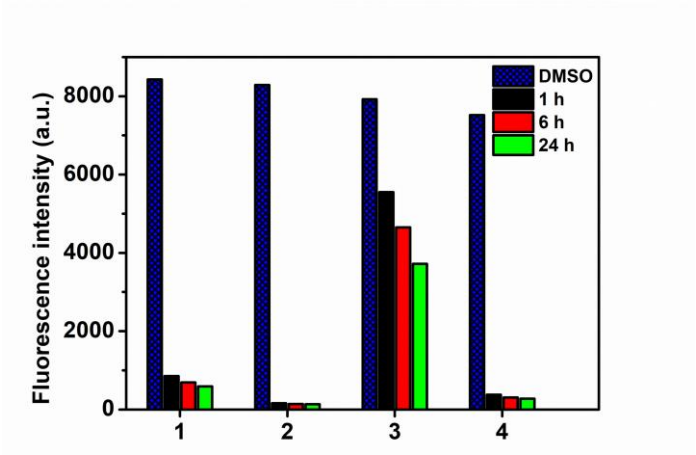

Figure S6.3. Fluorescence intensities of aqueous solutions of **1-4** (10 μM in 0.1 M HEPES, pH 7.00) at 1 (black), 6 (ref) and 24 hours (green). The excitation wavelength was set at 475 nm and the emission was recorded at 510 nm. The fluorescence intensities in DMSO under the same excitation conditions are shown for comparative purposes (blue).

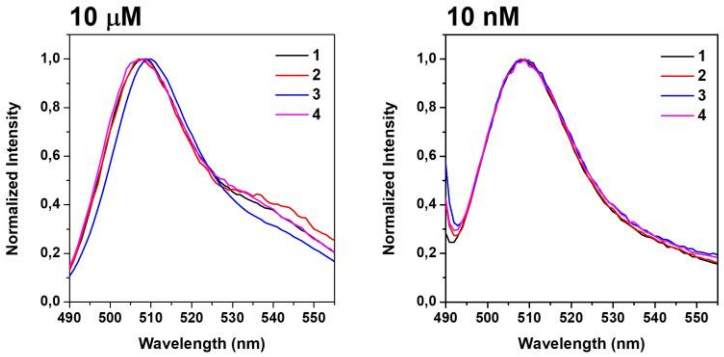

Figure S6.4. Normalized fluorescence spectra of **1-4** in 0.1 M HEPES pH 7.00 at different concentrations.

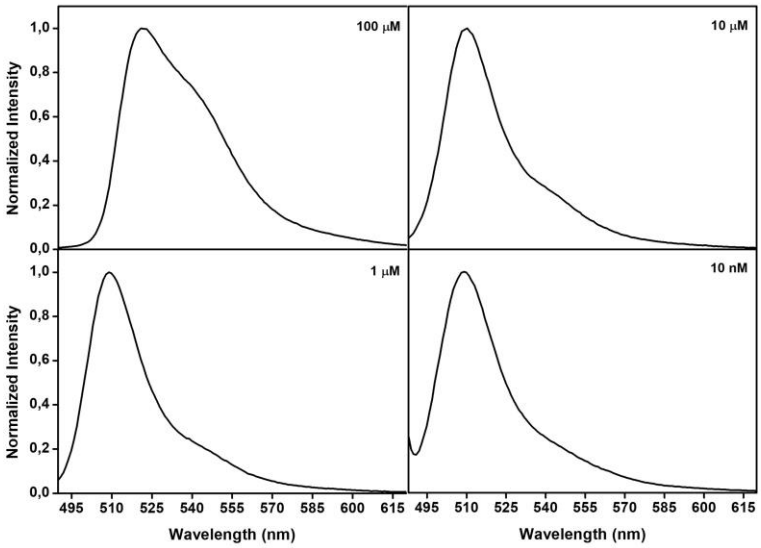

Figure S6.5. Fluorescence spectra of **3** at different concentrations in acidic aqueous solution (pH = 3, λ_{exc} = 475 nm).

3. Dynamic Light Scattering (DLS) studies

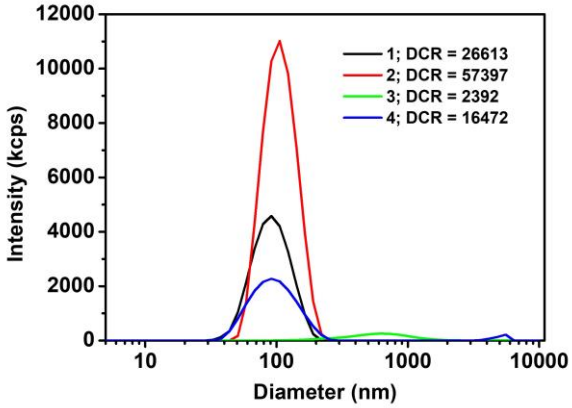

Figure S6.6. Intensity of scattered light measured by DLS for **1** – **4** (50 μM) in aqueous solution (0.1 M HEPES, pH 7.00). Size distribution of the aggregates and derived count rate (DCR) are shown.

4. Co-localisation assays

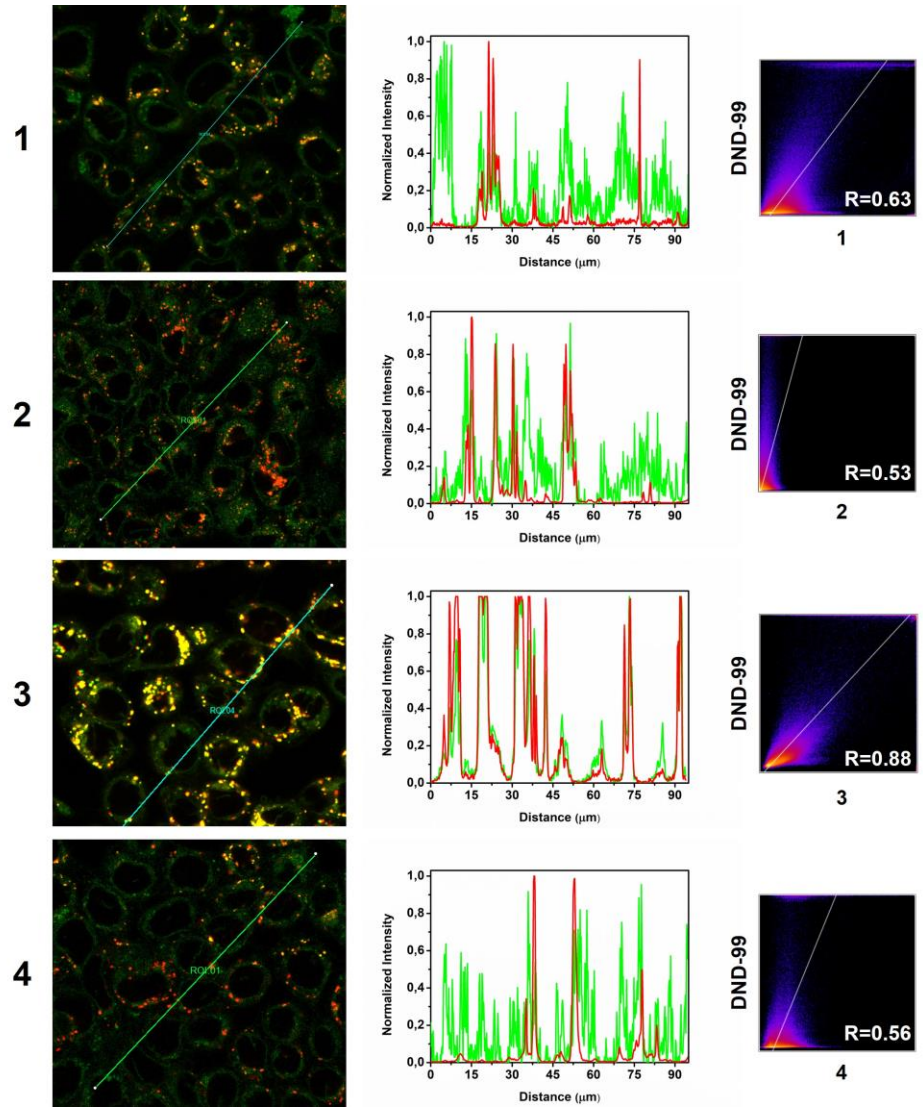

Figure S6.7. Colocalization of **1 – 4** with LysoTracker **DND-99** in HT-29 cells. Representative confocal fluorescence micrographs, fluorescence intensity profiles and the Pearson's correlation coefficients are shown. The fluorescence profiles, plotted along the green line, were obtained using LasX software (Leica Microsystems) and normalized to the maximum value; the Pearson's correlation coefficients were calculated from the whole image using the Coloc2 plugin in Image J.

5. Flow cytometry data

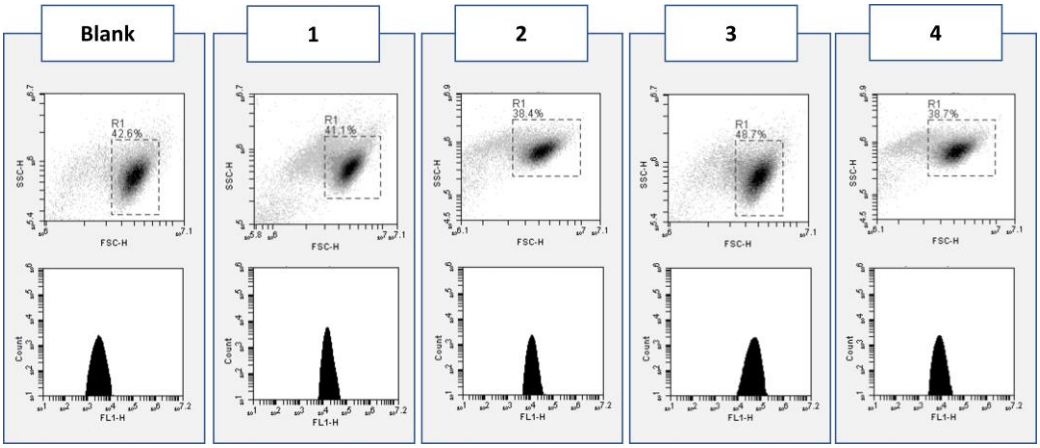

Figure S6.8. Analysis by flow cytometry of samples of HT-29 cells incubated with **1 – 4**. Top row: scatter plots for blank (no probe added) and molecules **1 – 4** showing SSC (side scatter) for cell size/granularity and FSC (forward scatter) for cell size. Bottom row: fluorescence intensity distributions in logarithmic scale (collected in the FL1 channel) corresponding to the selected region (R1). Representative data of one out of three independent samples is shown. The fluorescence intensities of each sample allowed the comparison shown in Figure 6.3 of the manuscript.

6. Synthesis

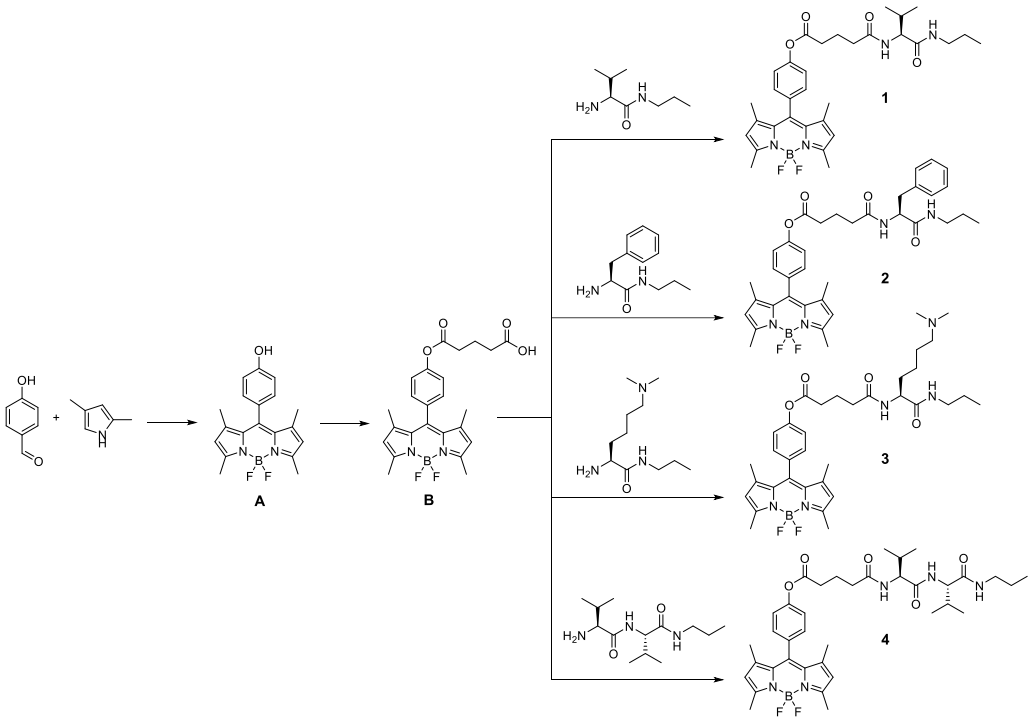

Scheme S6.1. The synthetic route to compounds **1** – **4**.

Synthesis of 4-(5,5-difluoro-1,3,7,9-tetramethyl-5H-4λ^4,5λ^4-dipyrrolo[1,2-c:2',1'-f][1,3,2]diazaborinin-10-yl)phenol (A).

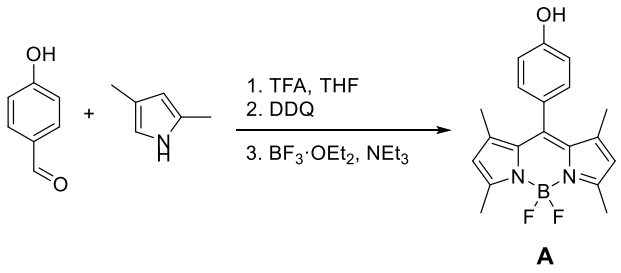

To a solution of 4-hydroxybenzaldehyde (2.32 mmol, 1.0 eq.) and 2,4-dimethylpyrrole (5.10 mmol, 2.2 eq.) in anhydrous THF (90 mL), several drops of TFA (20 drops) were added under nitrogen atmosphere. Then, 4 Å molecular sieves (0.25 g $mmol^{-1}$ aldehyde) were added and the resulting mixture was wrapped in aluminium foil and stirred for 24 h at room temperature in a nitrogen atmosphere. After that, a solution of 2,3-dichloro-5,6-dicyano-*p*-benzoquinone (2.32 mmol, 1.0 eq.) in anhydrous THF (95 mL) was added. The resulting mixture was further stirred for 4 hours at room temperature. Then, triethylamine (0.1 mol, 43.0 eq.) and $BF_3{\cdot}OEt_2$ (0.116 mol, 50.0 eq.) were added at 0 °C. The resulting mixture was kept stirring at room temperature overnight under a nitrogen atmosphere. The reaction was poured into sodium bicarbonate 5.0% solution (200 mL), and ethyl acetate (200 mL). The organic phase was dried over anhydrous sodium sulphate and evaporated to dryness under reduced pressure. The crude was redissolved in dichloromethane (*ca.* 50 mL), filtered through Cellite© and finally, purified by silica gel column chromatography using dichloromethane as eluent. The solvent was evaporated to dryness under reduced pressure to afford 5 as an orangish crystalline solid. Yield: 50%; **^{1}H-NMR (400 MHz, DMSO-d_6, δ)**: 9.81 (s, 1H), 7.12 (d, J = 8.6 Hz, 2H), 6.93 (d, J = 8.6 Hz, 2H), 6.16 (s, 2H), 2.44 (s, 6H), 1.43 (s, 6H); **^{13}C-NMR (101 MHz, $CDCl_3$, δ)**: 157.4, 155.1, 143.3, 142.3, 131.9, 129.2, 126.1, 121.1, 116.0, 14.5; **HRMS (ESI-TOF) m/z**: $[M+H]^+$ calcd for $C_{19}H_{19}BF_2N_2O$ 340.1672; found, 340.1673.

Synthesis of 5-(4-(5,5-difluoro-1,3,7,9-tetramethyl-5H-4λ^4,5λ^4-dipyrrolo[1,2-c:2',1'-f][1,3,2]diazaborinin-10-yl)phenoxy)-5-oxopentanoic acid (B).

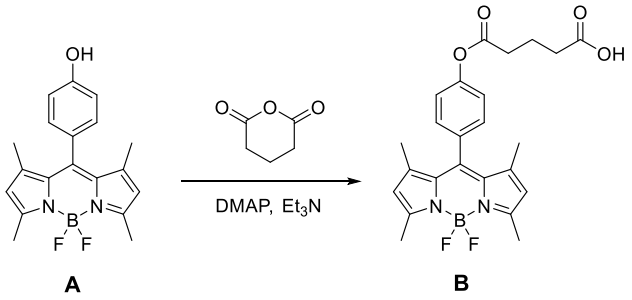

To a solution of *4-(5,5-difluoro-1,3,7,9-tetramethyl-5H-4λ^4,5λ^4-dipyrrolo[1,2-c:2',1'-f][1,3,2]diazaborinin-10-yl)phenol* (1.0 mmol, 1.0 eq.) in 25 mL dichloromethane, a solution of glutaric anhydride (4.0 mmol, 4.0 eq.), DMAP (0.1 mmol, 0.1 eq.) and triethylamine in dichloromethane (25 mL) were added and stirred at reflux for 5 hours under N_2 atmosphere. The reaction mixture was washed with 0.1 M HCl (2 x 50 mL) and finally, with brine (50 mL). The combined organic phase was dried with sodium sulphate anhydrous and the solvent was evaporated to dryness under reduced pressure, yielding the product as an orangish solid. **^{1}H-NMR (300 MHz, $CDCl_3$, *δ*)**: 7.32 – 7.10 (m, 4H), 5.92 (s, 2H), 2.81 – 2.58 (m, 4H), 2.58 – 2.39 (m, 6H), 2.16 – 1.94 (m, 2H), 1.35 (s, 6H); **^{13}C-NMR (101 MHz, $CDCl_3$, *δ*)** 171.0, 169.4, 155.9, 151.3, 147.9, 143.3, 140.7, 138.7, 132.8, 131.6, 129.4, 126.8, 122.6, 121.6, 119.4, 33.2, 32.6, 20.0, 14.7, 14.7; **HRMS (ESI-TOF) m/z**: $[M+H]^+$ calcd for $C_{24}H_{24}BF_2N_2O_4$ 454,1875; found, 454.1990.

Synthesis of (S)-2-amino-3-methyl-*N*-propylbutanamide (HValPr). **HValPr** was synthesized as previously reported.[53]

Synthesis of (S)-2-amino-3-phenyl-*N*-propylpropanamide (HPhePr). **HPhePr** was synthesized as previously reported.[54]

Synthesis of benzyl tert-butyl (6-oxo-6-(propylamino)hexane-1,5-diyl)(S)-dicarbamate (ZLys(Boc)Pr)

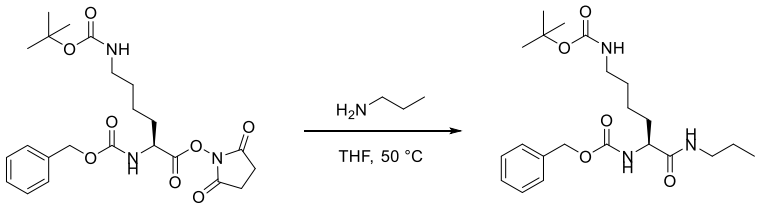

ZLys(Boc)OSu **ZLys(Boc)Pr**

The commercially available *N*-hydroxysuccinimide ester, ZLys(Boc)OSu (5.34 mmol, 1 eq.), was dissolved in THF (50 mL). *N*-propylamine (5.34 mmol, 1 eq.) dissolved in THF (30 mL) was added dropwise and the resulting solution was stirred at 50 °C overnight under a nitrogen atmosphere. Then, the solvent was evaporated under vacuum. The resulting solid was washed with 0.1 M HCl (3 × 30 mL), with 0.1 M NaOH (30 mL) and finally with water (3 × 25 mL). The solid was filtered off, washed with diethyl ether and dried in vacuo at 50 °C overnight to furnish **ZLys(Boc)Pr** as a white solid (Yield = 93%). **^{1}H-NMR (400 MHz, DMSO-d_6, δ)**: 7.81 (t, *J* = 5.5 Hz, 1H), 7.43 – 7.23 (m, 6H), 6.73 (t, *J* = 5.3 Hz, 1H), 5.01 (s, *J* = 13.1 Hz, 2H), 3.89 (dd, *J* = 13.7, 8.1 Hz, 1H), 3.11 – 2.92 (m, 2H), 2.92 – 2.79 (m, 2H), 1.62 – 1.45 (m, 2H), 1.42 – 1.17 (m, 15H), 0.82 (t, *J* = 7.4 Hz, 3H); **^{13}C-NMR (101 MHz, DMSO-d_6, δ)**: 171.7, 155.9, 155.6, 137.1, 128.3, 127.7, 127.7,

77.3, 65.3, 54.7, 31.8, 29.2, 28.3, 25.2, 22.8, 22.3, 11.3; **HRMS (ESI-TOF) m/z**: $[M+H]^+$ calcd for $C_{22}H_{35}N_3O_5$ 422.2655; found, 422.2646.

Synthesis of (S)-5-(((benzyloxy)carbonyl)amino)-6-oxo-6-(propylamino)-hexan-1-aminium trifluoroacetate (ZLys(Boc)Pr·TFA)

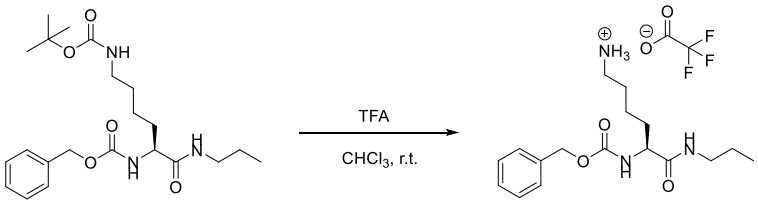

ZLys(Boc)Pr **ZLysPr·TFA**

To a solution of the *N*-protected compound **ZLys(Boc)Pr** (500 mg, 1.2 mmol) in chloroform (15 mL), TFA (2.4 mL, 2 mL $mmol^{-1}$ of Boc-protected amino derivative) was added. The mixture was stirred at room temperature for 4 h. The solvent was evaporated under vacuum and then the resulting crude oil was washed with diethyl ether to a white solid compound. The respective crude, deprotected amine TFA salt, was used in the next reaction without further purification.**^{1}H-NMR (300 MHz, DMSO-d_6, δ)**: 7.84 (t, *J* = 5.6 Hz, 1H), 7.63 (s, 3H), 7.42 – 7.24 (m, 6H), 5.02 (s, 2H), 3.91 (dd, *J* = 13.7, 8.9 Hz, 1H), 3.08 – 2.91 (m, 2H), 2.87 – 2.65 (m, 2H), 1.67 – 1.19 (m, 8H), 0.82 (t, *J* = 7.4 Hz, 3H).

Synthesis of benzyl (S)-(6-(dimethylamino)-1-oxo-1-(propylamino)hexan-2-yl)carbamate (ZLys(Me)$_2$Pr)

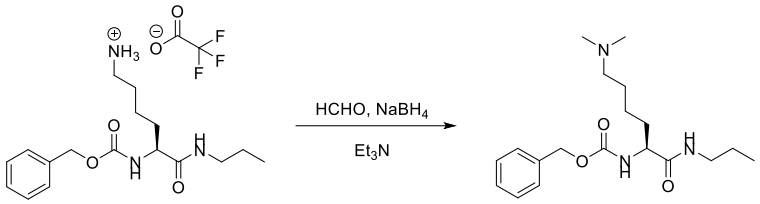

ZLysPr·TFA **ZLys(Me)$_2$Pr**

To a solution of **ZLysPr·TFA** (1.19 mmol, 1 eq.) in MeOH (15 mL), freshly distilled triethylamine (1.31 mmol, 1.1 eq.) was added. Then, a solution of 37% formaldehyde (4.52 mmol, 3.8 eq.) in MeOH (80.0 ml) was added dropwise and the mixture was stirred at room temperature for 45 minutes under a nitrogen atmosphere. The reaction mixture was cooled to 0 °C and solid $NaBH_4$ was added in portions (4.52 mmol, 3.8 eq.), stirring for further 30 minutes. After that, the ice bath is removed and the mixture is stirred for 4 hours at room temperature. The reaction was stopped by adding, dropwise, distilled water (5 mL). The organic solvent was evaporated under vacuum and then the resulting solution was extracted with ethyl acetate (2 x 30 mL). Then, the organic layer was washed with 0.1 M HCl (15 mL), 0.1 M NaOH (15 mL) and brine (15 mL), dried over Na_2SO_4, and finally, concentrated under reduced pressure to give **ZLys(Me)$_2$Pr** as a brownish solid (Yield = 76%). **^{1}H-NMR (400 MHz, $CDCl_3$, *δ*)**: 7.39 – 7.28 (m, 5H), 6.38 (s, 1H), 5.62 (d, *J* = 7.1 Hz, 1H), 5.10 (s, 2H), 4.12 – 4.01 (m, 1H), 3.26 – 3.11 (m, 2H), 2.36 – 2.22 (m, 2H), 2.20 (s, 6H), 1.90 – 1.74 (m, 1H), 1.70 – 1.58 (m, 1H), 1.58 – 1.44 (m, 4H), 1.44 – 1.31 (m, 2H), 0.90 (t, *J* = 7.4 Hz, 3H); **^{13}C-NMR (101 MHz, $CDCl_3$, *δ*)**: 171.7, 156.4, 136.4, 128.7, 128.3, 128.2, 67.1, 59.1, 55.2, 45.4, 41.4, 32.5, 27.1, 23.0, 23.0, 11.5; **HRMS (ESI-TOF) m/z**: $[M+H]^+$ calcd for $C_{19}H_{31}N_3O_3$ 350.2444; found, 350.2446.

Synthesis of (S)-2-amino-6-(dimethylamino)-N-propylhexanamide (HLys(Me)$_2$Pr)

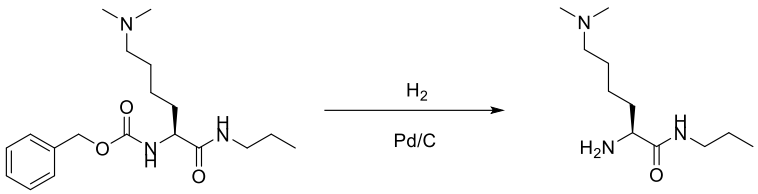

ZLys(Me)$_2$Pr **HLys(Me)$_2$Pr**

A similar procedure to that described for **HValValPr** was used starting from the *N*-Cbz-protected amino derivative **ZLys(Me)$_2$Pr**. A colorless oil was obtained (yield 84%). **^{1}H-NMR (400 MHz, CDCl$_3$, *δ*)**: 7.29 (s, 1H), 3.34 (m, 1H), 3.21 (m, 2H), 2.28 (t, *J* = 6.5 Hz, 2H), 2.22 (s, 6H), 1.88 (m, 1H), 1.63 – 1.35 (m, 9H), 0.93 (t, *J* = 7.4 Hz, 3H); **^{13}C-NMR (101 MHz, CDCl$_3$, *δ*)**: 175.1, 59.7, 55.4, 45.6, 40.9, 35.2, 27.6, 23.9, 23.1, 11.6; **HRMS (ESI-TOF) m/z**: $[M+H]^+$ calcd for $C_{11}H_{25}N_3O$ 216.2076; found, 216.2078.

Synthesis of benzyl ((S)-3-methyl-1-(((S)-3-methyl-1-oxo-1-(propylamino)butan-2-yl)amino)-1-oxobutan-2-yl)carbamate (ZValValPr)

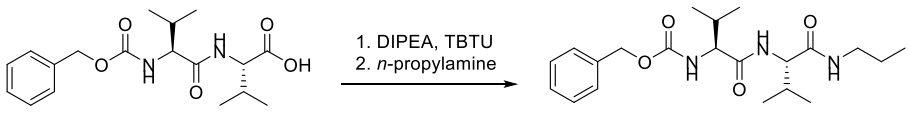

ZValValOH **ZValValPr**

To a stirred solution of commercially available carbobenzyloxy-L-amino acid (**ZValValOH**) (0.85 mmol, 1 eq.) in $CHCl_3$ (10 mL) at room temperature, DIPEA (*N*,*N*-diisopropyl-*N*-ethylamine, 0.94 mmol, 1.1 eq.) is added. Subsequently,

TBTU (*O*-(Benzotriazol-1-yl)-*N*,*N*,*N*',*N*',-tetramethyluronium tetrafluoroborate, 0.94 mmol, 1.1 eq.) is added, and the mixture is stirred for additional 25 minutes. Then, *n*-propylamine (0.85 mmol, 1 eq.) is added and the reaction mixture was stirred overnight. After, the reaction mixture was evaporated to dryness under reduced pressure. The residue is washed with 1 M HCl (10 mL, x2), 1 M NaOH (10 mL, x2) and finally, water (10 mL). The solid obtained was dried under reduced pressure at 50 ºC overnight. **^{1}H-NMR (400 MHz, DMSO-*d*$_6$, *δ*)**: 7.90 (t, *J* = 5.3 Hz, 1H), 7.65 (d, *J* = 9.0 Hz, 1H), 7.38 – 7.25 (m, 6H), 5.04 (s, *J* = 15.0 Hz, 2H), 4.17 – 4.04 (m, 1H), 3.90 (dd, *J* = 8.7, 7.1 Hz, 1H), 3.13 – 2.89 (m, 2H), 2.08 – 1.81 (m, 2H), 1.48 – 1.30 (m, 2H), 0.95 – 0.69 (m, 15H); **^{13}C-NMR (101 MHz, DMSO-*d*$_6$, *δ*)**: 170.9, 170.5, 156.1, 137.1, 128.3, 127.7, 127.6, 65.3, 60.4, 57.7, 30.7, 30.1, 22.2, 19.2, 19.1, 18.2, 18.1, 11.3; **HRMS (ESI-TOF) m/z**: $[M+H]^+$ calcd for $C_{21}H_{33}N_3O_4$ 392.2549; found, 392.2544.

Synthesis of (S)-2-amino-3-methyl-N-((S)-3-methyl-1-oxo-1-(propyl-amino)butan-2-yl)butanamide (HValValPr)

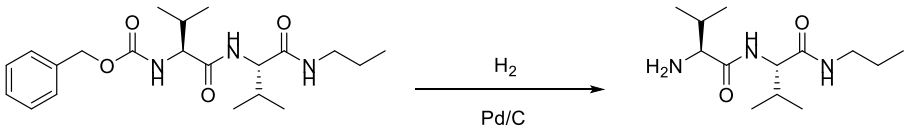

ZValValPr **HValValPr**

Palladium catalyst (10% w/w) was suspended in MeOH (250 mL) and stirred under H_2 at room temperature for 10 min. Subsequently, a solution of **ZValValPr** in MeOH (150 mL) was added via syringe, followed by stirring under H_2 at room temperature for 2–4 h. The reaction mixture was then filtered through HPLC filters (0.46 µm), and the solvent was removed under reduced pressure to yield respective amine, which was used in the next reaction without further

purification. **^{1}H-NMR (500 MHz, $CDCl_3$, δ)**: 7.88 (d, *J* = 8.4 Hz, 1H), 6.27 (t, 1H), 4.11 (dd, *J* = 8.9, 7.5 Hz, 1H), 3.32 – 3.08 (m, 3H), 2.35 – 2.22 (m, 1H), 2.22 – 2.10 (m, 1H), 1.56 – 1.44 (m, 2H), 1.30 (br s, 2H), 1.05 – 0.76 (m, 15H); **HRMS (ESI-TOF) m/z**: $[M+H]^+$ calcd for $C_{13}H_{27}N_3O_2$ 258.2176; found, 258.2182.

7. NMR Section

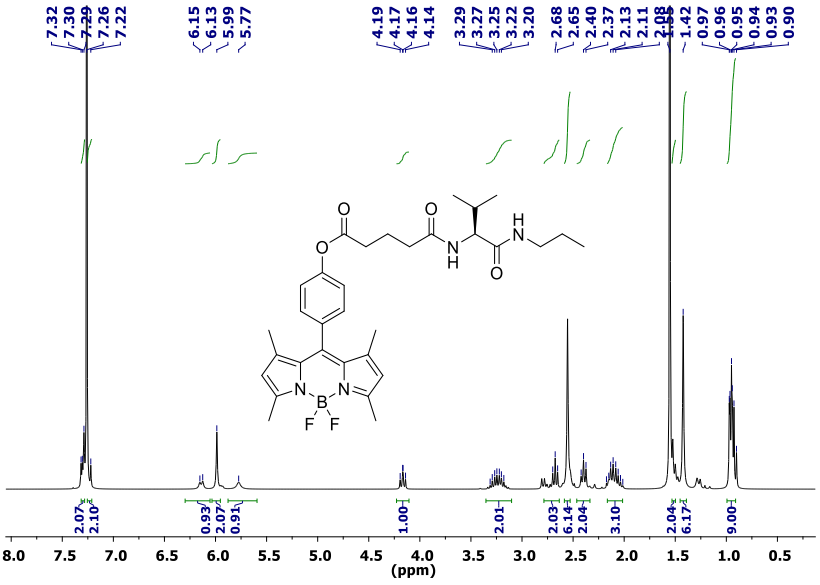

Figure S6.9. ^{1}H-NMR of **1**

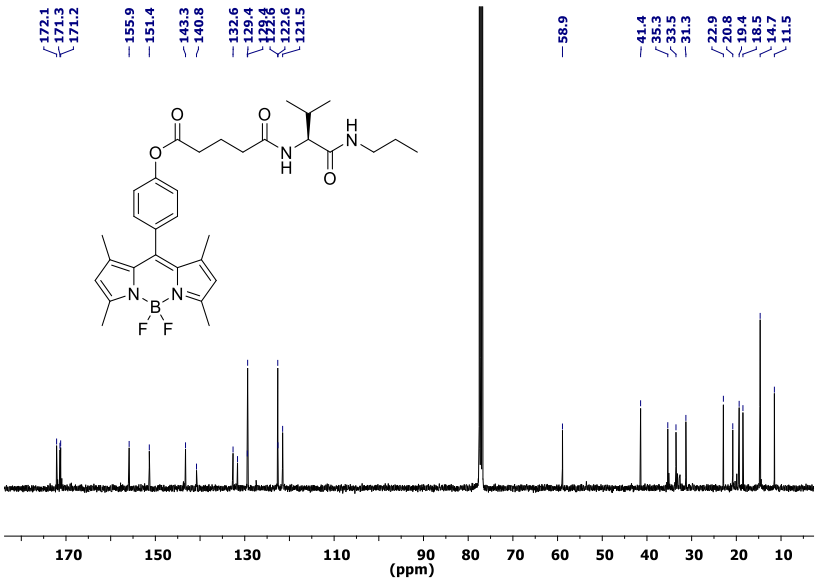

Figure S6.10. ^{13}C-NMR of **1**

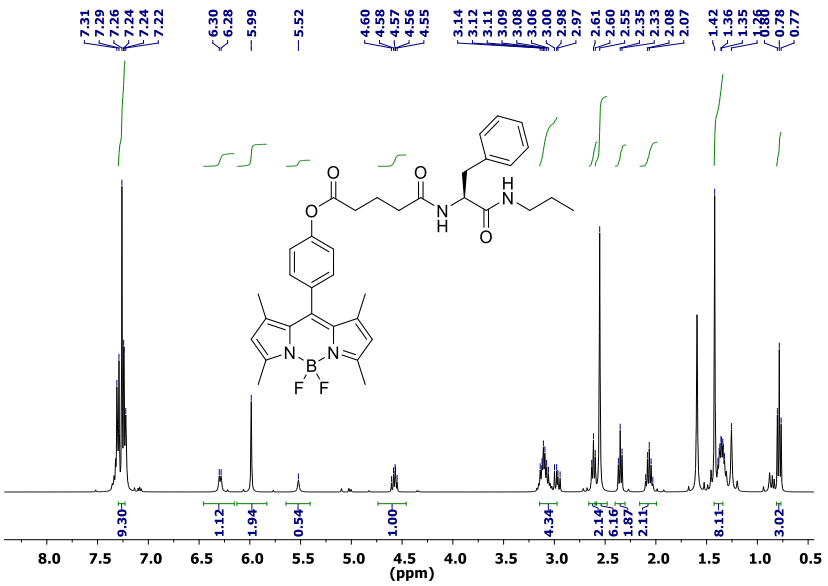

Figure S6.11. ^{1}H-NMR of **2**

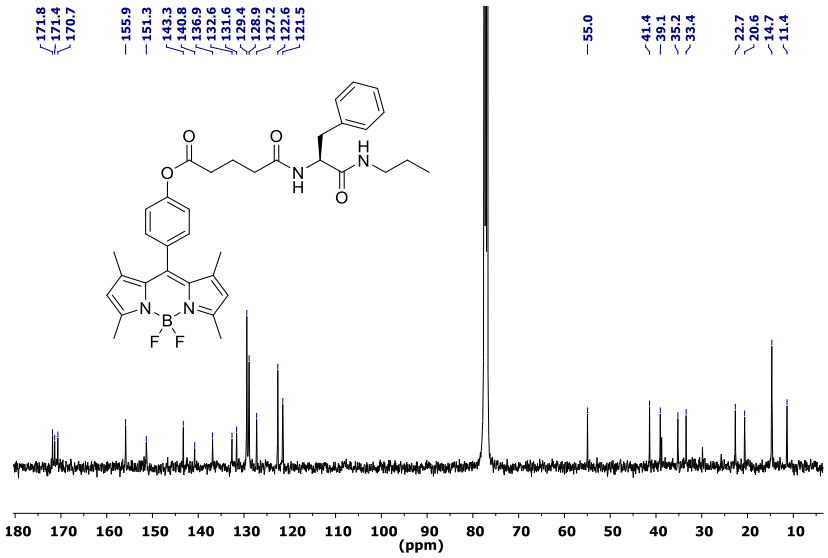

Figure S6.12. ^{13}C-NMR of **2**

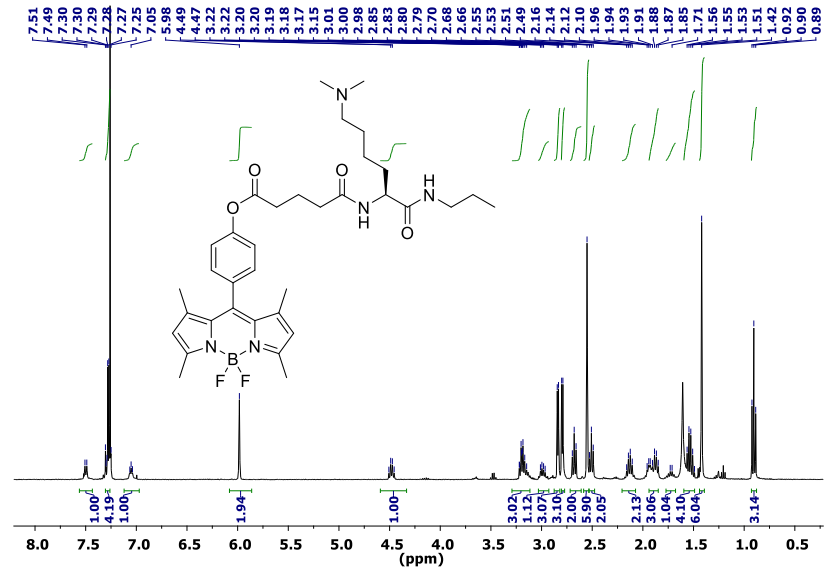

Figure S6.13. ^{1}H-NMR of **3**

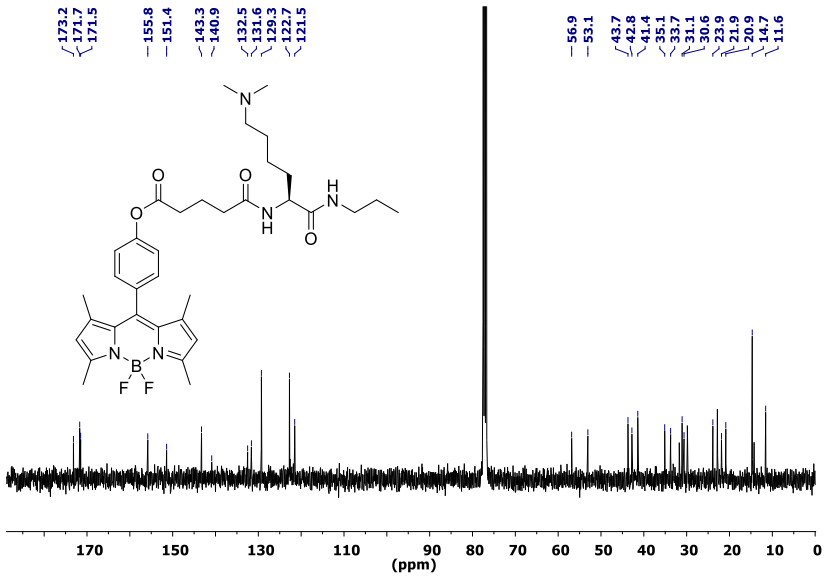

Figure S6.14. ^{13}C-NMR of **3**

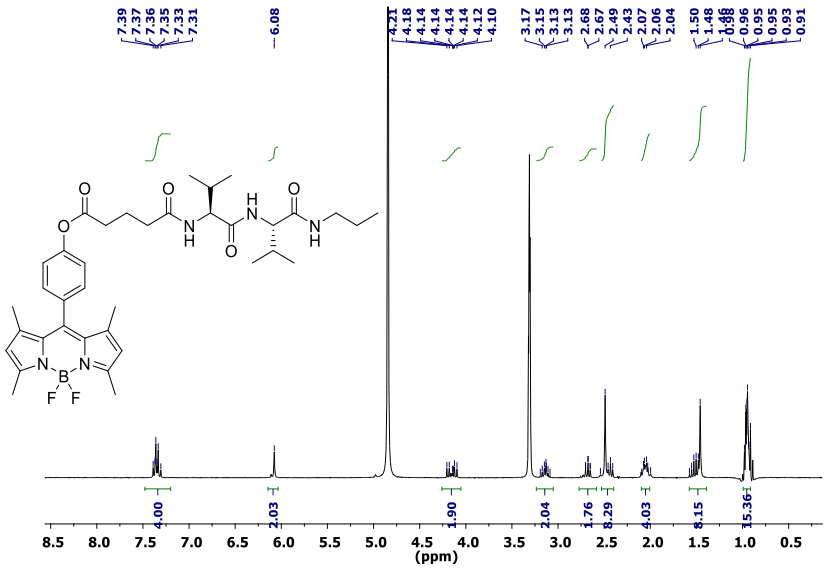

Figure S6.15. ^{1}H-NMR of **4**

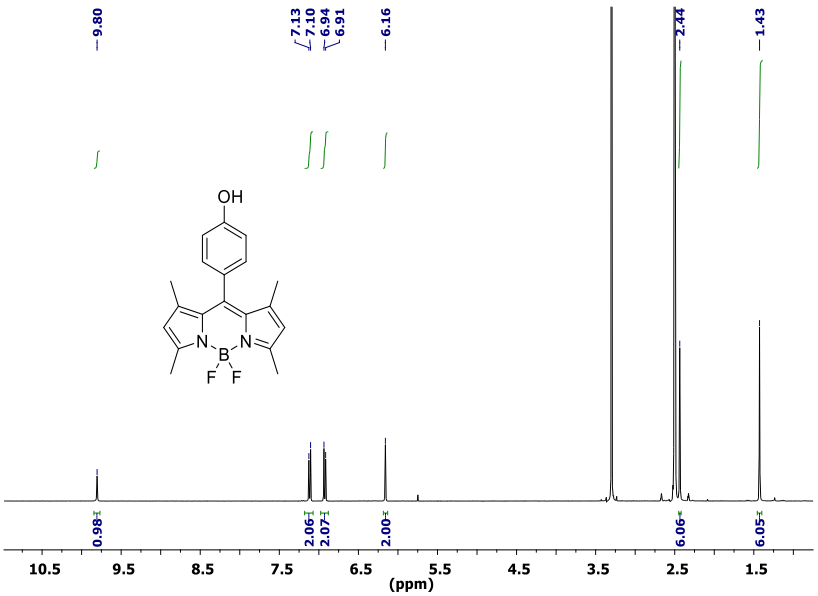

Figure S6.16. ^{1}H-NMR of A

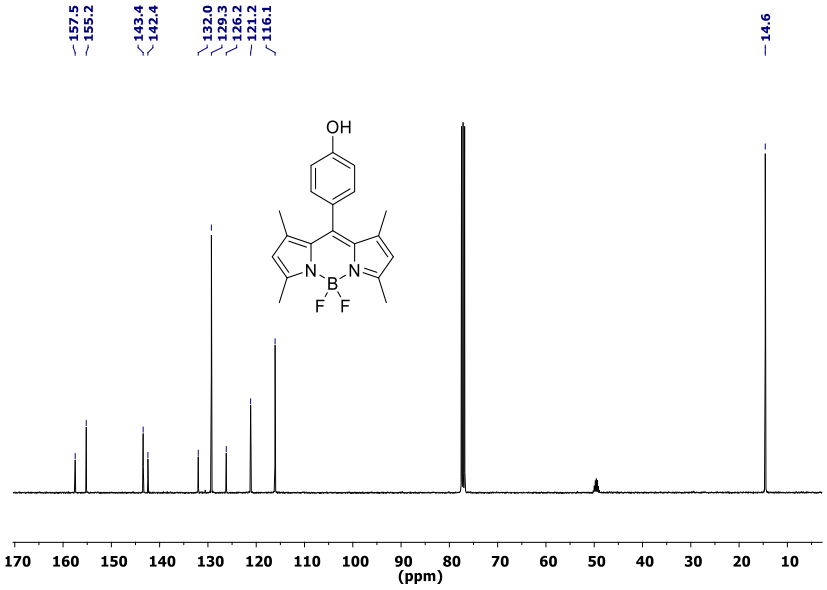

Figure S6.17. ^{13}C-NMR of A

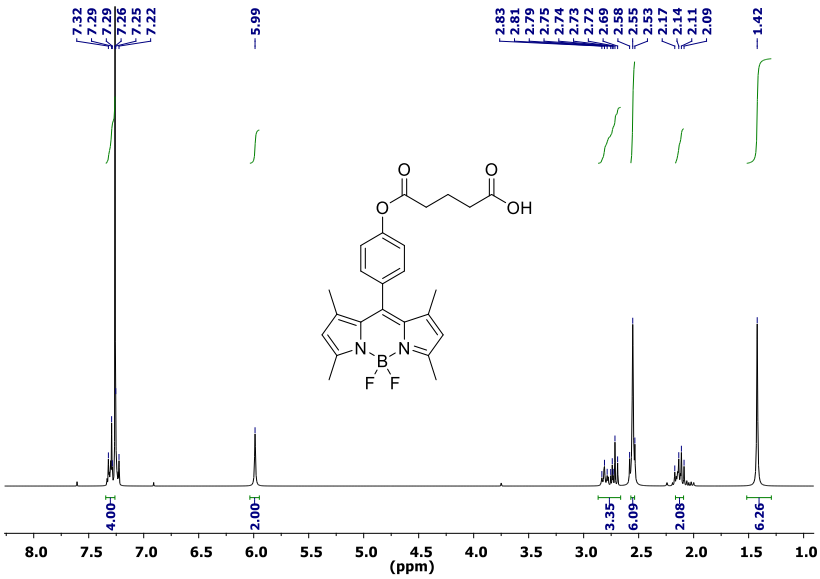

Figure S6.18. ^{1}H-NMR of B

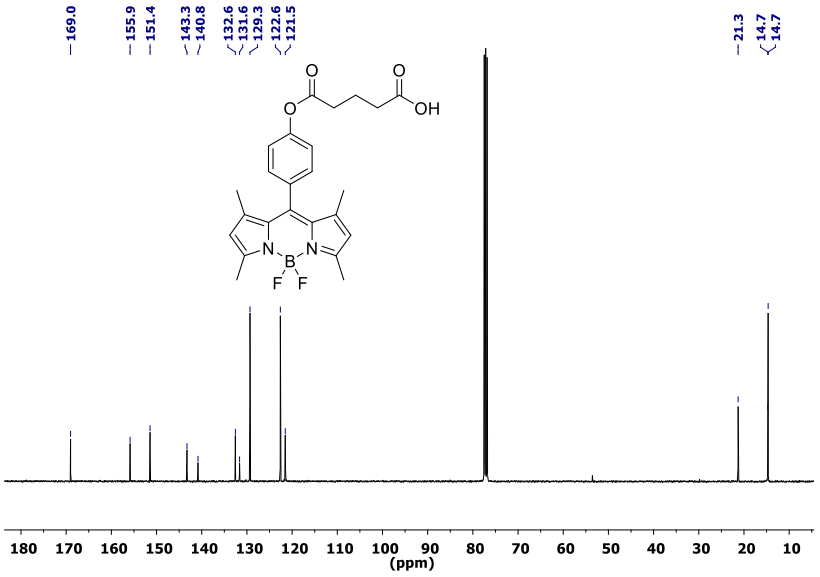

Figure S6.19. ^{13}C-NMR of B

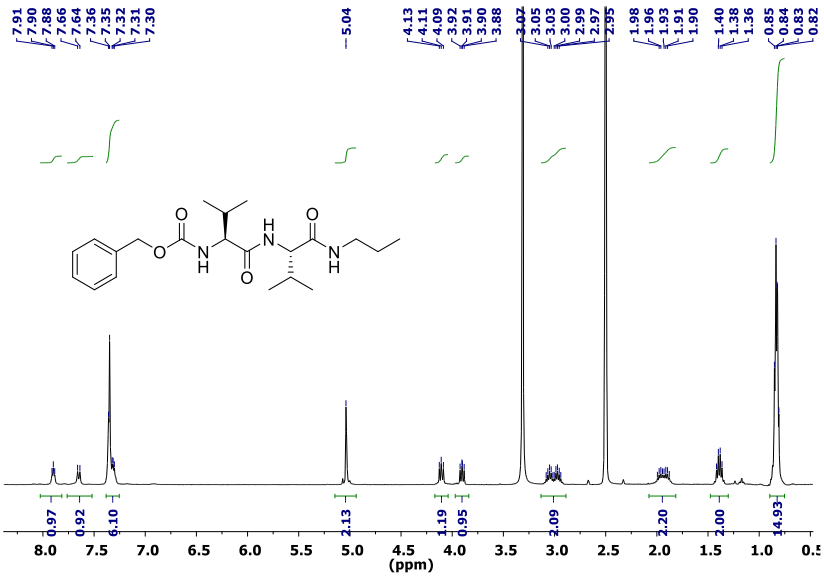

Figure S6.20. ^{1}H-NMR of ZValValPr

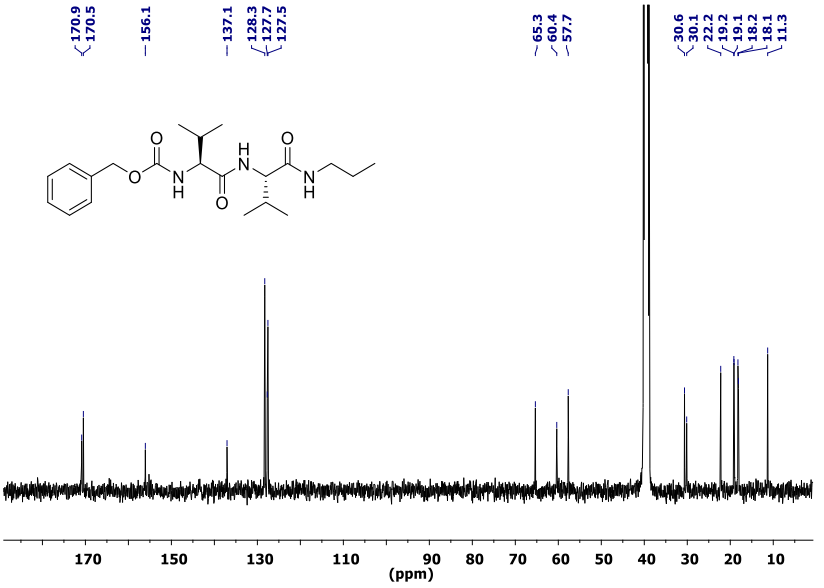

Figure S6.21. ^{13}C-NMR of ZValValPr

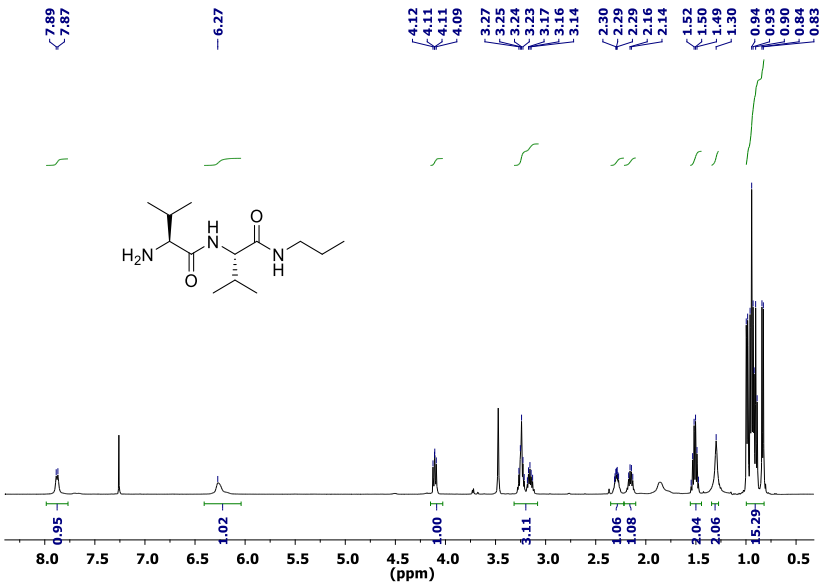

Figure S6.22. ^{1}H-NMR of HValValPr

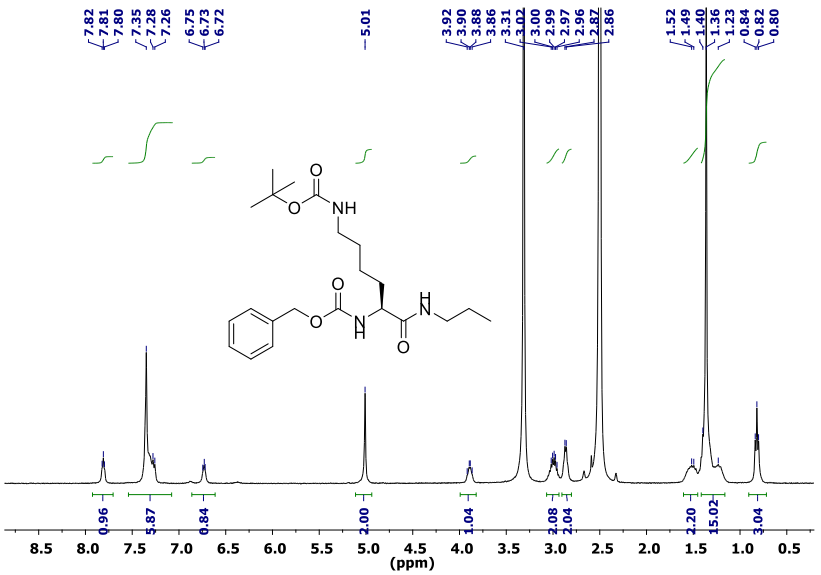

Figure S6.23. ^{1}H-NMR of ZLys(Boc)Pr

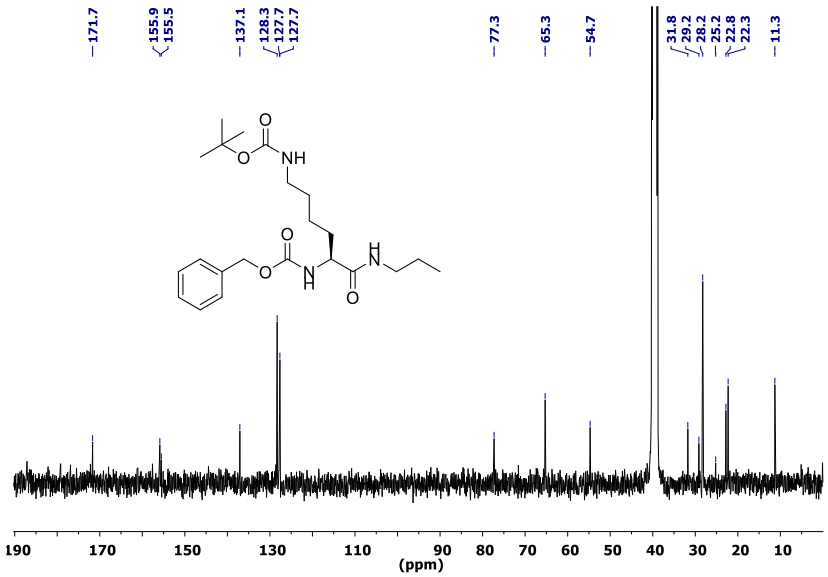

Figure S6.24. ^{13}C-NMR of ZLys(Boc)Pr

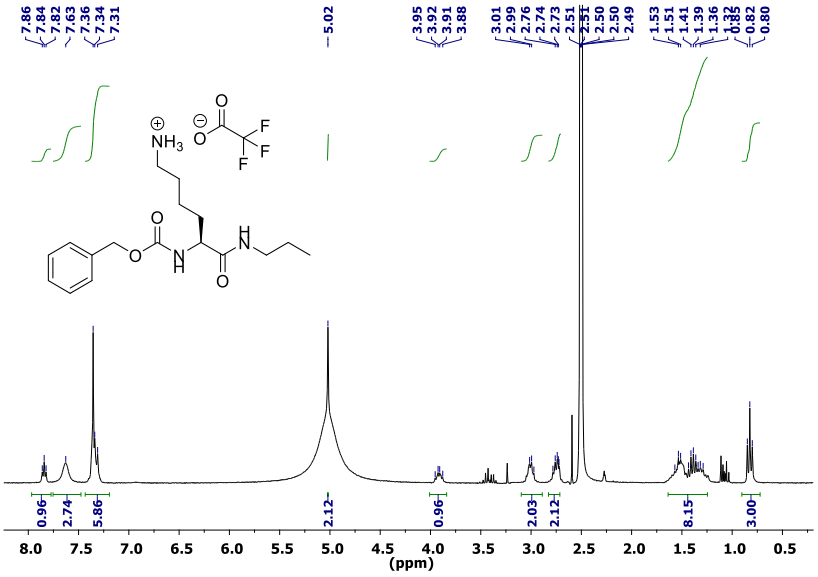

Figure S6.25. ^{1}H-NMR of ZLysPr·TFA

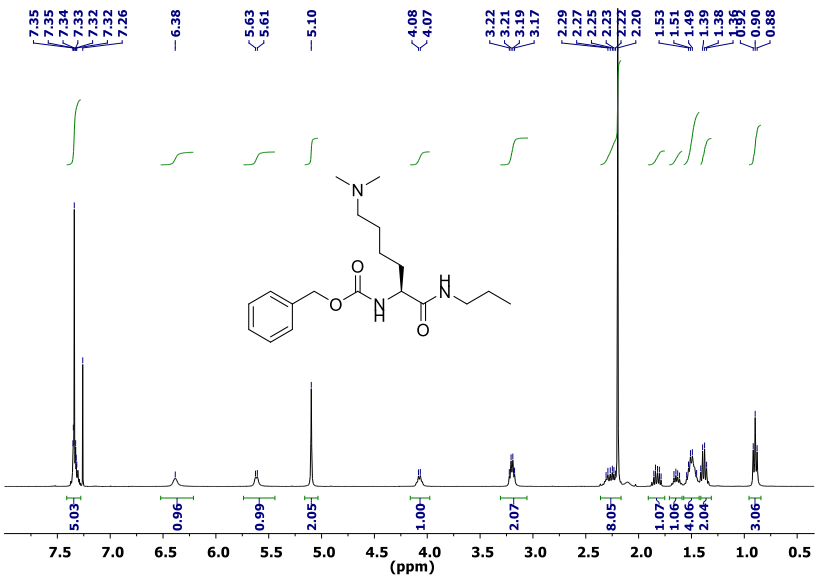

Figure S6.26. ^{1}H-NMR of ZLys(Me)$_2$Pr

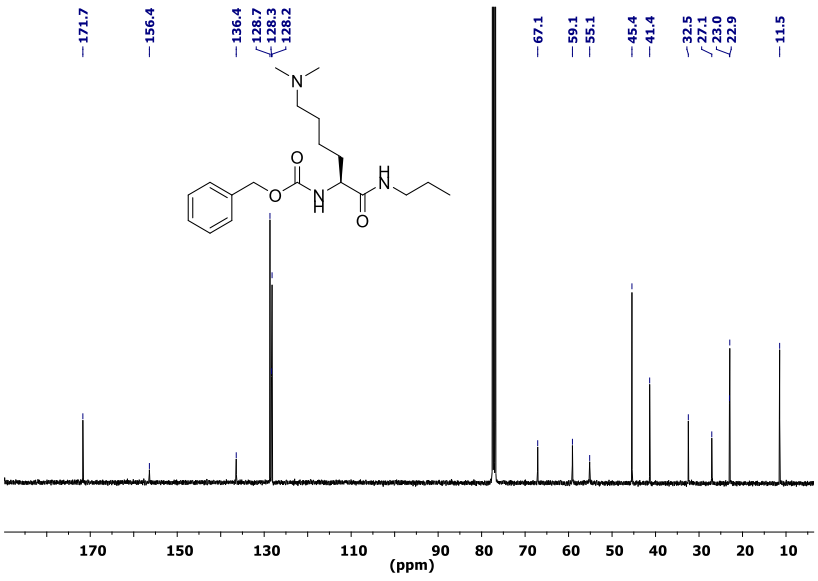

Figure S6.27. ^{13}C-NMR of ZLys(Me)$_2$Pr

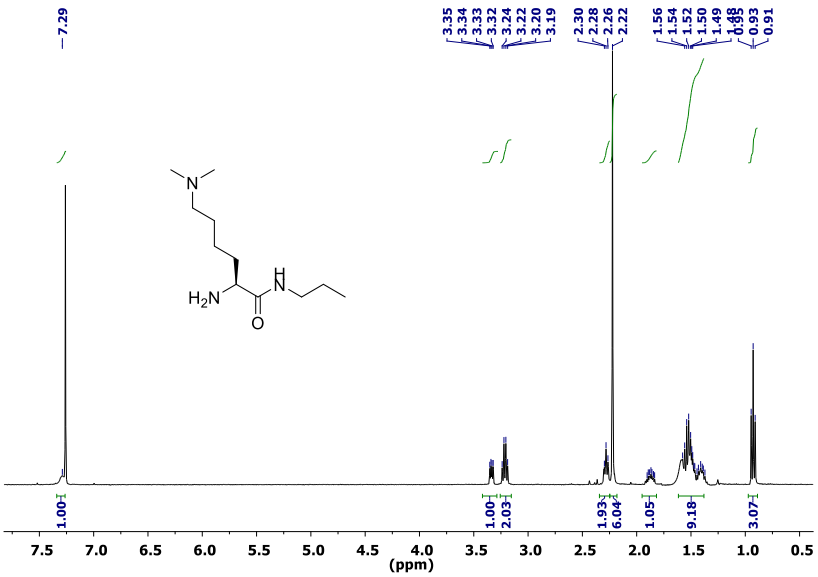

Figure S6.28. ^{1}H-NMR of HLys(Me)$_2$Pr

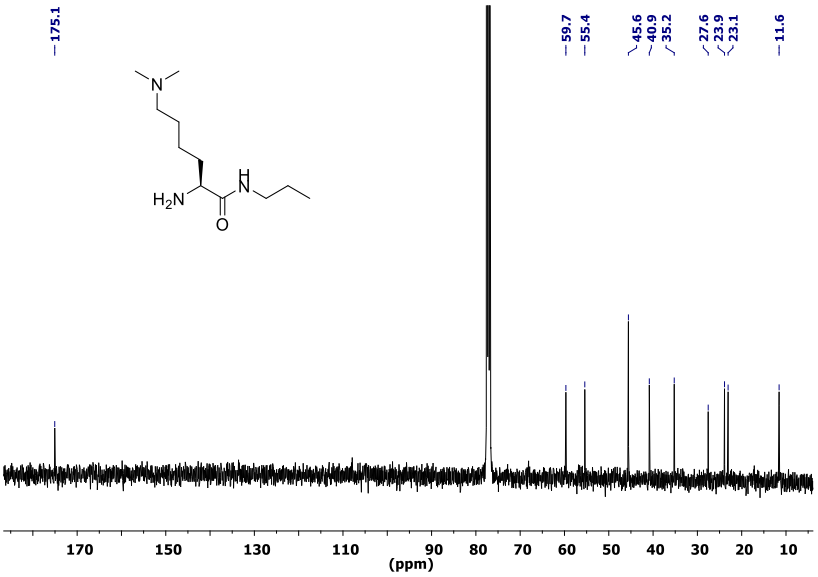

Figure S6.29. ^{13}C-NMR of HLys(Me)$_2$Pr

Chapter 7

General Discussions

The development of stimuli-responsive materials is undoubtedly a major focus for the scientific community and, particularly, for biomedical and health research. Stimuli-responsive materials constitute a new platform for preventing, diagnosing, and treating many diseases. These systems are sensitive to specific triggers changing their structures, compositions or conformations at a target site or tissue in the body to actuate therapeutic/diagnostic activities at the site of action. The triggers can be external (temperature, light, magnetic and electrical field, ultrasound, etc.) or internal (enzymes, pH, redox, etc.). In the latter case, these systems are also called "environmentally-responsive materials" as they respond to biological signals or pathological abnormalities. This responsive behaviour enhances the specificity, accuracy and efficacy of therapies that lead to non-invasive or minimally invasive approaches. Many of these 'smart' delivery systems are based on hydrogels and nanoparticles. In the hope of creating new intelligent delivery systems, a large part of the work carried out in this thesis has focused on the development of amino acid derivatives that are self-assembled into functional materials at the macro- and nanoscale.

A Dual Stimuli Responsive Supramolecular Gel Provides Insulin Hydrolysis Protection and Redox-Controlled Release of Actives (Chapter 3)

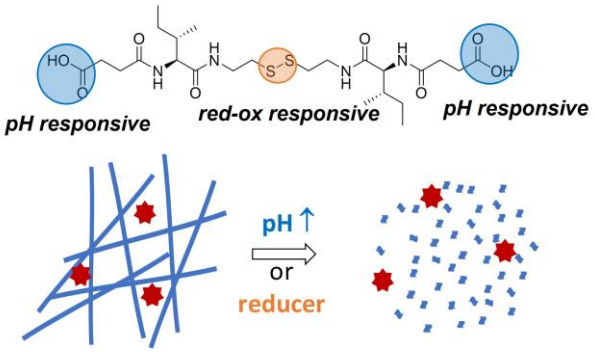

As described in **Chapter 3**, we prepared and studied two supra-molecular hydrogelators (named as **SucIleCsa** and **GltValCsa**) containing a central disulfide moiety and terminal carboxylic acid groups. The hydrogels reported were responsive to a reductive environment, which transforms the disulfide unit to the corresponding thiols, and showed pH-response associated with the presence of carboxylic acid units. We observed that gels were formed at acidic pH (neutral form, pK_a values of 4-5) while ionization of the gelators provoked gel disassembly at higher pH values. Gels were prepared by the precipitation method using hydrochloric acid/sodium hydroxide solutions. Their properties were assessed using T_{gel}, rheology, transmission electron microscopy, and confocal scanning laser microscopy. Very interestingly, we observed that **SucIleCsa** and **GltValCsa** fibrillar network morphology differed notably despite being isomers. The gels of **GltValCsa** were formed by flat and straight fibres whereas, in **SucIleCsa** gels, the fibres were curved and thinner. Unfortunately, the rationalization of these differences was far from trivial. The prediction of aggregate morphology based on the structure of the molecule involved is still a significant challenge today.

After demonstrating the reductive- and pH- responsiveness nature of the gels by NMR spectroscopy and visual inspections, we aimed to validate these systems as stimuli-responsive drug delivery systems (DDSs) as we envisaged that disulfide bond reduction and carboxylic acid ionization could potentially be used for the controlled, progressive discharge of species entrapped in the hydrogels. To test this idea, bromophenol blue dye (as a proof-of-concept) was loaded in hydrogels of **SucIleCsa** and **GltValCsa** in the presence of TCEP, a well-known reducing agent capable of breaking disulfide bonds into thiol units. The gels of **SucIleCsa** showed a steady release of the dye for 24 hours, because of the progressive gel disassembly triggered by TCEP-mediated disulfide bound

reduction. Control experiments in the absence of TCEP showed a partial liberation of bromophenol blue, which corresponds to the fraction of the dye loosely adsorbed on the fibrillary network and leaches out by diffusion. Similar results were obtained in the case of **GltValCsa,** although in this case the amount of dye released by diffusion out of the fibrillary network in the absence of TCEP was higher. We suggested that this behaviour was probably due to the differences in the morphology of the gel networks pointed by electron microscopy.

Regarding the pH-responsiveness nature of the gels, we exploited the entrapment and subsequent liberation of the hormone insulin. We wanted to do our bit in developing technology-driven medicine for diabetes, as one of the leading causes of premature death worldwide. Insulin oral delivery remains a preferential drug administration route as it is a non-invasive, on-demand approach. However, when it is administered orally, insulin is oxidized and denatured either in the acid environment of the gastrointestinal (GI) tract or by gastric enzymes losing their therapeutic activity.

We demonstrated that insulin loaded into the gels resisted degradation in the presence of simulated gastric fluid. The fibrillar network of the gel protects insulin from pepsin that, due to its macromolecular nature, probably diffuses very slowly into the gel. Changing pH from acidic to neutral (pH 7.4), as occurs in the gastrointestinal tract, results in gelator solubilization and insulin release. ELISA analysis shows that insulin released from the gel is recovered quantitatively whereas it is completely hydrolyzed in the absence of gel. Therefore, we underscore that the described hydrogelators showed successful results in the proof-of-concept experiment of protection and insulin release. This behaviour would permit the use of these new hydrogels for oral insulin delivery.

Glutathione-responsive molecular nanoparticles from a dianionic bolaamphiphile and their use as carriers for targeted delivery (Chapter 4)

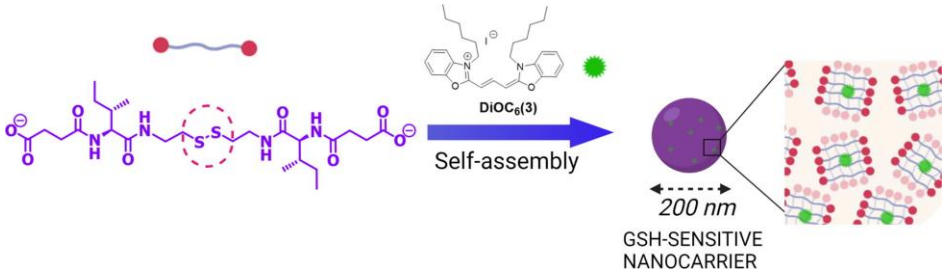

Nanomedicine, defined as the application of nanotechnology to medicine, has become the most promising approach to diagnosing and treating diseases, which was the strength that motivated us to enter the field of nanomaterials. To move a step beyond our previous studies in molecular nanoparticles, in **Chapter 4**, we described the formation of nanoparticles from the bolaamphiphile **SucIleCsa** (molecule previously used for the hydrogels in Chapter 3).

It was observed by dynamic light scattering (DLS) that this molecule formed negatively charged nanoparticles (zeta-potential measurements) with an averaged diameter of *ca.* 200 nm at neutral pH. To understand the aggregation phenomena of the nanoparticles, we carried out molecular modelling and electron microscopy experiments. Molecular modelling of the monosodium salt of SucIleCsa (AM1 calculations) did not show a sufficient separation of the hydrophobic and hydrophilic moieties to justify the formation of U-shaped micelles. We observed by electron microscopy that the particles presented a granular appearance, suggesting that the combination of smaller units could form them. Therefore, we conclude that **SucIleCsa** formed micelles by adopting

an extended conformation that evolved into micellar clusters, acting the cations in the medium as intermicellar bridges.

To reinforce this assumption, we studied the nanoparticles in diverse aqueous media (HEPES *vs.* PBS) and we noticed significant differences in the intensity of scattered light recorded by DLS. As the **SucIleCsa** molecule presents a disulfide bond, we envisaged that the resulting nanoparticles would be sensitive to reductive species, which allowed us to develop a stimuli-responsive nanosystem. DLS, NMR and mass spectrometry measurements confirmed the responsiveness of the nanoparticles to reducing agents (DTT and GSH). Here, we proposed the assessment of the intensity of the dispersed light (*derived count rate* parameter) as a reliable method to analyze particle disaggregation in response to stimuli, instead of size distribution or polydispersity changes.

From the applied point of view, we aimed to study the capabilities of **SucIleCsa** nanoparticles to be used as a nanocarrier. It is worth mentioning that the use of bolaamphiphilic molecules as building blocks of nanocarriers is almost unexplored, being our systems one of the first examples reported in the literature. Our UV-Vis studies indicated that the nanoparticles could load and release the lipophilic mitochondrial marker **$DiOC_6$(3)** efficiently. We demonstrated, using a biphasic system (DCM/H_2O), that the encapsulated dye was kept in the aqueous phase, but the addition of GSH provoked the disassembly of the nanoparticles leading to the release and subsequent migration of the lipophilic dye into the organic phase.

Next, we studied the transport into adenocarcinoma cells (HT-29) of the lipophilic mitochondrial dye $DiOC_6$(3) using the nanoparticles as a vehicle. From our observations using flow cytometry and confocal scanning fluorescence

microscopy, we stated that the use of the nanocarrier significantly improves the incorporation of the dye into the cells and that the increased fluorescence observed using the nanoparticles must be linked to particle disassembly, which is accelerated by the increased of GSH concentration when the cells are stimulated with NACET (a glutathione enhancer). Overall, GSH-sensitive nanoparticles are of foremost importance to target, treat and signal cells with overexpression of GSH, like those associated with many cancers. Our nanoparticles presented promising properties for both the enhanced internalization of payloads into cancer cells without altering their therapeutic activity and the signalling of cells with higher levels of GSH, hence making our nanoparticles an exciting candidate for their use in theranostics applications.

Photoreversible formation of nanotubes in water from an amphiphilic azobenzene derivative (Chapter 5)

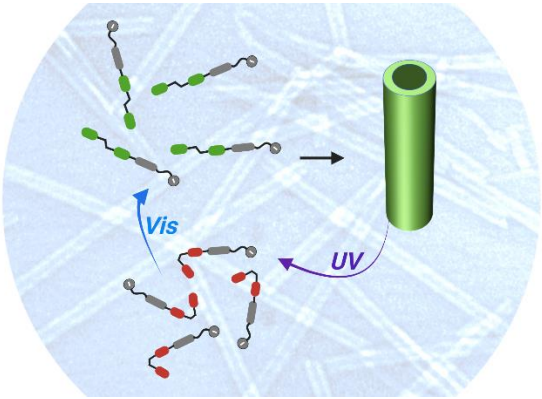

Light is one of the most outstanding external stimuli used for nanotechnology, chemical biology, and material science because it provides a non-invasive approach with spatial and temporal control by simply tuning the wavelengths and intensities of the light sources. Understanding such importance, we

proposed in **Chapter 5** developing a photoresponsive and adaptive (nano)material controlled by light.

For this purpose, we synthesized an amphiphilic dipeptide based on valine and glycine with an appended azobenzene, a photoresponsive moiety widely exploited in photocontrollable self-assembled switches. We observed by dynamic light scattering that **SucValGlyAzo**, in the anionic form (Tris buffer at pH 7.4), yielded a signal dispersion compatible with nanoobjects of *ca.* 100 nanometers.

Next, we studied the morphology of the objects detected by DLS and realized that they correspond to nanotubes with a monodisperse diameter distribution of 23 nm and a wall thickness of 9 nm. We also studied morphology by Cryo-TEM. The results supported the formation of nanotubes, although twisted tapes were also detected. We suggested that **SucValGlyAzo** formed an amphiphilic bilayer that originated a tape that twists into nanotubes, being the hydrophobic and aromatic stacking interactions the driving forces for the self-assembly process.

The photoresponsive of nanotubes was studied by UV-Vis spectroscopy. The reversible *trans-cis* photoisomerization upon irradiation with ultraviolet (365 nm) and visible (457 nm) light was confirmed by monitoring the absorption bands at *ca.* 340 nm and 440 nm. Interestingly, DLS analysis revealed that the *trans-cis* isomerization resulted in nanotube disassembly. The UV-promoted nanotube disassembly could be rationalized considering that *trans*-azobenzene is almost flat and has no dipole moment. In contrast, the *cis* isomer presents an angular geometry and a dipole moment. This dramatic change would affect

intermolecular interactions like aromatic stacking, which were responsible for the self-assembly process.

In our studies, we presented the DLS results as a function of the diffusion coefficients and the apparent diameter because DLS calculations assume spherical particles for the size distribution analysis. After thermal and photoinduced *cis-trans* isomerization, scattered light was detected in samples of **SucValGlyAzo**, which allow us to confirm that the thermal and photoinduced recovery of the *trans* isomer restored the nanotubes.

This photoisomerization-controlled self-assembly process was also monitored using the fluorescent probe Nile red. Nile red showed an intense emission (λ_{max} = 625 nm), indicating the incorporation of the dye in hydrophobic regions of the nanotubes. Irradiation with UV light results in fluorescence quenching and peak shift to 660 nm, indicating the exposition of Nile red to the aqueous solvent due to light-promoted nanotube disaggregation. Then, irradiation with 457 nm light (30 seconds) provoked a notable fluorescence recovery after 30 min.

All things considered, we could affirm that we managed to develop a photocontrolled self-assembled nanosystem that presents suitable reversibility to be applied as a relevant tool for developing smart for biomedical applications. Thus, the capacity to load hydrophobic active agents and the subsequent release triggered by light stimulus represented a considerable advantage for envisaged practical applications.

Structure-performance relationships of four lysosomal markers used for the imaging of HT-29 cancer cells and a cellular model of lysosomal storage disease (Niemann-Pick C) (Chapter 6)

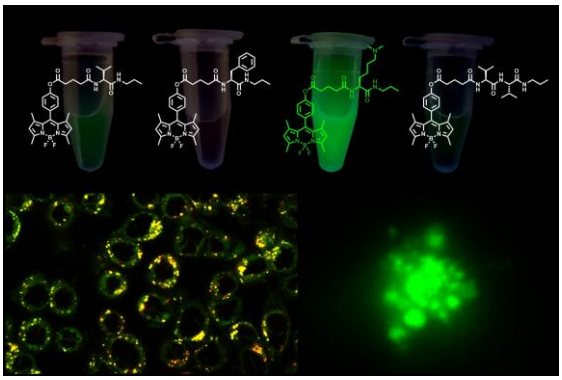

As stated throughout this thesis, the design of (nano)therapeutics/diagnostics to target and image specific cellular organelles (mitochondria, lysosomes, nucleus endoplasmic reticulum (ER), Golgi apparatus, etc.) is of utmost importance to fight and understand the processes that are going on in many human diseases. In particular, fluorescence imaging has emerged as a robust technique to study the disruption of intracellular homeostasis and alterations in organelle physiology.

BODIPY dyes can be highlighted among fluorescence probes for imaging due to their high photostabilities, high fluorescence quantum yields, and sharp absorption and emission spectra. By this account, we decided to synthesise four new molecules following the model of amino acid architectures previously described in our research group, which bore a BODIPY emitting core. In that study, we aimed to determine which structural factors of the pendant chain

influence most notably the cellular uptake, intracellular location and fluorescence imaging performance of the four molecules.

Before that, we assessed the photophysical properties of the synthesized BODIPY dyes. Our results indicated that all the described values were similar to the parameters reported in organic solvents for other BODIPY tagged molecules previously described in the literature. Nonetheless, it was noticed that in an aqueous environment (HEPES Buffer Solution, pH 7), three of the compounds (**1**, **2** and **4**) formed weakly emissive nanoparticles (DLS determination) at 10 μM. In contrast, one of them (**3**) remained soluble and thus, fluorescent. The absorption spectra of **1**, **2** and **4** were broadened, a type of spectral feature frequently described for BODIPY derivatives showing aggregation. We confirmed the formation of nanostructures at 10 μM is supported by Dynamic Light Scattering (DLS) measurements. Our studies indicated that samples of **1**, **2** and **4** in 0.1 M HEPES, pH 7.00 yielded signal dispersion compatible with nanoparticles of *ca.* 100 nm, but molecule **3** afforded only some background noise, which was ascribed to the complete solubilisation of this probe.

Once we noticed that aggregation preclude fluorescence performance, the ability of **1** - **4** to be incorporated intracellularly into human colon adenocarcinoma HT-29 cells was tested. A concentration of 10 nanomolar was employed to ensure that the molecules were unaggregated, at least at the initial state before intracellular accumulation. We observed that cells incubated with compounds **1** and **3** were those with higher fluorescence intensity, especially **3**, which provided a signal about 8-fold more intense.

As a next step, we attempted to study in more detail the fluorescence performance of our BODIPY family using confocal scanning laser microscopy.

Again, we demonstrated that molecule **3** was more accumulated, giving higher intensity signal and a more clear punctate pattern, which was tentatively assigned to the lysosomes. We confirm this hypothesis by doing colocalization assays using the commercially lysosomal marker LysoTracker DND-99 as a reference. Merging the images for the emissions of **1-4** and Lysotracker DND-99 gives a better matching (yellow colour) for **3** (Pearson's correlation coefficient of 0.88) than for **1, 2** and **4** (Pearson's correlation coefficients 0.63, 0.53 and 0.56, respectively). To expand the scope of application of the studied cellular probes, and considering the excellent lysosomal accumulation of **3**, we studied the distributions of **1** and **3** in a pharmacological cellular model of Niemann-Pick type C disease. We observed that **3** showed an excellent internalisation and lysosomal staining, reflecting the impact of the disorder. We suggested that the protonation of molecule **3** in the aqueous environment affords a better internalisation and fluorescence performance compared to the rest of the molecules. This mechanism of internalisation is found in many fluorescent dialkylamino-substituted probes.

Chapter 8

Conclusions

Amino acids derivatives attract attention for applications in biomedicine and biotechnology as they present good biocompatibility, reduce complexity in structural design and optimize synthetic costs, compared to polymers or long-chain peptides. Furthermore, depending on their molecular structures, these compounds can self-assemble, driven by intramolecular and intermolecular non-covalent forces, into diverse structures that range from a few nanometres to hundreds of microns (micelles, vesicles, nanotubes, fibres, gels, etc.). Interestingly, environmental factors can influence these structures, *e.g.*, pH, ionic strength, temperature, light, and chemical reactions, which provide the system with functionalities for specific outstanding applications (drug delivery, bioimaging, cell culture, and so on). Currently, there is widespread interest in developing stimuli-responsive materials.

The present Ph.D. thesis has focused on designing, developing, and studying self-assembled materials based on amino acids from fundamental science and applied research.

In **Chapter 3**, two **supra-molecular hydrogelators** containing a central disulfide moiety and terminal carboxylic acid groups were studied. Several conclusions could be drawn from this study: (i) relatively simple molecular gelators (named as **SucIleCsa** and **GltValCsa**) could be prepared quickly on a grams scale; (ii) the compounds formed fibrillar supra-molecular hydrogels in acidic media; (iii) the structural motif used in the preparation of the gelators (a cystamine core and carboxylic moieties) provided dual (red-ox and pH) stimuli responsiveness provoking gel disassembly; (iv) the described hydrogelators showed successful

results in the proof of concept experiment of loading, protection and controlled release of bioactive agents (a dye and insulin).

In **Chapter 4**, the formation in aqueous media of **molecular nanoparticles** from a bolaamphiphile (**SucIleCsa**) incorporating a disulfide moiety were described. There are several conclusions to draw from this work: (i) **SucIleCsa** formed negatively charged nanoparticles, seemingly constituted by micelle clusters with an averaged diameter of *ca.* 200 nm. (ii) the molecular nanoparticles, containing sensitive disulfide bonds, showed reduction responsiveness to reductants (DTT and GSH) in an aqueous environment; (iii) the nanoparticles could entrap hydrophobic substances (a mitochondrial dye), which demonstrated their use as nanocarriers; (iv) the fluorescence of **DiOC$_6$(3)** is quenched when loaded into the particles, most likely because of the proximity of the disulfide groups; (v) the addition of GSH provoked disassembly of the nanoparticles and controlled release of the payload; (vi) the nanocarrier significantly improves the incorporation of the dye into the cells; (vii) the increased fluorescence observed using the nanoparticles must be linked to particle disassembly; (viii) cells stimulated for overproduction of GSH shows a higher fluorescence, confirming that reductive nanoparticle disassembly is a crucial step in the process.

In **Chapter 5**, a light-controlled reversible formation of **nanotubes** from a derivative of L-ValGly with an appended azobenzene moiety was reported. From this study, it was concluded that: (i) An anionic azobenzene-appended derivative of L-ValylGlycine (named as **SucValGlyAzo**) was synthesized; (ii) **SucValGlyAzo** was a small, synthetically simple molecule that self-assembled into nanotubes in an aqueous environment at physiological pH values with a monodisperse diameter distribution of 23 nm and a wall thickness of 9 nm; (iii) the azobenzene unit imparted the required hydrophobic and presumably aromatic stacking

interactions for the self-assembly; (iv) irradiation with 365 nm light provoked *trans-cis* isomerization of the azobenzene unit and subsequent tube disassembly, (v) thermal or photoinduced (457 nm light) recovery of the trans isomer restored the nanotubes.

In **Chapter 6**, four new BODIPY derivatives bearing pendant amino acid building blocks were studied as **fluorescent biomarkers** of organelles within live cells. The conclusions resulting from this work were: (i) four BODIPY derivatives made with amino acid building blocks were synthesized and characterized; (ii) the photophysical properties of the new molecules are almost independent of the building blocks used to synthesize the pendant moieties (non-fluorogenic parts) in organic solvents; (iii) the BODIPY derivatives had a potential tendency to aggregation, as in an aqueous environment, three of the compounds (**1**, **2** and **4**) tend to form weakly emissive nanoparticles whereas one of them (**3**) remained soluble and highly fluorescent; (iv) the tendency to aggregation was also important for **3** at high concentration, whereas at the nanomolar range of concentration this phenomenon is absent for all the compounds; (v) all the compounds were internalized by HT-29 cells and localized subsequently in lysosomes, but notably molecule **3** (made with lysine as a building block) was the one displaying a higher loading and a more specific lysosomal location (Pearson's correlation coefficient 0.88); (vi) molecule **3** also performed as an efficient lysosomal marker in a cellular model of lysosomal storage disease (Niemann-Pick type C).

Finally, the overall conclusion that can be drawn from this thesis results is that amino acid-based (nano)systems are a promising class of structure for biomedical applications, given their high biocompatibility and functionality, stimuli-responsiveness, batch-to-batch reproducibility, and reduced synthetic

costs. Amino acids self-assemble into diverse hierarchical architectures with a broad range of properties (size, shape, agglomeration/aggregation state, morphology/topography, solubility…) allowing a scope of applications in chemistry, material science and medicine. We hope that the work presented here will contribute positively to developing smart systems based on different amino acid building blocks with improved properties for biomedical applications. Furthermore, we wish our studies will shed relevant and valuable light on appropriate building blocks, self-assembly process, stimuli-responsiveness, and fluorescence phenomena in practical applications, *e.g.*, developing innovative materials, targeted and controlled delivery and fluorescence imaging.